

**Nanostructured Metal Oxides and Carbides  
*via* Controlled Thermal Decomposition of  
Cyano-Bridged Coordination Polymers**

シアノ架橋配位高分子の熱処理によるナノ構造有する酸化物及び炭化物の合成

**July 2016**

**Mohamed Barakat Zakaria    MOHAMED**  
モハメッド    モハメッド    バラカット    ザカリア

**Nanostructured Metal Oxides and Carbides  
*via* Controlled Thermal Decomposition of  
Cyano-Bridged Coordination Polymers**

シアノ架橋配位高分子の熱処理によるナノ構造有する酸化物及び炭化物の合成

**July 2016**

**Waseda University**

**Graduate School of Advanced Science and Engineering**

**Department of Nanoscience and Nanoengineering**

**Research on Synthetic Chemistry of Nanomaterials**

**Mohamed Barakat Zakaria    MOHAMED**

モハメッド    モハメッド    バラカット    ザカリア

بِسْمِ اللَّهِ الرَّحْمَنِ الرَّحِيمِ  
شَهِدَ اللَّهُ أَنَّهُ لَا إِلَهَ إِلَّا هُوَ وَالْمَلَائِكَةُ وَأُولُو الْعِلْمِ قَائِمًا بِالْقِسْطِ ۚ لَا إِلَهَ إِلَّا هُوَ الْعَزِيزُ الْحَكِيمُ.

صَدَقَ اللَّهُ الْعَظِيمُ

سورة آل عمران (18)

**In the name of Allah, Most Gracious, Most Merciful**

Allah (God) bears witness none has the right to be worshipped but He, and *also do* the angels, and those having knowledge (Scientists) are standing for justice (also God gave this witness); (He is always) maintaining his creation in justice. None has the right to be worshipped but He, the All-Mighty, the All Wise.

**(Holy Quran, Chapter 3, Surat Al-Imran (18))**

# Preface

Coordination polymers (CPs), including metal organic frameworks (MOFs) and porous coordination polymers (PCPs), have attracted much attention for years because of their beneficial uses in catalysis, drug-delivery systems, energy, storage, separation, and environmental applications. Recent research efforts have been devoted to tailor-made nanoarchitected cyano-bridged coordination polymers (CPs) to meet the developments of the aforementioned applications. All 2D and 3D nanostructures can be simply synthesized by purposefully changing the precursor compositions (*e.g.*, types and concentrations of metal ions, ligands, and chelating agents) and synthetic conditions (*e.g.*, synthetic temperatures, aging temperatures and times, and pHs). The first target of my PhD thesis is the rational design of various 2D-shaped cyano-bridged coordination polymers (CPs) through a solution phase approach and then hybridization with graphene oxide sheets. But I also reported the 3D-shaped ones (Prussian Blue (PB) and PB analogues cubes) to show the effect of the synthetic parameters on the final morphology of products from the same family ( $-M-C\equiv N-\acute{M}-$ , where; M and  $\acute{M}$  are Co, Ni, Fe, Mn, etc.). So, it is a duty to show the potential of my synthetic approach for preparation of various morphologies and compositions. The effect of the synthetic parameters on the final morphology of products is carefully discussed.

As a second target, a controlled thermal treatment of both 2D and 3D nanostructures in air or in an inert atmosphere can yield nanoporous metal oxides and carbides, respectively. The large fraction of metal centers can be utilized as the metal source, and the removable organic components, by simple calcination, can provide nanopores. The original morphology is almost retained, even after the thermal treatments. My strategy has proven to be a promising solid-state method for the preparation of nanoporous metal oxides and carbides with fine crystal structures. This method has great potential to overcome difficulties in the preparation through traditional approaches, such as supramolecular templating. My obtained nanoporous materials show a superior performance as electrode materials for supercapacitors, electrocatalysts for an oxygen reduction reaction (ORR) and oxygen evolution reaction (OER), and drug carriers for drug delivery systems (DDSs).

**Chapter 1** introduces the recent progress related to coordination compounds. Their conversion into functional nanoporous materials is also mentioned.

**Chapter 2** explains a thermal decomposition of cyano-bridged Co-Fe CPs with cubic morphology to prepare nanoporous Co-Fe mixed oxides. During the thermal treatment, the organic units (carbon and nitrogen) are completely removed, and only metal contents are retained to prepare nanoporous metal oxides. The original nanocube shapes are retained well even after the thermal treatment. I further extend this concept to prepare nanoporous metal oxides with hollow interiors. Core-shell heterostructures consisting of different metal cyanide hybrid CPs are prepared first. Then, only the cores are dissolved by chemical etching using a hydrochloric acid solution (*i.e.*, the cores are used as sacrificial templates),

leading to the formation of hollow interiors in the nanocubes. These hollow nanocubes are also successfully converted to nanoporous metal oxides with hollow interiors by controlled thermal treatment.

**In Chapter 3**, an oriented and controlled crystal growth of various cyano-bridged CPs is realized by using trisodium citrate dihydrate (TSCD) as a chelating agent. After mixing manganese acetate with TSCD, the formed Mn-citrate complex tends to release a few  $\text{Mn}^{2+}$  ions steadily and slowly, which then react with the ligands at the initial stage of the reaction. Subsequently, the generated nuclei further grow from the interaction between the released  $\text{Mn}^{2+}$  and  $[\text{Mn}(\text{CN})_6]^{3-}$ ,  $[\text{Co}(\text{CN})_6]^{3-}$ , and  $[\text{Ru}(\text{CN})_6]^{4-}$  anions to form several types of cyano-bridged CPs (abbreviated as MnCNMn, MnCNCo, and MnCNRu, respectively). After thermal treatment in air, the as-prepared CPs can be decomposed into their corresponding nanoporous Mn-based oxides. Surprisingly, the electrochemical analysis reveals that the Mn-Ru oxide prepared from MnCNRu is a promising catalyst for the production of  $\text{H}_2\text{O}_2$  by selectively catalyzing the ORR through a 2-electron pathway.

**Chapter 4** shows potential applications of PB-derived nanoporous iron oxide. Nanoporous iron oxide nanoparticles with superparamagnetic behavior are successfully synthesized from Prussian blue (PB) cubes through a thermal conversion method and applied to the intracellular drug-delivery systems (DDSs) of bladder cancer cells (*i.e.*, T24) with controlled release and magnetic guiding properties. The synthesized materials show great potential as drug carriers with high biocompatibility, controlled release, and magnetic targeting features for future intracellular DDSs. Furthermore, by tuning the applied calcination temperatures, the crystalline degrees and phases of nanoporous Fe oxides can be controlled from the amorphous phase to the  $\gamma\text{-Fe}_2\text{O}_3$  and  $\alpha\text{-Fe}_2\text{O}_3$  phases. Nanoporous  $\alpha\text{-Fe}_2\text{O}_3$  with a high surface area is useful for photocatalytic applications.

The 2D CPs have a highly accessible surface area that permits guest molecules to effectively access the micropores in the CPs. Moreover, 2D CPs have many active sites for catalytic and electrochemical reactions, and furthermore assembled CPs can be used as membrane filters.

**Chapter 5** demonstrates a bottom-up synthesis of 2D cyano-bridged Cu-Pt CP nanoflakes using TSCD as a chelating agent, which controls the nucleation and the crystal growth. The citrate anions directly interact with Cu cations, as confirmed by a  $^1\text{H-NMR}$  spectroscopic study. The Cu ions gradually released from the Cu-citrate complex are gradually converted into Cu-Pt CPs in the reaction with  $[\text{Pt}(\text{CN})_4]^{2-}$ . The generation speed of Cu-Pt CPs was significantly delayed in the presence of citrate ions, thereby leading to the controlled growth of single crystalline Cu-Pt CPs with a plate morphology. The lateral sizes of the Cu-Pt CP flakes are controlled by changing the amount of trisodium citrate used. I strongly believe that my method will be useful for the preparation of other types of 2D CPs flakes. Such 2D CPs can be potentially used for preparation of nanoporous metal oxides and carbides with new solid state properties.

**Chapter 6** demonstrates the controlled synthesis of cyano-bridged Ni-Ni CPs with 2D morphology. After calcination in air, the 2D Ni-Ni CPs can be transformed into nanoporous nickel oxide

(NiO) with a highly accessible surface area. This strategy is adopted in order to form 2D nanoporous NiO with tunable porosity and crystallinity by changing the applied calcination temperatures. During this thermal treatment, organic units (carbon and nitrogen) are completely removed and only the metal content remains to take part in the formation of nanoporous NiO. The original 2D flake-shapes are almost retained, even after thermal treatment at low temperature, but they are completely destroyed at high temperature because of further crystallization in the framework. Nanoporous NiO with high surface area shows significant efficiency and interesting results for supercapacitor application. This concept is also applicable to nanoporous nickel-cobalt mixed oxides. These mixed oxides demonstrate high electrocatalytic activity for oxygen evolution reaction (OER).

**Chapter 7** discusses a novel strategy involving the hybridization of cyano-bridged CP flakes with graphene oxide (GO) sheets. The positively-charged cyano-bridged Ni-Ni CPs are spontaneously hybridized with the negatively-charged GO sheets and thermally treated in air, so the organic materials can be removed without affecting the integrity of the parent GO sheets. Thus, the layer-by-layer construction followed by a thermal treatment can produce a new hybrid nanoporous material consisting of NiO and GO. The obtained hybrid material exhibits an efficient catalytic activity and stability for the oxygen reduction reaction (ORR). I also demonstrate the in-situ crystallization of cyano-bridged Ni-Ni CP flakes on the surface of GO sheets. The GO sheets are utilized as a nucleation site, and then the NiC/Ni-coated GO sheets self-assemble to form ordered lamellar nanomaterials. This approach might be applied to many other inorganic-organic hybrids for ordered layer-by-layer (LbL) architectures. Thermal treatment under nitrogen yields a Ni<sub>3</sub>C-GO composite with a similar morphology to the starting material, and the Ni<sub>3</sub>C-GO composite exhibits good electrocatalytic activity and excellent durability for the ORR.

**Chapter 8** summarizes my thesis and future prospects. Through my thesis, I found that the chelating agent strongly affects the speed of the crystallization. With a reaction rate a hundred times slower, the synthetic conditions become optimal to trigger a controlled crystal growth. I have realized various cyano-bridged CP nanostructures with different compositions, which can serve as excellent precursors for the synthesis of many nanoporous metal oxides and carbides. In the future, my strategy can be extended for the synthesis of other tailor-made cyano-bridged CPs with their potential applications for the desired nanoporous inorganic materials.

# Contents

## Chapter 1

1.1.	General Introduction.....	7
1.2.	Essentials.....	9
1.2.1.	Nanoarchitectonics.....	10
1.2.2.	Interfacial Supramolecular Chemistry.....	12
1.3.	Coordination Nanoarchitectonics 1: Assembly in 2D.....	15
1.3.1.	Coordination Complexes at the Air-Water Interface.....	15
1.3.2.	Coordination and Patterning on Surface.....	20
1.3.3.	Two-Dimensional Coordination Polymer.....	24
1.4.	Coordination Nanoarchitectonics 2: Conversion into Materials in 3D.....	28
1.4.1.	Morphology Control of Coordination Polymer.....	29
1.4.2.	Thermal Conversion to Nanoporous Inorganic Materials.....	34
1.5.	Aims and objectives of this dissertation.....	39
1.6.	References.....	42

## Chapter 2

2.	<b>Single-Crystal-like Nanoporous Spinel Oxides: A Strategy for Synthesis of Nanoporous Metal Oxides Utilizing Metal-Cyanide Hybrid Coordination polymers.....</b>	<b>54</b>
2.1.	Introduction.....	54
2.2.	Experimental Section.....	57
2.2.1.	Chemicals.....	57
2.2.2.	Synthesis of Solid Metal-Cyanide Hybrid CPs and Their Thermal Conversion to Nanoporous Metal Oxides.....	57
2.2.2.1.	Synthesis of Solid CoCo Nanocubes.....	57
2.2.2.2.	Synthesis of Solid FeCo Nanocubes.....	58
2.2.2.3.	Synthesis of Solid FeFe Nanocubes.....	58
2.2.2.4.	Thermal Conversion to Nanoporous Metal Oxides.....	58
2.2.3.	Synthesis of Core-Shell Nanocubes of Metal-Cyanide Hybrid CPs, Creation of Hollow Interiors, and Their Thermal Conversion to Nanoporous Metal Oxides.....	59
2.2.3.1.	Synthesis of NiCr Nanocubes.....	59
2.2.3.2.	Synthesis of NiCr@CoCo Nanocubes.....	59
2.2.3.3.	Synthesis of NiCr@FeCo Nanocubes.....	59
2.2.3.4.	Synthesis of NiCr@CoFe Nanocubes.....	60
2.2.3.5.	Synthesis of NiCr@FeFe Nanocubes.....	60
2.2.3.6.	Preparation of Hollow Nanocubes by Removal of NiCr Cores and Thermal Conversion to Nanoporous Metal Oxides.....	60
2.2.4.	Characterizations.....	61

2.2.4.1. Materials Characterization.....	61
2.2.4.2. Electrochemical Measurement.....	61
2.3. Results and Discussion.....	62
2.3.1. Synthesis of Solid Metal-Cyanide Hybrid CPs and Their Thermal Conversion to Nanoporous Metal Oxides.....	62
2.3.2. Synthesis of Core-Shell Heterostructures of Metal-Cyanide Hybrid CPs, Creation of Hollow Interiors, and Their Thermal Conversion to Nanoporous Metal Oxides...	72
2.4. Conclusion.....	85
2.5. References.....	86

## Chapter 3

3. <b>Nanoporous Mn-Based Electrocatalysts through Thermal Conversion of Cyano-Bridged Coordination Polymers toward Ultra-High Efficient Hydrogen Peroxide Production.....</b>	92
3.1. Introduction.....	92
3.2. Experimental Sections.....	94
3.2.1. Synthesis of MnCNMn, MnCNCo, and MnCNRu PBAs and Their Thermal Conversion.....	94
3.2.2. Electrochemical Measurements.....	95
3.2.3. Characterizations.....	96
3.3. Results and Discussion.....	97
3.3.1. Preparation of MnCNRu, MnCNCo, and MnCNMn Precursors.....	97
3.3.2. Thermal Conversion of MnCNRu, MnCNCo, and MnCNMn Cubes.....	102
3.3.3. Electrochemical Catalysis Using the Obtained Oxides.....	109
3.4. Conclusions.....	115
3.5. References.....	116

## Chapter 4

4-1. <b>Prussian Blue Derived Nanoporous Iron Oxides as Anticancer Drug Carriers for Magnetic-Guided Chemotherapy.....</b>	121
4-1.1. Introduction.....	121
4-1.2. Experimental Section.....	124
4-1.2.1. Chemicals.....	124
4-1.2.2. Preparation of PB Nanocubes.....	124
4-1.2.3. Cell-Related Experiments.....	125
4-1.2.4. Characterization.....	126
4-1.3. Results and Discussion.....	126
4-1.4. Conclusion.....	135
4-1.5. Acknowledgements.....	135
4-1.6. References.....	135
4-2. <b>Thermal Conversion of Hollow Prussian Blue Nanoparticles into Nanoporous Iron Oxides with Crystallized Hematite Phase.....</b>	139



4-2.1.	Introduction.....	139
4-2.2.	Experimental Details.....	141
4-2.2.1.	Preparation of Hollow PB Nanoparticles.....	141
4-2.2.2.	Characterization.....	142
4-2.3.	Results and Discussion.....	142
4-2.4.	Conclusion.....	150
4-2.5.	Acknowledgments.....	150
4-2.6.	References.....	151

## Chapter 5

5.	<b>Controlled Crystallization of Cyano-Bridged Cu-Pt Coordination Polymers with Two-Dimensional Morphology.....</b>	154
5.1	Introduction.....	154
5.2.	Preparation of 2D Cu-Pt Nanosheets.....	156
5.3.	Apparatus.....	156
5.4.	Characterization of Various 2D Cu-Pt Nanosheets.....	157
5.5.	Conclusion.....	165
5.6.	References.....	165

## Chapter 6

6-1.	<b>Controlled Synthesis of Nanoporous Nickel Oxides with Two-Dimensional Shapes through Thermal Decomposition of Metal-Cyanide Hybrid Coordination Polymers.....</b>	168
6-1.1.	Introduction.....	168
6-1.2.	Experimental Section.....	171
6-1.2.1.	Chemicals.....	171
6-1.2.2.	Synthesis of 2D Ni-CP Nanoflakes.....	171
6-1.2.3.	Thermal Conversion from 2D Ni-CP Nanoflakes to Nanoporous NiO.....	172
6-1.2.4.	Electrochemical Measurements.....	172
6-1.2.5.	Characterization.....	173
6-1.3.	Results and Discussion.....	174
6-1.3.1.	Formation of 2D-Shaped Ni-CPs.....	174
6-1.3.2.	Conversion from 2D Ni-CPs to Nanoporous NiO.....	179
6-1.3.3.	Supercapacitor Application Using Nanoporous NiO.....	188
6-1.4.	Conclusion.....	190
6-1.5.	Acknowledgements.....	191
6-1.6.	References.....	191
6-2.	<b>Synthesis of Nanoporous Ni-Co Mixed Oxides by Thermal Decomposition of Metal-Cyanide Coordination Polymers.....</b>	195
6-2.1.	Introduction.....	195
6-2.2.	Experimental Section.....	197
6-2.2.1.	Materials Synthesis.....	197

6-2.2.2. Characterization.....	199
6-2.3. Results and Discussion.....	199
6-2.4. Conclusion.....	208
6-2.5. Acknowledgments.....	209
6-2.6. References.....	209

## Chapter 7

7-1. <b>Layer-by-Layer Motif Hybridization: Nanoporous Nickel Oxide Flakes Wrapped into Graphene Oxide Sheets toward Enhanced Oxygen Reduction Reaction.....</b>	212
7-1.1. Introduction.....	212
7-1.2. Experimental Details.....	214
7-1.2.1. Chemicals.....	214
7-1.2.2. Synthesis of NiCNNi Flakes.....	214
7-1.2.3. Synthesis of GO Sheets.....	215
7-1.2.4. Synthesis of NiO-GO Hybrids.....	215
7-1.2.5. Electrochemical Measurements.....	216
7-1.2.6. Characterization.....	216
7-1.3. Results and Discussion.....	217
7-1.4. Conclusion.....	226
7-1.5. References.....	226
7-2. <b>Self-Construction from 2D to 3D: One-Pot Layer-by-Layer Assembly of Graphene Oxide Sheets Held Together by Coordination Polymers.....</b>	229
7-2.1. Introduction.....	229
7-2.2. Experimental Details.....	231
7-2.2.1. Chemicals.....	231
7-2.2.2. Synthesis of GO Sheets.....	231
7-2.2.3. In-situ Growth of NiCNNi Flakes onto The Surface of GO Sheets and Thermal Conversion into Ni <sub>3</sub> C-GO Hybrid.....	231
7-2.2.4. Characterization.....	232
7-2.2.5. Electrochemical Measurements.....	233
7-2.3. Results and Discussion.....	234
7-2.4. Conclusion.....	249
7-2.5. References.....	250

## Chapter 8

8. General Conclusions and Future Prospects.....	253
8.1. General Conclusion.....	253
8.1.1. Direct Thermal Treatments.....	258
8.1.2. Kirkendall Effect.....	259
8.1.3. Etching.....	260
8.1.4. Hard-Templating Method.....	262

8.2.	Future Perspectives.....	262
8.3.	References.....	266
	<b>List of Achievements</b> .....	269
	<b>Acknowledgements</b> .....	274

# Chapter 1

# Chapter 1

## 1.1. General Introduction

The development of energy-efficient systems with well-designed functional materials is an important key to solve current energy and environmental issues. These problems are originating from the massive human activity, and controlling the nanosized structure of materials and systems is a crucial factor to start solving them [1]. Well-designed molecules and their highly sophisticated arrangement result in incredibly high efficiency as well as excellent specificity and selectivity at a macroscopic scale. Biological processes such as photosynthesis and materials conversions are attractive examples of newly designed materials/systems [2].

In order to produce highly functional artificial materials based on molecular (or nanomaterials) arrangement, key concepts such as nanotechnology, self-assembly (or self-organization), supramolecular chemistry, and materials science have to be appropriately combined. Ideally, nanoscale units (functional molecules and nanomaterials) produced by nanotechnologies are organized by spontaneous supramolecular processes into functional materials [3]. However, there are still some unbridgeable gaps between the concept of nanotechnology and supramolecular organization. Basically, the current nanoscience and nanotechnology mainly focus on fundamental aspects such as the observation of structures and phenomena at a nanometer-scale, while far advanced functions have yet not been fully explored.

Although the technologies related to device fabrication are regarded as highly successful accomplishments, they are actually categorized as a microtechnology (and not nanotechnology). Therefore, the contribution of nanotechnology to nanoscale fabrication is indeed rather ambiguous and still remains unrealistic. Combining nanotechnologies with realistic supramolecular chemistry and materials science have not yet been accomplished.

In order to solve this challenging situation, some novel notions have to be proposed and established. As a breakthrough concept, an advanced terminology, *nanoarchitectonics*, has been recently proposed by Aono and coworkers [4], aiming at architect functional materials and advanced systems from nanometer-scale unit objects and building blocks through the harmonization of various actions and events (*e.g.*, accurate regulation of atomic and molecular arrangements, chemical reaction-based conversion of materials, self-assembly/organization, structural controls with external physical stimuli, etc.). This novel notion is more suitable for describing supramolecular processes and materials synthesis.

Herein, I focus on ‘coordination’ as a structure-directing driving force during materials fabrication. Coordination chemistry has several distinct advantages in architecting materials [5]. The interactions between metals and ligands are strong and highly directional, which are favorable to arrange components and fixing structures in designable ways. Combining components, such as metals and organic ligands, is necessary to ensure diverse construction motifs. Metal-ligand coordination is multivalent and can be extended to multiple directions from one metal center, which is a desirable characteristic for structure grown from nano-to macro-scale. Therefore, coordination chemistry has a critical role to play in materials nanoarchitectonics, although its relevance is not yet well recognized in current science and technology. The main goal of this contribution is to inform the readers about the importance of the combination between nanoarchitectonics and coordination chemistry as well as their stabilities from a thermodynamic

standpoint.

I also add one additional concept to coordination nanoarchitectonics here: the effect of interfaces. Interfacial systems and their low-dimensional structure often consist in an appropriate media to bridge nanoscale phenomena and macroscopic 3D structures [6]. These media work as gateways for architecting 3D materials from nanoscale coordination chemistry. In addition, coordination materials with anisotropic and directional properties can be created through interfacial processes. In fact, the preparation of coordination polymers at the interfacial medium have been recently researched [7].

According to the above-mentioned backgrounds and motivations, I here summarize recent activities in coordination chemistry-driven materials science, mainly porous coordination polymers and metal-organic frameworks (MOF), to make readers aware of the deep relation between coordination chemistry and nanoarchitectonics. This work starts with a brief description of the essences behind nanoarchitectonics and interfacial supramolecular chemistry, followed by a summary of recent research divided into two sections: (i) materials construction in 2D, including coordination complex at the air-water interface, coordination and patterning on solid surfaces, and 2D coordination polymers; (ii) materials construction in 3D such as morphology control of coordination polymers and their conversion into nanomaterials (**Figure 1.1**).

## 1.2. Essentials

Before developing on recent examples of research activity, key terms in this contribution, namely ‘nanoarchitectonics’ and ‘interfacial supramolecular chemistry’, are briefly summarized in the following two sections.

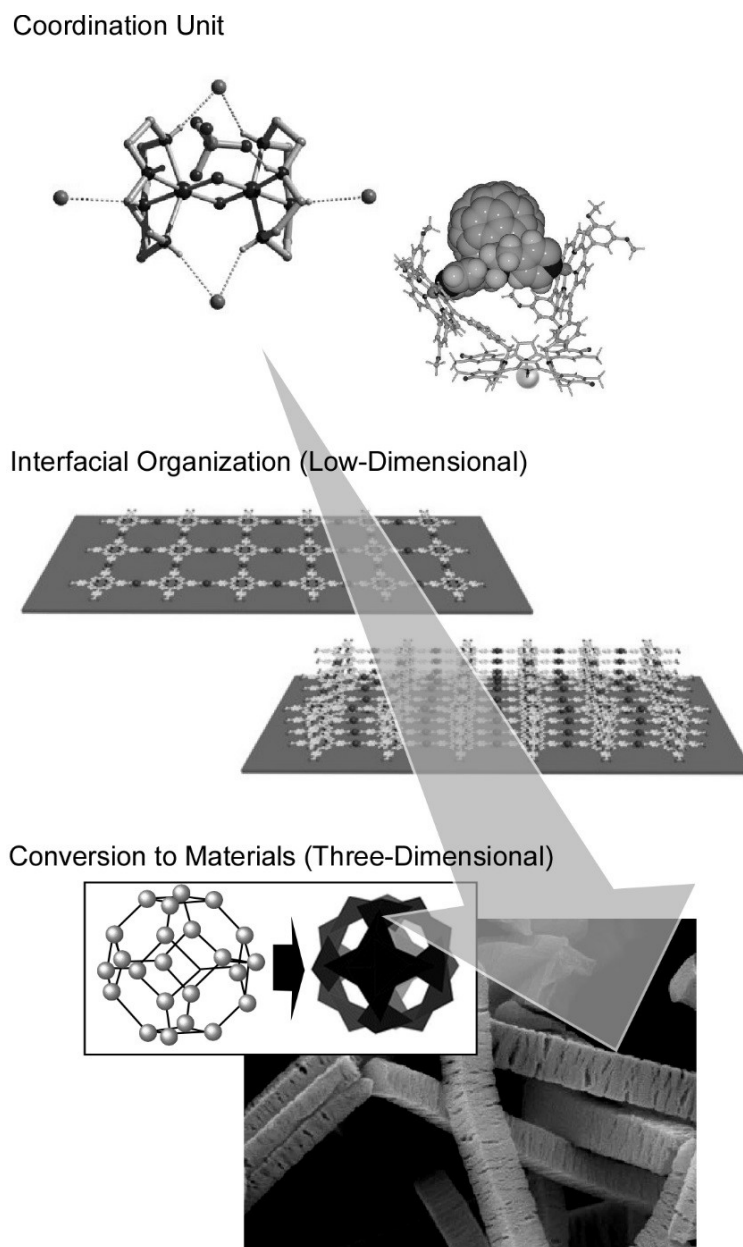


**Figure 1.1.** Synthetic strategy from coordination units to interfacial organization and 3D materials.

## 1.2.1. Nanoarchitectonics

In order to highlight the unique features which define nanoarchitectonics, rough outlines of the fabrication processes involved in macros- and microscopic technologies are summarized here (**Figure 1.2**). Macroscopic structures can be fabricated accurately according to their blueprints and



design drawings. Similar processes to the ones employed in macroscopic fabrication can also be found at a microscopic scale. At this level, microfabrication can create finely integrated structures with ultra-high precision, thanks to advanced methods (*e.g.*, lithographic techniques). Thus, microscale-objects exactly reflecting their blueprint can be constructed and implemented in finely designed tools and sophisticated processes.

Following further reduction of the material size to nanoscale, disturbances and uncertainties based on thermal/statistical fluctuations and mutual components interactions start to cause uncontrollable and unexpected effects. Thus, nanoscale fabrication cannot obey the chronology of a typical blueprint-based procedure. The preparation of functional nanomaterials have to be achieved in concert with the harmonization of various interactions and effects that control the organization of the structure through stimulating processes taking place spontaneously, such as self-assembly/organization, atomic/molecular manipulation, chemical reactions or application of external physical stimuli. These processes should be regarded as an entire architectonic scheme based on a set of building blocks, and not as the combination of individual mechanisms. This recent terminology, *nanoarchitectonics*, has been proposed as a new paradigm of materials science and technology in nanoscale fabrication [8]. According to Masakazu Aono, one of the founders of this concept, nanoarchitectonics permits (i) the production of reliable nanomaterials and nanosystems upon the organization of nanoscale structures with unavoidable unreliabilities, (ii) the development of new functionalities based on mutual interactions of individual components, (iii) the creation of unexpected emergent functionalities from assembling and organizing a huge number of nano-building blocks, and (iv) the exploration of a new theoretical field to describe the above-mentioned phenomena.

Not limited to a strict definition, the term *nanoarchitectonics* has been used in order to stress on the importance of organizing nano-components into functional materials in various

research fields, including functional and hybrid materials [9], nanoscale fabrication [10], energy and environmental technologies [11], physical and device applications [12], biological and biomedical usages [13], and supramolecular assemblies of functional materials [14], where various types of interactions promoting and maintaining the assembly are present. However, the use of coordination bondings has not been highlighted exhaustively, although they possess several advantages to form and preserve nanostructures. In particular, both structural (directional) precision and dynamic equilibrium are features which make coordination chemistry an attractive tool for novel nanoarchitectonics processes.

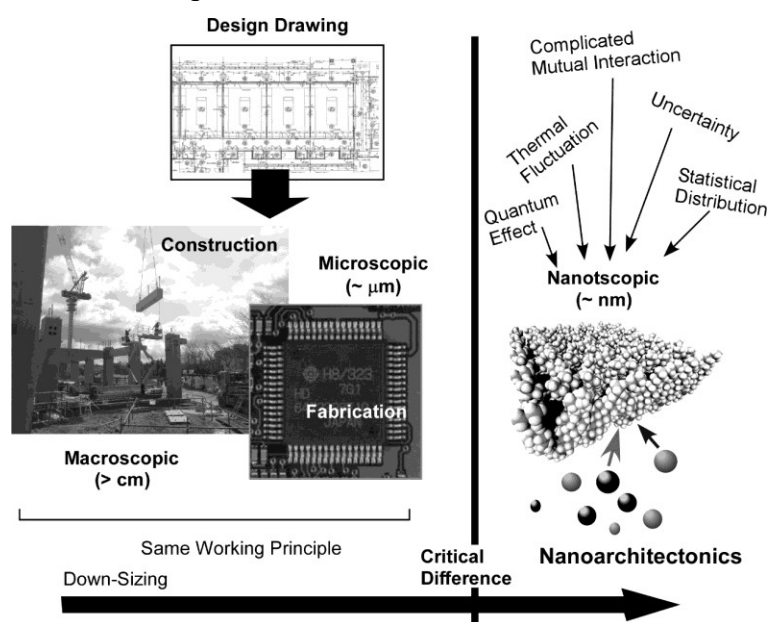


**Figure 1.2.** Nanoarchitectonics: nanoscale fabrication is different from those in macroscale and microscale dimensions.

### 1.2.2. Interfacial Supramolecular Chemistry

When architecting functional structures, supramolecular assemblies in low-dimensional media sometimes can become important processes, as was recently reported [15]. Prior to describing the interfacial processes of coordination nanoarchitectonics in the next section, basic features of

interfacial supramolecular chemistry are briefly explained here (**Figure 1.3**) [16].

The control over the association constants and binding energies in supramolecular assemblies are crucial factors. Therefore, most of the scientists in the field have made considerable efforts towards designing and synthesizing optimal chemical structures by assembling specific components. However, the resulting interfacial effects often interfere much more than through the modification of the chemical structures [17]. For example, the binding constant of a phosphate-guanidinium pair in aqueous bulk solution was found to be apparently small ( $1.4 \text{ M}^{-1}$ ), whereas the binding constants of the micelles, as mesoscopic surfaces, was measured to be  $10^2 - 10^4 \text{ M}^{-1}$  [18]. More interestingly, at the macroscopic air-water interface, this value becomes much greater ( $10^6 - 10^7 \text{ M}^{-1}$ ) [19]. These examples strikingly indicate that controlling the interfacial environment has a considerable effect on the structural chemistry, when compared to varying the binding constant.

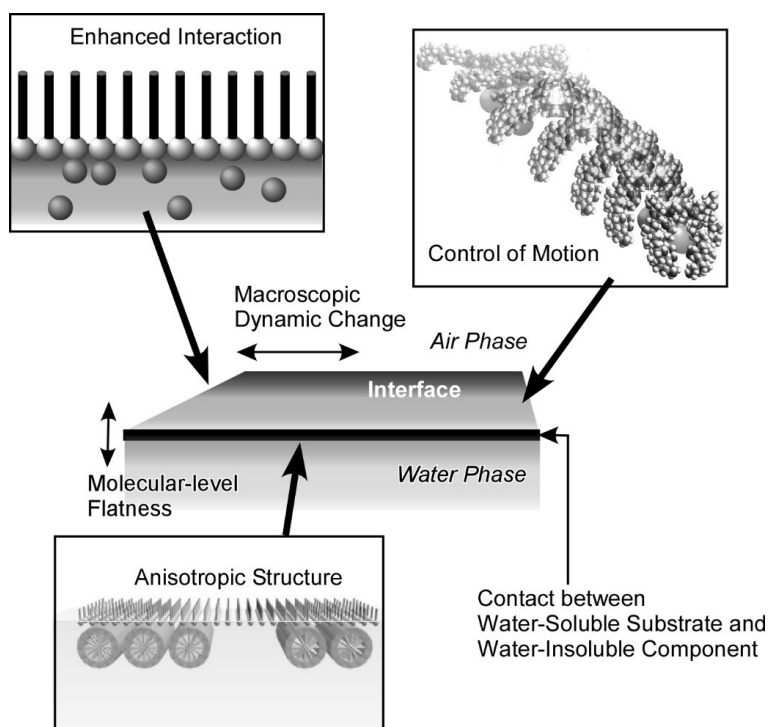


**Figure 1.3.** Unique features and advantages in supramolecular chemistry at interfacial media.

By using reaction field calculations combined with AM1 molecular orbital methods, Sakurai and

coworkers predicted enhanced molecular recognition efficiency at the interface [20]. A complementary pair of guanidinium-phosphate was put at various positions of a hetero-dielectric media (*i.e.*, an interfacial system with two far-off dielectric constants, ca. 80 for the aqueous phase and ca. 2 for the lipid phase). The binding constants were calculated after changing systematically the distance between guanidinium and phosphate. Consequently, it was deduced that the electrostatic hydrogen bonding of guanidinium-phosphate can be efficiently formed even when exposed to an aqueous environment. In a low dielectric medium, the electronic states of the recognition sites at the aqueous interface are remotely affected by the non-polar phase, which significantly increases the molecular association efficiency. The same research group also used the Poisson-Boltzmann equation with the Debye-Hückel approximation to study the air-water interface, which revealed a significant modulation of the potential on the water side upon contact with a nonpolar lipid phase [21].

Interfaces are media which can be as suitable for molecular interaction as for molecular manipulation [22]. The lateral direction of the interfacial medium appears infinite, and macroscopic manipulation in centimeter- and meter-scale can be easily applied. In contrast, the thickness is neighboring the nano- and molecular scale. Therefore, macroscopic mechanical deformations can be reinterpreted at a molecular level, *i.e.*, the molecular manipulation and nanoscopic functional control can be achieved manually at a dynamic interface such as at the junction between air and water. For example, upon hand-motion-like macroscopic movements, such as the compression and expansion of macroscopic Langmuir monolayer, the manipulation of molecular machines for reversible capture/release of guest molecules [23], chiral discrimination of amino acids [24] and discrimination of faint structural differences between thymine and uracil [25] become possible.

The enhanced confinement of molecular interactions and the dynamic nature of

functional molecules within interfacial media play important roles during structural fabrication. Applying highly directional and multivalent coordination chemistry to such anisotropic and heterogeneous interfacial media can be beneficial for functional nanoarchitectonics. Recently, several research activities on the fabrication of nanostructure based on coordination chemistry have been reported and will be summarized in the next sections.

## 1.3. Coordination Nanoarchitectonics 1: Assembly in 2D

### 1.3.1. Coordination Complexes at the Air-Water Interface

Interfacial media, such as the air-water interface have been used for molecular recognition and supramolecular assembly through non-covalent molecular interactions where the presence of coordination is negligible compared to hydrogen bondings and electrostatic interactions [26]. However, several examples using coordination complexes at the air-water interface were reported. Langmuir monolayers and Langmuir-Blodgett (LB) films can provide thin film structures for redox active coordination complexes as well as nano-assemblies useful for device fabrication.

For example, Talapatra, Goswami, and coworkers prepared a Langmuir monolayer of chromium(III) azo-anion-radical complexes using a 2-(aryloxy)pyridine-containing ligand with a long alkyl chain [27]. The formed monolayer was transferred onto a platinum working electrode by a Langmuir-Schaefer (LS) technique. Voltammograms of the electrode appeared to be stable and reproducible through more than 300 redox cycles, the first oxidation taking place only after several cycles, which is an advantageous characteristic. Sohn and coworkers used asymmetric fan-shaped dendrimers with benzoic acid functional group to coordinate with  $\text{Al}^{3+}$  and  $\text{Eu}^{3+}$  metal ions [28]. The bidentate chelation of these metal ions with the carboxylate oxygen atoms resulted in different ways for the monolayer to pack. The significant differences between  $\text{Al}^{3+}$  and  $\text{Eu}^{3+}$

originate from the intrinsic nature of the ions and their coordination number. A lateral mechanical modulation induces a better stacking in the case of the Eu ion-based coordination complex.

The process of transferring floating materials at interfaces with a solid surface would often provide the opportunity to spontaneously form micro- and nanoscopic regular structures upon various phenomena, such as dewetting [29]. Clemente-Leon and Coronado *et al.* reported the patterning of coordination nanoparticles of Prussian blue (PB) through LB transfer [30]. PB coordination nanoparticles are negatively charged and can interact with a Langmuir monolayer of phospholipid dipalmitoyl-L- $\alpha$ -phosphatidylcholine. Various patterns, including vertically or horizontally-aligned and tilted fringes, were prepared at various surface pressures and transfer speeds. The patterned surfaces are expected to be useful for the development of functional systems with magnetic anisotropy.

The above example emphasizes on the achievement of preformed coordination nanoparticles, where the coordination structures themselves are not altered. However, the creation and modification of novel coordination nanostructures based on coordination chemistry at the interface would be a more attractive process as the formation of multivalent coordination bonding can be favorable for the development of extended supramolecular structures. When the ligand and metal components meet each other at the interfacial medium, a network of interlinked supramolecular structures can be anisotropically developed. Liu and coworkers pioneered the formation of regular structures with supramolecular chirality based on the interaction between achiral components at the air-water interface based on various molecular interactions [31]. In one example by Guo and Liu, the structural formation of the interfacial coordination between Ag ions in a subphase and a Langmuir monolayer of amphiphilic 2-(heptadecyl) naphtha[2,3]imidazole was investigated (**Figure 1.4**) [32].

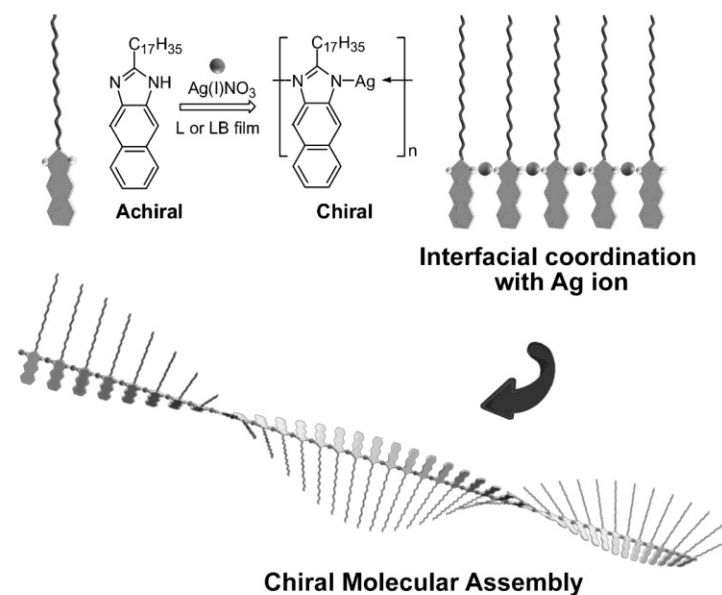


**Figure 1.4.** Chiral nanostructure formation of interfacial coordination between a Langmuir monolayer of achiral amphiphilic 2-(heptadecyl) naphtha[2,3]imidazole with Ag ion.

At the air-water interface, substituted benzimidazoles coordinate with Ag<sup>+</sup> from the subphase to produce coordination polymers showing a distinct chirality, although both the components are achiral. Neighboring naphtha[2,3]imidazole groups were linked through coordination with the Ag<sup>+</sup> ions, but the significant steric hindrance in this coordination geometry makes the alignment of the ligand arrays twisted along the backbone of the coordination polymer. Once the distorted assembly is formed, it extends as a chiral helical structure. In this process, the chiral sense from the achiral components can be determined by the accidental formation of an initial twisted coordination complex. In a recent publication, they discussed the mutual importance of the ligand structure and the metal species [33].

The formation of structure-defined network linkage driven by metal-ligand interactions at the air-water interface was accomplished by Talham and coworkers [34]. The monolayer is based on an amphiphilic pentacyanoferrate complex spread on the surface of an aqueous solution of Ni<sup>2+</sup> ions (**Figure 1.5**).

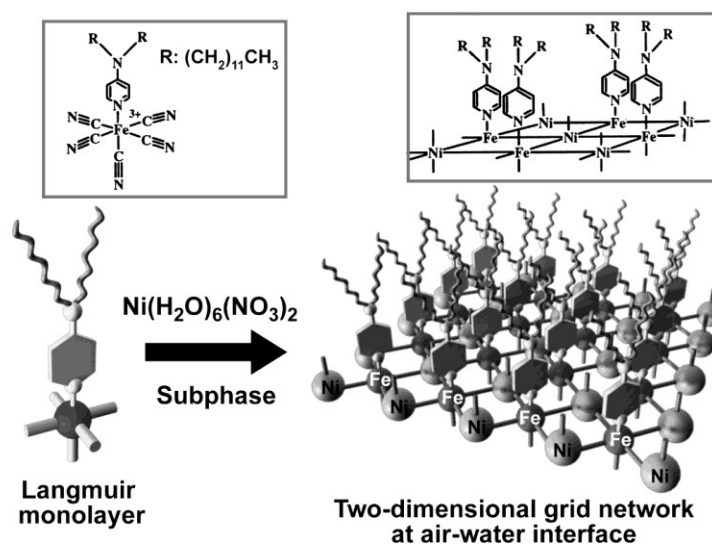


**Figure 1.5.** Formation of 2D grid structure from amphiphilic pentacyanoferrate complex as a monolayer component with aqueous  $\text{Ni}^{2+}$  ion.

This combination induces the formation of iron-nickel cyanide-bridged network within a 2D plane. The formation of a face-centered square grid structure was confirmed by characterizing the transferred LB films by grazing incidence synchrotron X-ray diffraction, which indicated that their average domain size became ca.  $36 \text{ nm}^2$ . The same 2D structure cannot be obtained from a homogeneous reaction under similar conditions. Confining the reactants within a 2D interface would be advantageous to form an anisotropic growth probably because of restricted diffusion. The ferromagnetically ordered state of LB films below 8 K was observed by magnetic measurements, revealing a significant dependence on the applied field.

A more sophisticated design for interfacial coordination structures was developed by Makiura, Kitagawa, and coworkers who prepared 2D MOF network structures and layer-by-layer architectures by taking advantage of the directional feature of coordination chemistry and structural anisotropy (**Figure 1.6**) [35]. 5,10,15,20-tetrakis(4-carboxyphenyl)porphyrinato-cobalt and pyridine were used as monolayer components and were spread from their chloroform/methanol solution onto an aqueous subphase of  $\text{Cu}^{2+}$  ions. The 2D copper-mediated



array of the porphyrin units was formed at the air-water interface and the resulting MOF sheet was transferred onto a solid substrate, such as Si(100) or quartz. After removing the unreacted or physisorbed components by intermediate washing, the next layer was deposited in order to make a layer-by-layer structure based on  $\pi$ - $\pi$  interaction. The high crystalline ordering of both in-plane and out-of-plane of the prepared layered films were confirmed by synchrotron X-ray surface crystallography. This strategy to prepared anisotropic ordered films of functional MOF can open new routes in the technologies of device fabrication.

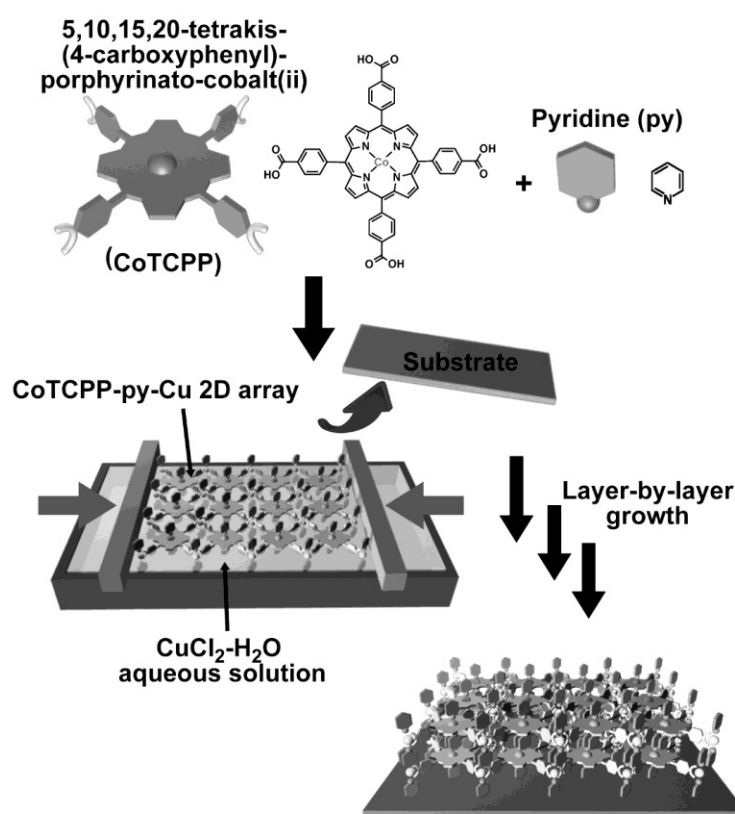


**Figure 1.6.** Formation of 2D MOF network structures and their layer-by-layer building-up wisely using 5,10,15,20-tetrakis(4-carboxyphenyl)porphyrinato-cobalt and pyridine monolayer on aqueous subphase including Cu<sup>2+</sup> ion.

Sakamoto, Schlüter, and coworkers demonstrated the preparation of free-standing 2D nanosheets based on coordination at the air-water interface (**Figure 1.7**) [36]. In their method, they used

hexafunctional terpyridine-based  $D_{6h}$ -symmetric ligand in which each terpyridine from the core ligand can be connected with the neighboring ligand through coordination with an appropriate metal ion, such as  $Fe^{2+}$ . Confining the ligand structure at the air-water interface prevents them from forming 3D coordination networks. In addition, they recently demonstrated trans-metalation within the sheets such as exchanges from  $Zn^{2+}$  to  $Fe^{2+}$ ,  $Co^{2+}$ , and  $Pd^{2+}$  [37]. The demonstrated transmetalation, consisting in positioning metal ions at defined intervals and arrangements, is usually regarded as a difficult nanofabrication technique.

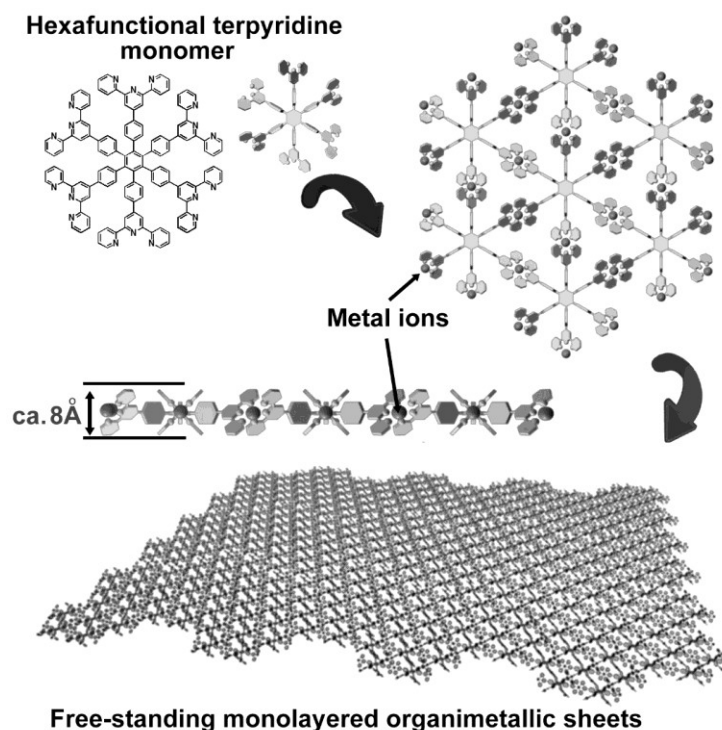


**Figure 1.7.** Preparation of free-standing 2D nanosheets base on coordination between hexafunctional terpyridine-based  $D_{6h}$ -symmetric ligand and appropriate metal ions such as  $Fe^{2+}$ .

### 1.3.2. Coordination and Patterning on Surface

As mentioned above, the 2D coordination networks at dynamic interfaces, such as air-water, provides attractive approaches for the formation of anisotropic nanoarchitectures with well-defined geometries. Because such dynamic interfaces are not convenient for practical

applications, the resulting 2D coordination structures are usually transferred onto solid substrates for proper implementation. From a practical viewpoint, the preparation of regular coordination structures directly on solid interfaces is also a promising strategy.

Auwarter and coworkers reported several approaches to prepare MOF structures through the codeposition of carbonitrile-functionalized porphyrin derivatives with an appropriate metal [38]. They codeposited the free-base form of tetra[(4-cyanophenyl)phen-4-yl]porphyrin with Co atoms onto a BN monolayer grown on Cu(111) substrate under ultrahigh vacuum conditions. The CN-Co coordination resulted in 4-fold coordination nanosheet motifs. Upon exposure to an atomic beam of Co, both the metalation of the tetrapyrrolic macrocycle with Co and the formation of a network occurred and could be regulated by controlling the deposition temperature. They also demonstrated another method for the preparation of d-f hetero-bimetallic coordination network structures through a multistep procedure (**Figure 1.8**) [39]. In the initial step, the free-base form of tetra[(4-cyanophenyl)phen-4-yl]porphyrin was codeposited on Ag(111) with Gd atoms, resulting in a well-packed structure with a square unit cell, similarly based on 4-fold coordination of CN ligands with the rare-earth atoms. In the following step, the resulting coordination structure is exposed to a beam of Co atoms which leads to the porphyrin metalation and completion of a grid-like 2D coordination network. The prepared surface network structure includes both lanthanides and transition-metals with a defined 2D arrangement and magnetic exchange interactions between the 3d and 4f elements. Therefore, these coordination networks have a great potential for applications such as magneto-responsive devices and molecular spintronics.

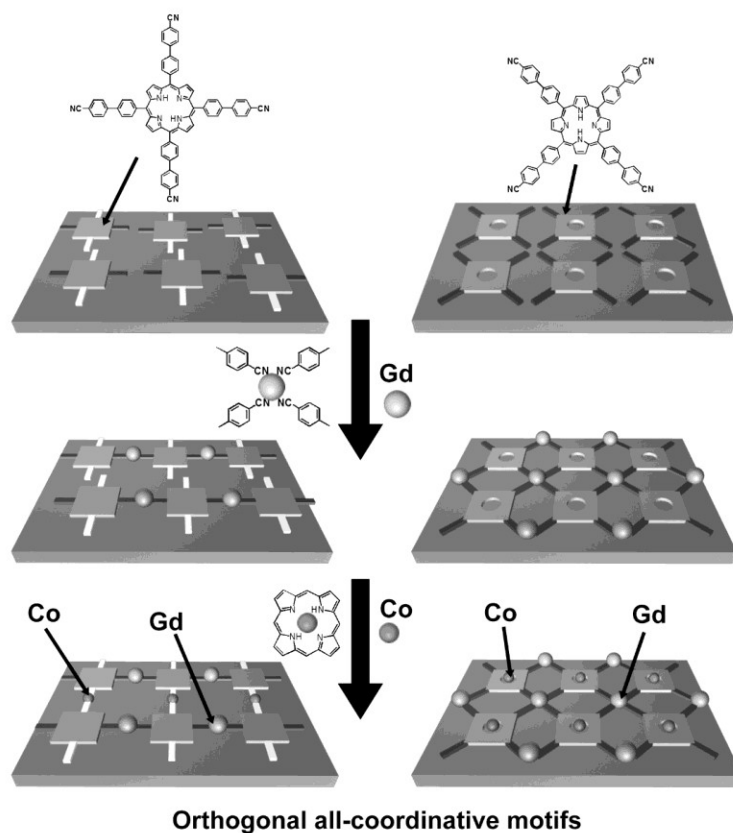


**Figure 1.8.** Preparation of d-f hetero-bimetallic coordination network structures through multistep procedure.

Shchyrba *et al.* reported a strategy to control the dimensionality of coordination polymers on a solid surface through *in-situ* modification of organic ligand [40]. As illustrated in **Figure 1.9**, the organic ligand molecule, 4,9-diaminoperylene quinone-3,10-diimine, undergoes a regulated dehydrogenation (removal of  $\text{H}_2$  or  $3\text{H}_2$ ) depending on the coexisting metal atoms on surface, such as Fe, Co, Ni, or Cu. The presence of Ni, Fe, and Co induces the transformation of 4,9-diaminoperylene quinone-3,10-diimine (DPDI) into an endo-ligand through one  $\text{H}_2$  dehydrogenation (DPDI to deh-DPDI in **Figure 1.9**). At one side of the endo-ligand, two amino groups coordinate with one metal atom, thus chelating the structures by adjacent endo-ligands and resulting in one-dimensional (1D) coordination polymers. Different metal species, such as Cu ions, can lead to further dehydration of 4,9-diaminoperylene quinone-3,10-diimine to provide

exo-ligand upon three  $H_2$  removal (DPDI to 3deh-DPDI in **Figure 1.9**). Two amino groups at the side of the ligand are converted into one azo-linkage that can coordinate with two metal atoms. In the latter case, coordination polymers with a 2D network are formed. This is a typical example of nanoarchitectonics driven by chemical reactivity.

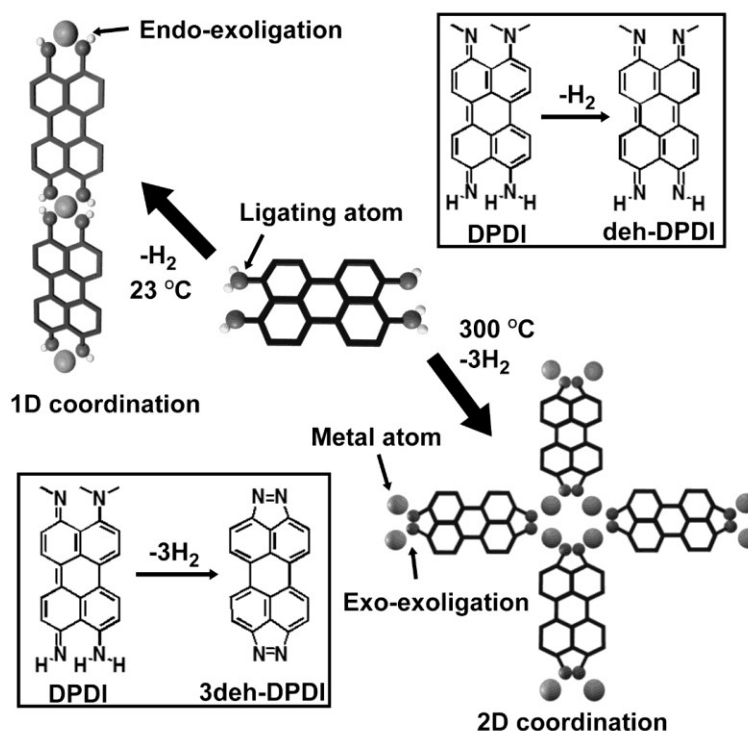


**Figure 1.9.** Modulation of coordination pattern through regulated dehydrogenation (removal of  $H_2$  or  $3H_2$ ) of ligand molecule, 4,9-diaminoperylene quinone-3,10-diimine (DRDI).

The formation of coordination nanostructures on solid interfaces as a coating technique can offer a wide spectrum of opportunities for multiple applications. For example, Zhang and coworkers reported the fabrication of various 2D nanomaterials including  $MoS_2$  nanosheets, graphene oxide, and reduced graphene oxide with zeolitic imidazolate frameworks [41]. Such hybridization strategy can lead to enhanced performance in various applications, such as device preparation. In this case, write-once-read-many-times memory devices were prepared using hybrid materials made of  $MoS_2$  and zeolitic imidazolate frameworks and exhibited high ON/OFF ratio and long

operating lifetime. The obtained device showed a bistable electrical behavior: a low (OFF) and a high (ON) current states. The OFF to ON transition worked as a writing step. Both the ON and OFF states did not show any significant fluctuations, even after more than 1500 s of test under ambient conditions. The carrier transport process is expected to be governed by a space-charge-limited-current (trap limited). The charges were transferred from the zeolitic imidazolate frameworks and trapped by MoS<sub>2</sub> at lower energy levels due to quantum confinement effect. The insulating nature of the zeolitic imidazolate framework can be used in nonvolatile memory devices. Similarly, core-shell-type coating structures, based on 2D functional materials as a core and coordination structures as a shell, are expected to be useful for various applications including catalysis and energy storage, as well as information storage devices. The coating 3D nanomaterials with coordination structures was also reported. Yang, Yaghi, and coworkers reported the preparation of MOF structures on octahedral silver nanocrystals [42]. Atomic layer deposition of aluminum oxide on silver nanocrystals was first conducted. Adding of 4,4',4'',4'''-(porphyrin-5,10,15,20-tetrayl)-tetrabenzoic acid induced the formation of MOF coating around silver nanocrystals. The deposition thickness of the aluminum layer was precisely regulated from 0.1 to 3 nm, resulting in an accurate control over the thickness of the MOF layer (10 to 50 nm).

### 1.3.3. Two-Dimensional Coordination Polymer

The anisotropic properties of coordination nanostructures are not limited to materials located on the surface or at the interfaces, but can also be expressed on the basis of dimensionally-restricted natures. Several 3D coordination polymers often have an inherent 2D structural nature. These materials are often called 2D coordination polymers and MOF [43]. In this section, recent research activities on such materials are briefly summarized. Lotsch and coworkers assembled

lamellar structures of 2D coordination polymer nanosheets with regular surfactant interlayers (Figure 1.10) [44].

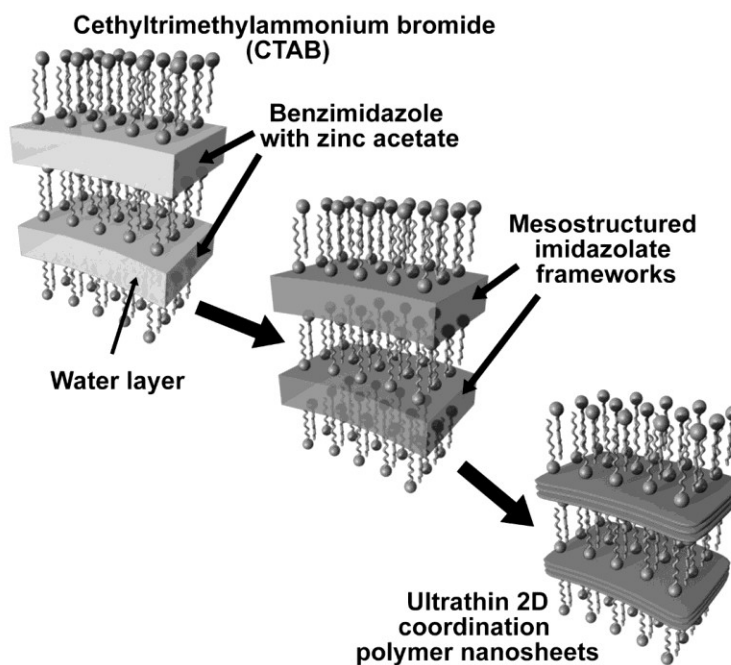


**Figure 1.10.** 2D coordination polymer nanosheets with regular surfactant interlayers

Imidazole derivatives were mixed with zinc acetate to react under reverse microemulsion conditions, involving cetyltrimethylammonium bromide (CTAB) as a surfactant component, resulting in the self-assembly of 2D zinc coordination polymer interweaved with CTAB. Probably due to structural confinement and free energy minimization at the organic-hybrid interface, a layered phase of Zn-based coordination polymer nanosheets sandwiched between the organic liquid crystal phases was formed. The layered assemblies can be liberated into sheet and belt-like structures after being treated with organic solvents. In addition, the sheet-type structures sometimes exhibited morphological transformation into highly regular coordination polymer-based multi-walled nanotube structures. Delgado, Zamora, and coworkers also reported the delamination of 2D coordination polymers just by immersing the corresponding crystals in water [45]. These solvent-assisted soft processes can be useful for the production of

one-molecule thick structurally designed 2D materials, a potential alternative to graphene.

2D structural motifs of coordination polymers can provide a conduction path for various objects. Horike, Kitagawa, and coworkers synthesized coordination polymers that showed an intrinsic proton conduction pathway oriented parallel to the layers [46]. The coordination polymer was made from  $\text{Zn}^{2+}$ , 1,2,4-triazole, and orthophosphates having acidic protons. These acidic ligands are connected to form extended hydrogen bonding within the layers. The appropriate interval and arrangement of mobile protons in 2D structures are important factors for such conduction, according to the proton-hopping model in solids. Zheng, Kitagawa, and coworkers reported proton conduction regulated by the phase transition of 2D Co-La coordination polymers [47]. The used coordination polymers consist of acidic phosphonate groups possessing both coordinated water molecules at the intralayer space and lattice water molecules at the interlayer space, providing an efficient proton conducting pathway. A solid-state phase transition of the coordination polymers occurred above 45 °C and 93% relative humidity, resulting in a new phase. This transition induced the release of the protons from the intralayer region to the interlayer region. As a result, the proton conductivity of the material was significantly enhanced. Jenkins and coworkers reported a possible breathing behavior of coordination frameworks, which can be used as an interesting switching property [48]. Here, the coordination polymers, semirigid bis(1,2,4-triazole) ligands in their syn conformation, were coordinated with  $\text{Cu}^+$  chains to form a series of 2D metal-organic frameworks to form topologically 1D nanotubes. These anisotropic frameworks underwent two different solid state transformations as a result of the solvation. When guest molecules were incorporated, the size of the coordination tubes was altered upon rotation of the phenyl rings.

Various functions have been explored with 2D coordination polymers. Zhang *et al.* developed turn-on fluorescence sensors for organic volatile compounds which can be detected



through dynamic changes within the 2D MOF structures made from  $Zn_4O$ -like building units and 4,4'-(2,2-diphenylethene-1,1-diyl)dibenzoic acid ligands [49]. The coplanar conformation of the peripheral phenyl rings can induce a bathochromic shift (red shift) upon the promotion of  $\pi$  electron conjugation. On the other hand, the weakening of  $\pi$  electron conjugation at a perpendicular conformation leads to a hypsochromic shift (blue shift), which is caused by the conformational change of dangling phenyl rings. In addition, the presence of analytes, such as benzenes, increased the quantum yield, resulting in effective turn-on fluorescence sensing. Two dangling phenyl rings with unrestricted motions in 2D MOFs and molecular interactions with guest analytes can restrict motions by causing turn-on fluorescence. Lee, Vittal and coworkers reported sensing properties of polyrotaxane coordination polymers from  $Zn^{2+}$  and 1,4-bis[2-(4'-pyridyl)ethenyl]benzene and 4,4'-sulfonyldibenzoate for nitro compounds [50]. The obtained coordination polymers exhibited selective photoluminescent quenching for 2,4-dinitrophenylhydrazine compared to other nitro derivatives.

Huang *et al.* prepared 2D p-d conjugated coordination polymers that exhibited high electrical conductivity and ambipolar transport properties [51]. The coordination polymers containing a Cu ion and benzenhexathiol (BHT) as a form of a highly crystalline thin film were synthesized by liquid-liquid interface reaction (**Figure 1.11A**). The prepared materials were characterized by four-probe measurements which revealed high electrical conductivity at room temperature. Ambipolar charge transport properties with extremely high electron and hole mobilities were also confirmed under field-effect geometry (**Figure 1.11B**). This case is a good example of coordination polymers which can be synthesized into dimension-defined structures with desired components. The formed structures can also be integrated into devices. Therefore, the implementation of 2D polymers into various applications such as photocatalysts [52] and solar cells [53] has been actively researched. Not limited to these examples, various 2D

coordination polymers and related 2D materials have been rapidly paid attention to [54].

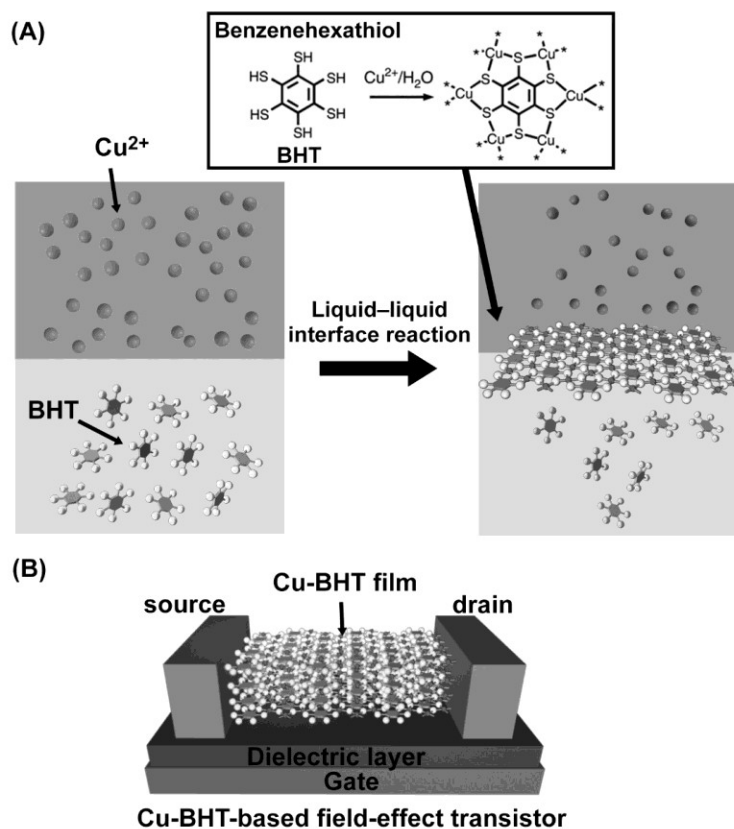


**Figure 1.11.** (A) Formation of 2D p-d conjugated coordination polymer with Cu ion and benzenehexathiol (BHT) through liquid-liquid interface reaction. (B) Device application for field-effect geometry.

## 1.4. Coordination Nanoarchitectonics 2: Conversion into Materials in 3D

For more advanced coordination nanoarchitectonics, assembling and integrating coordination structures into 3D motifs with functional properties are required. In the following sections, two aspects are discussed and exemplified, namely morphological control and 3D materials conversion.

### 1.4.1. Morphology Control of Coordination Polymer

So far, various coordination polymers with different shapes (*e.g.*, nanocubes, nanowires, plates, and sheets) have been reported (**Figure 1.12**). Their size and shape can be tuned by controlling the synthetic conditions or by using different precursors. A 1D morphology (*e.g.*, nanowires) extends in a straight line (along the one axis), a 2D morphology (*e.g.*, plates, sheets) extends in a plane (two directions), and a 3D morphology (*e.g.*, nanocubes) extends in all three directions (*x*-, *y*-, and *z*-axes). Among well-known coordination polymers, PB and its analogues (PBAs) can offer a broad range of compounds which can be useful for many practical applications. Cyanide groups can act as a bridge between transition metals ions. They are convenient for many applications, such as gas storage [55], batteries [56], catalysis [57], gas capture and separation [58], charge transfer [59], drug delivery [60], sensing and environmental clean-up [61].

Qu *et al.* have reported the preparation of PB nanowires which are vertically oriented to the substrate *via* a simple electrochemical deposition inside the pores of a polycarbonate membrane [62]. After dissolving the membrane with chloroform, only straight PB nanowires are obtained. By systematically tuning the pH value of the solution, the concentration of  $K_3[Fe(CN)_6]$ , and the addition of a capping agent (*e.g.*, polyvinylpyrrolidone (PVP)), several types of PB particles with different particle sizes can be obtained [63]. PVP mainly serves as a capping agent which stabilizes the nuclei in the initial stage. When the concentration of PVP is low, the particles tend to directly precipitate without further crystal growth. When the amount of PVP is sufficient, the nuclei can first stabilize, and then self-assemble in an ordered fashion. The acid concentration controls the dissociation of  $K_3[Fe(CN)_6]$  and generates  $Fe^{3+}$  ions which react with the  $[Fe(CN)_6]^{4-}$  ions.

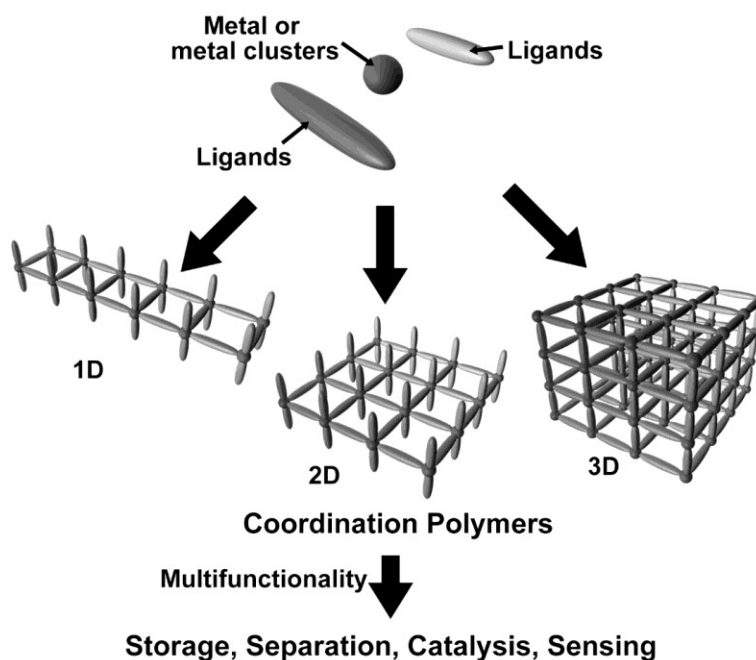


**Figure 1.12.** An illustration of 1-, 2-, and 3-dimensional shape controls of CPs.

Previous synthetic methods have mostly aimed to prepare PB crystals with well-defined morphologies. Lee *et al.* have reported the morphology of PB converting from cubic to hexapod shape [64]. The change in the morphology is confirmed by using different concentration of nitric acid. By increasing the acidic concentration, the shape of the particles evolves from cubic to star-like hexapods, passing through several stages such as truncated cubes, cuboctahedrons, truncated octahedrons, and hexapods with arms. This indicates that the oxidation reaction start at the corners of the nanocubes. It is common for the larger PB particles to form by aggregation and fusion of smaller crystals. More defects are present at the edges and corners, which makes the etching process faster than at the center. Furthermore, a new morphology of PB microcrystals has been prepared *via* controlled selective chemical etching, as reported by Hu *et al* [65]. Using a surfactant (*e.g.*, CTAB) to protect the surface of PB, the etching of the corners and edges can be enhanced. By carefully tuning the reaction conditions, selective etching of specific facets results in materials with fine structures.

By replacing Fe ions with other transition metals ions, one can obtain PBAs. The structural model used to understand their properties have been studied extensively. PBAs have attracted much attention over the past decade because of the diversity and tunability of their chemical and physical properties. Some PBAs have the same cubic structure ( $Fm-3m$ ) as PB. Yamauchi and co-workers have synthesized  $\text{KCo}^{\text{III}}_4[\text{Fe}^{\text{II}}(\text{CN})_6]_3$  and  $\text{Fe}^{\text{II}}_3[\text{Co}^{\text{III}}(\text{CN})_6]_2$  by simple wet-chemical synthesis at room temperature [66]. The atomic ratios of  $\text{Co}^{\text{II}}/\text{Fe}^{\text{III}}$  and  $\text{Fe}^{\text{II}}/\text{Co}^{\text{III}}$  estimated by inductively coupled plasma analyses were 4/3 and 3/2, respectively, which is in good agreement with the reported stoichiometric ratios. As another example,  $\text{Mg}^{\text{II}}_3[\text{Co}^{\text{III}}(\text{CN})_6]_2$  and  $\text{Co}^{\text{II}}_3[\text{Fe}^{\text{III}}(\text{CN})_6]_2$  were recently synthesized with  $\text{Mg}^{\text{II}}/\text{Co}^{\text{III}}$  and  $\text{Co}^{\text{II}}/\text{Fe}^{\text{III}}$ , respectively [67].

The synthesis of hollow coordination polymers have been reported *via* different ways. Maurin-Pasturel *et al.* reported the growth of a cyano-bridged coordination network on gold nanoparticles (**Figure 1.13**) [68]. The design of such an intricate core-shell structured material is a promising way to realize functional nanomaterials combining multiple properties in a single system. Finally, by dissolving the Au cores, hollow PBAs nanoparticles can be successfully obtained. Another layer of PBAs can also be formed on the surface of Au@PBA by epitaxial growth, leading to the formation of double-shelled Au@PBA@PBA heterostructures. As another promising way, PBA@PBA core-shell heterostructures prepared by epitaxial crystal growth can be utilized as starting materials [69]. After subsequently removing the core, hollow PBAs nanoparticles can be obtained. Risset *et al.* have been reporting a facile surfactant-free route to synthesize uniform  $\text{Rb}_{0.4}\text{M}_4[\text{Fe}(\text{CN})_6]_{2.8} \cdot 7.2\text{H}_2\text{O}$  (M=Co, Ni) hollow nanoparticles.  $\text{Rb}_{1.6}\text{Mn}_4[\text{Fe}(\text{CN})_6]_{3.2} \cdot 4.8\text{H}_2\text{O}$  serves as a sacrificial/removable core in the synthesis of the core@shell heterostructures. After the dissolution of the cores under mild conditions, hollow nanocubes with crystallized walls can be obtained.

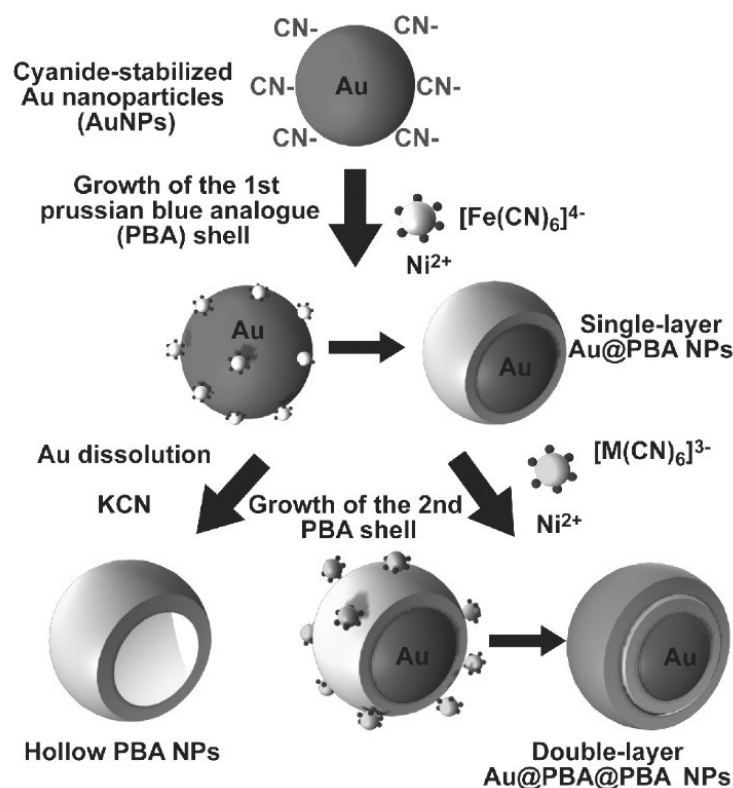


**Figure 1.13.** Schematic representation of hollow PBA and double-layer  $\text{Au}@PBA@PBA$  nanoparticles obtained through the cyano network growth on the Au surface.

Recently, Hu *et al.* have succeeded to prepare various hollow PB nanocubes [70]. During the etching process, the reaction normally starts from the outer surface of the particles. The PB mesocrystals used in this study possess voids because the large particles are formed by aggregations and fusion of the smaller crystals. Thus, it is possible for the etching agents (*i.e.*, HCl) to diffuse into the inner parts of the mesocrystals through these defects, leading to the formation of an inner cavity. PVP plays a crucial role in the etching process, acting as a surface protecting agent which can locally decrease the etching rate.

Microemulsions are isotropic liquid mixtures consisting of oil, water, and surfactants. The aqueous phase can contain salts and/or other ingredients, and the oil phase (or any water-immiscible liquids) can be a complex mixture of different hydrocarbons and olefins. Depending on the proportion of each phase, one can form a system consisting of oil dispersed in

water (oil-in-water, O/W) or water dispersed in oil (water-in-oil, W/O). The surfactant molecules form a monolayer at the interface between oil and water, with the hydrophobic tails of the surfactant molecules dissolved in the oil phase and the hydrophilic head groups in the aqueous phase [71]. The syntheses of PB and PBAs have been synthesized by mixing water-in-oil and/or oil-in-water microemulsions containing the appropriate reactants (**Figure 1.14**). Cao *et al.* have reported the synthesis of polyhedrons, cubes, and rods of  $\text{Co}_3[\text{Co}(\text{CN})_6]_2$  nanostructures with good control over the shape [72]. The microemulsion consisted of an aqueous solution of  $\text{K}_3[\text{Co}(\text{CN})_6]$  mixed with cyclohexane, *n*-pentanol, and CTAB.

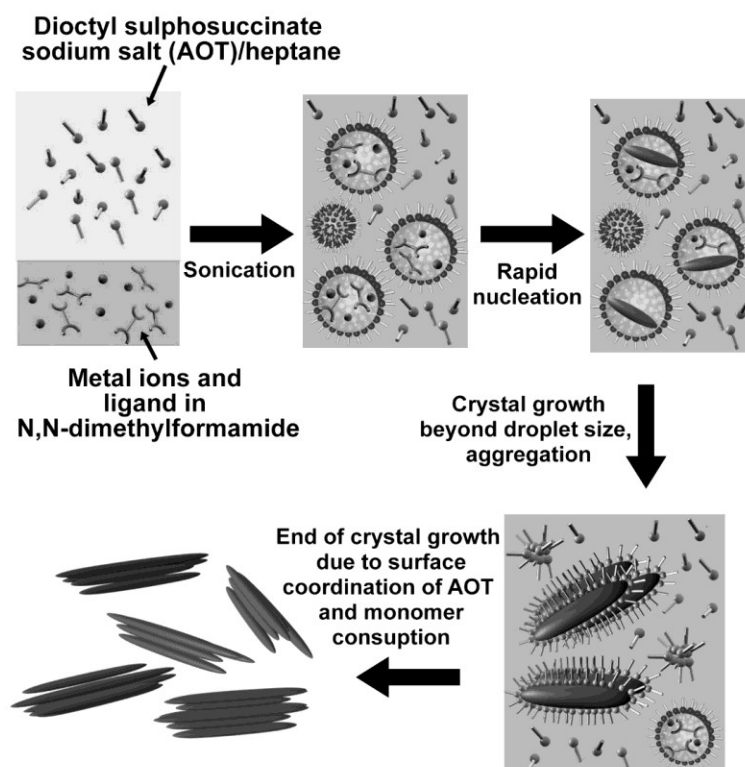


**Figure 1.14.** Model for CPs growth in non-aqueous inverse microemulsion with ultrasonication.

The size of the synthesized PB nanocubes can be controlled by applying external forces. Wu *et al.* have been synthesizing monocrystalline nanocubes of PB with several sizes by a direct dissociation of the single-source precursor under ultrasonic conditions [73]. The reaction temperature and the concentration of  $\text{K}_4[\text{Fe}(\text{CN})_6]$  aqueous solution combined with the ultrasonic

conditions allowed a fine control over the final particle size and size distribution. The first step is the dissociation of  $K_4[Fe(CN)_6]$  salt in an acidic solution, resulting in the formation of ferrous ions which are directly oxidized and converted into the ferric ions, as they are highly unstable in air. A slow dissociation is preferred for fine crystal growth. Then, the resulted ferric ions react with the undissociated  $K_4[Fe(CN)_6]$  to form PB nanocubes through preferential crystal growth. Ultrasonication provides better conditions than hydrothermal treatment to generate uniform size distribution of PB nanocubes.

Microwave-assisted heating was also used for several decades to synthesize organic compounds, and was recently applied to the preparation of coordination polymers. Microwave heating allows short reaction times, fast kinetics of crystal nucleation and growth, as well as high yields of the desired products. The most significant development in the use of microwave heating for the preparation of coordination polymers is attributed to the growth of nano-sized crystallites in a short time and may find direct applications in functional nanodevices. Stefanczyk *et al.* reported the synthesis of novel cyano-bridged coordination polymers with different morphologies *via* microwave-assisted construction [74].

### 1.4.2. Thermal Conversion to Nanoporous Inorganic Materials

The urgent need for nanoporous metals oxides with well-defined compositions, fine morphologies, and highly crystallized frameworks is motivating scientists to discover novel and facile synthetic methods. A solid-state strategy for preparing nanoporous inorganic materials with a predictable nanostructure is highly promising and necessary for large scale production. By using cyano-bridged coordination polymers, such as PB and PBAs, many nanoporous metals oxides can be prepared by annealing. PB and PBAs have a large fraction of metals ions among the organic ligands which can be used as metal sources, while the organic components can be

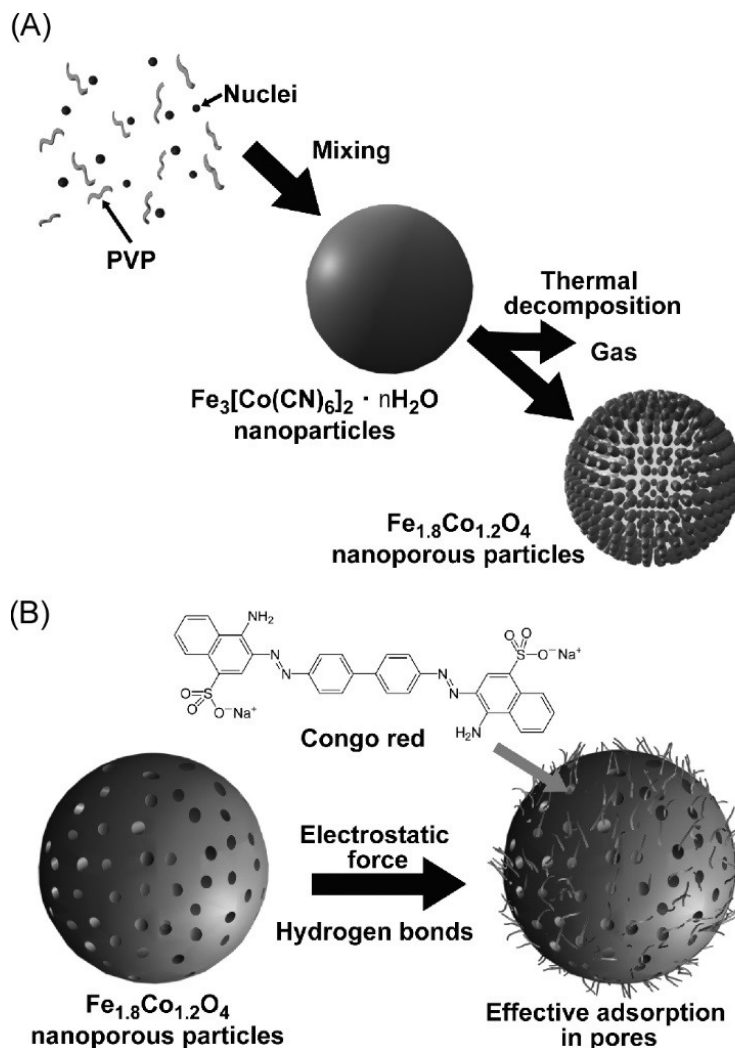


removed by simple calcination and produce abundant pores [75]. Thus, during the thermal treatment, the metal content is retained and takes part in the formation of the framework.

Pang *et al.* have synthesized  $\text{Mn}_3[\text{Co}(\text{CN})_6]_2 \cdot n\text{H}_2\text{O}$  which was further thermally converted into  $\text{Mn}_3\text{O}_4\text{-Co}_3\text{O}_4$  composite materials with corner-truncated nanocubic shapes [76]. The decomposition process is carried out by two steps. First, water is removed at 160 °C. Then, heating up to 370 °C allows the removal of the cyanide groups. It is clear that the  $\text{Mn}_3\text{O}_4\text{-Co}_3\text{O}_4$  composite is formed after heating at 370 °C. This is the normal decomposition behavior of CN-containing compounds. Yamauchi and coworkers have also reported the thermal decompositions of PB and PBAs under optimal thermal conditions for the preparation of many nanoporous metals oxides [77]. Different temperatures were systematically applied to prepare nanoporous iron oxides from the PB nanocubes in order to investigate their impact. The morphology of the obtained samples after calcination at 250 °C and 400 °C remains nanocubic, but the particle size is slightly reduced and the surface roughness increased. The reduction of the particles size is mainly caused by removing the cyano-groups and the interstitial water molecules during the heating treatment. On the basis of XRD results and magnetic measurements, a  $\gamma\text{-Fe}_2\text{O}_3$  phase is mainly obtained. Other spinel metal oxides (*e.g.*,  $\text{Co}_2\text{O}_3$  and  $\text{NiCo}_2\text{O}_4$ ) are also obtained by thermal treatment in air of CoCo and NiCo PBAs [78].

Hu *et al.* have reported a facile strategy for the fabrication of binary  $\text{Fe}_x\text{Co}_{3-x}\text{O}_4$  nanoporous structures, which involves the pyrolysis-induced transformation of PBA (*i.e.*,  $\text{Fe}_3[\text{Co}(\text{CN})_6]_2 \cdot n\text{H}_2\text{O}$ ) nanoparticles (**Figure 1.15A**) [79]. Before pyrolysis, spherical-like particles of  $\text{Fe}_3[\text{Co}(\text{CN})_6]_2 \cdot n\text{H}_2\text{O}$  are observed. After pyrolysis, binary nanoporous  $\text{Fe}_x\text{Co}_{3-x}\text{O}_4$  is formed. The  $\text{Fe}_x\text{Co}_{3-x}\text{O}_4$  product consists of many nanoparticles without major aggregation and with a morphology similar to the original PBA precursor. When evaluated as an absorbent for dye molecules in water, the nanoporous  $\text{Fe}_x\text{Co}_{3-x}\text{O}_4$  particles not only exhibit a high absorption

capacity, but can also be recycled easily and quickly *via* a simple magnetic separation, showcasing their potential in applications such as water treatment (**Figure 1.15B**). This excellent absorption ability can be attributed to the interconnected nanopores and the large surface area.



Hu *et al.* have reported the controlled synthesis of superparamagnetic nanoporous iron oxide particles with hollow interiors by using PB coordination polymers (**Figure 1.16**) [80]. The thermal treatment of PB nanoparticles at 250 °C and 400 °C leads to the formation of amorphous iron oxide, while using the hollow PB nanoparticles leads to the formation of  $\gamma\text{-Fe}_2\text{O}_3$  with an

amorphous phase at low temperature and a mixed phase of crystalline  $\alpha$ - and  $\gamma$ - $\text{Fe}_2\text{O}_3$  at higher temperature. The large hollow PB particles yield a pure phase of crystalline  $\gamma$ - $\text{Fe}_2\text{O}_3$  at low temperature and  $\alpha$ - $\text{Fe}_2\text{O}_3$  at higher temperature. Thus, introducing the hollow structures with a tunable size effectively accelerates the oxidization of the iron walls.

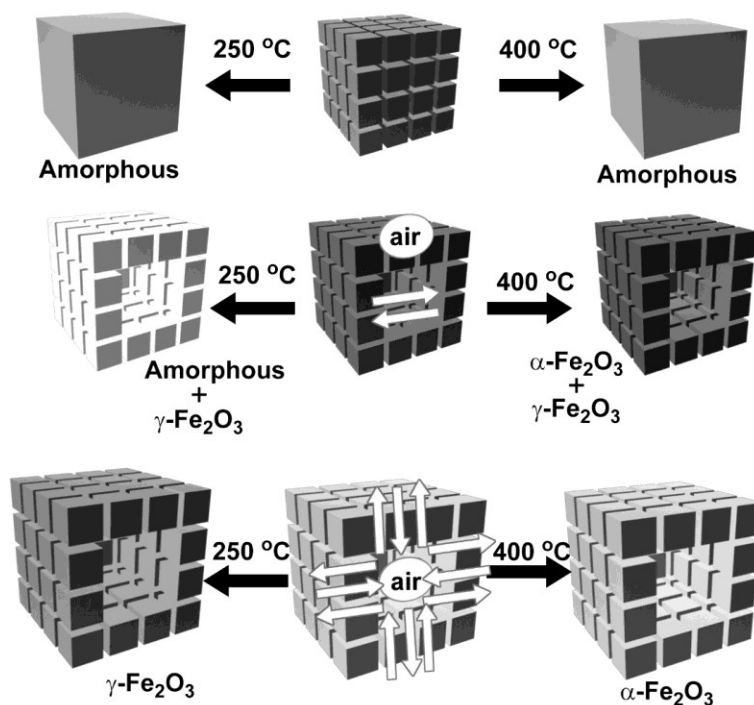


**Figure 1.16.** Schematic illustrations on thermal decomposition of solid PB particles, small hollow PB particles, and large hollow PB particles, respectively.

Recently, the growth of CoCo, FeCo, CoFe, and FeFe PBAs shells on the surface of a NiCr core was reported [66]. Since the core and the shell have the same crystal structure, the shell can grow epitaxially and crystallize along the same orientation as the core. After a selective chemical etching of the core-shell heterostructured nanocubes using a hydrochloric acid solution, hollow interiors can form. In this method, hydrochloric acid penetrates the voids of the shell to further dissolve the core, thereby leading to the formation of hollow CoCo, FeCo, CoFe, and FeFe PBAs nanocubes. In this case, the NiCr cores can be used as a removable/sacrificial template. After subsequent thermal treatments of the hollow PBAs in the air, the nanoporous hybrid metals

oxides with hollow cavities can be obtained. This new type of nanostructured oxides can be used in applications such as drug delivery, water treatment, etc.

The Kirkendall effect has been recently proposed as the main phenomenon responsible for the formation of hollow particles. Originally, the term “Kirkendall effect” refers to the different atomic diffusive rates of the elements atoms under thermal treatments, leading to the generation of pores in the lower-melting component side near the interface. For example, the CoCo-PBA nanocubes can be thermally converted into  $\text{Co}_3\text{O}_4$  nanocages in air (**Figure 1.17**). This phenomenon can be explained by the Kirkendall effect which is based on a nonequilibrium interdiffusion process [81]. During the first stage of the thermal oxidation, a thin intermediate shell is formed on the surface of the CoCo-PBA nanocubes. This thin film acts as a barrier to separate the inner part of the CoCo-PBA from the oxygenated environment. During the first stage, only the shells are immediately oxidized due to the difficulty for oxygen to diffuse towards the inside. Therefore, free metal ions tend to move towards the shell region after the decomposition of the organic units in order to react with oxygen, leading to the formation of a hollow interior.

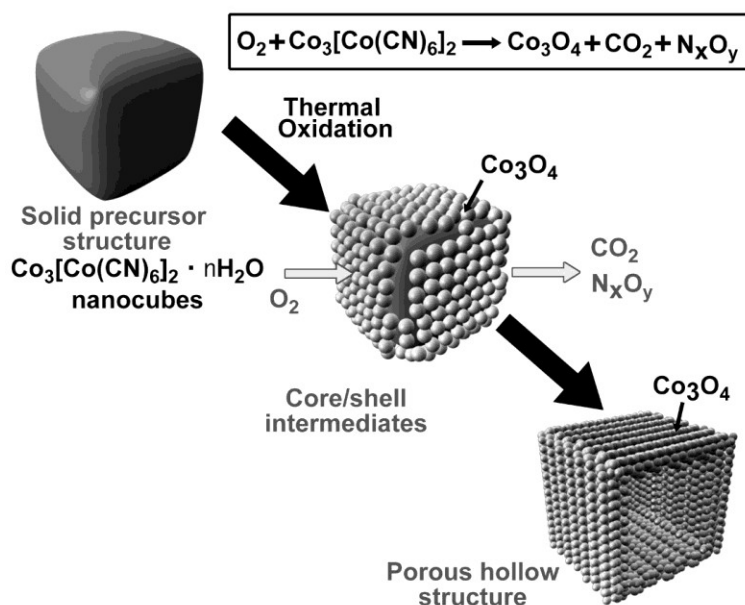


**Figure 1.17.** A reaction pathway for preparation of  $\text{Co}_3\text{O}_4$  nanocages *via* thermal decomposition of Co-based PBA.

Recently, Ostwald ripening process has been proposed as a template-free strategy for fabricating nanoporous inorganic materials. The basic principle of the Ostwald ripening concept is that the larger crystals grow by the fusion of the smaller ones, which results in the formation of dendritic nanoarchitectures. Yan *et al.* have prepared  $\text{Co}_3\text{O}_4$  dendritic structure by a facile strategy which involves the thermal decomposition of cobalt-based PBAs nanoparticles (**Figure 1.18**) [82]. Calcining  $\text{Co}_3[\text{Co}(\text{CN})_6]_2 \cdot n\text{H}_2\text{O}$  nanocubes at  $450\text{ }^\circ\text{C}$  leads to the formation of  $\text{Co}_3\text{O}_4$  porous nanocages; this mechanism can also be described by the Kirkendall effect. After calcination at  $650\text{ }^\circ\text{C}$ , the morphology starts to change, and by further increasing the temperature up to  $850\text{ }^\circ\text{C}$ , the grains become aggregated, recrystallized, and rearranged into a dendritic shape.

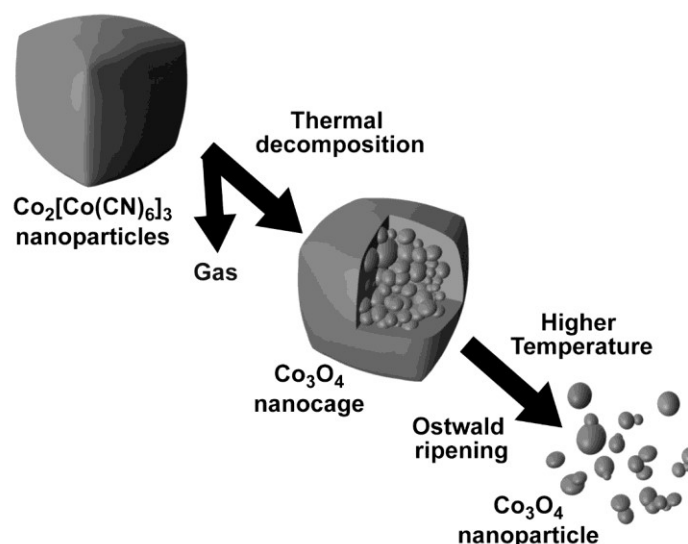


**Figure 1.18.** Schematic illustration of formation of  $\text{Co}_3\text{O}_4$  dendritic structure by the Ostwald ripening, which involves the thermal decomposition of nanoparticles of cobalt-based PBAs.

## 1.5. Aims and objectives of this dissertation

The aim of this study could be summarized in three main points which are a surprise, a challenge and an interest as illustrated in **Figure 1.19**. About the surprise, on my way to the results presented in this dissertation I was surprised and delighted to witness how the chelating agent

(trisodium citrate dihydrate (TSCD)) combined with my precursors. It is always a good feeling to observe a successful reaction. I was also impressed to see the impact of the chelating agent on the speed of the crystal growth. With a reaction rate a thousand times slower, the conditions were perfect to trigger a controlled crystal growth process. By this approach, I rationally designed various cyano-bridged coordination polymers nanostructures with two dimensional (2D) and three dimensional (3D) uniform shapes and sizes through facile and cheap solution phase approach.

But about the challenge, the difficulties encountered during this work reside in various aspects of this dissertation. Firstly, determining which precursors and co-reactants would be the most suitable for such reactions required long study and many trials to catch the optimum conditions. I then spent considerable time optimizing the synthetic parameters to lead to the desired morphology. All the cyano-bridged CPs nanostructures could be simply synthesized by purposefully changing the precursor compositions (*e.g.*, types and concentrations of metal ions, ligands, and chelating agents) and synthetic conditions (*e.g.*, synthetic temperatures, aging temperatures and times, and pHs).

Finally, my interest is divided into two main parts. First, a more focus on the 2D cyano-bridged CPs is reported for four reasons. i) 2D CPs have a highly accessible surface area that permits guest molecules to effectively access the micropores in the CPs (as described in **Chapter 5**), ii) 2D CPs have many active sites for catalytic and electrochemical reactions (as described in **Chapter 6**, the 2D CoNi-oxide flakes showed better electrocatalytic performance for oxygen evolution reaction (OER) than 3D NiCo-oxide cubes, however they have the same composition, iii) Assembled 2D CPs can be used as membrane filters, and iv) 2D CPs could growth into the surface of GO sheets and the resulted 2D CPs coated GO sheets then self-assemble and are stabilized in an ordered lamellar nanomaterials, this part is reported in

**Chapter 7.** As a second, the thermal treatment of coordination polymers (2D and 3D) has proven to be a promising solid-state method for the preparation of nanoporous metal oxides. The large fraction of metal centers can be utilized as the metal source, and the removable organic components, by simple calcination, can provide pores. It is possible to prepare different nanoporous metal oxides from various coordination polymers. This method has the potential to overcome the difficulties in the preparation of nanoporous metal oxides through surfactant-assisted approaches.

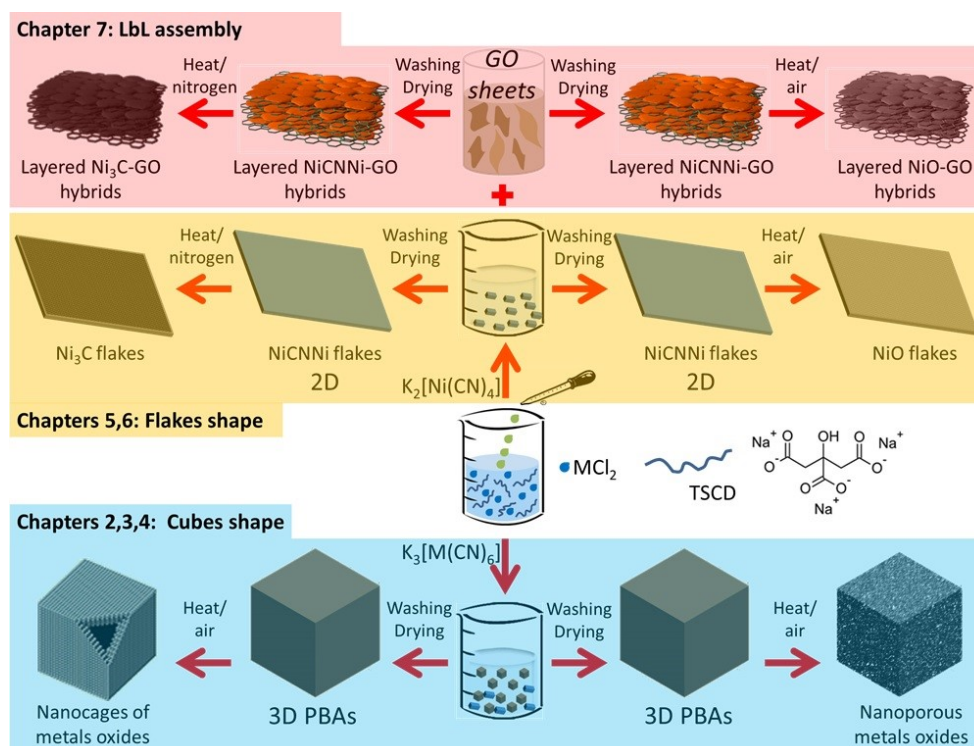


**Figure 1.19.** Schematic illustration of a controlled crystal growth pathway of 2D and 3D cyano-bridged CPs nanostructures as well as the LbL assembly of CPs flakes with GO sheets involving the thermal decomposition into well-retained nanostructured oxides and carbides.

## 1.6. References

- [1] (a) I. Moriguchi, *Chem. Lett.* **2014**, *43*, 740-745; (b) S. Banya, T. Akiyama, T. Matsumoto, K. Fujita, T. Oku, *Bull. Chem. Soc. Jpn.* **2014**, *87*, 1335-1342; (c) Y. Hasegawa, *Bull. Chem. Soc. Jpn.* **2014**, *87*, 1029-1057; (d) Z. Zhao, Y. Sun, F. Dong, *Nanoscale* **2015**, *7*, 15-37; (e) Z. Yu, L. Tetard, L. Zhai, J. Thomas, *Energy Environ. Sci.* **2015**, *8*, 702-730; (f) M. Wang, K. Han, S. Zhang, L. Sun, *Coord. Chem. Rev.* **2015**, *284*, 206-235; (g) M.M. Huie, D.C. Bock, E.S. Takeuchi, A.C. Marschilok, K.J. Takeuchi, *Coord. Chem. Rev.* **2015**, *287*, 15-27; (h) K. Zhang, X. Han, Z. Hu, X. Zhang, Z. Tao, J. Chen, *Chem. Soc. Rev.* **2015**, *44*, 699-728.
- [2] (a) J.-L. Duprey, H.-A. Jean-Louis, H.R. Tucker, *Chem. Lett.* **2014**, *43*, 157-163; (b) U.G.K. Wegst, H. Bai, E. Saiz, A.P. Tomsia, R.O. Ritchie, *Nat. Mater.* **2015**, *14*, 23-36; (c) M.R. Jones, N.C. Seeman, C.A. Mirkin, *Science* **2015**, *347*, 1260901; (d) X. Yang, H. Shang, C. Ding, J. Li, *Polym. Chem.* **2015**, *6*, 668-680; (e) W. Auwaerter, D. Ecija, F. Klappenberger, J. V. Barth, *Nat. Chem.* **2015**, *7*, 105-120; (f) M. Zhang, Z.-Y. Gu, M. Bosch, Z. Perry, H.-C. Zhou, *Coord. Chem. Rev.* **2015**, *293*, 327-356.
- [3] (a) F. Niess, V. Duplan, J.-B. Sauvage, *Chem. Lett.* **2014**, *43*, 964-974; (b) Y. Wang, J. He, C. Liu, W.H. Chong, H. Chen, *Angew. Chem. Int. Ed.* **2015**, *54*, 2022-2051; (c) J.H. Jordan, B.C. Gibb, *Chem. Soc. Rev.* **2015**, *44*, 547-585; (d) P. Wei, X. Yan, F. Huang, *Chem. Soc. Rev.* **2015**, *44*, 815-832; (e) J. Parmar, X. Ma, J. Katuri, J. Simmchen, M. M Stanton, C. Trichet-Paredes, L. Soler, S. Sanchez, *Sci. Technol. Adv. Mater.* **2015**, *16*, 014802; (f) H. Wang, S. Liu, Y.-L. Zhang, J.-N. Wang, L. Wang, H. Xia, Q.-D. Chen, H. Ding, H.-B. Sun, *Sci. Technol. Adv. Mater.* **2015**, *16*, 024805; (g) E. Mattia, S. Otto, *Nat. Chem.* **2015**, *10*, 111-119.
- [4] (a) K. Arga, Y. Yamauchi, M. Aono, *APL Mater.* **2015**, *3*, 061001; (b) K. Ariga, Q. Ji, W.



- Nakanishi, J.P. Hill, M. Aono, *Mater. Horiz.* **2015**, *2*, 406-413; (c) M. Aono, K. Ariga, *Adv. Mater.* **2016**, *28*, 989-992.
- [5] (a) Y. Inokuma, M. Fujita, *Bull. Chem. Soc. Jpn.* **2014**, *87*, 1161-1176; (b) S. Tashiro, M. Shionoya, *Bull. Chem. Soc. Jpn.* **2014**, *87*, 643-654; (c) H. Nishihara, *Chem. Lett.* **2014**, *43*, 388-395; (d) N.A. Khan, S.H. Jung, *Coord. Chem. Rev.* **2015**, *285*, 11-23; (e) W.-X. Zhang, P.-Q. Liao, R.-B. Lin, Y.-S. Wei, M.-H. Zeng, X.-M. Chen, *Coord. Chem. Rev.* **2015**, *293*, 263-278; (f) J.-D. Lin, C.I. Onet, W. Schmitt, *Sci. Technol. Adv. Mater.* **2015**, *16*, 024803.
- [6] K. Ariga, T. Mori, S. Ishihara, K. Kawakami, J.P. Hill, *Chem. Mater.* **2014**, *26*, 519-532.
- [7] (a) R. Makiura, H. Kitagawa, *Eur. J. Inorg. Chem.* **2010**, 3715-3724; (b) O. Shekhah, J. Liu, R.A. Fischer, C. Woll, *Chem. Soc. Rev.* **2011**, *40*, 1081-1106; (c) D. Zacher, R. Schmid, C. Woll, R.A. Fischer, *Angew. Chem. Int. Ed.* **2011**, *50*, 176-199; (d) D. Bradshaw, A. Garai, J. Huo, *Chem. Soc. Rev.* **2012**, *41*, 2344-2381; (e) S. Horike, D. Umeyama, S. Kitagawa, *Acc. Chem. Res.* **2013**, *46*, 2376-2384.
- [8] (a) K. Ariga, M. Li, G.J. Richards, J.P. Hill, *J. Nanosci. Nanotechnol.* **2011**, *11*, 1-13; (b) K. Ariga, Q. Ji, J.P. Hill, Y. Bando, M. Aono, *NPG Asia Mater.* **2012**, *4*, e17; (c) K. Ariga, J. Li, J. Fei, Q. Ji, J.P. Hill, *Adv. Mater.* **2016**, *28*, 1251-1286.
- [9] (a) K. Ariga, A. Vinu, Y. Yamauchi, Q. Ji, J.P. Hill, *Bull. Chem. Soc. Jpn.* **2012**, *85*, 1-32; (b) T. Govindaraju, M.B. Avinash, *Nanoscale* **2012**, *4*, 6102-6117; (c) W. Nakanishi, K. Minami, L.K. Shrestha, Q. Ji, J.P. Hill, K. Ariga, *Nano Today* **2014**, *9*, 378-394; (d) R. Rajendran, L.K. Shrestha, K. Minami, M. Subramanian, R. Jayavel, K. Ariga, *J. Mater. Chem. A* **2014**, *2*, 18480-18487; (e) H. Pan, S. Zhu, L. Mao, *J. Inorg. Organomet. Polym. Mater.* **2015**, *25*, 179-188; (f) S. Cordier, F. Grasset, Y. Molard, M. Amela-Cortes, R. Boukherroub, S. Ravaine, M. Mortier, N. Ohashi, N. Saito, H. Haneda, *J. Inorg. Organomet. Polym. Mater.* **2015**, *25*, 189-204; (g) V. Malgras, Q. Ji, Y. Kamachi, T. Mori, F.-K. Shieh,

- K. C.-W. Wu, K. Ariga, Y. Yamauchi, *Bull. Chem. Soc. Jpn.* **2015**, *88*, 1171-1200.
- [10] (a) S. Hecht, *Angew. Chem. Int. Ed.* **2003**, *42*, 24-26; (b) K.L. Wang, K. Galatsis, R. Ostroumov, A. Khitun, Z. Zhao, S. Han, *Proc. IEEE* **2008**, *96*, 212-229; (c) K. Ariga, M.V. Lee, T. Mori, X.-Y. Yu, J.P. Hill, *Adv. Colloid Interface Sci.* **2010**, *154*, 20-29; (d) K. Ariga, T. Mori, J.P. Hill, *Langmuir* **2013**, *29*, 8459-8471; (e) K. Ariga, Y. Yamauchi, G. Rydzek, Q. Ji, Y. Yonamine, K. C.-W. Wu, J.P. Hill, *Chem. Lett.* **2014**, *43*, 36-68; (f) H. Hamoudi, *Nanoscale Res. Lett.* **2014**, *9*, 287; (g) K. Ariga, Q. Ji, W. Nakanishi, J.P. Hill, *J. Inorg. Organomet. Polym. Mater.* **2015**, *25*, 466-479; (h) G. Rydzek, Q. Ji, M. Li, P. Schaaf, J.P. Hill, F. Boulmedais, K. Ariga, *Nano Today* **2015**, *10*, 138-167.
- [11] (a) K. Ariga, S. Ishihara, H. Abe, M. Li, J.P. Hill, *J. Mater. Chem.* **2012**, *22*, 2369-2377; (b) K. Takada, N. Ohta, Y. Tateyama, *J. Inorg. Organomet. Polym. Mater.* **2015**, *25*, 205-213; (c) R. Rajendran, L.K. Shrestha, R.M. Kumar, R. Jayavel, J.P. Hill, K. Ariga, *J. Inorg. Organomet. Polym. Mater.* **2015**, *25*, 267-274; (d) C.-M. Puscasu, E.M. Seftel, M. Mertens, P. Cool, G. Carja, *J. Inorg. Organomet. Polym. Mater.* **2015**, *25*, 259-266; (e) H. Abe, J. Liu, K. Ariga, *Mater. Today* **2016**, *19*, 12-18.
- [12] (a) K. Ariga, Y. Yamauchi, Q. Ji, Y. Yonamine, J.P. Hill, *APL Mater.* **2014**, *2*, 030701; (b) S. Ishihara, J. Labuta, W. Van Rossom, D. Ishikawa, K. Minami, J.P. Hill, K. Ariga, *Phys. Chem. Chem. Phys.* **2014**, *16*, 9713-9746.
- [13] (a) K. Ariga, Q. Ji, M.J. McShane, Y.M. Lvov, A. Vinu, J.P. Hill, *Chem. Mater.* **2012**, *24*, 728-737. (b) S. Howorka, *Langmuir* **2013**, *29*, 7344-7353; (c) K. Ariga, Q. Ji, T. Mori, M. Naito, Y. Yamauchi, H. Abe, J.P. Hill, *Chem. Soc. Rev.* **2013**, *42*, 6322-6345; (d) P. Kujawa, F.M. Winnik, *Langmuir* **2013**, *29*, 7354-7361; (e) M.B. Avinash, T. Govindaraju, *Nanoscale* **2014**, *6*, 13348-13369; (f) A.P. Pandey, N.M. Girase, M.D. Patil, P.O. Patil, D.A. Patil, P.K. Deshmukh, *J. Nanosci. Nanotechnol.* **2014**, *14*, 828-840; (g) K. Ariga, K. Kawakami, M.

- Ebara, Y. Kotsuchibashi, Q. Ji, J.P. Hill, *New J. Chem.* **2014**, *38*, 5149-5163; (h) E. Psarra, U. Konig, Y. Ueda, C. Bellmann, A. Janke, E. Bittrich, K.-J. Eichhorn, P. Uhlmann, *ACS Appl. Mater. Interfaces* **2015**, *7*, 12516-12529; (i) M. Pandeewar, T. Govindaraju, *J. Inorg. Organomet. Polym. Mater.* **2015**, *25*, 293-300.
- [14] (a) M. Ramanathan, L.K. Shrestha, T. Mori, Q. Ji, J.P. Hill, K. Ariga, *Phys. Chem. Chem. Phys.* **2013**, *15*, 10580-10611; (b) L.K. Shrestha, Q. Ji, T. Mori, K. Miyazawa, Y. Yamauchi, J.P. Hill, K. Ariga, *Chem. Asian J.* **2013**, *8*, 1662-1679; (c) M. Ramanathan, K. Hong, Q. Ji, Y. Yonamine, J.P. Hill, K. Ariga, *J. Nanosci. Nanotechnol.* **2014**, *14*, 390-401; (d) L.K. Shrestha, K.M. Strzelczyk, R.G. Shrestha, K. Ichikawa, K. Aramaki, J.P. Hill, K. Ariga, *Nanotechnology* **2015**, *26*, 204002.
- [15] (a) K. Ariga, X. Hu, S. Mandal, J.P. Hill, *Nanoscale* **2010**, *2*, 198-214; (b) K. Sakakibara, J.P. Hill, K. Ariga, *Small* **2011**, *7*, 1288-1308; (c) K. Sakakibara, P. Chithra, B. Das, T. Mori, M. Akada, J. Labuta, T. Tsuruoka, S. Maji, S. Furumi, L.K. Shrestha, J.P. Hill, S. Acharya, K. Ariga, A. Ajayaghosh, *J. Am. Chem. Soc.* **2014**, *136*, 8548-8551; (d) N.A. Wasio, R.C. Quardokus, R.P. Forrest, C.S. Lent, S.A. Corcelli, J.A. Christie, K.W. Henderson, S.A. Kandel, *Nature* **2014**, *507*, 86-89; (e) J.M. MacLeod, F. Rosei, *Small* **2014**, *10*, 1038-1049; (f) Z.M. Hudson, C.E. Boott, M.E. Robinson, P.A. Rupar, M.A. Winnik, I. Manners, *Nat. Chem.* **2014**, *6*, 893-898; (g) J.-J. Shao, W. Lv, Q.-H. Yang, *Adv. Mater.* **2014**, *26*, 5586-5612; (h) D. Kim, W.D. Kim, M.S. Kang, M.S. Kang, S.-H. Kim, D. C. Lee, *Nano Lett.* **2015**, *15*, 714-720.
- [16] K. Ariga, Y. Yamauchi, T. Mori, J.P. Hill, *Adv. Mater.* **2013**, *25*, 6477-6512.
- [17] (a) K. Ariga, J.P. Hill, *Chem. Rec.* **2011**, *11*, 199-211; (b) K. Ariga, H. Ito, J.P. Hill, H. Tsukube, *Chem. Soc. Rev.* **2012**, *41*, 5800-5835.
- [18] M. Onda, K. Yoshihara, H. Koyano, K. Ariga, T. Kunitake, *J. Am. Chem. Soc.* **1996**, *118*,

8524-8530.

- [19] (a) D.Y. Sasaki, K. Kurihara, T. Kunitake, *J. Am. Chem. Soc.* **1991**, *113*, 9685-9686; (b) D. Y. Sasaki, K. Kurihara, T. Kunitake, *J. Am. Chem. Soc.* **1992**, *114*, 10994-10995.
- [20] (a) M. Sakurai, H. Tamagawa, T. Furuki, Y. Inoue, K. Ariga, T. Kunitake, *Chem. Lett.* **1995**, 1001-1002; (b) M. Sakurai, H. Tamagawa, Y. Inoue, K. Ariga, T. Kunitake, *J. Phys. Chem. B* **1997**, *101*, 4810-4816.
- [21] H. Tamagawa, M. Sakurai, Y. Inoue, K. Ariga, T. Kunitake, *J. Phys. Chem. B* **1997**, *101*, 4817-4825.
- [22] (a) K. Ariga, H. Mori, J.P. Hill, *Chem. Sci.* **2011**, *2*, 195-203; (b) K. Ariga, S. Ishihara, H. Izawa, H. Xia, J.P. Hill, *Phys. Chem. Chem. Phys.* **2011**, *13*, 4802-4811; (c) K. Ariga, T. Mori, J.P. Hill, *Adv. Mater.* **2012**, *24*, 158-176; (d) K. Sakakibara, L.A. Joyce, T. Mori, T. Fujisawa, S.H. Shabbir, J.P. Hill, E.V. Anslyn, K. Ariga, *Angew. Chem. Int. Ed.* **2012**, *51*, 9643-9646; (e) D. Ishikawa, T. Mori, Y. Yonamine, W. Nakanishi, D. Cheung, J.P. Hill, K. Ariga, *Angew. Chem. Int. Ed.* **2015**, *54*, 8988-8991.
- [23] (a) K. Ariga, Y. Terasaka, D. Sakai, H. Tsuji, J. Kikuchi, *J. Am. Chem. Soc.* **2000**, *122*, 7835-7836; (b) K. Ariga, T. Nakanishi, Y. Terasaka, H. Tsuji, D. Sakai, J. Kikuchi, *Langmuir* **2005**, *21*, 976-981; (c) K. Ariga, T. Nakanishi, Y. Terasaka, J. Kikuchi, *J. Porous Mater.* **2006**, *13*, 427-430.
- [24] (a) T. Michinobu, S. Shinoda, T. Nakanishi, J.P. Hill, K. Fujii, T.N. Player, H. Tsukube, K. Ariga, *J. Am. Chem. Soc.* **2006**, *128*, 14478-14479; (b) K. Ariga, T. Michinobu, T. Nakanishi, J.P. Hill, *Curr. Opin. Colloid Interface Sci.* **2008**, *13*, 23-30; (c) T. Michinobu, S. Shinoda, T. Nakanishi, J.P. Hill, K. Fujii, T.N. Player, H. Tsukube, K. Ariga, *Phys. Chem. Chem. Phys.* **2011**, *13*, 4895-4900.
- [25] (a) T. Mori, K. Okamoto, H. Endo, J.P. Hill, S. Shinoda, M. Matsukura, H. Tsukube, Y.

- Suzuki, Y. Kanekiyo, K. Ariga, *J. Am. Chem. Soc.* **2010**, *132*, 12868-12870; (b) T. Mori, K. Okamoto, H. Endo, K. Sakakibara, J.P. Hill, S. Shinoda, M. Matsukura, H. Tsukube, Y. Suzuki, Y. Kanekiyo, K. Ariga, *Nanoscale Res. Lett.* **2011**, *6*, 304.
- [26] (a) X. Cha, K. Ariga, T. Kunitake, *J. Am. Chem. Soc.* **1996**, *118*, 9545-9551; (b) K. Ariga, T. Kunitake, *Acc. Chem. Res.* **1998**, *31*, 371-378; (c) K. Ariga, J.P. Hill, Y. Wakayama, *Phys. Stat. Sol. (a)* **2008**, *205*, 1249-1257; (d) K. Ariga, K. Sakakibara, G.J. Richards, J.P. Hill, *Supramol. Chem.* **2011**, *23*, 183-194.
- [27] S. Joy, P. Pal, T.K. Mondal, G.B. Talapatra, S. Goswami, *Chem. Eur. J.* **2012**, *18*, 1761-1771
- [28] J. Yang, S. Lee, H. Lee, J. Lee, H. K. Kim, S.U. Lee, D. Sohn, *Langmuir* **2011**, *27*, 8898-8904
- [29] (a) M. Gleiche, L.F. Chi, H. Fuchs, *Nature* **2000**, *403*, 173-175; (b) M. Shimomura, T. Sawadaishi, *Curr. Opin. Colloid Interface Sci.* **2001**, *6*, 11-16; (c) T. Mori, K. Sakakibara, H. Endo, M. Akada, K. Okamoto, A. Shundo, M.V. Lee, Q. Ji, T. Fujisawa, K. Oka, M. Matsumoto, H. Sakai, M. Abe, J.P. Hill, K. Ariga, *Chem. Lett.* **2012**, *41*, 170-172; (d) T. Mori, K. Sakakibara, H. Endo, M. Akada, K. Okamoto, A. Shundo, M.V. Lee, Q. Ji, T. Fujisawa, K. Oka, M. Matsumoto, H. Sakai, M. Abe, J.P. Hill, K. Ariga, *Langmuir* **2013**, *29*, 7239-7248; (e) D. Gentili, F. Valle, C. Albonetti, F. Liscio, M. Cavallini, *Acc. Chem. Res.* **2014**, *47*, 2692-2699.
- [30] M. Clemente-Leon, E. Coronado, Á. Lopez-Muñoz, D. Repetto, L. Catala, T. Mallah, *Langmuir* **2012**, *28*, 4525-4533.
- [31] (a) Y. Zhang, P.L. Chen, Y. Ma, S. He, M. Liu, *ACS Appl. Mater. Interfaces* **2009**, *1*, 2036-2043. (b) M. Liu, L. Zhang, T. Wang, *Chem. Rev.* **2015**, *115*, 7304-7397.
- [32] J. Yuan, M. Liu, *J. Am. Chem. Soc.* **2003**, *125*, 5051-5056.

- [33] P. Guo, M. Liu, *Chem. Lett.* **2012**, *41*, 1199-1200.
- [34] J.T. Culp, J.-H. Park, D. Stratakis, M.W. Meisel, D.R. Talham, *J. Am. Chem. Soc.* **2001**, *124*, 10083-10090.
- [35] R. Makiura, S. Motoyama, Y. Umemura, H. Yamanaka, O. Sakata, H. Kitagawa, *Nat. Mater.* **2010**, *9*, 565-571.
- [36] T. Bauer, Z. Zheng, A. Renn, R. Enning, A. Stemmer, J. Sakamoto, A.D. Schlüter, *Angew. Chem. Int. Ed.* **2011**, *50*, 7879-7884
- [37] Z. Zheng, L. Opilik, F. Schiffmann, W. Liu, G. Bergamini, P. Ceroni, L.-T. Lee, A. Schütz, J. Sakamoto, R. Zenobi, J. VandeVondele, A.D. Schlüter, *J. Am. Chem. Soc.* **2014**, *136*, 6103-6110.
- [38] J.I. Urgel, M. Schwarz, M. Garnica, D. Stassen, D. Bonifazi, D. Ecija, J. V. Barth, W. Auwarter, *J. Am. Chem. Soc.* **2015**, *137*, 2420-2423
- [39] J.I. Urgel, D. Ecija, W. Auwarter, D. Stassen, D. Bonifazi, J. V. Barth, *Angew. Chem. Int. Ed.* **2015**, *54*, 6163-6167
- [40] A. Shchyrba, C. Wackerlin, J. Nowakowski, S. Nowakowska, J. Björk, S. Fatayer, J. Girovsky, T. Nijs, S.C. Martens, A. Kleibert, M. Stöhr, N. Ballav, T.A. Jung, L.H. Gade, *J. Am. Chem. Soc.* **2014**, *136*, 9355-9363.
- [41] X. Huang, B. Zheng, Z. Liu, C. Tan, J. Liu, B. Chen, H. Li, J. Chen, X. Zhang, Z. Fan, W. Zhang, Z. Guo, F. Huo, Y. Yang, L.-H. Xie, W. Huang, H. Zhang, *ACS Nano* **2014**, *8*, 8695-8701.
- [42] Y. Zhao, N. Kornienko, Z. Liu, C. Zhu, S. Asahina, T.-R. Kuo, W. Bao, C. Xie, A. Hexemer, O. Terasaki, P. Yang, O.M. Yaghi, *J. Am. Chem. Soc.* **2015**, *137*, 2199-2202.
- [43] (a) H.A. Habib, J. Sanchiz, C. Janiak, *Dalton Trans.* **2008**, *36*, 4877-4884; (b) H. Kajiro, A. Kondo, K. Kaneko, H. Kanoh, *Int. J. Mol. Sci.* **2010**, *11*, 3803-3845; (c) T. Yamada, K.

- Otsubo, R. Makiura, H. Kitagawa, *Chem. Soc. Rev.* **2013**, *42*, 6655-6669.
- [44] S.C. Junggeburth, L. Diehl, S. Werner, V. Duppel, W. Sigle, B.V. Lotsch, *J. Am. Chem. Soc.* **2013**, *135*, 6157-6164.
- [45] A. Gallego, C. Hermosa, O. Castillo, I. Berlanga, C.J. Gómez-García, E. Mateo-Martí, J.I. Martínez, F. Flores, C. Gómez-Navarro, J. Gómez-Herrero, S. Delgado, F. Zamora, *Adv. Mater.* **2013**, *25*, 2141-2146.
- [46] D. Umeyama, S. Horike, M. Inukai, T. Itakura, S. Kitagawa, *J. Am. Chem. Soc.* **2012**, *134*, 12780-12785.
- [47] S.-S. Bao, K. Otsubo, J.M. Taylor, Z. Jiang, L.-M. Zheng, H. Kitagawa, *J. Am. Chem. Soc.* **2014**, *136*, 9292-9295.
- [48] C.R. Murdock, N.W. McNutt, D.J. Keffer, D.M. Jenkins, *J. Am. Chem. Soc.* **2014**, *136*, 671-678.
- [49] M. Zhang, G. Feng, Z. Song, Y.-P. Zhou, H.-Y. Chao, D. Yuan, T.T.Y. Tan, Z. Guo, Z. Hu, B.Z. Tang, B. Liu, D. Zhao, *J. Am. Chem. Soc.* **2014**, *136*, 7241-7244.
- [50] I.-H. Park, R. Medishetty, J.-Y. Kim, S.S. Lee, J.J. Vittal, *Angew. Chem. Int. Ed.* **2014**, *53*, 5591-5595.
- [51] X. Huang, P. Sheng, Z. Tu, F. Zhang, J. Wang, H. Geng, Y. Zou, C. Di, Y. Yi, Y. Sun, W. Xu, D. Zhu, *Nat. Commun.* **2015**, *6*, 7408.
- [52] X.-X. Xu, H.-Y. Yang, Z.-Y. Li, X.-X. Liu, X.-L. Wang, *Chem. Eur. J.* **2015**, *21*, 3821-3830
- [53] K. Yan, M. Long, T. Zhang, Z. Wei, H. Chen, S. Yang, J. Xu, *J. Am. Chem. Soc.* **2015**, *137*, 4460-4468.
- [54] (a) A.K. Srivastava, P. Divya, B. Praveenkumar, R. Boomishar, *Chem. Mater.* **2015**, *27*, 5222-5229; (b) S. Khatua, S. Goswami, S. Biswas, K. Tomar, H.S. Jena, S. Konar, *Chem. Mater.* **2015**, *27*, 5349-5360; (c) I. H. Park, R. Medishetty, H.H. Lee, C.E. Mulijanto, H.S.

- Quah, S.S. Lee, J.J. Vittal, *Angew. Chem. Int. Ed.* **2015**, *54*, 7313-7317; (d) R. Ohtani, M. Inukai, Y. Hijikata, T. Ogawa, M. Takenaka, M. Ohba, S. Kitagawa, *Angew. Chem. Int. Ed.* **2015**, *54*, 1139-1143; (e) Z. Sun, T. Liao, Y. Dou, S.M. Hwang, M.-S. Park, L. Jiang, J.H. Kim, S.X. Dou, *Nat. Commun.* **2015**, *5*, 3813.
- [55] S. Bureekaew, S. Shimomura, S. Kitagawa, *Sci. Technol. Adv. Mater.* **2008**, *9*, 014108.
- [56] C.D. Wessells, R.A. Huggins, Y. Cui, *Nat. Commun.* **2011**, *2*, 550.
- [57] S.S. Kumar, J. Joseph, K.L. Phani, *Chem. Mater.* **2007**, *19*, 4722-4730.
- [58] P.K. Thallapally, R.K. Motkuri, C.A. Fernandez, B.P. McGrail, G S. Behrooz, *Inorg. Chem.* **2010**, *49*, 4909-4915.
- [59] M.V. Bennett, L.G. Beauvais, M.P. Shores, J.R. Long, *J. Am. Chem. Soc.* **2001**, *123*, 8022-8032.
- [60] H. Yuan, M. Hu, C.H. Liu, Y. Yamauchi, K.C.-W. Wu, *Chem. Commun.* **2012**, *48*, 5151-5153.
- [61] N.L. Torad, M. Hu, M. Imura, M. Naito, Y. Yamauchi, *J. Mater. Chem.* **2012**, *22*, 18261-18267.
- [62] F. Qu, A. Shi, M. Yang, J. Jiang, G. Shen, R. Yu, *Anal. Chim. Acta* **2007**, *605*, 28-33.
- [63] H. Ming, N.L. Torad, Y.-D. Chiang, K. C.-W. Wu, Y. Yamauchi, *CrystEngComm* **2012**, *14*, 3387-3396.
- [64] S.-H. Lee, Y.-D. Huh, *Bull. Korean Chem. Soc.* **2012**, *33*, 1078-1080.
- [65] M. Hu, J.-S. Jiang, Y. Zeng, *Chem. Commun.* **2010**, *46*, 1133-1135.
- [66] M.B. Zakaria, M. Hu, M. Imura, R.R. Salunkhe, N. Umezawa, H. Hamoudi, A.A. Belik, Y. Yamauchi, *Chem. Eur. J.* **2014**, *20*, 17375-17384.
- [67] J. Jiménez-Gallegos, J. Roque, H. Yee-Madeira, E. Reguera, *Z. Anorg. Allg. Chem.* **2012**, *638*, 1146-1150.



- [68] G. Maurin-Pasturel, J. Long, Y. Guari, F. Godiard, M.-G. Willinger, C. Guerin, J. Larionova, *Angew. Chem. Int. Ed.* **2014**, *53*, 3872-3876.
- [69] O.N. Risset, E.S. Knowles, S. Ma, M.W. Meisel, D.R. Talham, *Chem. Mater.* **2013**, *25*, 42-47.
- [70] M. Hu, S. Furukawa, R. Ohtani, H. Sukegawa, Y. Nemoto, J. Reboul, S. Kitagawa, Y. Yamauchi, *Angew. Chem. Int. Ed.* **2012**, *51*, 984-988.
- [71] S. Kawano, D. Kobayashi, S. Taguchi, M. Kunitake, T. Nishimi, *Macromolecules* **2010**, *43*, 473-479.
- [72] M. Cao, X. Wu, X. He, C. Hu, *Chem. Commun.* **2005**, 2241-2243.
- [73] X. Wu, M. Cao, C. Hu, X. He, *Cryst. Growth Des.* **2006**, *6*, 26-28.
- [74] O. Stefanczyk, T. Korzeniak, W. Nitek, M. Rams, B. Sieklucka, *Inorg. Chem.* **2011**, *50*, 8808-8816.
- [75] M.B. Zakaria, M. Hu, Y. Tsujimoto, Y. Sakka, N. Suzuki, Y. Kamachi, M. Imura, S. Ishihara, K. Ariga, Y. Yamauchi, *Chem. Asian J.* **2014**, *9*, 1511-1514.
- [76] H. Pang, J. Deng, J. Du, S. Li, J. Li, Y. Ma, J. Zhang, J. Chen, *Dalton Trans.* **2012**, *41*, 10175-10181.
- [77] M.B. Zakaria, A.A. Belik, C.-H. Liu, H.-Y. Hsieh, Y.-T. Liao, V. Malgras, Y. Yamauchi, K.C.-W. Wu, *Chem. Asian J.* **2015**, *10*, 1457-1462.
- [78] M.B. Zakaria, M. Hu, M. Pramanik, C. Li, J. Tang, A. Aldalbahi, S.M. Alshehri, V. Malgras, Y. Yamauchi, *Chem. Asian J.* **2015**, *10*, 1541-1545.
- [79] L. Hu, Y. Huang, Q. Chen, *J. Alloys Compd.* **2013**, *559*, 57-63.
- [80] M. Hu, A. A. Belik, M. Imura, K. Mibu, Y. Tsujimoto, Y. Yamauchi, *Chem. Mater.* **2012**, *24*, 2698-2707.
- [81] L. Hu, N. Yan, Q. Chen, P. Zhang, H. Zhong, X. Zheng, Y. Li, X. Hu, *Chem. Eur. J.* **2012**,

18, 8971-8977.

- [82] N. Yan, L. Hu, Y. Li, Y. Wang, H. Zhong, X. Hu, X. Kong, Q. Chen, *J. Phys. Chem. C* **2012**, *116*, 7227-7235.

# Chapter 2

## Chapter 2

# 2. Single-Crystal-like Nanoporous Spinel Oxides: A Strategy for Synthesis of Nanoporous Metal Oxides Utilizing Metal-Cyanide Hybrid Coordination Polymers

### 2.1. Introduction

Chemically synthesized nanoporous metal oxides are of great potential in many applications, such as catalysis, water purification, energy storage, and sensing, because of their high accessible surface areas and large number of active sites provided by their nanoporous structure [1,2]. Until now, many nanoporous metal oxides with different compositions have been reported utilizing self-organization of surfactants or block copolymers [1,2]. In almost all cases, however, the frameworks are poorly crystallized and/or amorphous. This fact can limit their practical usage.

Therefore, many efforts have been made to develop novel synthetic approaches to prepare nanoporous materials with perfectly crystalline frameworks [3]. Controlled thermal and hydrothermal treatments can induce effective crystallization in frameworks [4-6]. However, large mesostructural changes can occur in some cases through the fusion of several pores during

framework crystallization, significantly reducing the surface area. Several groups have also reported mesoporous organosilica with perfectly crystallized frameworks showing unique chemical and physical properties that are not attainable by mesoporous organosilica with amorphous frameworks [7-12]. Mesoporous zeolites have also been reported by designed surfactants, and their high catalytic activity for various acid-catalyzed reactions involving bulky molecules has been shown [13]. The hard-templating method is very effective for the preparation of mesoporous crystallized metal oxides [14-20]. In this case, some solvents, such as water and alcohols, are used to dissolve target metal precursors and to fill hard-templates (*e.g.*, mesoporous silica, carbon, and alumina) before the final thermal treatment. Although highly robust and crystallized frameworks are realized, relatively complicated operation processes are required. Thus, by considering highly crystalline frameworks, I can discover novel solid-state properties or dramatically upgrade inherent properties, which cannot be realized with amorphous or poorly crystallized frameworks.

Mesocrystals, which are a highly oriented aggregation of nanocrystals, have often exhibited well-developed porous structures with single-crystal-like frameworks [21-24]. Single-crystalline solid precursors can be converted to nanoporous materials with close crystal structures after insertion, substitution, and removal of some atoms. By the shrinkage of crystal lattices and the removal of unstable elements, nanoporous structures are formed inside the crystals. Topotactic conversion has been reported as a sophisticated synthetic method. Anatase  $\text{TiO}_2$  mesocrystals have been prepared by topotactic conversion from  $\text{NH}_4\text{TiOF}_3$  mesocrystals [25]. Growth of mesoporous quasi-single-crystalline  $\text{Co}_3\text{O}_4$  has been also reported by topotactic chemical transformation [26]. However, the requirement of similarity between the solid precursor and targeted metal oxide is hard to satisfy.

A solid-state conversion method is a promising way to synthesize nanoporous metal

oxides with crystalline frameworks. As a new solid-state strategy, I have been focused on thermal decomposition of coordination polymers, which are hybrids containing metals and organic linkers. Coordination polymers (CPs), such as metal-organic frameworks (MOFs) and porous coordination polymers (PCPs), have received attention as a novel class of nanoporous materials in recent years because of their adjustable pore structures and wide framework compositions [27-32]. The diverse structures, high surface area, and large pore volume of MOFs (or PCPs) have inspired their consideration as precursors to prepare nanoporous carbons. Since the first report by Xu *et al.* [33-35] several MOFs, such as MOF-5, Al-PCP, and ZIF-8, have been demonstrated as promising precursors, yielding highly nanoporous carbons showing excellent properties in gas adsorption, electrochemical capacitance, sensing, and catalysis [36-40]. CPs have also been utilized as novel precursors for making various metal oxides [41-45]. Although the obtained metal oxides show well-defined shapes, the surface areas are relatively low. Nanoporous metal oxides with oriented frameworks have never been reported using this strategy.

In contrast, metal-cyanide hybrid CPs, in which the metal ions were bridged by  $-C\equiv N-$  organic units, contain a large amount of metals [46-48]. The cyano groups can be removed by calcination in air to form the corresponding metal oxides because the metal ions can be oxidized and the organic units removed [49-52]. The metal ions are uniformly separated by cyano groups in the cubic crystal system, so it is expected that nanoporous metal oxides can be obtained. In this work, I report a preparation of mesoporous crystalline metal oxides by a thermal conversion of metal-cyanide hybrid CPs. The main goal in this study is to demonstrate a direct thermal conversion to single-crystal-like nanoporous metal oxides which have been never realized yet [49-52]. This strategy based on thermally induced solid-state conversion can realize the preparation of single-crystal-like nanoporous metal oxides by changing the compositions of the precursors. For proof of concept, in this study, metal oxides with a spinel crystal structure are

selected as the model targeted material. Nanoporous spinel metal oxides composed of Fe and/or Co atoms are successfully synthesized, showing a stable magnetic property at room temperature.

## 2.2. Experimental Section

### 2.2.1. Chemicals

Potassium hexacyanoferrate(III) ( $\text{K}_3[\text{Fe}(\text{CN})_6] \cdot 3\text{H}_2\text{O}$ ) was purchased from Merck KGaA, Germany. Potassium hexacyanochromate(III) ( $\text{K}_3[\text{Cr}(\text{CN})_6]$ ), potassium hexacyanocobaltate(III) ( $\text{K}_3[\text{Co}(\text{CN})_6]$ ), and iron(II) chloride tetrahydrate ( $\text{FeCl}_2 \cdot 4\text{H}_2\text{O}$ ) were purchased from Sigma-Aldrich, USA. Cobalt(II) chloride anhydrous ( $\text{CoCl}_2$ ), nickel(II) chloride hexahydrate ( $\text{NiCl}_2 \cdot 6\text{H}_2\text{O}$ ), trisodium citrate dihydrate, polyvinylpyrrolidone-K30, and hydrochloric acid were purchased from Nacalai Tesque, Japan. All chemical reagents were used without further purification.

### 2.2.2. Synthesis of Solid Metal-Cyanide Hybrid CPs and Their Thermal Conversion to Nanoporous Metal Oxides

#### 2.2.2.1. Synthesis of Solid CoCo Nanocubes

$\text{CoCl}_2$  (77.9 mg) and trisodium citrate dihydrate (397.1 mg) were dissolved in 20 mL of water to form a clear solution. Meanwhile,  $\text{K}_3[\text{Co}(\text{CN})_6]$  (130 mg) was dissolved into 20 mL of water. Then the above two solutions were combined by stirring until the mixture became clear. The obtained solution was aged for 24 h. The precipitate was collected by centrifugation. After being washed extensively with water and ethanol, the precipitate was dried at room temperature. The obtained composition is  $\text{Co}^{\text{II}}_3[\text{Co}^{\text{III}}(\text{CN})_6]_2$ , abbreviated as solid CoCo.

### 2.2.2.2. Synthesis of Solid FeCo Nanocubes

$\text{FeCl}_2 \cdot 4\text{H}_2\text{O}$  (59.6 mg) and trisodium citrate dihydrate (100 mg) were dissolved in 20 mL of water to form a clear solution. Meanwhile,  $\text{K}_3[\text{Co}(\text{CN})_6]$  (130 mg) was dissolved into 20 mL of water. Then the above two solutions were combined by stirring until the mixture became clear. The obtained solution was aged for 24 h. The precipitate was collected by centrifugation. After being washed extensively with water and ethanol, the precipitate was dried at room temperature. The obtained composition is  $\text{Fe}^{\text{II}}_3[\text{Co}^{\text{III}}(\text{CN})_6]_2$ , abbreviated as solid FeCo.

### 2.2.2.3. Synthesis of Solid FeFe Nanocubes

PVP (K30, 3.0 g) and  $\text{K}_3[\text{Fe}(\text{CN})_6] \cdot 3\text{H}_2\text{O}$  (132 mg) were added to 40 mL of a 0.01 M HCl solution by stirring. After 30 min, a clear solution was obtained. Then the solution was heated at 80 °C for 20 h. The precipitate was collected by centrifugation. After being washed extensively with water and ethanol, the precipitate was dried at room temperature. The obtained composition is  $\text{Fe}^{\text{III}}_4[\text{Fe}^{\text{II}}(\text{CN})_6]_3$ , abbreviated as solid FeFe.

### 2.2.2.4. Thermal Conversion to Nanoporous Metal Oxides

The above-obtained three solid CPs with cube shapes (solid CoCo, solid FeCo, and solid FeFe) were used as the precursor. The powders (50.0 mg) were heated inside an electronic furnace from room temperature to desired temperatures at a heating rate of 5 °C min<sup>-1</sup>. After arriving at the desired temperature (260 °C), the samples were annealed for 4 h. During this stage, organic units were removed to obtain the corresponding nanoporous metal oxides, abbreviated as solid cal-CoCo, solid cal-FeCo, and solid cal-FeFe. After that, the samples were cooled inside the furnace naturally. Finally, the obtained powder was collected for further characterization. All calcination processes were performed in air.



### 2.2.3. Synthesis of Core-Shell Nanocubes of Metal-Cyanide Hybrid CPs, Creation of Hollow Interiors, and Their Thermal Conversion to Nanoporous Metal Oxides

#### 2.2.3.1. Synthesis of NiCr Nanocubes

NiCl<sub>2</sub>·6H<sub>2</sub>O (143 mg) and trisodium citrate dihydrate (220 mg) were dissolved in 20 mL of water to form a clear solution. Meanwhile, K<sub>3</sub>[Cr(CN)<sub>6</sub>] (130 mg) was dissolved into 20 mL of water. Then the above two solutions were combined by stirring until the mixture became clear. The obtained solution was aged for 24 h. The precipitate was collected by centrifugation. After being washed extensively with water and ethanol, the precipitate was dried at room temperature. The obtained composition is Ni<sup>II</sup><sub>3</sub>[Cr<sup>III</sup>(CN)<sub>6</sub>]<sub>2</sub>, abbreviated as NiCr.

#### 2.2.3.2. Synthesis of NiCr@CoCo Nanocubes

NiCr nanocubes (10 mg) were dispersed in a mixed solution containing CoCl<sub>2</sub> (77.9 mg), trisodium citrate dihydrate (397.1 mg), and distilled water (20 mL). Meanwhile, K<sub>3</sub>[Co(CN)<sub>6</sub>] (133 mg) was dissolved into distilled water (20 mL). Then the above two solutions were combined by stirring. The obtained solution was aged for 24 h. The precipitate was collected by centrifugation. After being washed extensively with water and ethanol, the precipitate was dried at room temperature. The obtained product is abbreviated as NiCr@CoCo.

#### 2.2.3.3. Synthesis of NiCr@FeCo Nanocubes

NiCr nanocubes (10 mg) were dispersed in a mixed solution containing FeCl<sub>2</sub>·4H<sub>2</sub>O (59.6 mg), trisodium citrate dihydrate (100 mg), and distilled water (20 mL). Meanwhile, K<sub>3</sub>[Co(CN)<sub>6</sub>] (130 mg) was dissolved into distilled water (20 mL). Then the above two solutions were combined by stirring. The obtained solution was aged for 24 h. The precipitate was collected by centrifugation.

After being washed extensively with water and ethanol, the precipitate was dried at room temperature. The obtained product is abbreviated as NiCr@FeCo.

#### **2.2.3.4. Synthesis of NiCr@CoFe Nanocubes**

NiCr nanocubes (10 mg) were dispersed in a mixed solution containing CoCl<sub>2</sub> (77.9 mg), trisodium citrate (397 mg), and distilled water (20 mL). Meanwhile, K<sub>3</sub>[Fe(CN)<sub>6</sub>] (132 mg) was dissolved into distilled water (20 mL). Then the above two solutions were combined by stirring. The obtained solution was aged for 24 h. The precipitate was collected by centrifugation. After being washed extensively with water and ethanol, the precipitate was dried at room temperature. The obtained product is abbreviated as NiCr@CoFe.

#### **2.2.3.5. Synthesis of NiCr@FeFe Nanocubes**

NiCr nanocubes (10 mg) were dispersed in a mixed solution containing PVP (K30, 3.0 g), K<sub>3</sub>[Fe(CN)<sub>6</sub>]·3H<sub>2</sub>O (132 mg), and 0.01 M HCl solution (40.0 mL) by stirring. After 30 min, the vial was placed into an electric oven and heated at 80°C for 24 h. The precipitate was collected by centrifugation. After being washed extensively with water and ethanol, the precipitate was dried at room temperature. The obtained product is abbreviated as NiCr@FeFe.

#### **2.2.3.6. Preparation of Hollow Nanocubes by Removal of NiCr Cores and Thermal Conversion to Nanoporous Metal Oxides**

The above-obtained core-shell nanocubes (NiCr@CoCo, NiCr@FeCo, NiCr@CoFe, and NiCr@FeFe) (40 mg) were dispersed in a 2 M HCl solution (40 mL) by stirring. After 3 h, the vessels were transferred into stainless autoclaves and heated at 130 °C for 3 h. (Caution! CN groups may be converted to HCN gas in hot acidic solution. Therefore, the preparation should be

always carried out under a fume hood). During this stage, the NiCr cores were completely removed to obtain hollow nanocubes, abbreviated as hollow CoCo, hollow FeCo, hollow CoFe, and hollow FeFe. After aging, the precipitates were collected by centrifugation and washed several times in distilled water and ethanol. After drying at room temperature, the hollow CoCo, FeCo, CoFe, and FeFe nanocubes were annealed at 350 °C for 1 h to obtain the corresponding nanoporous metal oxides, abbreviated as hollow cal-CoCo, hollow cal-FeCo, hollow cal-CoFe, and hollow cal-FeFe, respectively.

## 2.2.4. Characterizations

### 2.2.4.1. Materials Characterization

Scanning microscopic microscope (SEM) images were taken with a Hitachi SU8000 scanning microscope at an accelerating voltage of 5 kV. TEM observation was performed using a JEM-2100F TEM system that was operated at 200 kV and equipped with energy-dispersive spectrometer analysis. Wide-angle powder X-ray diffraction (XRD) patterns were obtained with a Rigaku RINT 2500X diffractometer using monochromated  $\text{Cu}_{K\alpha}$  radiation (40 kV, 40 mA) at a scanning rate of  $5^\circ \text{ min}^{-1}$ . Nitrogen adsorption-desorption isotherms were obtained using a Quantachrome Autosorb Automated Gas Sorption System at 77 K. X-ray photoelectronic spectroscopy (XPS) spectra were recorded at room temperature using JPS-9010TR (JEOL) instrument with  $\text{Mg}_{K\alpha}$  X-ray source.

### 2.3.4.2. Electrochemical Measurement

The graphite substrates were first polished using a fine polisher in a water flow. Then the substrates were rinsed with distilled water in an ultrasonic bath for 30 min. The mass of electrodes was measured using the ultra-microbalance (METTLER TOLEDO). Each electrode

contained  $1.0 \text{ mg cm}^{-2}$  of electroactive material. Samples were mixed with a polyvinylidene difluoride (PVDF, 20%) in N-methylpyrrolidinone (NMP) solvent. The resulting slurry was homogenized by ultrasonication and coated onto graphite substrates ( $1 \times 1 \text{ cm}^2$ ), which was followed by drying at  $80 \text{ }^\circ\text{C}$  for 2 h in a vacuum oven. The electrochemical measurement was conducted in a three-electrode electrochemical cell with a Pt counter electrode and Ag/AgCl as a reference electrode in a 6 M KOH solution. The graphite substrate coated with the samples was used as the working electrode. Cyclic voltammetry (CV) measurements were obtained using an electrochemical workstation (CHI 660E CH Instruments, USA) in the scan range of  $-0.1 \text{ V}$  to  $0.5 \text{ V}$ . The specific capacitance ( $C_{sp}$ ) is calculated by using the following equation:

$$C = \frac{1}{ms(V_f - V_i)} \int_{V_i}^{V_f} I(V) dv \quad (2.1)$$

In which  $C_{sp}$  is the specific capacitance ( $\text{F g}^{-1}$ ),  $m$  is the mass of the active electrode material (g),  $s$  is the potential scan rate ( $\text{mV s}^{-1}$ ),  $V_f$  and  $V_i$  are the integration limits of the voltammetric curve (V), and  $I(V)$  denotes the response current density ( $\text{A cm}^{-2}$ ).

## 2.3. Results and Discussion

### 2.3.1. Synthesis of Solid Metal-Cyanide Hybrid CPs and Their Thermal Conversion to Nanoporous Metal Oxides

Here I synthesized three metal-cyanide hybrid CPs;  $\text{Co}^{\text{II}}_3[\text{Co}^{\text{III}}(\text{CN})_6]_2$  (abbreviated as solid CoCo),  $\text{Fe}^{\text{II}}_3[\text{Co}^{\text{III}}(\text{CN})_6]_2$  (abbreviated as solid FeCo), and  $\text{Fe}^{\text{III}}_4[\text{Fe}^{\text{II}}(\text{CN})_6]_3$  (abbreviated as solid FeFe). Thermal conversion of solid CPs (solid CoCo, solid FeCo, and solid FeFe) to the corresponding nanoporous metal oxides is carefully discussed in this section. The morphology of the precursors before and after calcination is shown in **Figures 2.1.1** and **2**. Well-defined nanocubes with 200 nm in size were observed without any irregularly shaped products.

Wide-angle XRD patterns for solid CoCo, solid FeCo, and solid FeFe before calcination were assigned to be a face-center cubic (*fcc*) structure (**Figure 2.2**). Selected-area electron diffraction (ED) patterns proved that an individual nanocube possessed a single-crystalline structure. As a typical example, the ED patterns for a solid FeCo nanocube are shown in **Scheme 2.1a-2**, which is a typical one for metal-cyanide hybrid CPs [48].

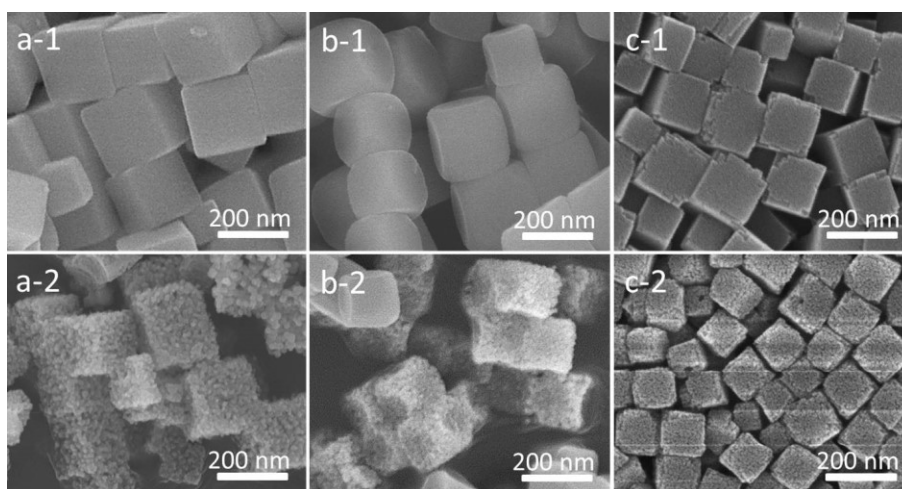


**Figure 2.1.1.** SEM images of (a-1) solid CoCo nanocubes, (a-2) solid cal-CoCo nanocubes, (b-1) solid FeCo nanocubes, (b-2) solid cal-FeCo nanocubes, (c-1) solid FeFe nanocubes, and (c-2) solid cal-FeFe nanocubes.

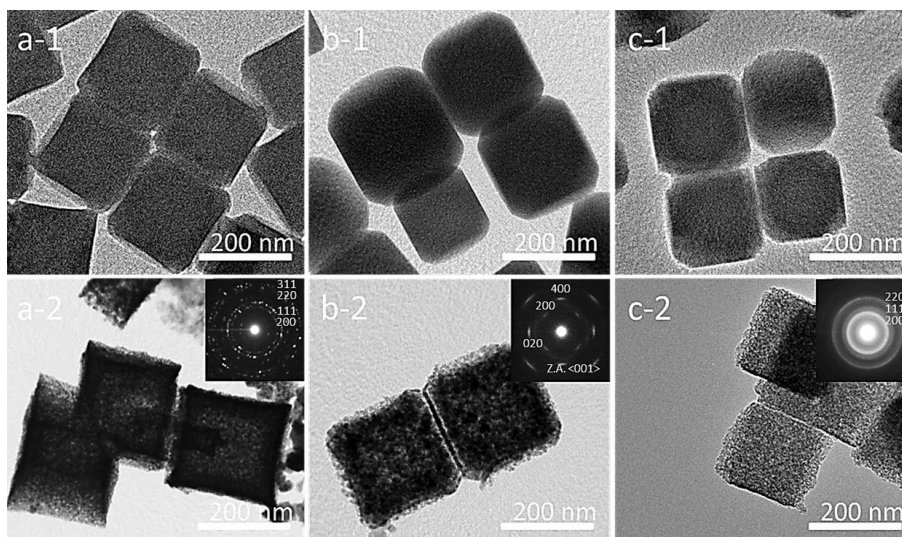


**Figure 2.1.2.** TEM images of (a-1) solid CoCo nanocubes, (a-2) solid cal-CoCo nanocubes, (b-1) solid FeCo nanocubes, (b-2) solid cal-FeCo nanocubes, (c-1) solid FeFe nanocubes, and (c-2) solid cal-FeFe nanocubes. The corresponding selected-area ED patterns of individual nanocubes are shown as inset images.

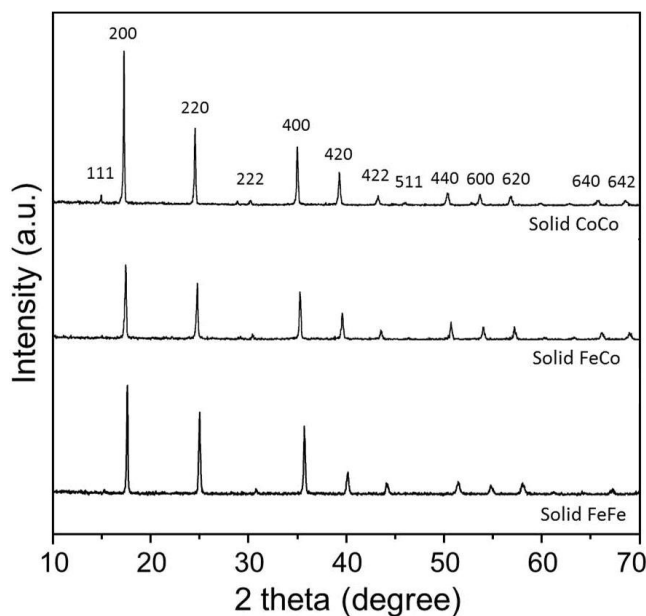


**Figure 2.2.** Wide-angle XRD patterns of solid CoCo nanocubes, solid FeCo nanocubes, and solid FeFe nanocubes.

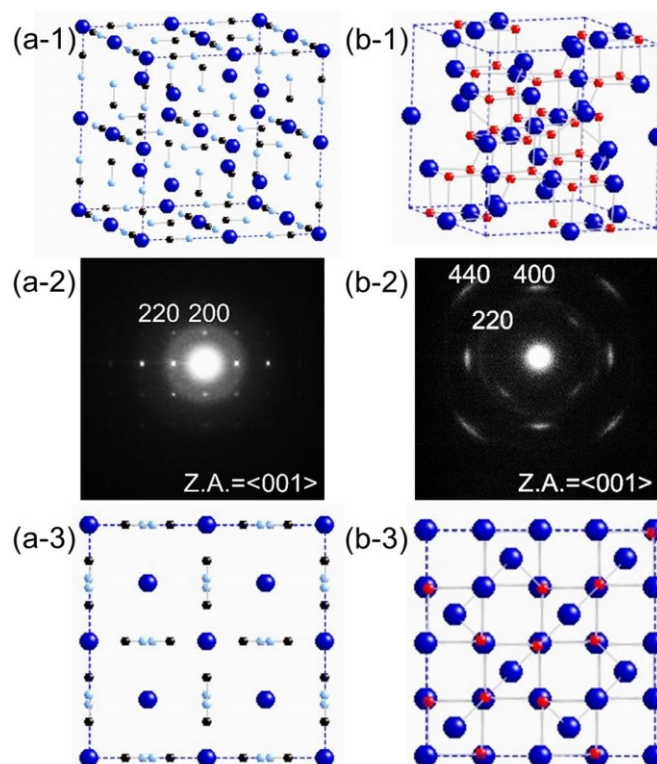
To prepare nanoporous FeCo oxide, solid FeCo nanocubes were calcined in air for 4 h (**Scheme 2.2**), which is abbreviated as solid cal-FeCo. During this stage, organic units ( $-\text{C}\equiv\text{N}-$ ) were completely removed. Previously, I studied the thermal decomposition process by thermogravimetry/differential thermal analysis/mass spectrometry (TG-DTA-MS) under He/O<sub>2</sub> flow and the results indicated several exothermic peaks at approximately 260-310 and 470 °C, accompanied with the production of CO<sub>2</sub> and/or N<sub>2</sub>O ( $m/z = 44$ ) as well as N<sub>2</sub> and/or CO ( $m/z = 28$ ), which is typical for the combustion reaction of a CN-containing material [49]. Even after removal of the organic units, the products retained the original cubic shape (**Figure 2.1.1**). A high-resolution TEM image indicated the formation of nanopores inside the nanocubes (**Figure 2.3a**). Wide-angle XRD patterns proved that the calcined powder (solid cal-FeCo) possessed a highly crystallized spinel structure ( $Fd-3m$ ) without any formation of other crystalline phases (**Figure 2.4**). To understand the oxidation states of Fe and Co atoms, the obtained solid cal-FeCo was studied by XPS analysis (**Figure 2.5**). The Fe 2*p* spectrum contained Fe 2*p*<sub>3/2</sub> (711 eV), Fe

$2p_{1/2}$  (724 eV), and the satellite peak, indicating that the Fe atoms existed as  $\text{Fe}^{3+}$ . It has been known that  $\text{Fe}^{2+}$  is not stable but is easily converted to the stable form of  $\text{Fe}^{3+}$  by heating. The Co  $2p$  spectrum shows a typical doublet consisting of a low-energy band (780 eV) and a high-energy band (795 eV), which belong to Co  $2p_{3/2}$  and Co  $2p_{1/2}$ , respectively (**Figure 2.5**). The energy difference between the Co  $2p_{3/2}$  and  $2p_{1/2}$  splitting is approximately 15 eV, which coincides with the previous work on the formation of a  $\text{Co}_3\text{O}_4$  spinel crystal [26]. From the XPS result, the chemical formula of solid cal-FeCo can be defined as  $\text{Co}^{\text{II}}_{1.0}\text{Co}^{\text{III}}_{0.2}\text{Fe}^{\text{III}}_{1.8}\text{O}_4$  (Fe-Co oxide), which matches the ICP elemental analysis. No residual carbon or nitrogen content was observed, which was confirmed by CHN analysis.

The most interesting point is that selected-area ED patterns taken from an individual nanocube particle exhibited well-defined crystallographic orientation inside the nanocubes (**Scheme 2.1b-2**). Intense periodic spots belong to highly oriented crystalline pore walls. From high-resolution TEM data, it was proved that the atomic lattice fringes were well oriented in the same direction (**Figure 2.3b**). This means that the nanocubes are composed by connected nanoparticles in the same direction, which often have been known as mesocrystals. Thus, the Fe and Co contents in solid Fe-Co with a *fcc* crystal structure are perfectly rearranged into the spinel crystalline framework in an oriented way during the annealing process, as shown in **Schemes 2.1** and **2.2**.

To fully understand this phenomenon, another two precursors (solid CoCo and solid FeFe) with the same *fcc* crystalline structures were calcined under the same conditions (**Scheme 2.2**), which are abbreviated as solid cal-CoCo and solid cal-FeFe, respectively. SEM and TEM images of the starting solid CoCo nanocubes and solid FeFe nanocubes are shown in **Figure 2.1.1** and **2**. In both cases, uniform cube shapes 200 nm in size were observed. Wide-angle XRD patterns proved that both the nanocubes possessed *fcc* structures (**Figure 2.2**). After calcination,

the cubic shapes were retained, and well-developed nanoporous structures were confirmed by SEM and TEM images (Figure 2.1.1 and 2). Unlike solid cal-FeCo nanocubes, however, the crystalline degrees of both solid cal-CoCo and solid cal-FeFe nanocubes were very low.



**Scheme 2.1.** Crystal models and the corresponding selected-area ED patterns of (a) solid FeCo nanocubes with an *fcc* crystal structure and (b) solid cal-FeCo nanocubes with a spinel crystal structure. (a-1, b-1) Three-dimensional crystal models; (a-2, b-2) selected-area ED patterns taken from an individual nanocube; and (a-3, b-3) atomic arrangements viewed from the  $\langle 001 \rangle$  direction.

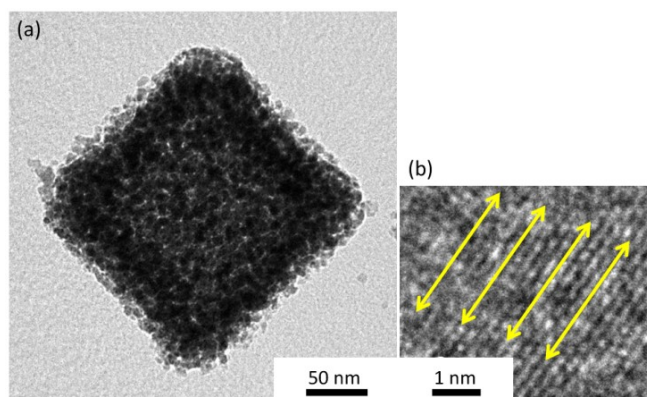


**Figure 2.3.** (a) Low-magnification TEM image and (b) high-magnification TEM image of solid cal-FeCo nanocubes.



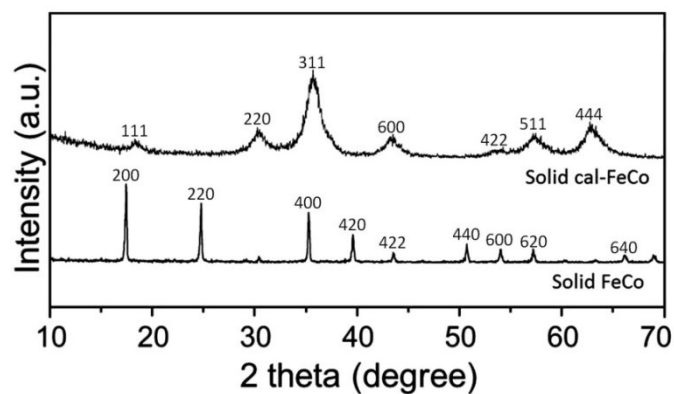
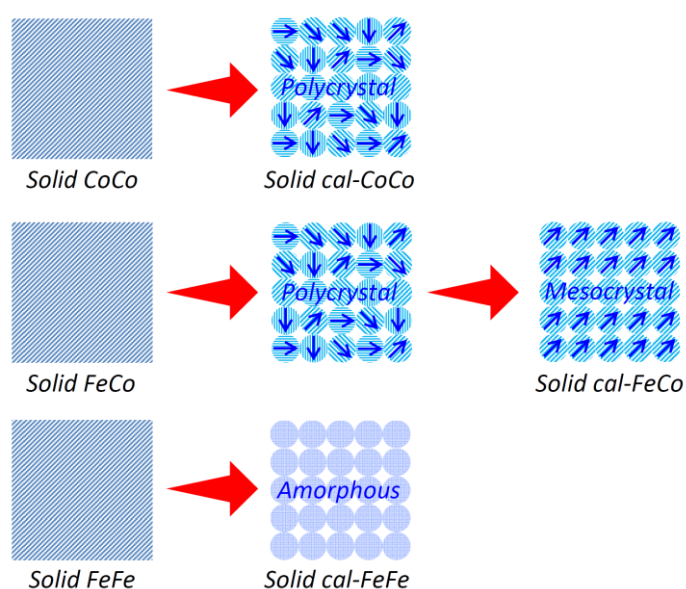


**Figure 2.4.** Wide-angle XRD patterns of solid FeCo nanocubes and solid cal-FeCo nanocubes.



**Scheme 2.2.** Illustration of thermal conversion process for solid CoCo nanocubes, solid FeCo nanocubes, and solid FeFe nanocubes.

In the case of solid cal-CoCo, a wide-angle XRD pattern was assigned to be a pure crystalline spinel  $\text{Co}_3\text{O}_4$  structure (not shown), but selected-area ED patterns taken from an individual nanocube exhibited ring-like patterns with intense spots showing a polycrystalline state (**Figure 2.1.2**). Thus, the crystalline orientation in the framework was random inside the nanocubes. The Co  $2p$  XPS spectrum of solid cal-CoCo nanocubes was similar to that observed in solid cal-FeCo nanocubes, suggesting the co-existence of both  $\text{Co}^{2+}$  and  $\text{Co}^{3+}$  states (**Figure 2.5**). According to

elemental analysis, the production composition was very close to  $\text{Co}_3\text{O}_4$ . Thus, direct calcination of solid CoCo nanocubes resulted in the formation of nanoporous  $\text{Co}_3\text{O}_4$  with polycrystallized walls (**Scheme 2.2**). On the other hand, in the case of solid cal-FeFe, the wide-angle XRD pattern showed no obvious peaks, suggesting neither a polycrystalline nor an amorphous state. Selected-area ED patterns showed amorphous rings without intense spots (**Figure 2.1.2c-2**). Similar to cal-FeCo nanocubes, the majority were present as  $\text{Fe}^{(\text{III})}$  (**Figure 2.5**). Thus, direct calcination of solid FeFe nanocubes resulted in the formation of nanoporous Fe oxides with amorphous walls (**Scheme 2.2**).

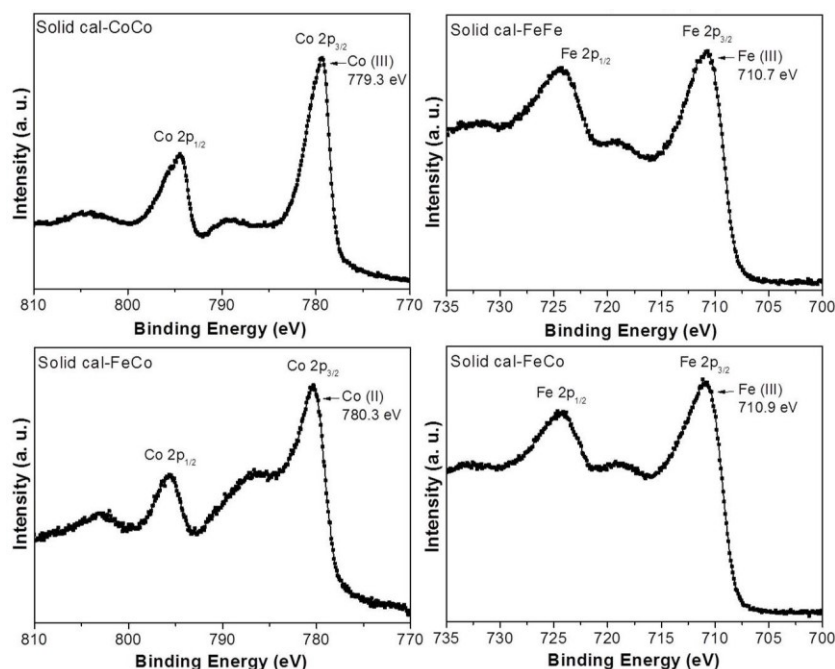


**Figure 2.5.** XPS spectrum for solid cal-CoCo nanocubes, solid cal-FeCo nanocubes, and solid cal-FeFe nanocubes.

The surface areas of solid cal-CoCo, solid cal-FeCo, and solid cal-FeFe were measured by  $\text{N}_2$  adsorption-desorption isotherms. Solid cal-FeFe exhibited the highest specific surface area (larger than  $200 \text{ m}^2 \text{ g}^{-1}$ ) among the three samples. However, this value is not surprising, because the amorphous Fe oxide frameworks can preserve micropores originating from the precursor. It was

interesting that the surface area of solid cal-FeCo ( $105 \text{ m}^2 \text{ g}^{-1}$ ) with a single-crystal-like framework was much higher than that of solid cal-CoCo ( $32 \text{ m}^2 \text{ g}^{-1}$ ) with a polycrystalline framework. Considering two facts ((i) Fe and Co are of similar molecular weight, and (ii) both have the same spinel crystal structure), the surface areas for cal-FeCo and cal-CoCo nanocubes should be the same. In the case of solid cal-CoCo nanocubes, the microporosity of the precursor is probably lost during the re-arrangement of crystalline domains, thereby leading to a low specific surface area.

From the above results, it is found that the crystalline structures, degrees, and orientations in the obtained nanoporous metal oxides obviously depend on the compositions in the precursors. As seen in wide-angle XRD patterns (**Figure 2.4**), the precursors have entirely different crystalline structures from those of the finally obtained nanoporous metal oxides, indicating that the arrangements/locations of metal atoms are quite different from each other, thus ruling out the possibility of topotactical conversion. To seek a possible solution, intermediate products during the thermal decomposition of solid FeCo nanocubes were investigated by high-resolution TEM. After calcination for 1 h, a single particle was composed by many crystalline domains, which were randomly oriented inside the nanocube (**Figure 2.6**). After annealing for 2 h, the crystalline domains were oriented in the same direction, although a few amorphous parts still existed. It is well known that a multiple-step transformation often happens, and it is driven by the need to decrease the surface energy. In general, amorphous phases are formed at the first step. Then the amorphous phases are aggregated to each other, and small crystalline domains with random orientations are generated among the amorphous aggregations. Finally, the crystalline domains are gradually rotated and attached to each other to form highly oriented crystalline phases, as shown in **Scheme 2.2**. Nanoporous products are obtained from a recrystallization event (*i.e.*, a transformation from the amorphous state (less dense phase) to a

crystalline state (more dense phase). **Figure 2.7** shows the (100) surface model of two spinel structures ( $\text{Co}_3\text{O}_4$  and  $\text{Fe}_2\text{CoO}_4$ ). I guess that there is the significant difference of the surface energy between two crystal surfaces. The crystal surface with lower surface energy tends to be exposed more easily, meaning minute nanocrystals are stabilized without further crystal growth. While, the crystal surface with higher surface energy is not generally exposed, in which larger crystals are formed in order to mineralize the total surface energy by rotating the crystalline domains, as shown in **Scheme 2.2**.

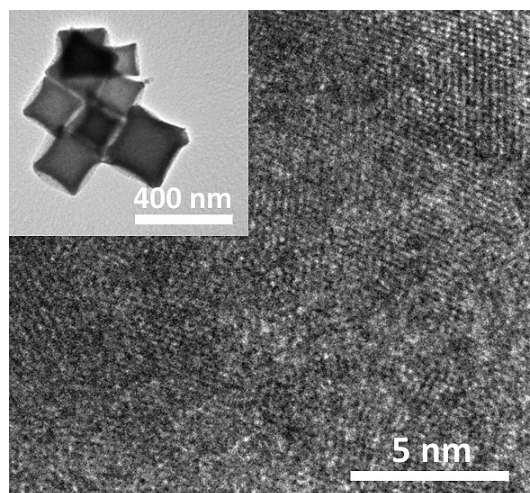


**Figure 2.6.** Low- and high-magnification TEM images for solid FeCo nanocubes. High-magnification TEM image shows that the nanocube is composed by many crystalline domains oriented randomly.

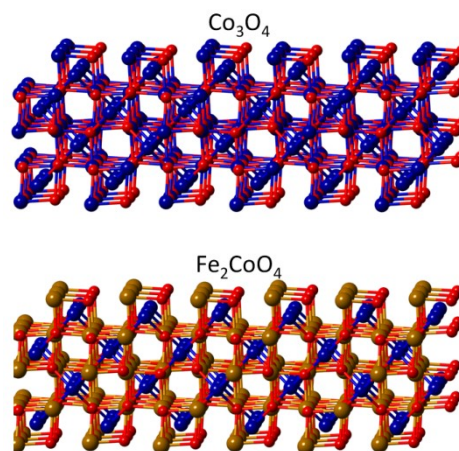


**Figure 2.7.** Crystal models of (100) surface in  $\text{Co}_3\text{O}_4$  and  $\text{Fe}_2\text{CoO}_4$  spinel structures.

Because spinel metal oxides are one of the famous magnetic materials, I evaluated the magnetic properties for solid cal-CoCo, solid cal-FeCo, and solid cal-FeFe. Room-temperature magnetization curves of the obtained samples are shown in **Figure 2.8**. In the cases of solid cal-CoCo nanocubes and solid cal-FeFe nanocubes, the pore walls were composed of minute crystalline sizes and/or an amorphous-like state, as observed in the selected-area ED patterns (**Figure 2.1.2**). Generally, such small ferromagnetic grains show superparamagnetic behavior. Each grain does not show a ferromagnetic state because of the thermal fluctuation of the magnetic moment at room temperature. From the magnetization curve (**Figure 2.8**), no hysteresis was observed at all, and both the coercive forces ( $H_c$ ) and the residual magnetization ( $M_r$ ) were nearly zero. This is typical of superparamagnetic behavior. The  $M_s$  values measured at 10000 Oe were  $3.4 \text{ emu g}^{-1}$  (for solid cal-CoCo nanocubes) and  $13.5 \text{ emu g}^{-1}$  (for solid cal-FeFe nanocubes), respectively.

It is well known that the metal compositions strongly affect  $M_s$  values [53-54].  $\text{Fe}^{3+}/\text{Fe}^{2+}$  ions have larger numbers of unpaired electrons than  $\text{Co}^{3+}/\text{Fe}^{2+}$  ions, and Fe-Fe interaction is usually stronger than the Co-Co interaction (*e.g.*,  $TC = 858 \text{ K}$  for  $\text{Fe}_3\text{O}_4$  and  $TN = 33 \text{ K}$  for  $\text{Co}_3\text{O}_4$ ). Therefore, solid cal-FeFe nanocubes showed a higher  $M_s$  value compared to solid cal-CoCo nanocubes. As another factor, the  $M_s$  values are gradually increased with an increase in the crystalline size. As seen in **Scheme 2.1b-2** and **Figure 2.3**, solid cal-FeCo nanocubes showed a single-crystal-like structure in which the metal atoms were perfectly oriented in the same direction, thereby showing high  $M_s$  value and a stable hysteresis loop. The  $M_s$  value for cal-FeCo nanocubes was significantly higher than those of the other two samples, although solid cal-FeCo nanocubes ( $\text{Co}^{\text{II}}_{1.0}\text{Co}^{\text{III}}_{0.2}\text{Fe}^{\text{III}}_{1.8}\text{O}_4$ ) contained a large amount of Co with lower magnetic moment. Based on these results, the significant difference of  $M_s$  definitely comes from the different crystallinity.

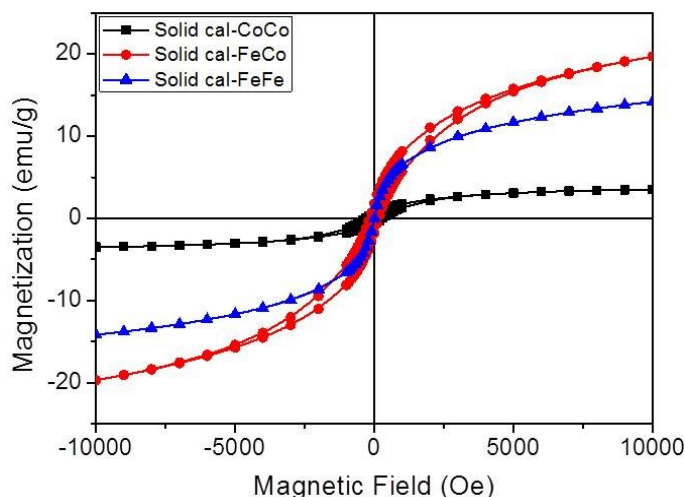


**Figure 2.8.** Magnetic hysteresis loops of solid cal-CoCo nanocubes, solid cal-FeCo nanocubes, and solid cal-FeFe nanocubes.

### 2.3.2. Synthesis of Core-Shell Heterostructures of Metal-Cyanide

#### Hybrid CPs, Creation of Hollow Interiors, and Their Thermal Conversion to Nanoporous Metal Oxides

**Figure 2.9.1a** shows SEM images of solid NiCr nanocubes, which are used as cores for the preparation of core-shell heterostructures. An average particle size of around 80 nm was observed. These solid NiCr nanocubes were used as seeds. The shells of CoCo, FeCo, CoFe, and FeFe layers were successfully formed on the NiCr cores, and their average particle sizes were increased to around 200 nm, as shown in **Figure 2.9.1** and **2**. The above-obtained core-shell nanocubes are abbreviated as NiCr@CoCo, NiCr@FeCo, NiCr@CoFe, and NiCr@FeFe, respectively. The elemental mapping for NiCr@CoFe and NiCr@FeFe nanocubes is shown in **Figure 2.10a-b**. Except for NiCr@FeFe nanocubes, the other core-shell particles were cubic structures with sharp edges (**Figure 2.9.1** and **2**). NiCr@FeFe nanocubes possessed very rough surfaces at the edges and corners of the cubes, suggesting that the shell is composed of

aggregated FeFe nanoparticles [55]. Selected-area ED patterns taken from a whole core-shell particle showed a single-crystalline state, indicating that the shell parts epitaxially grew on the core part due to their same *fcc* crystal structures (**Figure 2.10c-d**). To study the crystalline structures of core-shell nanocubes, wide-angle XRD patterns were measured. As examples, wide-angle XRD patterns for NiCr nanocubes, NiCr@CoCo nanocubes, and NiCr@FeFe are shown in **Figure 2.11**. All of them showed typical diffraction patterns of face-center-cubic (*fcc*) crystals. No peaks derived from the impurities were detected, which indicates the high purity of our products. Considering the slight difference in the crystal constants between NiCr and CoCo nanocubes, their peak positions are a little different. However, only the outer shells were detected. Due to a large shell thickness, the NiCr core became undetectable by normal X-ray analysis.

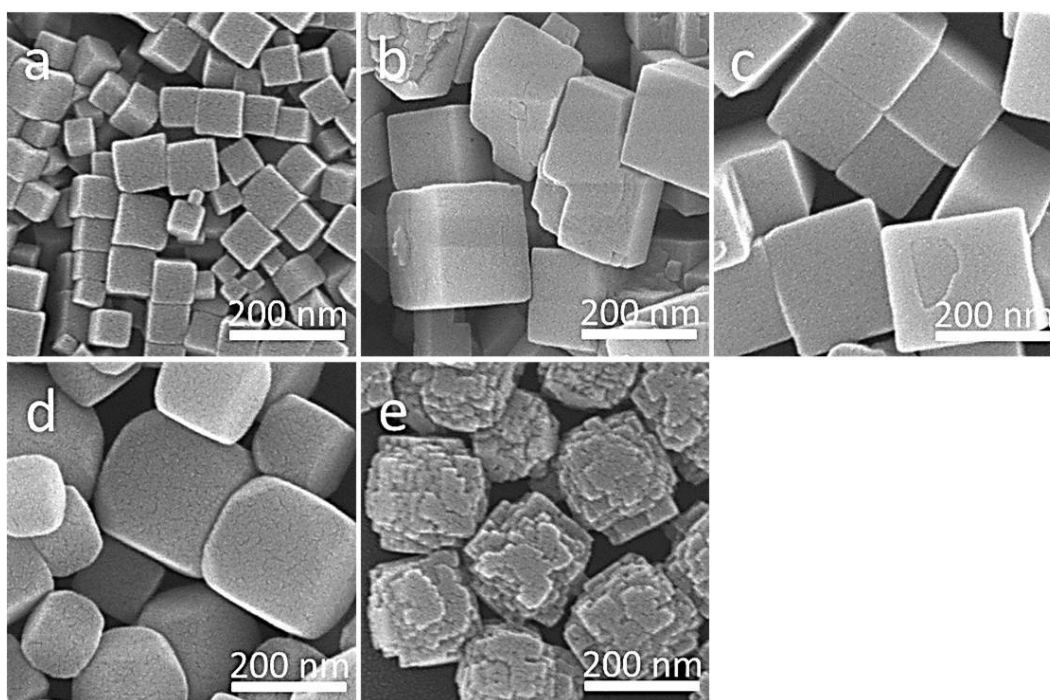


**Figure 2.9.1.** SEM images of (a) NiCr seeds, (b) NiCr@CoCo nanocubes, (c) NiCr@FeCo nanocubes, (d) NiCr@CoFe nanocubes, and (e) NiCr@FeFe nanocubes.

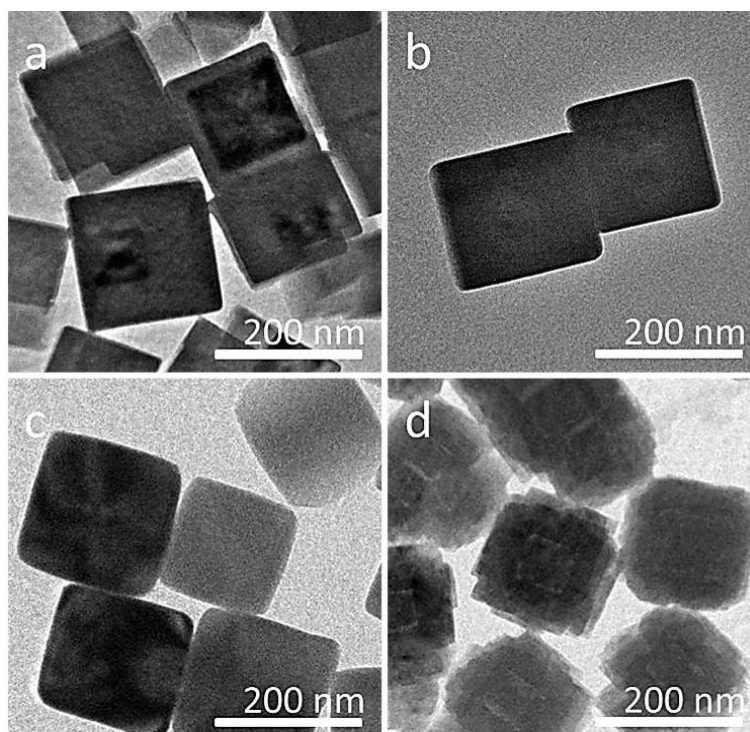


**Figure 2.9.2.** TEM images of (a) NiCr@CoCo nanocubes, (b) NiCr@FeCo nanocubes, (c) NiCr@CoFe nanocubes, and (d) NiCr@FeFe nanocubes.

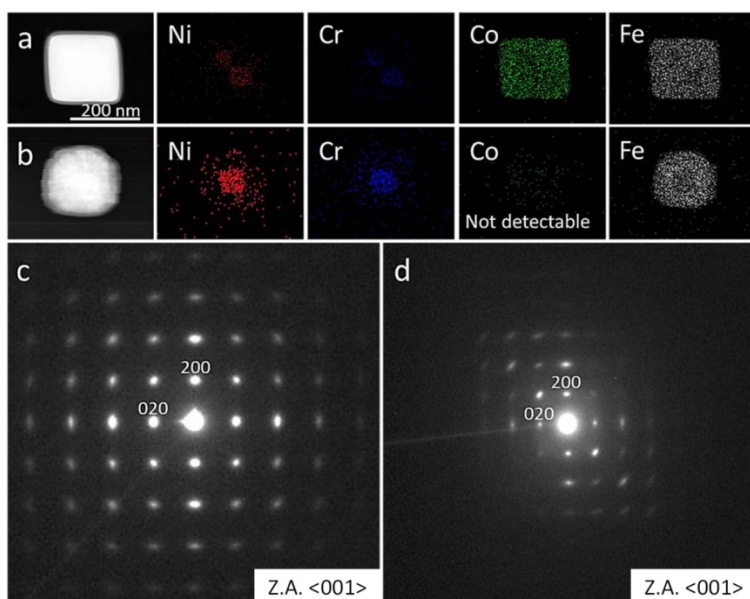


**Figure 2.10.** (a-b) Elemental mapping of NiCr@CoFe nanocubes and NiCr@FeFe nanocubes. (c-d) the selected-area ED patterns of individual (c) NiCr@CoFe nanocubes and (d) NiCr@FeFe nanocubes.



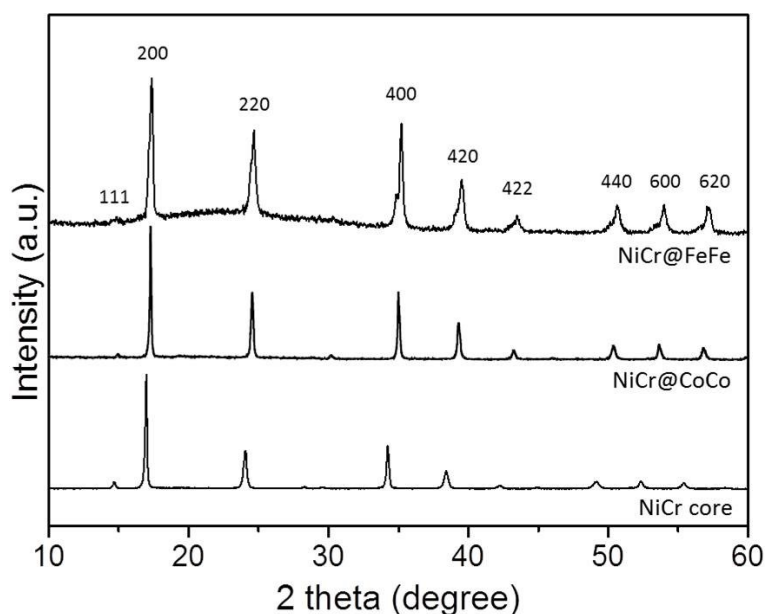


**Figure 2.11.** Wide-angle XRD patterns of NiCr seeds, NiCr@CoCo nanocubes, and NiCr@FeFe nanocubes.

After the selective chemical etching of the core-shell heterostructured nanocubes using a hydrochloric acid solution, hollow interiors in the nanocubes were formed (**Figure 2.12**). These obtained hollow nanocubes are abbreviated as hollow CoCo, hollow FeCo, hollow CoFe, and hollow FeFe, respectively. On almost the particles, the hollow interiors were existed inside the nanocubes, which could not be seen by SEM observation. But, here I looked for the crack parts and confirmed the presence of hollow interiors through the cracks. From elemental mapping data, it was proved that neither Ni nor Cr elements were observed, indicating the complete removal of the cores after chemical etching (**Figure 2.13**). In this method, hydrochloric acid penetrates the voids/holes in the shell region, and the cores are dissolved, thereby creating a cavity inside the nanocubes. Even after the etching, the average diameters of the original nanocubes were not significantly changed (**Figures 2.9** and **2.12**). Thus, the cores can be used as a removable/sacrificial template. It should be noted that the hollow sizes of hollow CoFe and FeFe are larger than those of hollow CoCo and FeCo, even though the same NiCr seeds were used in

this experiment. The dissolution rates of CoFe and FeFe are high, so the shell region is also slightly dissolved by hydrochloric acid. (A detailed comparison is given in a later section.) To study the crystal structures and phase purity, the obtained hollow nanocubes after chemical etching were measured by wide-angle XRD (**Figure 2.14**). All of them showed the same diffraction patterns assignable to typical *fcc* crystals, although the peak positions were slightly varied due to the small difference in the crystal constants. It is indicated that the original crystalline structure in the shell was retained well.

To discuss the significant difference in the dissolution rates, I performed a dissolution study by using solid NiCr, CoCo, FeCo, CoFe, and FeFe nanocubes. I prepared the solid NiCr, CoCo, FeCo, CoFe, and FeFe nanoparticles separately. Each sample (40 mg) was dispersed in a 2 M HCl solution (40 mL). After stirring for 3 h at room temperature, the vessels were transferred into stainless autoclaves and heated at 130 °C for different intervals. The photographs of time-dependent colloidal suspensions during the etching process are shown in **Figure 2.15**. The solutions before etching showed typical colors for each solid nanocube. After 3 h, only solid NiCr nanocubes were completely dissolved. Other nanocubes were still undissolved and precipitated. This fact is reasonable for the selection of NiCr as a sacrificial template for the creation of a hollow interior. After 9 h, solid CoFe and FeFe nanocubes were completely dissolved without any precipitation, which refers to the different dissolution rates of nanocubes. Therefore, the obtained hollow nanocubes possessed different shell thicknesses, as shown in **Figure 2.12.1** and **2**. For further confirmation of the fast dissolution of NiCr, the following experimental was carried out. I first prepared solid FeFe seeds and further coated the NiCr shell on the FeFe seeds. After etching treatment under the same conditions, it was found that the core FeFe particles were not dissolved at all, while the NiCr shell particles were partially dissolved to form the porous shell (**Figure 2.16**).

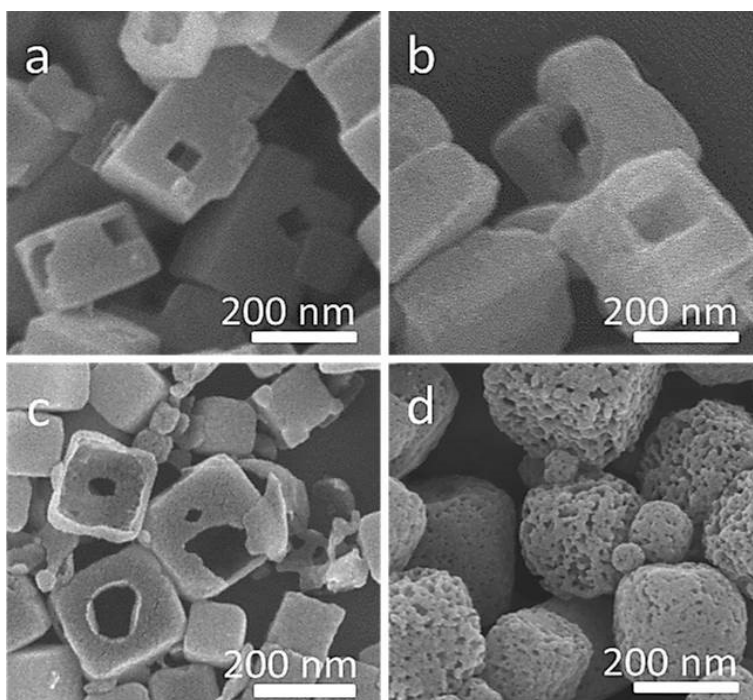


**Figure 2.12.1.** SEM images of (a) hollow CoCo nanocubes, (b) hollow FeCo nanocubes, (c) hollow CoFe nanocubes, and (d) hollow FeFe nanocubes.

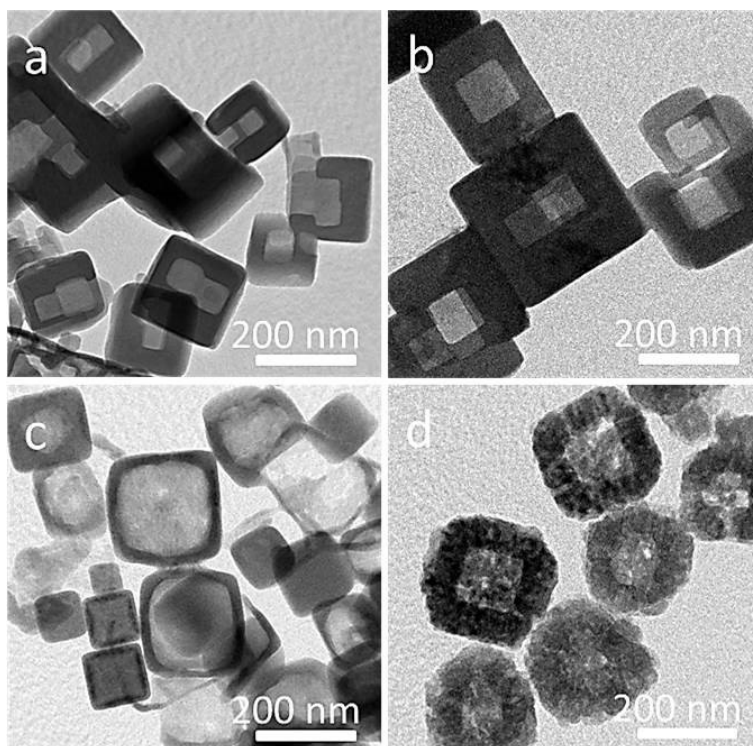


**Figure 2.12.2.** TEM images of (a) hollow CoCo nanocubes, (b) hollow FeCo nanocubes, (c) hollow CoFe nanocubes, and (d) hollow FeFe nanocubes.

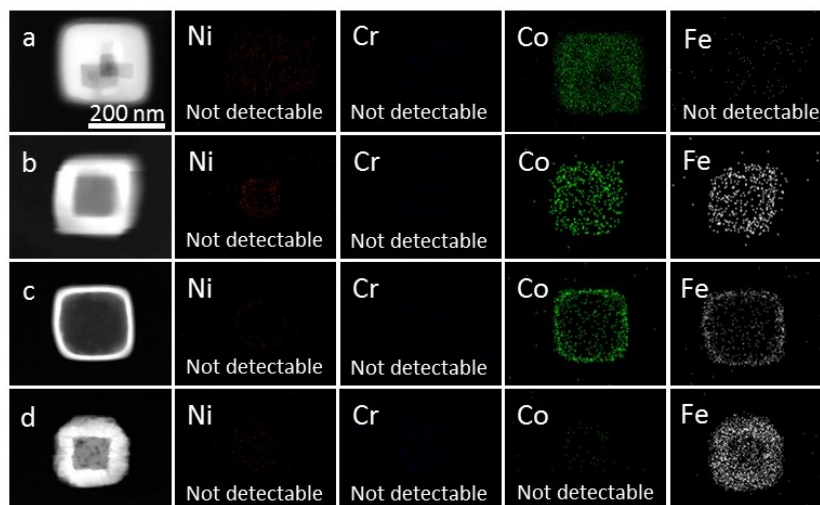


**Figure 2.13.** Elemental mapping data of (a) hollow CoCo nanocubes, (b) hollow FeCo nanocubes, (c) hollow CoFe nanocubes, and (d) hollow FeFe nanocubes.

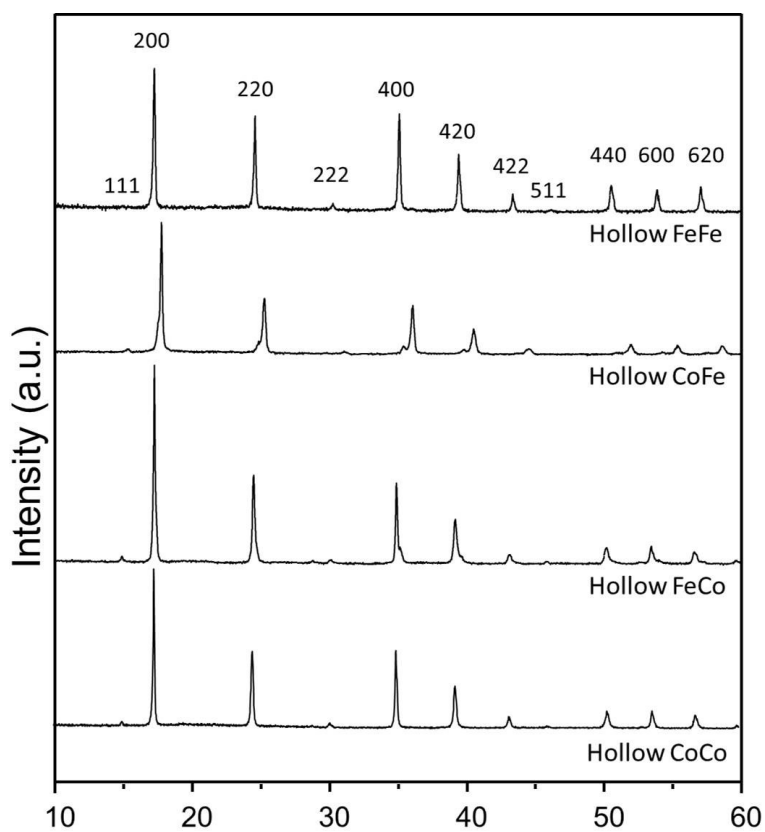


**Figure 2.14.** Wide-angle XRD patterns of hollow CoCo nanocubes, hollow FeCo nanocubes, hollow CoFe nanocubes, and hollow FeFe nanocubes.



**Figure 2.15.** Dissolution test of solid NiCr nanocubes, solid CoCo nanocubes, solid FeCo nanocubes, solid CoFe nanocubes, and solid FeFe nanocubes.

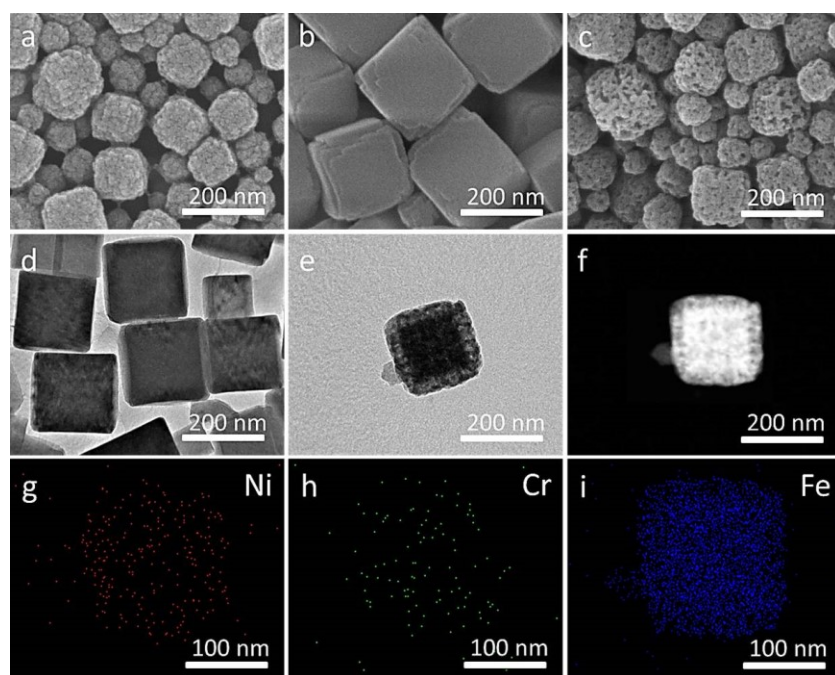


**Figure 2.16.** (a-c) SEM images of (a) solid FeFe nanocubes, (b) FeFe@NiCr nanocubes, and (c) FeFe@NiCr nanocubes after chemical etching. (d-f) TEM and HADDF-STEM images of (d) FeFe@NiCr nanocubes and (e-f) FeFe@NiCr nanocubes after chemical etching. (g-i) Elemental mapping of FeFe@NiCr nanocubes after chemical etching.

Several efforts have been made to prepare hollow CP nanocubes [55-60], my systematic experimentals are very convincing, I believe, and it is widely useful to other compositions. It is known that CoCo nanocubes are electrochemically active. To show the advantage of hollow interiors, electrochemical performance of solid and hollow CoCo nanocubes was carried out using a cyclic voltammetric study. Cyclic voltammograms (CVs) at different scan rates at a potential window of -0.10 to 0.45 V (*v.s.* Ag/AgCl) are shown in **Figure 2.17a-c**.

In the case of hollow CoCo nanocubes, the shape of the CV was rectangular. The CV shape showed more symmetry than that of solid CoCo nanocubes. This data shows an obvious advantage of the hollow structure, which provides higher surface area as well as more oxidation and reduction reaction site. In the case of hollow CoCo nanocubes, the hollow interiors of the cubes can provide easy access for electrolyte ions, thereby showing a symmetric rectangular shape. The capacitance values of these materials were found to be 97 and 84 F g<sup>-1</sup> for hollow and solid CoCo CPs, respectively, at a scan rate of 20 mV s<sup>-1</sup>. With the increase in scan rates, the capacitance value was found to gradually decrease (**Figure 2.17d**). At a higher scan rate, electrolyte ions have less time to complete redox reactions, which results in the capacitance decrease. Interestingly, hollow CoCo nanocubes showed a good rate capability in comparison to solid CoCo nanocubes. This is an obvious advantage of the porous interior space in hollow CoCo nanocubes, which realizes effective access of electrolyte ions even at high scan rates.

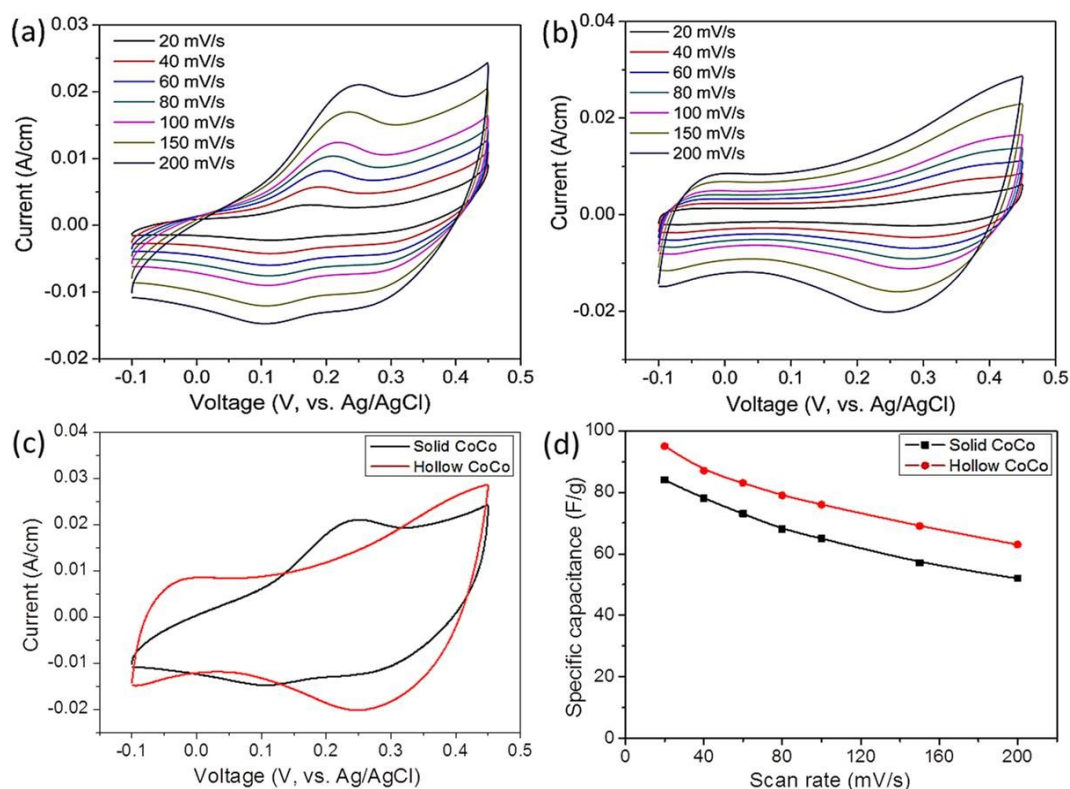


**Figure 2.17.** (a-c) Cyclic voltammograms (CVs) at different scan rates of solid CoCo nanocubes and hollow CoCo nanocubes. (d) Specific capacitance at different scan rates of solid CoCo nanocubes and hollow CoCo nanocubes.

As mentioned in the above section, metal-cyanide hybrid CPs are considered excellent precursors for nanoporous metal oxides. Based on this concept, I demonstrated a thermal conversion of hollow CP nanocubes to the corresponding nanoporous metal oxides with hollow interiors. The hollow CoCo, FeCo, CoFe, and FeFe nanocubes were annealed at 350 °C to obtain the corresponding nanoporous metal oxides, abbreviated as hollow cal-CoCo, hollow cal-FeCo, hollow cal-CoFe, and hollow cal-FeFe, respectively. The surface morphologies and the internal structures of the obtained nanoporous metal oxides were studied by using SEM and TEM (**Figure 2.18.1** and **2**). The shapes of the obtained metal oxides were not changed, although the collapsing of a few particles was observed. The obtained nanoporous metal oxides were further characterized using HAADF-STEM and elemental mapping (**Figure 2.19**). The different contrast

between the inner parts and the outer shells indicates the formation of the hollow structures.

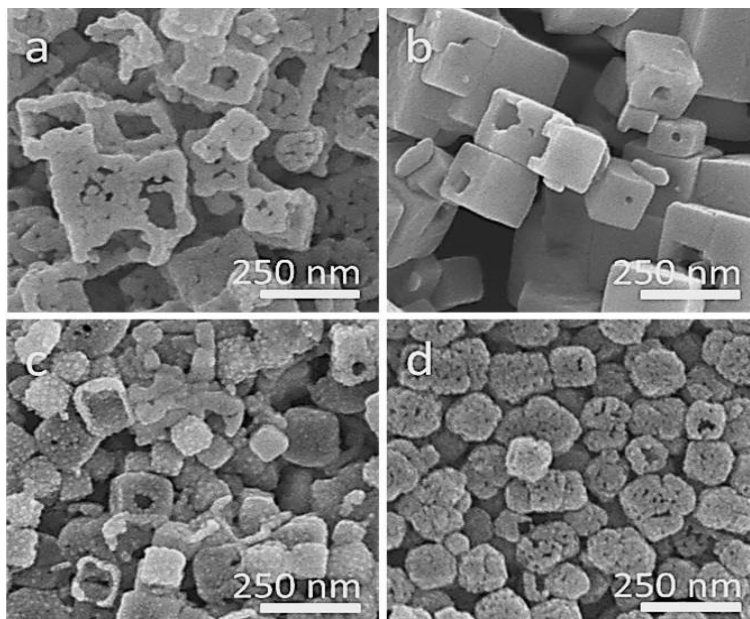


**Figure 2.18.1.** SEM images of (a) hollow cal-CoCo nanocubes, (b) hollow cal-FeCo nanocubes, (c) hollow cal-CoFe nanocubes, and (d) hollow cal-FeFe nanocubes.

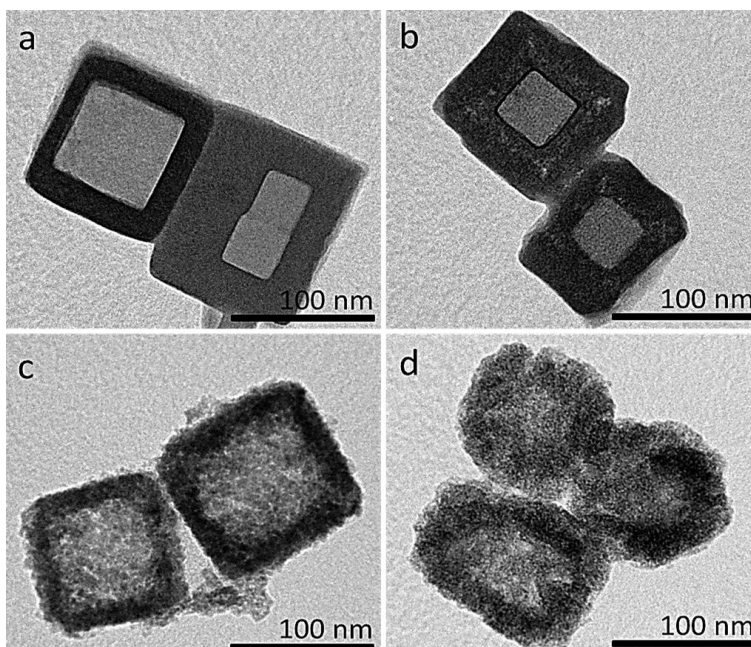


**Figure 2.18.2.** TEM images of (a) hollow cal-CoCo nanocubes, (b) hollow cal-FeCo nanocubes, (c) hollow cal-CoFe nanocubes, and (d) hollow cal-FeFe nanocubes.



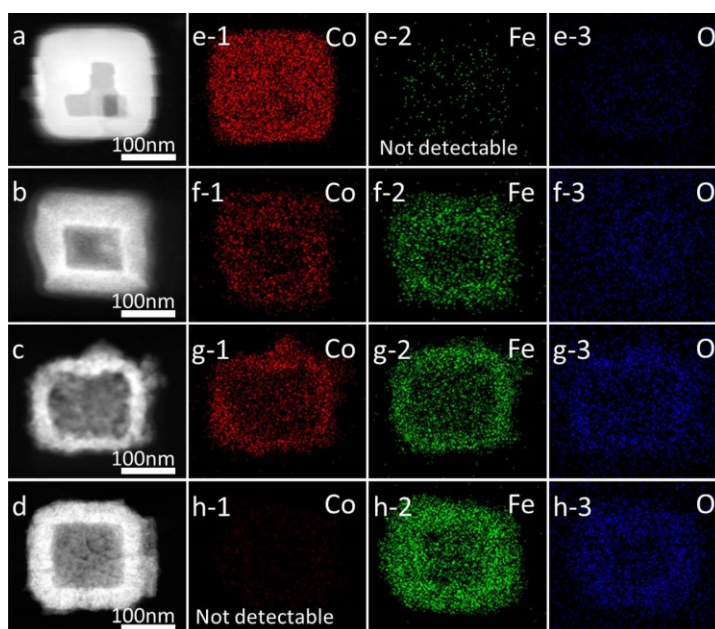


**Figure 2.19.** Elemental mapping data of (a) hollow cal-CoCo nanocubes, (b) hollow cal-FeCo nanocubes, (c) hollow cal-CoFe nanocubes, and (d) hollow cal-FeFe nanocubes.

The overall structures and crystal phases of the obtained oxides were determined by wide-angle XRD (**Figure 2.20a**). Hollow FeCo and CoFe nanocubes were successfully converted to hollow nanoporous FeCo oxides with a single-crystal-like spinel structure. Selected-area ED patterns taken from one hollow particle showed very intense spots which was exactly the same ones as solid cal-FeCo nanocubes as shown in **Scheme 2.1**, suggesting that the same thermal conversion process happened in the hollow systems. In contrast, the pore walls of hollow cal-CoCo and hollow cal-FeFe nanocubes were poorly crystallized and/or amorphous (not shown). The same situation was observed in the solid systems, as shown **Scheme 2.2**.

The atomic ratios of  $\text{Fe}^{2+}/\text{Co}^{3+}$  and  $\text{Co}^{2+}/\text{Fe}^{3+}$  in FeCo and CoFe nanocubes are examined before and after thermal treatment. The ideal insoluble form of solid and hollow FeFe (Prussian blue, PB) is  $\text{Fe}_4^{\text{III}}[\text{Fe}^{\text{II}}(\text{CN})_6]_3$  which can be synthesized by mixing aqueous solutions of  $\text{Fe}^{3+}$  and  $[\text{Fe}^{\text{II}}(\text{CN})_6]^{4-}$  ions. In this form, there are interstitial water molecules between metal-cyanide frameworks. A similar compound, soluble PB ( $\text{KFe}_4^{\text{II}}[\text{Fe}^{\text{III}}(\text{CN})_6]_3$ ), contains interstitial potassium

ions. This soluble PB can be synthesized by the chemical reaction between  $\text{Fe}^{2+}$  and  $[\text{Fe}^{\text{III}}(\text{CN})_6]^{3-}$  ions and the ideal molar ratio of  $\text{Fe}^{2+}/\text{Fe}^{3+}$  is 4/3 [61-64]. Furthermore,  $\text{Mg}_3^{\text{II}}[\text{Co}^{\text{III}}(\text{CN})_6]_2$  and  $\text{Co}_3^{\text{II}}[\text{Fe}^{\text{III}}(\text{CN})_6]_2$  as PB analogues were synthesized recently in which the molar ratios of  $\text{Mg}^{2+}/\text{Co}^{3+}$  and  $\text{Co}^{2+}/\text{Fe}^{3+}$  are 3/2, respectively [65-66]. Therefore, the ideal molar ratios of  $\text{M}^{2+}/\text{M}^{3+}$  in the ideal structures of PB and its analogues is evidenced to be 4/3 or 3/2. In this study, I have synthesized FeCo ( $\text{Fe}_3^{\text{II}}[\text{Co}^{\text{III}}(\text{CN})_6]_2$ ) and CoFe ( $\text{KCo}_4^{\text{II}}[\text{Fe}^{\text{III}}(\text{CN})_6]_3$ ), using  $\text{Fe}^{2+}$  and  $[\text{Co}^{3+}(\text{CN})_6]^{3-}$ , and  $\text{Co}^{2+}$  and  $[\text{Fe}^{\text{III}}(\text{CN})_6]^{3-}$ , respectively (**Figure 2.21**).

The atomic ratios of  $\text{Fe}^{2+}/\text{Co}^{3+}$  and  $\text{Co}^{2+}/\text{Fe}^{3+}$  estimated by ICP analysis were 3/2 and 4/3, respectively, and they were in a good agreement with the above ideal ratios. After thermal treatment of FeCo and CoFe nanocubes, they were converted into the corresponding nanoporous hybrid metals oxides (FeCo oxide and CoFe oxide) and the atomic ratios of Fe/Co and Co/Fe estimated by ICP analysis were 3/2 and 4/3, respectively, close to the starting FeCo and CoFe nanocubes. This means that the organic groups ( $-\text{C}\equiv\text{N}-$ ) and water were removed without any effect on the original metals ratios. Although both hollow FeCo and CoFe nanocubes have different compositional ratios of Fe/Co, their corresponding metal hybrid FeCo oxides exhibited single-crystal-like spinel structures (**Figure 2.20**). This is because the presence of Fe atoms significantly would increase the surface energy, which can facilitate the formation of large crystals.

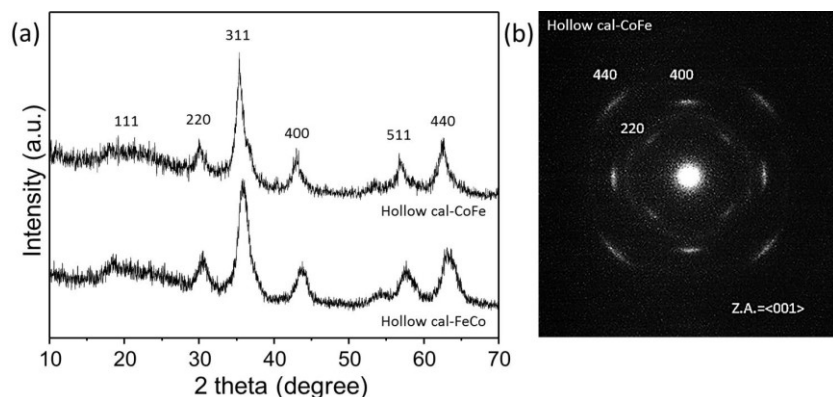


**Figure 2.20.** (a) Wide-angle XRD patterns of hollow cal-FeCo nanocubes and hollow cal-CoFe

nanocubes and (b) the selected-area ED patterns of individual nanocube (hollow cal-CoFe nanocubes).

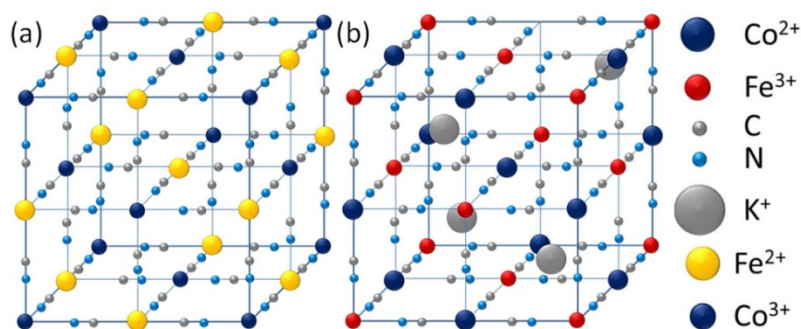


**Figure 2.21.** Ideal crystal structures of FeCo ( $\text{Fe}_3^{\text{II}}[\text{Co}^{\text{III}}(\text{CN})_6]_2$ ) and CoFe ( $\text{KCo}_4^{\text{II}}[\text{Fe}^{\text{III}}(\text{CN})_6]_3$ ).

## 2.4. Conclusion

I demonstrated that metal-cyanide hybrid CPs with cubic morphology and uniform particles sizes were converted into the corresponding nanoporous hybrid metals oxides after thermal treatment in air. During calcination,  $-\text{C}\equiv\text{N}-$  groups and interstitial water molecules were removed, leaving pores/voids between the original frameworks. Interestingly, the thermal conversion of solid FeCo nanocubes resulted in the formation of single-crystal-like nanoporous spinel oxides with enhanced magnetic property. This thermal conversion process was also applicable to hollow CP nanocubes. To prepare the hollow CP nanocubes, CoCo, FeCo, CoFe, and FeFe shells epitaxially grew on the surface of NiCr core, because they have the same crystal structure. After selective chemical etching, the NiCr cores were removed and hollow interiors inside the nanocubes were formed. By direct calcination of these hollow CP nanocubes, single-crystal-like nanoporous spinel oxides with hollow interiors were also successfully prepared, for the first time. I strongly believe that our method should be useful in the future for the preparation of more complicated architectures with controlled hollow interiors and tunable particles sizes.

## 2.5. References

- [1] K. Ariga, A. Vinu, Y. Yamauchi, Q. Ji, J.P. Hill, *Bull. Chem. Soc. Jpn.* **2012**, *85*, 1-32.
- [2] Y. Yamauchi, *J. Ceram. Soc. Jpn.* **2013**, *121*, 831-840.
- [3] W. Chaikittisilp, K. Muraoka, Q. Ji, K. Ariga, Y. Yamauchi, *J. Mater. Chem. A* **2014**, *2*, 12096-12103.
- [4] B. Lee, D. Lu, J.N. Kondo, K. Domen, *Chem. Commun.* **2001**, 2118-2119.
- [5] V.N. Urade, H.W. Hillhouse, *J. Phys. Chem. B* **2005**, *109*, 10538-10541.
- [6] M.B. Zakaria, N. Suzuki, N.L. Torad, M. Matsuura, K. Maekawa, H. Tanabe, Y. Yamauchi, *Eur. J. Inorg. Chem.* **2013**, 2330-2335.
- [7] S. Inagaki, S. Guan, T. Ohsuna, O. Terasaki, *Nature* **2002**, *416*, 304-307.
- [8] M.P. Kapoor, Q. Yang, S. Inagaki, *J. Am. Chem. Soc.* **2002**, *124*, 15176-15177.
- [9] S.S. Park, M.S. Moorthy, C.S. Ha, *NPG Asia Mater.* **2014**, *6*, e96.
- [10] F. Hoffmann, M. Cornelius, J. Morell, M. Fröba, *Angew. Chem. Int. Ed.* **2006**, *45*, 3216-3251; *Angew. Chem.* **2006**, *118*, 3290-3328.
- [11] S. Fujita, S. Inagaki, *Chem. Mater.* **2008**, *20*, 891-908.
- [12] S. Inagaki, O. Ohtani, Y. Goto, K. Okamoto, M. Ikai, K. Yamanaka, T. Tani, T. Okada, *Angew. Chem. Int. Ed.* **2009**, *48*, 4042-4046; *Angew. Chem.* **2009**, *121*, 4102-4106.
- [13] K. Na, C. Jo, J. Kim, K. Cho, J. Jung, Y. Seo, R.J. Messinger, B.F. Chmelka, R. Ryoo, *Science* **2011**, *333*, 328-332.
- [14] C. Dickinson, W. Zhou, R.P. Hodgkins, Y. Shi, D. Zhao, H. He, *Chem. Mater.* **2006**, *18*, 3088-3095.
- [15] H. Wang, M. Imura, Y. Nemoto, S.-E. Park, Y. Yamauchi, *Chem. Asian J.* **2012**, *7*, 802-808.
- [16] H. Yang, Q. Shi, B. Tian, Q. Lu, F. Gao, S. Xie, J. Fan, C. Yu, B. Tu, D. Zhao, *J. Am. Chem. Soc.* **2003**, *125*, 4724-4725.

- [17] A. Stein, *Microporous Mesoporous Mater.* **2001**, 44-45, 227-239.
- [18] A.H. Lu, F. Schüth, *Adv. Mater.* **2006**, 18, 1793-1805.
- [19] W.C. Li, A. H. Lu, C. Weidenthaler, F. Schüth, *Chem. Mater.* **2004**, 16, 5676-5681.
- [20] A. Ruplecker, F. Kleitz, E.L. Salabas, F. Schüth, *Chem. Mater.* **2007**, 19, 485-496.
- [21] L. Zhou, P. O'Brien, *Small* **2008**, 4, 1566-1574.
- [22] H. Cölfen, M. Antonietti, *Angew. Chem. Int. Ed.* **2005**, 44, 5576-5591; *Angew. Chem.* **2005**, 117, 5714-5730.
- [23] H. Imai, Y. Oaki, A. Kotachi, *Bull. Chem. Soc. Jpn.* **2006**, 79, 1834-1851.
- [24] B. Liu, H.C. Zeng, *Chem. Mater.* **2008**, 20, 2711-2718.
- [25] L. Zhou, D. Smyth-Boyle, P. O'Brien, *J. Am. Chem. Soc.* **2008**, 130, 1309-1320.
- [26] S. Xiong, J.S. Chen, X.W. Lou, H.C. Zeng, *Adv. Funct. Mater.* **2012**, 22, 861-871.
- [27] O.M. Yaghi, M. O'Keeffe, N.W. Ockwig, H.K. Chae, M. Eddaoudi, J. Kim, *Nature* **2003**, 423, 705-714.
- [28] S. Kitagawa, R. Kitaura, S. Noro, *Angew. Chem. Int. Ed.* **2004**, 43, 2334-2375; *Angew. Chem.* **2004**, 116, 2388-2430.
- [29] X. Zhao, B. Xiao, A.J. Fletcher, K.M. Thomas, D. Bradshaw, M.J. Rosseinsky, *Science* **2004**, 306, 1012-1015.
- [30] O.K. Farha, A.Ö. Yazaydin, I. Eryazici, C.D. Malliakas, B.G. Hauser, M.G. Kanatzidis, S.T. Nguyen, R.Q. Snurr, J.T. Hupp, *Nat. Chem.* **2010**, 2, 944-948.
- [31] M.C. Das, S. Xiang, Z. Zhang, B. Chen, *Angew. Chem. Int. Ed.* **2011**, 50, 10510-10520; *Angew. Chem.* **2011**, 123, 10696-10707.
- [32] S.T. Meek, J.A. Greathouse, M.D. Allendorf, *Adv. Mater.* **2011**, 23, 249-267.
- [33] B. Liu, H. Shioyama, T. Akita, Q. Xu, *J. Am. Chem. Soc.* **2008**, 130, 5390-5391.
- [34] B. Liu, H. Shioyama, H. Jiang, X. Zhang, Q. Xu, *Carbon* **2010**, 48, 456-463.

- [35] H.-L. Jiang, B. Liu, Y.-Q. Lan, K. Kuratani, T. Akita, H. Shioyama, F. Zong, Q. Xu, *J. Am. Chem. Soc.* **2011**, *133*, 11854-11857.
- [36] W. Chaikittisilp, K. Ariga, Y. Yamauchi, *J. Mater. Chem. A* **2013**, *1*, 14-19.
- [37] L. Radhakrishnan, J. Reboul, S. Furukawa, P. Srinivasu, Kitagawa, S.Y. Yamauchi, *Chem. Mater.* **2011**, *23*, 1225-1231.
- [38] M. Hu, J. Reboul, S. Furukawa, L. Radhakrishnan, Y. Zhang, P. Srinivasu, H. Iwai, H. Wang, Y. Nemoto, N. Suzuki, S. Kitagawa, Y. Yamauchi, *Chem. Commun.* **2011**, *47*, 8124-8126.
- [39] M. Hu, J. Reboul, S. Furukawa, N.L. Torad, Q. Ji, P. Srinivasu, K. Ariga, S. Kitagawa, Y. Yamauchi, *J. Am. Chem. Soc.* **2012**, *134*, 2864-2867.
- [40] W. Chaikittisilp, M. Hu, H. Wang, H.-S. Huang, T. Fujita, K. C.-W. Wu, L.-C. Chen, Y. Yamauchi, K. Ariga, *Chem. Commun.* **2012**, *48*, 7259-7261.
- [41] W. Cho, S. Park, M. Oh, *Chem. Commun.* **2011**, *47*, 4138-4140.
- [42] S. Jung, W. Cho, H.J. Lee, M. Oh, *Angew. Chem. Int. Ed.* **2009**, *48*, 1459-1462; *Angew. Chem.* **2009**, *121*, 1487-1490.
- [43] W. Wang, Y. Li, R. Zhang, D. He, H. Liu, S. Liao, *Catal. Commun.* **2011**, *12*, 875-879.
- [44] M.S.Y. Parast, A. Morsali, *Inorg. Chem. Commun.* **2011**, *14*, 645-648.
- [45] T.K. Kim, K.J. Lee, J.Y. Cheon, J.H. Lee, S.H. Joo, H.R. Moon, *J. Am. Chem. Soc.* **2013**, *135*, 8940-8946.
- [46] Y.-D. Chiang, M. Hu, Y. Kamachi, S. Ishihara, K. Takai, Y. Tsujimoto, K. Ariga, K. C.-W. Wu, Y. Yamauchi, *Eur. J. Inorg. Chem.* **2013**, 3141-3145.
- [47] M. Hu, S. Ishihara, K. Ariga, M. Imura, Y. Yamauchi, *Chem. Eur. J.* **2013**, *19*, 1882-1885.
- [48] M. Hu, A. A. Belik, M. Imura, Y. Yamauchi, *J. Am. Chem. Soc.* **2013**, *135*, 384-391.
- [49] M.B. Zakaria, M. Hu, N. Hayashi, Y. Tsujimoto, S. Ishihara, M. Imura, N. Suzuki, Y.-Y.

- Huang, Y. Sakka, K. Ariga, K. C.-W. Wu, Y. Yamauchi, *Eur. J. Inorg. Chem.* **2014**, 1137-1141.
- [50] M. Hu, S. Ishihara, Y. Yamauchi, *Angew. Chem. Int. Ed.* **2013**, *52*, 1235-1239; *Angew. Chem.* **2013**, *125*, 1273-1277.
- [51] M. Hu, A.A. Belik, M. Imura, K. Mibu, Y. Tsujimoto, Y. Yamauchi, *Chem. Mater.* **2012**, *24*, 2698-2707.
- [52] L. Hu, N. Yan, Q. Chen, P. Zhang, H. Zhong, X. Zheng, Y. Li, X. Hu, *Chem. Eur. J.* **2012**, *18*, 8971-8977.
- [53] T. Osaka, M. Takai, K. Hayashi, K. Ohashi, M. Saito, K. Yamada, *Nature* **1998**, *392*, 796-798.
- [54] *Ferromagnetism* (Ed.: R. M. Bozorth), Wiley-VCH, Weinheim, **1993**, pp. 160-169.
- [55] M. Hu, S. Furukawa, R. Ohtani, H. Sukegawa, Y. Nemoto, J. Reboul, S. Kitagawa, Y. Yamauchi, *Angew. Chem. Int. Ed.* **2012**, *51*, 984-988; *Angew. Chem.* **2012**, *124*, 1008-1012.
- [56] M. Hu, N.L. Torad, Y. Yamauchi, *Eur. J. Inorg. Chem.* **2012**, 4795-4799.
- [57] O.N. Risset, E.S. Knowles, S. Ma, M.W. Meisel, D.R. Talham, *Chem. Mater.* **2013**, *25*, 42-47.
- [58] G. Liang, J. Xu, X. Wang, *J. Am. Chem. Soc.* **2009**, *131*, 5378-5379.
- [59] X. Roy, J. K.-H. Hui, M. Rabnawaz, G. Liu, M.J. MacLachlan, *J. Am. Chem. Soc.* **2011**, *133*, 8420-8423.
- [60] R. McHale, N. Ghasdian, Y. Liu, M.B. Ward, N.S. Hondow, H. Wang, Y. Miao, R. Brydson, X. Wang, *Chem. Commun.* **2010**, *46*, 4574-4576.
- [61] H. Ming, N.L.K. Torad, Y.-D. Chiang, K. C. W. Wu, Y. Yamauchi, *CrystEngComm.* **2012**, *14*, 3387-3396.
- [62] S.-H. Lee, Y.-D. Huh, *Bull. Korean Chem. Soc.* **2012**, *33*, 1078-1080.

- [63] A.A. Karyakin, *Electroanalysis* **2001**, *13*, 813-819.
- [64] H.J. Buser, D. Schwarzenbach, W. Petter, A. Ludi, *Inorg. Chem.* **1977**, *16*, 2704-2710.
- [65] F. Shiba, R. Fujishiro, T. Kojima, Y. Okawa, *J. Phys. Chem. C* **2012**, *116*, 3394-3399.
- [66] J. Jiménez-Gallegos, J. Roque, H. Yee-Madeira, E. Reguera, *Z. Anorg. Allg. Chem.* **2012**, *638*, 1146-1150.



# Chapter 3

## Chapter 3

# 3. Nanoporous Mn-Based Electrocatalysts through Thermal Conversion of Cyano-Bridged Coordination Polymers toward Ultra-High Efficient Hydrogen Peroxide Production

### 3.1. Introduction

Manganese (Mn)-based oxides have attracted a great interest from scientists because they have an excellent catalytic activity toward several reactions such as oxygen reduction reaction (ORR). The ORR in aqueous solutions occurs mainly by two pathways. One is the direct 4-electron reduction pathway (from  $O_2$  to  $H_2O$ ) which is highly preferred in fuel cells, and the other one is the 2-electron reduction pathway (from  $O_2$  to  $H_2O_2$ ) which is used in industry for the production of  $H_2O_2$  [1,2]. The latter pathway is often followed by further reduction (from  $H_2O_2$  to  $H_2O$ ), and thus, in order to form  $H_2O_2$  efficiently, materials with a high selectivity on the 2-electron reduction pathway are necessary. Because of the existence of various oxidation states (*i.e.*, II, III, and IV), different manganese oxides, such as  $MnO$ ,  $MnO_2$ ,  $Mn_2O_3$ , and  $Mn_3O_4$ , can be prepared and used in catalysis or battery technologies [3-5]. Various nanostructured Mn oxides with

different shapes, such as dendritic clusters, nanocrystals, nanowires, multipods, nanotubes, nanoneedles, or nanoflowers, have been reported so far [6-11]. Especially,  $\text{Mn}_3\text{O}_4$  is also well-known to be an active catalyst in various oxidation reactions [12,13] or as a promising electrode material for capacitors because of its specific capacitance [14].

Despite the above-mentioned advantages of Mn oxides, their catalytic efficiency is limited [15,16]. One promising way to overcome such limitations and to further enhance their electrocatalytic activity is to introduce other metals oxides (*e.g.*, Co, Ru, Ni, Fe, and Zn) [17]. The elegant combination of different transition metal oxides can achieve a superior electrocatalytic activity. It has been demonstrated that these mixed transition-metal oxides usually exhibit higher electrical conductivity than their respective single counterparts. Zhang *et al.* have designed  $\text{Mn}_x\text{Co}_{3-x}\text{O}_4$  catalysts for the selective reduction of NO and elimination of  $\text{NO}_x$  pollutants [18]. Moreover, Liang *et al.* have been developed a  $\text{MnCo}_2\text{O}_4$ /graphene hybrid as a highly efficient electrocatalyst for the ORR in alkaline conditions [19]. Recently, the intrinsic electrocatalytic activity of Ru has been extensively investigated, but its low abundance and high cost tend to exclude it from practical uses [20-22]. Thus, combining Ru with other abundant metals is an economically favorable way to enhance the electrocatalytic activity.

In addition to a desirable composition, the nanostructure of a material can also affect the electrocatalytic activity. Nanoporous structures are greatly beneficial to the performance of catalysts since they show high specific surface area, numerous active sites, and shorter diffusion lengths for the reaction pathway [23]. For this reason, Prussian blue analogues (PBAs) were selected as promising precursors for the preparation of nanoporous metal oxides with unique properties [24,25]. PBAs are a class of crystalline coordination polymers consisting of divalent and trivalent metals ions bridged by cyanide groups (*i.e.*,  $\text{M}^{2+}-\text{C}\equiv\text{N}-\text{M}'^{3+}$ ; M or M' = Fe, Co, Ni, Mn, *etc.*). By removing the cyanide ligands through controlled aerobic thermal treatments,

nanoporous metals oxides can be obtained. The large fraction of metal nodes can be utilized as metal sources, while the removable organic components can generate nanopores [26,27].

Herein, I report the controlled and oriented crystal growth of PBAs (*i.e.*,  $\text{Mn}_3[\text{Mn}(\text{CN})_6]_2$  (abbreviated as MnCNMn),  $\text{Mn}_3[\text{Co}(\text{CN})_6]_2$  (abbreviated as MnCNCo), and  $\text{Mn}_2[\text{Ru}(\text{CN})_6]$  (abbreviated as MnCNRu)) with tunable particle size and shape. After aerobic calcination, the PBAs are successfully converted into nanoporous Mn-based oxides with different compositions, as shown in **Figure 3.1**. The electrochemical analysis reveals that the Mn-Ru oxide prepared from  $\text{Mn}_2[\text{Ru}(\text{CN})_6]$  is a promising catalyst for the production of  $\text{H}_2\text{O}_2$  by selectively catalyzing the ORR through a 2-electron pathway. Our electrocatalyst demonstrates a high activity, strict selectivity, and long-term stability for the production of  $\text{H}_2\text{O}_2$ .

## 3.2. Experimental Sections

### 3.2.1. Synthesis of MnCNMn, MnCNCo, and MnCNRu PBAs and Their Thermal Conversion

In a typical synthesis of MnCNRu, trisodium citrate dihydrate (TSCD) (350 mg) was dissolved in 40 mL of manganese (II) acetate aqueous solution (0.058 mM) to form a clear solution, followed by the addition of 40 mL of  $\text{K}_4[\text{Ru}(\text{CN})_6]$  solution (0.025 mM) under magnetic stirring. For the synthesis of MnCNCo, TSCD (200 mg) was dissolved in 40 mL of manganese (II) acetate solution (0.085 mM) to form a clear solution, followed by the addition of 40 mL of  $\text{K}_3[\text{Co}(\text{CN})_6]$  solution (0.04 mM) under magnetic stirring. For synthesis of MnCNMn nanocubes, TSCD (200 mg) was dissolved in 40 mL of manganese (II) acetate solution (0.085 mM) to form a clear solution, followed by the addition of 40 mL of  $\text{K}_3[\text{Mn}(\text{CN})_6]$  solution (0.037 mM) under magnetic stirring. The solutions were aged for 24 h to allow the crystal growth, followed by the

formation of a precipitates. The obtained precipitates were collected by centrifugation. After washing with water and ethanol several times, the precipitates were dried at room-temperature for 48 h. For the conversion to nanoporous metal oxides, the as-prepared powders (100.0 mg) were placed in a melting pot and heated from room temperature to the desired temperature (360 °C) at 5 °C min<sup>-1</sup> using an electronic furnace. After reaching the desired temperature, the samples were annealed for 2 h to a complete thermal decomposition. Finally, the obtained powder was collected for characterization. All calcination processes were performed aerobically.

### 3.2.2. Electrochemical Measurements

The electrochemical activities of the catalysts were evaluated by using cyclic voltammetry and linear sweep voltammetry in a three-electrode electrochemical cell in a rotating ring-disk electrode (RRDE) with Pt ring and glassy carbon disk (GC, 4 mm in diameter) configuration. Counter electrode was a graphite rod (10 mm in diameter) and the reference electrode was an Ag/AgCl (3 M NaCl) electrode. The working electrode was prepared as follows. The RRDE was firstly polished in a circle motion using alumina suspensions with decreasing particle size (typically from 1.0 to 0.05 μm). The as-prepared catalyst (5 mg) was dispersed in a mixture of water/ethanol solution (3:1 volume ratio) (950 μL) and 5 wt% Nafion solution (50 μL) under ultrasonication for 30 min to get a homogenous suspension. Then, 5 μL of the above suspension was dropped onto the GC disk of the RRDE, resulting in catalyst loading of 200 μg cm<sup>-2</sup>. To get a uniform catalyst layer, the RRDE was set horizontally at room temperature. The electrolyte was 0.1 M KOH and was bubbled with high pure oxygen to get O<sub>2</sub>-saturated 0.1 M KOH. The GC disk electrode was subjected to potential cycling at a sweep rate of 10 mV s<sup>-1</sup> with a rotation speed of 1600 rpm. Solution ohmic drop (*i.e.*, *i*R drop) was compensated. The background capacitive current was recorded in the same potential range and scan rate, but in N<sub>2</sub>-saturated

electrolyte. The current recorded in O<sub>2</sub>-saturated solution was corrected for the background current to yield net ORR current of the tested catalyst.

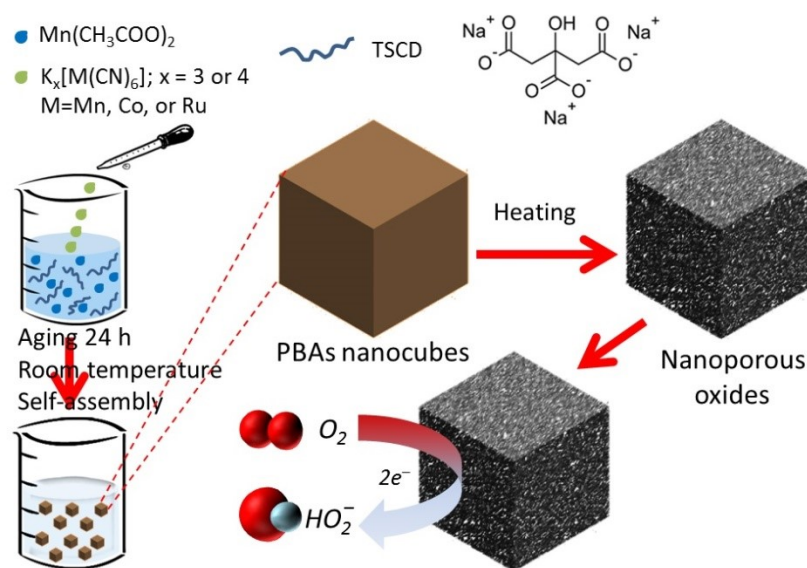


**Figure 3.1.** Schematic illustration of PBAs undergoing thermal decomposition to produce the corresponding metal oxides for electrocatalytic production of H<sub>2</sub>O<sub>2</sub>.

### 3.2.3. Characterizations

SEM images were taken with a Hitachi S-4800 scanning microscope at an accelerating voltage of 10 kV. TEM observations were performed using a JEM-2100F TEM system operated at 200 kV and equipped for energy-dispersive spectrometer analysis. Wide-angle powder X-ray diffraction (XRD) patterns were obtained with a Rigaku RINT 2500X diffractometer using monochromated Cu K $\alpha$  radiation (40 kV, 40 mA) at a scanning rate of 0.5 °C min<sup>-1</sup>. X-ray photoelectronic spectroscopy (XPS) spectra were recorded at room temperature using JPS-9010TR (JEOL) instrument with Mg K $\alpha$  X-ray source. Thermo-gravimetric (TG) analysis was carried out using a Hitachi HT-Seiko instrument Exter 6300 TG-DTA in O<sub>2</sub>-heating from room temperature to 700 °C with a heating rate of 5 °C min<sup>-1</sup>. Nitrogen adsorption-desorption data were obtained by using a Quantachrome Autosorb Automated Gas Sorption System at 77 K. The production of H<sub>2</sub>O<sub>2</sub> is

checked by an off-line fourier transform infrared (FTIR) spectroscopy to the small volume of solution sampled from the electrolyte very close to the electrode.

## 3.3. Results and Discussion

### 3.3.1. Preparation of MnCNRu, MnCNCo, and MnCNMn

#### Precursors

To understand the role of TSCD in the formation of PBAs, two reactions, with and without TSCD, were compared. In the absence of TSCD, more Mn species dissolved in the solution can react immediately with the  $[\text{Mn}(\text{CN})_6]^{3-}$ ,  $[\text{Co}(\text{CN})_6]^{3-}$ , or  $[\text{Ru}(\text{CN})_6]^{4-}$  anions and resulting in the formation of irregularly-shaped MnCNMn, MnCNCo, and MnCNRu particles, respectively (**Figure 3.2**). In contrast, in the presence of TSCD, the resulting materials have a well-defined cubic morphology and homogeneous particle size distribution (**Figure 3.3**). My previous  $^1\text{H}$  nuclear magnetic resonance (NMR) study reveals that TSCD bonds to the metal cations through chelating effect [28]. Therefore, in the present study, Mn-citrate complex is thought to be formed. Free  $\text{Mn}^{2+}$  ions are steadily released from the Mn-citrate complex to react with  $[\text{Mn}(\text{CN})_6]^{3-}$ ,  $[\text{Co}(\text{CN})_6]^{3-}$ , or  $[\text{Ru}(\text{CN})_6]^{4-}$  anions at the initial stage of the reaction. Subsequently, the generated nuclei further grow through the interaction taking place between the free  $\text{Mn}^{2+}$  ions and the anions. Thus, the presence of TSCD plays an important role as it induces the preferential crystal growth of MnCNMn, MnCNCo, and MnCNRu PBAs. A different concentration of TSCD was used for the preparation of MnCNRu. Interestingly, it is found that the final size and shape can be controlled depending on the concentration of TSCD employed (**Figure 3.4**). From scanning electron microscope (SEM) images, well-defined cubes with sharp edges can be observed when the concentration of TSCD is above 350 mg (**Figure 3.4**). With increasing the concentration of

TSCD, the number of nuclei formed at the early stage of the reaction is thought to decrease, based on the above-mentioned idea. These few nuclei undergo crystal growth by interacting with  $[\text{Ru}(\text{CN})_6]^{4-}$ , leading to a final product with a larger particle size (**Figure 3.4f**).

The obtained PBA particles prepared with TSCD under a typical condition were examined by SEM (**Figure 3.3**) and wide-angle X-ray diffraction (XRD) (**Figure 3.5**). The MnCNRu sample shows cubic shapes of approximately 600 nm (**Figure 3.3c**). The XRD patterns can be assigned to face-center cubic ( $Fm-3m$ ) structures, similar to typical Prussian blue crystals (**Figure 3.5c**). MnCNMn and MnCNCo have a similar crystal structure but with an average particle size of  $\sim 1 \mu\text{m}$  and  $\sim 2 \mu\text{m}$ , respectively (**Figures 3.3a and b, 3.5a and b, and Figure 3.6**).

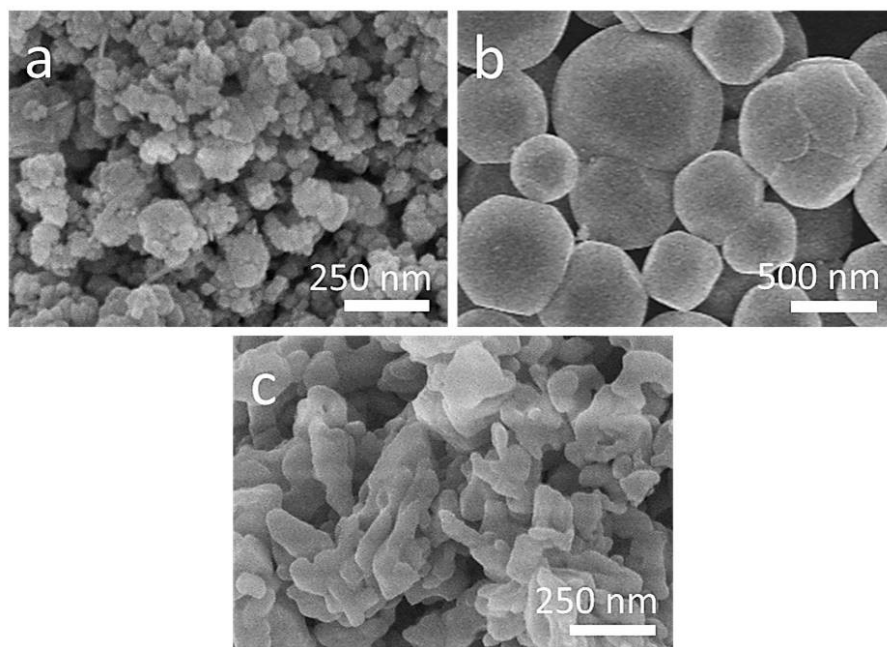


**Figure 3.2.** SEM images of the (a) MnCNMn, (b) MnCNCo, and (c) MnCNRu PBAs, prepared in the absence of TSCD.



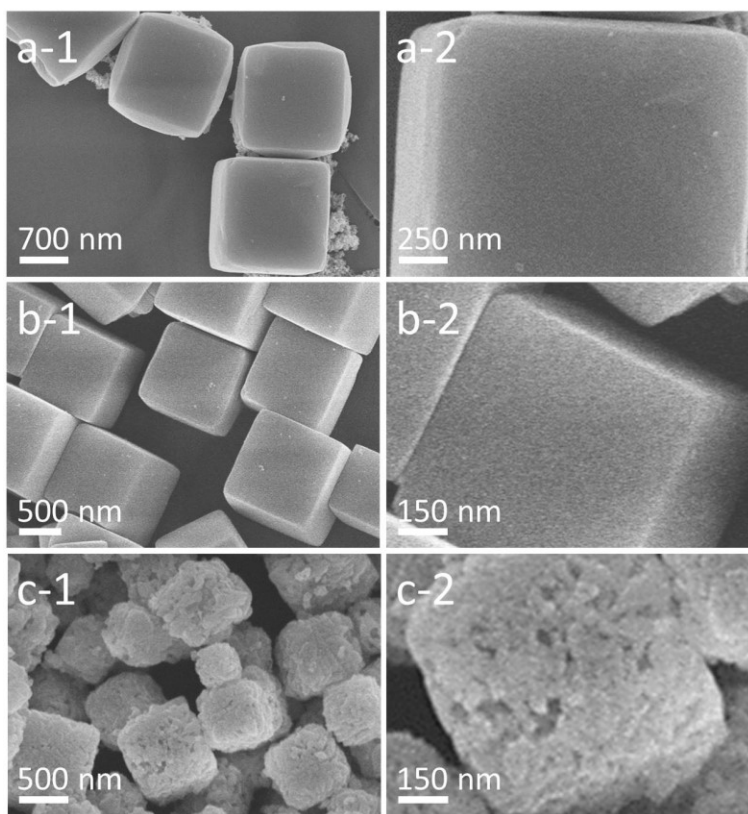


**Figure 3.3.** SEM images of the (a) MnCNMn, (b) MnCNCo, and (c) MnCNRu PBAs.

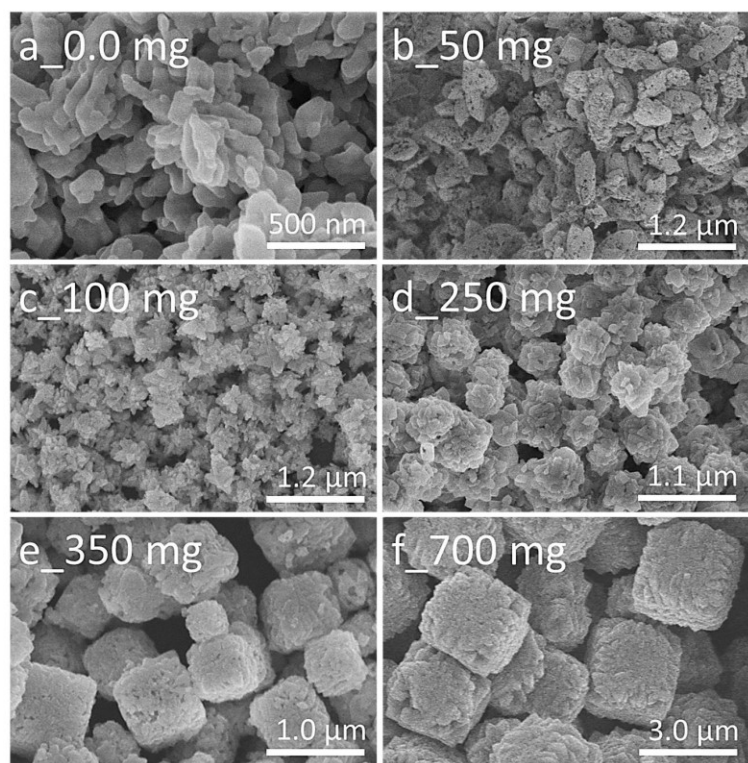


**Figure 3.4.** SEM images of the MnCNRu prepared with various amounts of TSCD.

High angle annular dark field scanning transmission electron microscopy (HAADF-STEM) and elemental mapping are powerful tools to determine structure and atomic distribution. Mn, Co, Ru, C, and N can be clearly identified and observed to be homogeneously distributed over the whole area of the cubes (**Figure 3.7**). HAADF-STEM images show that the MnCNRu and MnCNMn cubes possess a rough surface around the edges and corners, suggesting that the final cubes are composed of aggregated nanocrystals [25]. On the other hand, MnCNCo cubes with sharp corners are formed by more densely packing nanocrystals. The elemental composition was investigated by ICP analysis. Mn/Co (in MnCNCo) and Mn/Ru (in MnCNRu) atomic ratios are found to be 1.50 and 1.00, respectively.

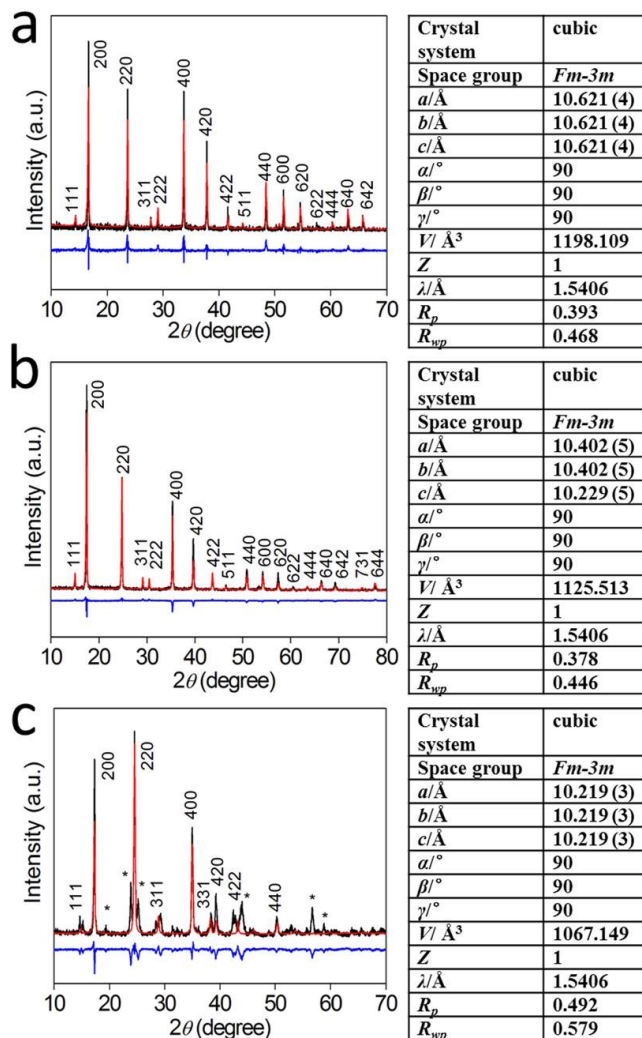


**Figure 3.5.** Experimental XRD patterns (black line), computed XRD patterns (red line), and the

residuals (blue line) of (a) MnCNMn, (b) MnCNCo, and (c) MnCNRu. The peaks indicated by (\*) are generated from impurities.

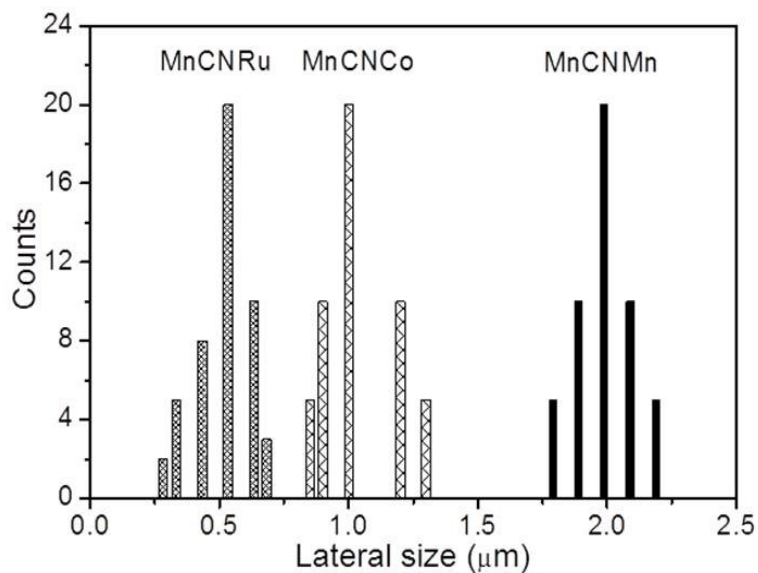


**Figure 3.6.** The particle size distributions obtained from TEM images of (a) MnCNMn, (b) MnCNCo, and (a) MnCNRu PBAs.

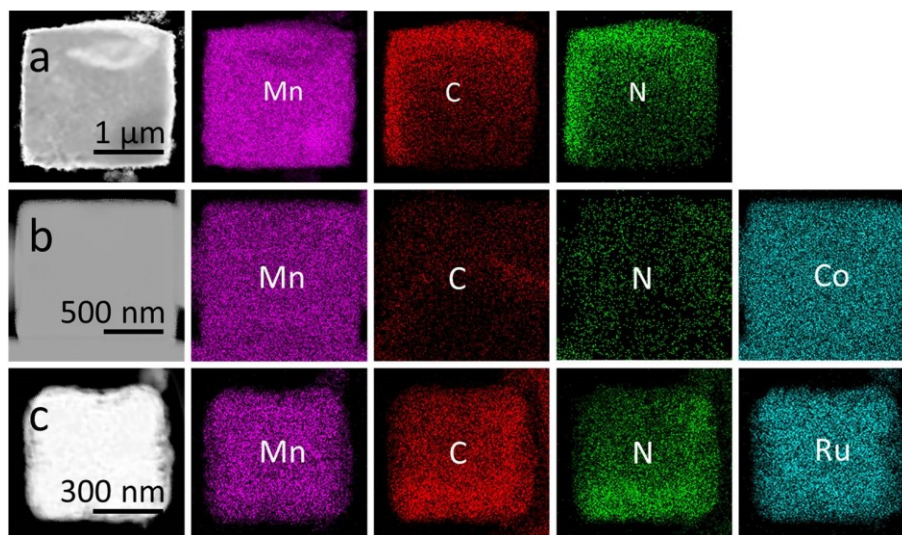


**Figure 3.7.** HAADF-STEM and elemental mapping images of the (a) MnCNMn, (b) MnCNCo, and (c) MnCNRu PBAs.

### 3.3.2. Thermal Conversion of MnCNRu, MnCNCo, and MnCNMn

#### Cubes

The inorganic-organic hybrids nature of PBAs allows them to decompose into nanostructured metal oxides through thermal treatments. PBAs have a large fraction of metal ions beside the organic ligands. Therefore, the metal atoms can be utilized as a metal source, while the removable organic components act as porogens. The thermal decomposition process of MnCNCo cubes is monitored by thermogravimetric (TG) analysis (**Figure 3.8**). A first sharp mass loss of around 25% can be observed up to temperature and 150 °C, attributable to the removal of interstitial water molecules from the inorganic-organic framework. The second mass loss of around 25%, between 300 and 400 °C, is due to the complete removal of the cyanide bridges. This behavior is typical of the combustion reaction of CN-containing materials.

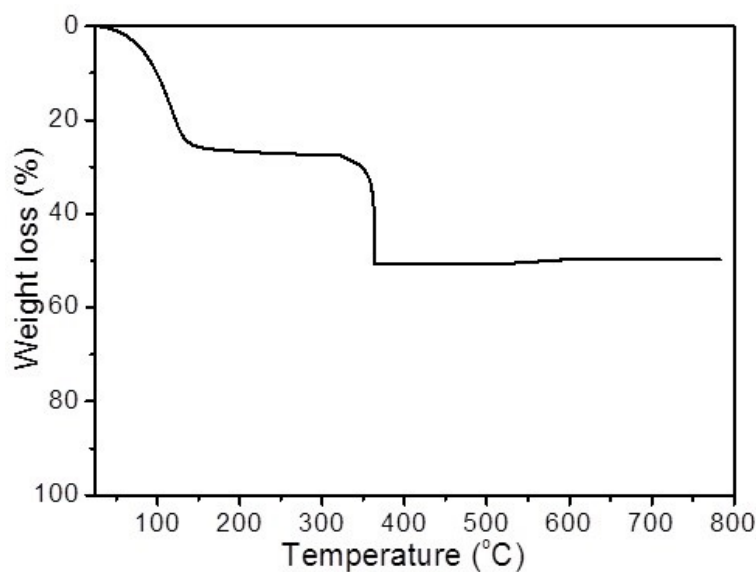


**Figure 3.8.** TGA curve of MnCNCo at a heating rate of 5 °C min<sup>-1</sup> from room temperature to 800 °C.

In the present study, the samples were heated at 360 °C for 2 h to ensure a complete thermal decomposition during which the PBAs were converted into their corresponding metal oxides while retaining their original shapes. During the thermal process, organic residues and water molecules are removed, leaving behind pores/voids inside the metal oxide framework formed by the oxidization/rearrangement of the metal components. The porous structure gives surface areas as high as 24.5 m<sup>2</sup> g<sup>-1</sup> (Mn<sub>3</sub>O<sub>4</sub>), 23.9 m<sup>2</sup> g<sup>-1</sup> (Mn<sub>x</sub>Co<sub>3-x</sub>O<sub>4</sub>) and 24.3 m<sup>2</sup> g<sup>-1</sup> (Mn-Ru oxide), which was confirmed from the N<sub>2</sub> adsorption-desorption isotherms (**Figure 3.9**).

No obvious predominant pore sizes were observed in the BJH pore size distribution curves, which is in agreement with the irregular nanoporous structures observed by SEM (**Figure 3.10**). It can be observed from the wide-angle XRD patterns of the obtained oxides that both the samples prepared from MnCNMn and MnCNCo possess a spinel crystal structure (*i.e.*, Mn<sub>3</sub>O<sub>4</sub>, Mn<sub>x</sub>Co<sub>3-x</sub>O<sub>4</sub>). The peaks assigned to Mn<sub>3</sub>O<sub>4</sub> are slightly sharper and stronger than those from Mn<sub>x</sub>Co<sub>3-x</sub>O<sub>4</sub>. The weaker crystallinity of Mn<sub>x</sub>Co<sub>3-x</sub>O<sub>4</sub> can be due to the incorporation of the Co atoms. On the other hand, in the case of the sample prepared from MnCNRu, additional peaks corresponding to Ru and RuO<sub>2</sub> can also be observed as impurities in addition to the peaks assignable to Mn<sub>3</sub>O<sub>4</sub> with a spinel crystal structure [29], implying that the Ru atoms are hardly incorporated in the spinel crystal. Although it is generally known that Ru is sensitive to air and easily oxidized, pure Ru metal coexists because oxygen molecules have not reached all the parts of the MnCNRu cubes.

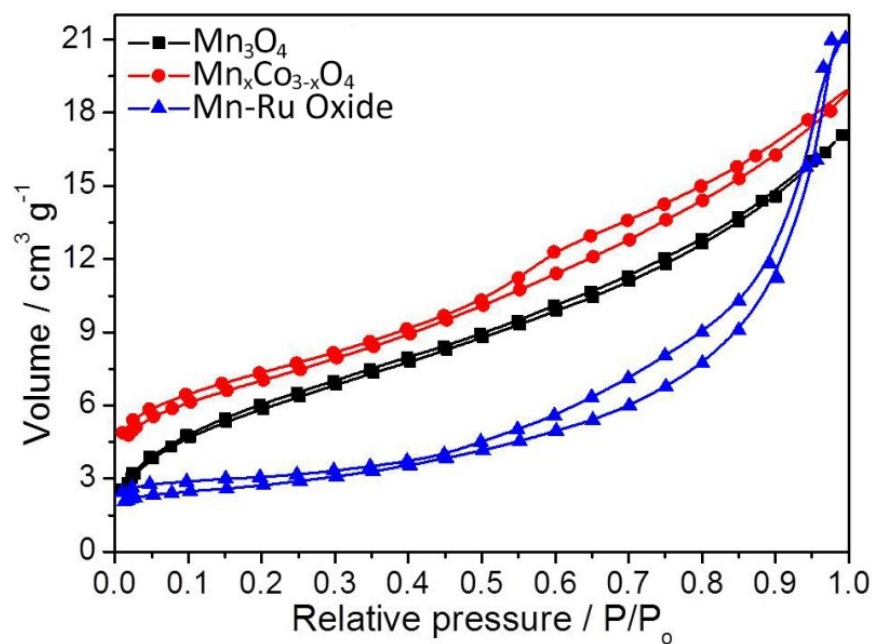


**Figure 3.9.**  $N_2$  gas adsorption-desorption isotherms of  $Mn_3O_4$ ,  $Mn_xCo_{3-x}O_4$ , and Mn-Ru oxide, respectively.

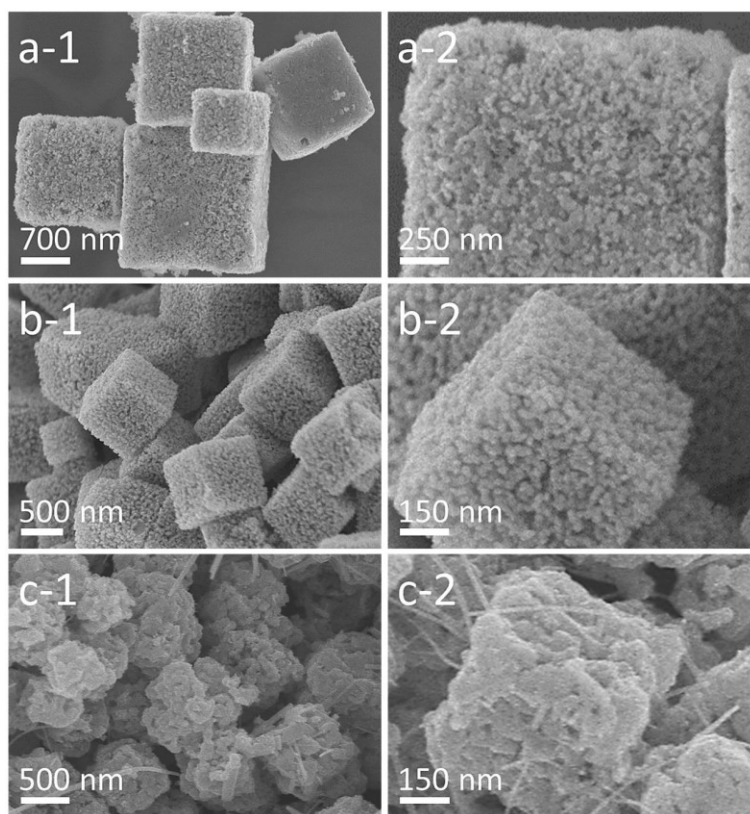


**Figure 3.10.** SEM images of the corresponding metal oxides prepared from (a) MnCNMn, (b) MnCNCo, and (c) MnCNRu PBAs.

From the high-resolution TEM (HRTEM) data, one can observe the highly crystallized oxides obtained from the PBAs along with the lattice fringes (**Figures 3.11**). Several small crystals are randomly oriented inside the cubes. As shown in **Figures 3.12** and **3.13**, metal and oxygen atoms are well-distributed, suggesting that Mn, Co, and Ru from the solid PBA crystals are uniformly rearranged into the highly crystalline oxides (any phase segregations were not observed at the nanometer scale. But, at the atomic scale, it is believed that some phase segregations (*i.e.*,  $\text{Mn}_3\text{O}_4$ , Ru, and  $\text{RuO}_2$ ) occurred, as mentioned above. The atomic ratios (Mn, Co, and Ru) of the oxides obtained by ICP analysis indicate that the compositions are similar to that of the PBAs, meaning that only water, cyanide groups and other organic residues are removed while the metals are maintained in place. The Mn/Co (in  $\text{Mn}_x\text{Co}_{3-x}\text{O}_4$ ) and Mn/Ru (in Mn-Ru oxide) atomic ratios are calculated to be 1.45 and 0.95, respectively.

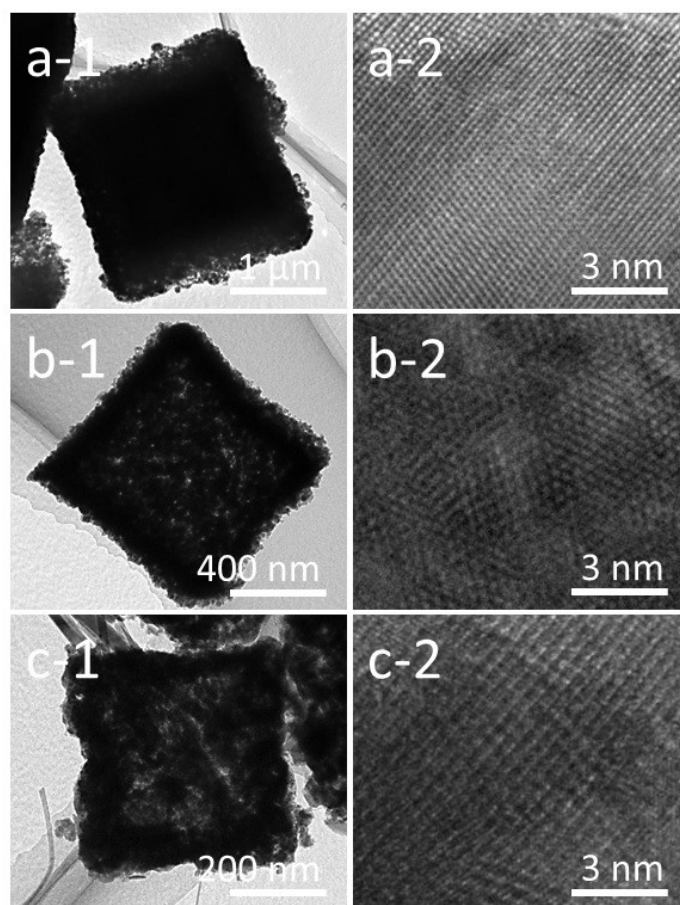


**Figure 3.11.** TEM and HRTEM images of the corresponding metal oxides prepared from (a)

MnCNMn, (b) MnCNCo, and (c) MnCNRu PBAs. The zone axes are  $\langle 011 \rangle$ ,  $\langle 100 \rangle$ , and  $\langle 021 \rangle$  of the spinel crystalline structures, respectively.

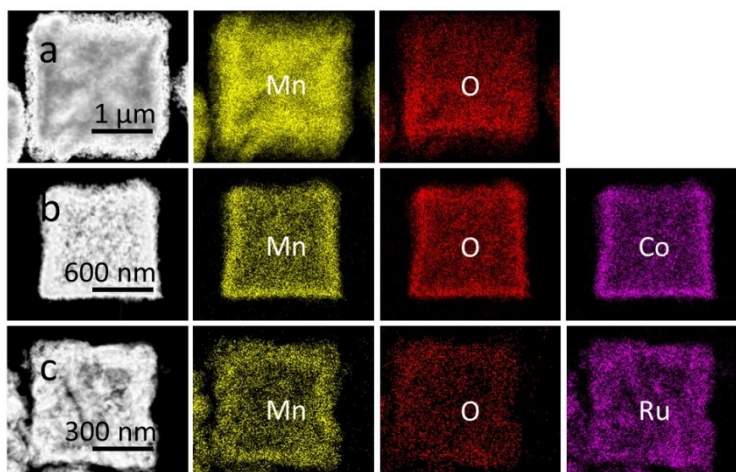


**Figure 3.12.** HAADF-STEM and elemental mapping images of the corresponding metal oxides prepared from (a) MnCNMn, (b) MnCNCo, and (c) MnCNRu PBAs.

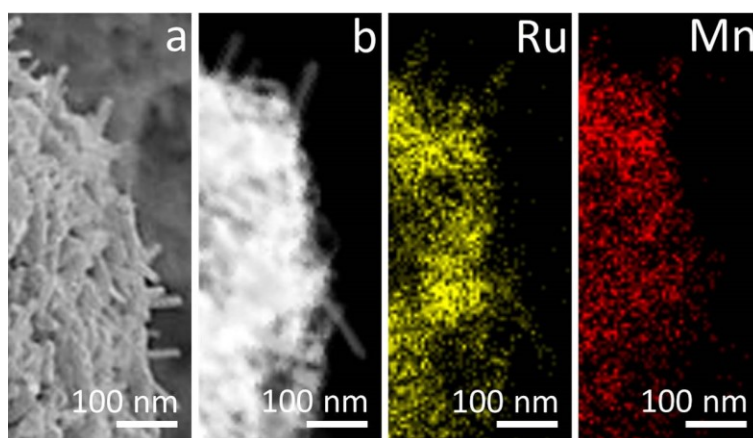


**Figure 3.13.** (a) SEM image and (b) HAADF-STEM images and the corresponding elemental mapping of the Mn-Ru oxides prepared from MnCNRu PBAs.

To determine the electronic states of Mn, Co, and Ru, X-ray photoelectron spectroscopy (XPS) measurement was carried out on the obtained metal oxides. In the case of the oxide prepared from MnCNMn, the high resolution spectrum centered on Mn  $2p_{3/2}$  can be deconvoluted into two contributions positioned at 641.6 eV and 643.2 eV corresponding to  $\text{Mn}^{2+} 2p_{3/2}$  and  $\text{Mn}^{3+} 2p_{3/2}$ , respectively, suggesting the presence of spinel  $\text{Mn}_3\text{O}_4$  (**Figure 3.14a**) [30,31]. The Mn  $3s$  peak is also observed at 83.2 eV with a satellite peak at 88.8 eV, probably due to different oxidation



states of Mn, which is an additional evidence of the formation of  $\text{Mn}_3\text{O}_4$  [32]. The O/Mn ratio is 1.32, which is almost the same as the expected stoichiometric value for  $\text{Mn}_3\text{O}_4$  (*i.e.*, 1.33). The calculated  $\text{Mn}^{2+}/\text{Mn}^{3+}$  molar ratio is 1.00/2.18, which is consistent with the theoretical value of typical  $\text{Mn}^{\text{II}}\text{Mn}^{\text{III}}_2\text{O}_4$  spinel oxides (*i.e.*, 0.5). In the case of the oxide prepared from MnCNCo PBAs, the XPS spectra of Mn  $2p$  and Co  $2p$  are shown in **Figure 3.14b-c**. As for the previous sample, the Mn  $2p_{3/2}$  spectrum can be deconvoluted into  $\text{Mn}^{2+} 2p_{3/2}$  and  $\text{Mn}^{3+} 2p_{3/2}$  contributions. The Co  $2p_{3/2}$  can be divided into two contributions at 780 eV and 781.2 eV, attributed to  $\text{Co}^{2+} 2p_{3/2}$  and  $\text{Co}^{3+} 2p_{3/2}$ , respectively. The O/(Mn+Co) atomic ratio is 1.32, which is in accordance with the calculated value of spinel  $\text{Mn}_x\text{Co}_{3-x}\text{O}_4$ . In addition, the calculated  $(\text{Mn}^{2+}+\text{Co}^{2+}):(\text{Mn}^{3+}+\text{Co}^{3+})$  ratio is 1:2.07 which is consistent with the calculated value of a typical spinel oxides (*i.e.*, 0.5).

The XPS spectrum of Mn  $2p$  of the Mn-Ru oxide prepared from MnCNRu reveals a peak centered at 641.8 eV which can be deconvoluted into two contributions corresponding to  $\text{Mn}^{2+}$  and  $\text{Mn}^{3+}$  (**Figure 3.15**), respectively, similar to the ones observed in **Figure 3.14a-b**. In the spectrum centered on Ru  $3p$  shown in **Figure 3.14d**, the deconvolution confirms the presence of  $\text{Ru}^0$  and  $\text{Ru}^{4+}$  chemical states, located at 642.6 eV and 645.4 eV, respectively [33,34]. A higher O/(Mn+Ru) atomic ratio (1.90) was confirmed in the Mn-Ru oxide which is probably due to the existence of high valence of Ru (*i.e.*,  $\text{Ru}^{4+}$  as  $\text{RuO}_2$ ). It is known that the  $\text{Ru}^{2+}$  and  $\text{Ru}^{3+}$  species are unstable in non-molecular solid, except in a few complex oxides<sup>[35]</sup> and therefore, as previously mentioned, they are unlikely to be present in the spinel crystal. All the results illuminated that both Ru and  $\text{RuO}_2$  are formed as impurities.

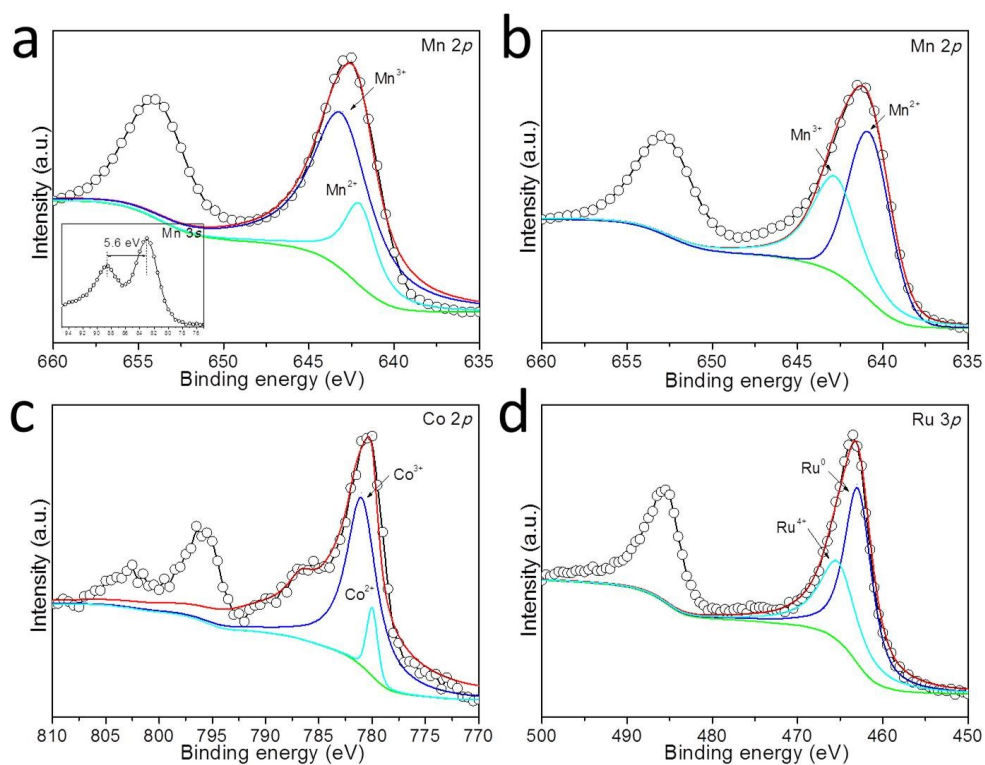


**Figure 3.14.** XPS spectra centered on the (a) Mn  $2p$  and Mn  $3s$  in the  $\text{Mn}_3\text{O}_4$ , (b) Mn  $2p$  and (c) Co  $2p$  in the  $\text{Mn}_x\text{Co}_{3-x}\text{O}_4$ , and (d) Ru  $3p$  in the Mn-Ru oxide.

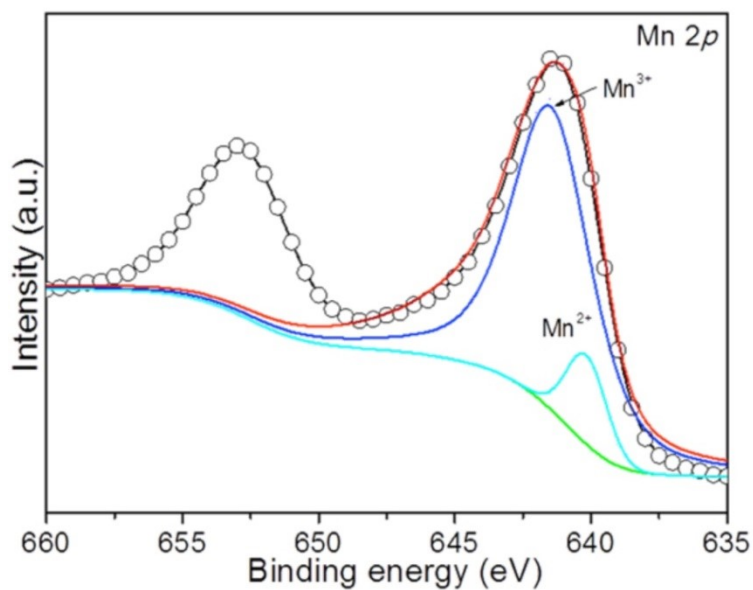


**Figure 3.15.** XPS spectra centered on the Mn  $2p$  in the Mn-Ru oxide.

### 3.3.3. Electrochemical Catalysis Using the Obtained Oxides

Hydrogen peroxide ( $\text{H}_2\text{O}_2$ ) has previously been synthesized by directly combining hydrogen and oxygen in the presence of catalysts [36-40]. In the case of ORR, the reduction of  $\text{O}_2$  includes two different pathways: the direct four-electron transfer (reaction 1) and the two-by-two electron pathway (stepwise, reactions 2-3) [41-43]:



The stepwise process goes through the formation of a hydroperoxide intermediate ( $\text{HO}_2^-$ ). If a catalyst is capable of selectively stop the oxygen reduction at this stage, it then leads to a convenient way to produce hydrogen peroxide. Recently, such an alternative approach for the synthesis of  $\text{H}_2\text{O}_2$  based on a two-electron reduction pathway-based ORR has been demonstrated [44-47]. It is well-known that the ORR activity of the manganese oxides ( $\text{Mn}_x\text{O}$ ) is valence- and particle size-dependent [5,15,16], so it is possible to obtain a  $\text{Mn}_x\text{O}$ -based catalyst with a specific activity (*i.e.*, high-selectivity of two-electron transfer) for catalyzing ORR.

In this study, the activity of Mn-Ru oxide catalyst toward ORR was carefully studied and compared to the  $\text{Mn}_3\text{O}_4$  and  $\text{Mn}_x\text{Co}_{3-x}\text{O}_4$  catalysts. From the cyclic voltammograms (CV) in the presence of oxygen (**Figure 3.16**), the Mn-Ru oxide catalyst shows a positively shifted oxygen reduction peak, compared to the other two samples. The ORR performance is further characterized by using a rotating ring-disk electrode (RRDE) in an  $\text{O}_2$ -saturated 0.1 M KOH solution at a rotation speed of 1600 rpm (**Figure 3.17**). The onset-potential catalyzed by the Mn-Ru oxide at 0.79 V is positively shifted (around 200 mV) compared to that of the  $\text{Mn}_3\text{O}_4$  and  $\text{Mn}_x\text{Co}_{3-x}\text{O}_4$  catalysts. Commercially available  $\text{RuO}_2$  catalyst gives a similar onset-potential to that of the Mn oxide and Mn-Co oxide catalysts, which strongly suggests the presence of a

synergistic effect between Mn and Ru in the Mn-Ru oxide catalyst. From the viewpoint of both the onset potential and the limitation current, the Mn-Ru oxide catalyst exhibits superior ORR performances.

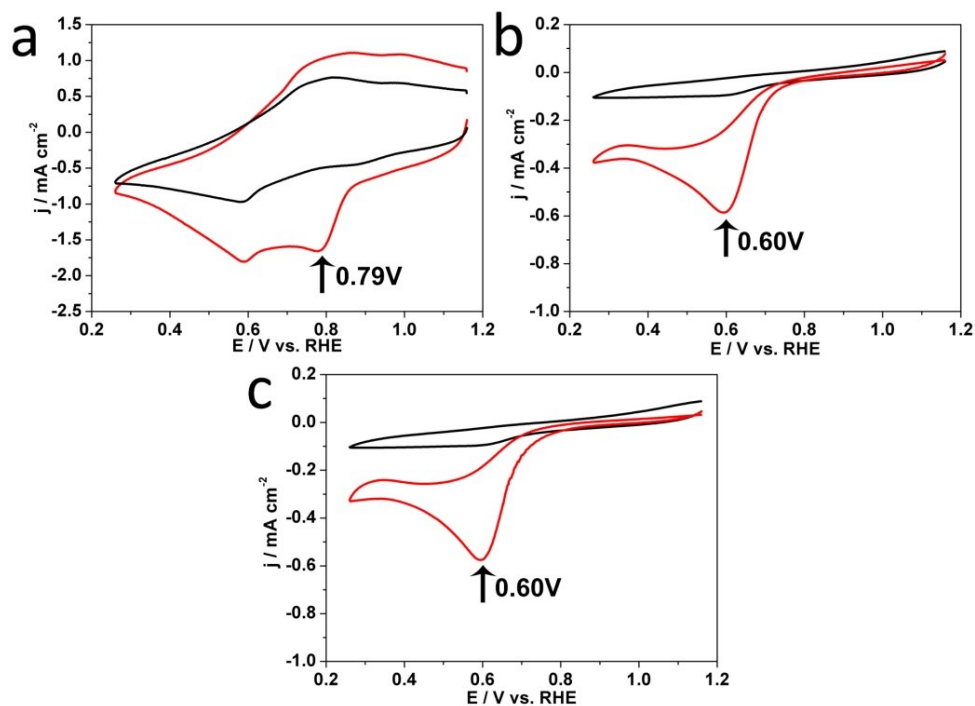


**Figure 3.16.** CV curves obtained under (black plot)  $\text{N}_2$ - and (red plot)  $\text{O}_2$ -saturated 0.1 M KOH catalyzed by (a) Mn oxide, (b) Mn-Co oxide, and (c) Mn-Ru oxide prepared from MnCNMn, MnCNCo, and MnCNRu PBAs, respectively.

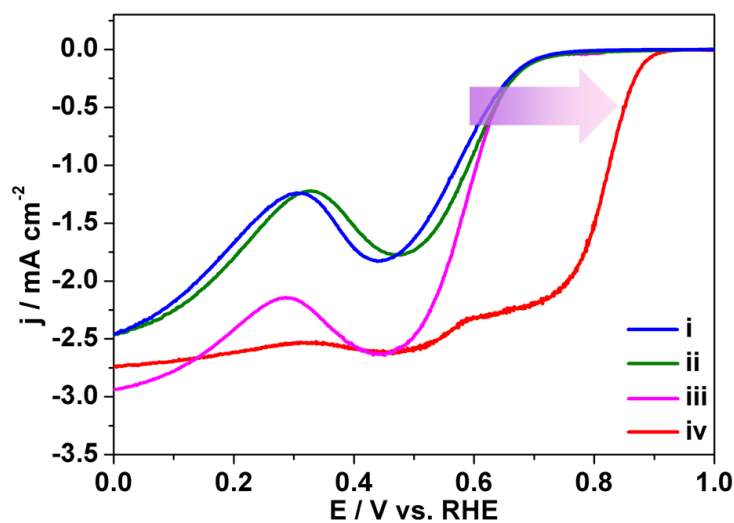


**Figure 3.17.** ORR polarization curves of (i) Mn oxide prepared from MnCNMn, (ii) Mn-Co

oxide prepared from MnCNCo, (iii) commercially available RuO<sub>2</sub>, and (iv) Mn-Ru oxide prepared from MnCNRu, respectively.

The polarization curves catalyzed by the Mn-Ru oxide exhibit two distinct potential regions: the diffusion-limiting region (from 0.0 V to 0.8 V) and the mixed kinetic-diffusion control region (from 0.8 V to 1.0 V) [48,49] (**Figure 3.18a**). The Koutecky-Levich (*K-L*) plots obtained from the polarization curves at various rotation speeds are employed for the calculations. In the *K-L* model, the current density (*j*) combines a kinetic (*j<sub>k</sub>*) and a diffusion (*j<sub>d</sub>*) components:

$$1/j = 1/j_k + 1/j_d = 1/j_k + 1/B\omega^{1/2} \quad (3.4)$$

$$B = 0.62 nFD^{2/3} \nu^{-1/6} C_{O_2} \quad (3.5)$$

where *n* is the number of transferred electrons, *F* is Faraday's constant (96,485 C mol<sup>-1</sup>), *D* is the diffusion coefficient of O<sub>2</sub> in 0.1 M KOH solution (1.9 × 10<sup>-5</sup> cm<sup>2</sup> s<sup>-1</sup>), *ν* is the kinematic viscosity of the electrolyte (0.01 cm<sup>2</sup> s<sup>-1</sup>) and *C<sub>O<sub>2</sub></sub>*

is the concentration of molecular oxygen in 0.1 M KOH (1.2 × 10<sup>-6</sup> mol cm<sup>-3</sup>). *B* should equal to 0.44 mA cm<sup>-2</sup> s<sup>1/2</sup> for a four-electron process and to 0.22 mA cm<sup>-2</sup> s<sup>1/2</sup> for a two-electron process. **Figure 3.18b** clearly shows that the slopes determined experimentally, at various potentials, are in good agreement with the calculated slope for the two-electron process, evidencing the selective formation of H<sub>2</sub>O<sub>2</sub> during the ORR. From the slopes of the plot derived from the experimental data, *B* is calculated as 0.22 mA cm<sup>-2</sup> s<sup>1/2</sup>, suggesting that a pure two-electron reduction process is achieved by using the Mn-Ru oxide catalyst. So far, several materials for ORR have been reported by other research groups, but catalysts suitable for two-electron reduction processes are rare, and their onset potentials are lower compared to that of our Mn-Ru oxide catalyst (**Table 3.1**). The ORR pathway catalyzed by Mn-Ru oxide in a wide potential range was further studied by using the RRDE (**Figure 3.18c**). The electron number (*n*) transferred in the ORR was calculated from the following equation:

$$n = 4 \times I_d / (I_d + I_r/N) \quad (3.6)$$

Where  $I_d$  is the disk current,  $I_r$  is the ring current and  $N = 0.4$  is the current collection efficiency of Pt ring electrode.

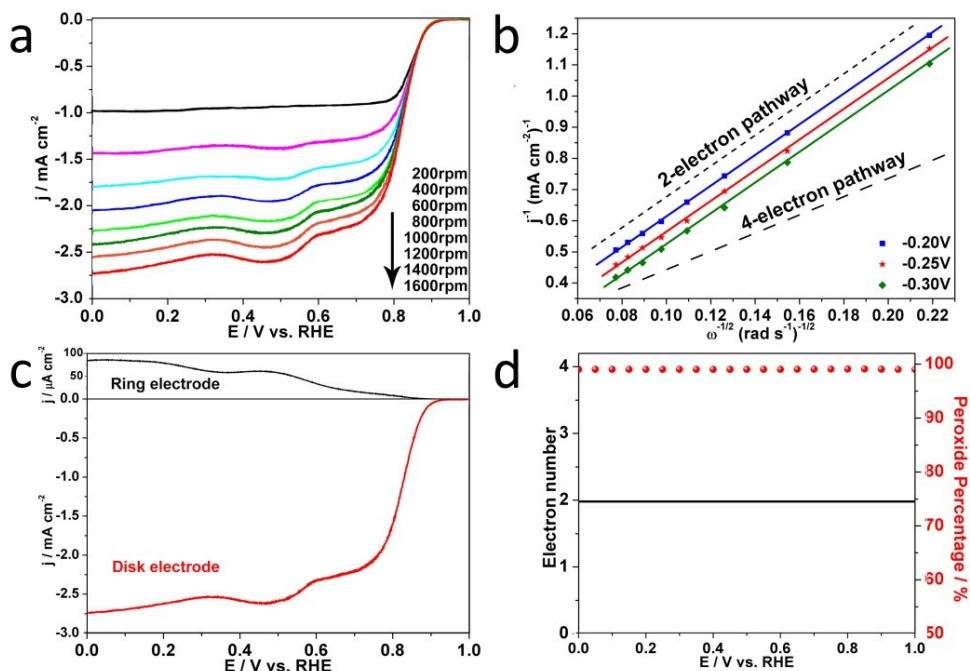


**Figure 3.18.** (a) ORR polarization curves of Mn-Ru oxide at different rotation rates in O<sub>2</sub>-saturated 0.1 M KOH. (b) Koutecky-Levich plots for the determination of the number of electrons transferred during the reaction. (c) The current collected on disk and ring electrodes catalyzed by Mn-Ru oxide in O<sub>2</sub>-saturated 0.1 M KOH at a rotation speed of 1600 rpm. (d) The electron number transferred and the percentage of peroxide at various potentials, calculated by using the currents collected on the rotating ring-disk electrode shown in panel (c).

**Table 3.1.** Comparison between the electrocatalytic activity toward ORR of our catalysts and other previously reported materials.  $n$  is the number of electron transferred during the ORR.

Sample information	Electrolyte	Onset potential* (mV vs. RHE)	$n$	References
Mn-Ru oxide	0.1M KOH	910	2.0	Present work
Mn <sub>x</sub> Co <sub>3-x</sub> O <sub>4</sub>	0.1M KOH	762	2.0	Present work
Mn <sub>3</sub> O <sub>4</sub>	0.1M KOH	762	2.0	Present work
Mesoporous N-doped carbon	0.1M KOH	730	2.6	Adv. Funct. Mater. 2012, 22, 4584
Reduced graphene oxide	0.1M KOH	810	2.7	Chem. Commun. 2013, 49, 6334
N-doped graphene	0.1M KOH	800	2.7	Nat. Mater. 2011, 10, 780
CoMn <sub>2</sub> O <sub>4</sub>	0.1M KOH or KCl	780	2.9	Nat. Chem. 2011, 3, 79

Co <sub>2</sub> MnO <sub>4</sub>	0.1M KOH or KCl	850	3.3	Nat. Chem. 2011, 3, 79
Co <sub>x</sub> Mn <sub>3-x</sub> O <sub>4</sub>	0.1M KOH or KCl	860	3.4	Nat. Chem. 2011, 3, 79
Porous calcium-manganese oxide (Ca <sub>2</sub> Mn <sub>3</sub> O <sub>8</sub> ) microspheres	0.1M KOH	850	3.5	Chem. Sci. 2013, 4, 368
Co <sub>x</sub> Mn <sub>3-x</sub> O <sub>4</sub>	0.1 M KOH or KCl	880	3.7	Nat. Chem. 2011, 3, 79
Co <sub>3</sub> O <sub>4</sub> /graphene composite	1.0M KOH	864	3.7	J. Am. Chem. Soc. 2012, 134, 3517
Manganese oxide containing mesoporous N-doped carbon	0.1M KOH	810	3.8	Adv. Funct. Mater. 2012, 22, 4584
Flower-like manganese oxide on reduced graphene oxide	0.1M KOH	840	3.8	Chem. Commun. 2013, 49, 6334
Spinel MnCo <sub>2</sub> O <sub>4</sub> / graphene composite	1.0M KOH	885	3.9	J. Am. Chem. Soc. 2012, 134, 3517
Co <sub>3</sub> O <sub>4</sub> nanocrystals on graphene	0.1M KOH	880	3.9	Nat. Mater. 2011, 10, 780
Iron-based catalyst (Fe-N/C)	0.1M KOH	700	3.9	Nat. Mater. 2011, 10, 780
Platinum/carbon	0.1M KOH or KCl	50	3.9	Nat. Chem. 2011, 3, 79
Spinel MnCo <sub>2</sub> O <sub>4</sub> nanoparticles + graphene sheet mixture	1.0M KOH	845	4.0	J. Am. Chem. Soc. 2012, 134, 3517
N-doped graphene sheets	1.0M KOH	830	4.0	J. Am. Chem. Soc. 2012, 134, 3517
Manganese oxide (β-MnO <sub>2</sub> )	0.1M KOH	800	4.0	Angew. Chem. Int. Ed. 2013, 52, 2474
Layer-by-layer structured NiO-GO nanocomposite	0.1M KOH	860	---	Chem. Commun. 2015, 51, 16409
Cobalt and nitrogen-functionalized graphene	0.1M KOH	862	---	J. Mater. Chem. A 2013, 1, 3593

\*: All the onset potentials referenced to RHE are calculated through by the following equation:

$$E_{(vs. RHE)} = E_{(vs. Ag/AgCl)} + 0.0592 \cdot \text{pH}.$$

The  $n$  value was estimated to be about 2.0, which is consistent with the high yield of peroxide (over 99 %) (**Figure 3.18d**) [50,51]. The selectivity for H<sub>2</sub>O<sub>2</sub> production was further confirmed by using RRDE measurements at different constant potentials (e.g., 0.65 V and 0.55 V vs. RHE), in which a constant potential (e.g., 0.65 and 0.55 V vs. RHE), in which a constant was fixed at 1.50 V to the ring electrode vs. RHE. From **Figure 3.19**, it is obvious that the calculated efficiency for H<sub>2</sub>O<sub>2</sub> is close to 100% for all the detection times, which is consistent with the electron number of 2. Thus, it is clear that the Mn-Ru oxide is the critical factor leading to such highly efficient catalysts for the production of H<sub>2</sub>O<sub>2</sub> through a two-electron reduction pathway. The excellent capability of the Mn-Ru oxides for the production of H<sub>2</sub>O<sub>2</sub> can be explained from three aspects. Firstly, improved mass transport inside the nanoporous architectures is achieved, due to the enhanced wettability of the catalyst layer caused by the self-humidification of RuO<sub>2</sub>,

which highly facilitate the transport of the formed  $\text{H}_2\text{O}_2$  from the electrode to the bulk electrolyte [52]. In addition, the nanoscale distribution of  $\text{RuO}_2$  content, which possesses good electronic conductivity, facilitates the electron transfer between the active  $\text{Mn}_3\text{O}_4$  sites, and finally improves the activity of  $\text{Mn}_3\text{O}_4$  toward the ORR. Thirdly, a bi-functional effect between the adjacent  $\text{Mn}_3\text{O}_4$  and  $\text{RuO}_2$  sites particularly changed the adsorption of oxygen molecules, which avoids the O-O bond breaking [40,53], thus enhancing the formation of  $\text{H}_2\text{O}_2$ . The synergistic effect of enhanced mass transportation and adjacent sites with different activities are responsible for the high-efficiency of  $\text{H}_2\text{O}_2$  production.

Because of its importance in catalyzing reactions, the catalytic stability of the as-prepared Mn-Ru oxide was further evaluated by employing a chronoamperometric approach in a time period of 5 h. For comparison, a commercially available Pt, 5% on carbon (abbreviated as PtC-5%) catalyst was also studied by the same method. The large current retention of the as-prepared Mn-Ru oxide reveals an addition of the better catalytic stability in catalyzing ORR (**Figure 3.20a**). The superior catalytic stability is probably supported by the shape and crystallinity retention of the catalyst even after electrocatalyzing ORR for long time (**Figure 3.20b** and **c**).

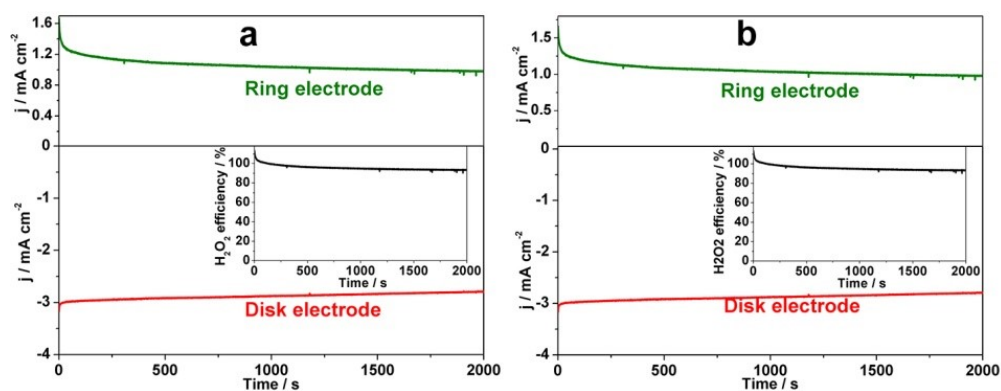


**Figure 3.19.** Chronoamperometric curves obtained at disk and ring electrodes at different constant potentials: (a) 0.65V and (b) 0.55V. The measurements were carried out in  $\text{O}_2$ -saturated 0.1M KOH at a rotation speed of 1600 rpm. The corresponding  $\text{H}_2\text{O}_2$  production efficiencies were shown in the insets.



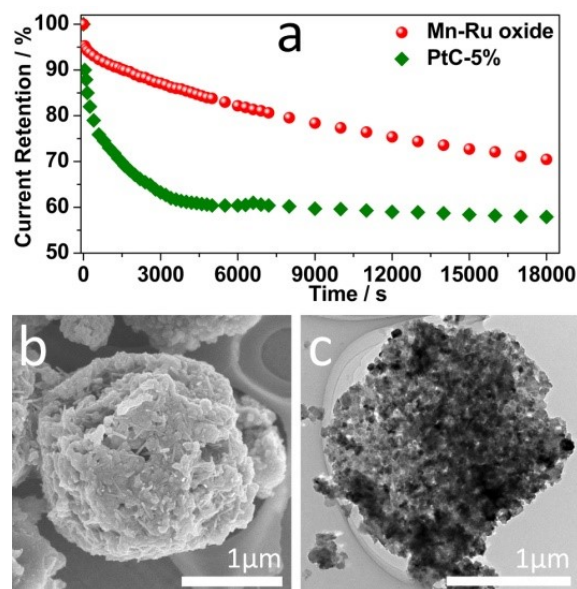


**Figure 3.20.** (a) Current retention plot during chronoamperometric measurements for the Mn-Ru oxide and commercially available PtC-5% catalysts. (b) SEM and (c) TEM images of the Mn-Ru oxide after long-term stability measurement.

### 3.4. Conclusions

I have demonstrated a novel approach for the preparation of Mn-Ru oxide with a nanoporous structure through the thermal treatment of a MnCNRu PBA in which the CN-groups act as a bridge between Mn and Ru. During the thermal process, the organic residues and the water molecules are removed, leaving pores/voids inside the metal frameworks subject to further oxidation. When compared with the Mn and Mn-Co oxide catalysts, the Mn-Ru oxide catalyst shows a significantly enhanced electrocatalytic activity toward ORR. Importantly, my Mn-Ru oxide catalyst can selectively reduce oxygen in a two-electron pathway, which is a promising result for further application in the production  $\text{H}_2\text{O}_2$  in a convenient and environmentally friendly way. All the results indicate that the superior performance toward  $\text{H}_2\text{O}_2$  production can be achieved due to the proper catalyst compositions. The present strategy makes the preparation of PBAs with well-defined compositions and morphologies easier, so it is now possible to prepare

various nanoarchitected hybrid metals oxides as promising candidates for electrocatalytic applications. I strongly believe that this method has the potential to overcome the typical difficulties encountered during the fabrication of nanoporous/mesoporous metal oxides by other traditional approaches.

### 3.5. References

- [1] Y. Lu, Y. Jiang, X. Gao, W. Chen, *Chem. Commun.* **2014**, *50*, 8464.
- [2] J. Vondrák, B. Klápště, J. Velická, M. Sedlaříková, V. Novák, J. Reiter, *J. New Mat. Electrochem. Syst.* **2015**, *8*, 1.
- [3] Z.-R. Tian, W. Tong, J.-Y. Wang, N.-G. Duan, V.V. Krishnan, S.L. Suib, *Science* **1997**, *276*, 926.
- [4] T. Ahmad, K.V. Ramanujachary, S.E. Lofland, A.K. Ganguli, *J. Mater. Chem.* **2004**, *14*, 3406.
- [5] Y. Gorlin, C.-J. Chung, D. Nordlund, B.M. Clemens, T.F. Jaramillo, *ACS Catal.* **2012**, *2*, 2687.
- [6] H. Zhang, G. Cao, Z. Wang, Y. Yang, Z. Shi, Z. Gu, *Nano Lett.* **2008**, *8*, 2664.
- [7] W.-N. Li, J. Yuan, X.-F. Shen, S. Gomez-Mower, L.-P. Xu, S. Sithambaram, M. Aindow, S.L. Suib, *Adv. Funct. Mater.* **2006**, *16*, 1247.
- [8] D. Zitoun, N. Pinna, N. Frolet, C. Belin, *J. Am. Chem. Soc.* **2005**, *127*, 15034.
- [9] J. Zhang, J. Jiang, X. S. Zhao, *J. Phys. Chem. C* **2011**, *115*, 6448.
- [10] F. Cheng, J. Zhao, W. Song, C. Li, H. Ma, J. Chen, P. Shen, *Inorg. Chem.* **2006**, *45*, 2038.
- [11] T.D. Schladt, T. Graf, W. Tremel, *Chem. Mater.* **2009**, *21*, 3183.
- [12] E.R. Stobbe, B.A. Boer, J.W. Geus, *Cata. Today* **1999**, *47*, 161.
- [13] M. Takayanagi, Y. Imai, K. Tajima, *Chem. Lett.* **2008**, *37*, 14.

- [14] G. An, P. Yu, M. Xiao, Z. Liu, Z. Miao, K. Ding, L. Mao, *Nanotechnology* **2008**, *19*, 275709.
- [15] Y. Liang, Y. Li, H. Wang, J. Zhou, J. Wang, T. Regier, H. Dai, *Nat. Mater.* **2011**, *10*, 780.
- [16] Y. Tan, C. Xu, G. Chen, X. Fang, N. Zheng, Q. Xie, *Adv. Funct. Mater.* **2012**, *22*, 4584.
- [17] C. Yuan, H.B. Wu, Y. Xie, X.W. Lou, *Angew. Chem. Int. Ed.* **2014**, *53*, 1488.
- [18] L. Zhang, L. Shi, L. Huang, J. Zhang, R. Gao, D. Zhang, *ACS Catal.* **2014**, *4*, 1753.
- [19] Y. Liang, H. Wang, J. Zhou, Y. Li, J. Wang, T. Regier, H. Dai, *J. Am. Chem. Soc.* **2012**, *134*, 3517.
- [20] J. Ohyama, T. Sato, Y. Yamamoto, S. Arai, A. Satsuma, *J. Am. Chem. Soc.* **2013**, *135*, 8016.
- [21] J. Chen, Z.-L. Tao, S.-L. Li, *J. Am. Chem. Soc.* **2004**, *126*, 3060.
- [22] E. Antolini, F. Colmati, E.R. Gonzalez, *Electrochem. Commun.* **2007**, *9*, 398.
- [23] V. Malgras, Q. Ji, Y. Kamachi, T. Mori, F.-K. Shieh, K. C.-W. Wu, K. Ariga, Y. Yamauchi, *Bull. Chem. Soc. Jpn.* **2015**, *88*, 1171.
- [24] M. Hu, S. Furukawa, R. Ohtani, H. Sukegawa, Y. Nemoto, J. Reboul, S. Kitagawa, Y. Yamauchi, *Angew. Chem. Int. Ed.* **2012**, *51*, 984.
- [25] M. Hu, A.A. Belik, M. Imura, Y. Yamauchi, *J. Am. Chem. Soc.* **2013**, *135*, 384.
- [26] M.B. Zakaria, M. Hu, R.R. Salunkhe, M. Pramanik, K. Takai, V. Malgras, S. Choi, S.X. Dou, J.H. Kim, M. Imura, S. Ishihara, Y. Yamauchi, *Chem.-Eur. J.* **2015**, *21*, 3605.
- [27] M.B. Zakaria, A.A. Belik, C.-H. Liu, H.-Y. Hsieh, Y.-T. Liao, V. Malgras, Y. Yamauchi, K. C.-W. Wu, *Chem.-Asian J.* **2015**, *10*, 1457.
- [28] M. Hu, S. Ishihara, K. Ariga, M. Imura, Y. Yamauchi, *Chem.-Eur. J.* **2013**, *19*, 1882.
- [29] Y.C. Choi, B.S. Lee, *Jpn. J. Appl. Phys.* **1999**, *38*, 4876.
- [30] A.M.E. Raj, S.G. Victoria, V.B. Jothy, C. Ravidhas, J. Wollschläger, M. Suendorf, M. Neumann, M. Jayachandran, C. Sanjeeviraja, *Appl. Sur. Sci.* **2010**, *256*, 2920.

- [31] Z.-Y. Tian, P.M. Kouotou, N. Bahlawane, *J. Phys. Chem. C* **2013**, *117*, 6218.
- [32] J.W. Lee, A.S. Hall, J.-D. Kim, T.E. Mallouk, *Chem. Mater.* **2012**, *24*, 1158.
- [33] N. Chakroune, G. Viau, S. Ammar, L. Poul, D. Veautier, M.M. Chehimi, C. Mangeney, F. Villain, F. Fiévet, *Langmuir* **2005**, *21*, 6788.
- [34] Y. Ma, C.-W. Tai, R. Younesi, T. Gustafsson, J.Y. Lee, K. Edström, *Chem. Mater.* **2015**, *27*, 7698.
- [35] F.D. Romero, S.J. Burr, J.E. McGrady, D. Gianolio, G. Cibir, M.A. Hayward, *J. Am. Chem. Soc.* **2013**, *135*, 1838.
- [36] E.W. Miller, N. Taulet, C.S. Onak, E.J. New, J.K. Lanselle, G.S. Smelick, C.J. Chang, *J. Am. Chem. Soc.* **2010**, *132*, 17071.
- [37] W. Adamiak, J. Jedraszko, O. Krysiak, W. Nogala, J.C. Hidalgo-Acosta, H.H. Girault, M. Opallo, *J. Phys. Chem. C* **2014**, *118*, 23154.
- [38] C. Samanta, *Appl. Catal., A* **2008**, *350*, 133.
- [39] R. Burch, P.R. Ellis, *Appl. Catal. B* **2003**, *42*, 203.
- [40] N.M. Wilson, D.W. Flaherty, *J. Am. Chem. Soc.* **2016**, *138*, 574.
- [41] D.A. Slanac, W.G. Hardin, K.P. Johnston, K.J. Stevenson, *J. Am. Chem. Soc.* **2012**, *134*, 9812.
- [42] D.A. Finkelstein, N.D. Mota, J.L. Cohen, H.D. Abruña, *J. Phys. Chem. C* **2009**, *113*, 19700.
- [43] I. Katsounaros, W.B. Schneider, J.C. Meier, U. Benedikt, P.U. Biedermann, A.A. Auer, K.J.J. Mayrhofer, *Phys. Chem. Chem. Phys.* **2012**, *14*, 7384.
- [44] T.-P. Feller, F. Hasché, P. Strasser, M. Antonietti, *J. Am. Chem. Soc.* **2012**, *134*, 4072.
- [45] Y. Nisimoto, B.A. Diebold, D. Cosentino-Gomes, J.D. Lambeth, *Biochemistry* **2014**, *53*, 5111.
- [46] J.S. Jirkovský, I. Panas, E. Ahlberg, M. Halasa, S. Romani, D.J. Schiffrin, *J. Am. Chem.*

*Soc.* **2011**, *133*, 19432.

- [47] M. Campos, W. Siritwacharapiboon, R.J. Potter, S.L. Horswell, *Catal. Today* **2013**, *202*, 135.
- [48] S. Guo, S. Zhang, L. Wu, S. Sun, *Angew. Chem. Int. Ed.* **2012**, *51*, 11770.
- [49] Q. Wang, Z.-Y. Zhou, Y.-J. Lai, Y. You, J.-G. Liu, X.-L. Wu, E. Terefe, C. Chen, L. Song, M. Rauf, N. Tian, S.-G. Sun, *J. Am. Chem. Soc.* **2014**, *136*, 10882.
- [50] N. Ramaswamy, U. Tylus, Q. Jia, S. Mukerjee, *J. Am. Chem. Soc.* **2013**, *135*, 15443.
- [51] V.R. Stamenkovic, B. Fowler, B.S. Mun, G. Wang, P.N. Ross, C.A. Lucas, N.M. Marković, *Science* **2007**, *315*, 493.
- [52] C. Chauvin, T. Saida, W. Sugimoto, *J. Electrochem. Soc.* **2014**, *161*, F318.
- [53] H.C. Ham, J.A. Stephens, G.S. Hwang, J. Han, S.W. Nam, T.H. Lim, *Catal. Today* **2011**, *165*, 138.

# Chapter 4

## Chapter 4-1

# 4-1. Prussian Blue Derived Nanoporous Iron Oxides as Anticancer Drug Carriers for Magnetic-Guided Chemotherapy

### 4-1.1. Introduction

In recent years, cancer has become one of the most serious diseases causing a high rate of casualties. Chemotherapy, radiotherapy and surgical resection are three common therapies to treat cancer, chemotherapy being the one inflicting the least pain to the patients. However, the multidrug resistance (MDR) of cancer cells is responsible for 90% of chemotherapeutic failures upon treatment [1]. Generally, MDR originates from the overexpression of ATP-binding cassette transporter proteins effluxing the anticancer drugs from the cytoplasm of cancer cells to reduce the accumulation of drugs [2]. Fortunately, an appropriate drug delivery system (DDS) can change the release behavior of chemotherapeutic agents, thus improving effectively the anticancer activity and overcoming the prevalent MDR issues affecting cancer chemotherapy [3,4]. So far, many organic materials have been utilized as carriers for DDS, such as liposomes [5], alginate [6], albumin [7], and poly(lactic-co-glycolic acid) (PLGA) [8]. In addition to these,

inorganic nanoparticles exhibiting specific compositional and structural features can also circumvent MDR. For instance, the family of nontoxic, biocompatible, and mechanically stable mesoporous silica nanoparticles [9,10] is a well-known carrier for drug delivery. Other inorganic nanoparticles, such as gold, silver, and iron oxide, exhibit intrinsic physicochemical properties suitable for transferring irradiated energy into heat or toxic radicals for hyperthermia [11] and photothermal [12] or photodynamic therapy [13]. The unique properties of inorganic nanoparticles make them good potential candidates for DDS applications.

As the carriers circulate in the human body, it is a big challenge to impart the cell-targeting ability to drug carriers. Modifying the surface of the synthesized drug carriers is a common method to increase their affinity towards cancer cells. For example, the PEGylation of carriers lets them accumulate in the tumor, owing to an enhanced permeability and retention (EPR) effect [14]. Folic acid [15], transferrin [16], and antibodies [17] are also commonly used for targeting cancer cells which express specific receptors for these ligands. However, the variation in receptor expression from patient to patient and the non-specific expression of receptors in normal cells are extremely limiting factors when it comes to applying this strategy in the clinical environment [18]. Compared to molecular targeting, magnetic targeting based on physical operation is therefore more reliable and is not limited by the expression of a receptor in cancer cells. One only needs to employ an external magnetic field on the patient in order to direct the magnetic nanoparticles circulating in the vicinity of the tumor. It is well known that iron oxide is a highly biocompatible material suitable for magnetically guided drug delivery. Many reports have shown that magnetically guided drug delivery could enhance the accumulation of magnetic carriers on targeted cells both *in vitro* and *in vivo*. Moreover, magnetic iron oxide has other physical benefits in other applications such as hyperthermia and magnetic resonance imaging, the latter providing real-time drug distribution [19]. Namiki *et al.* [20] guided



successfully nucleic acid-loaded LipoMag, which is composed of a magnetic nanocrystal core and cationic lipid shell, to gastric tumors in mice. Cheng *et al.* [18] synthesized a new class of multifunctional nanoparticles consisting of a core, a thin layer of iron oxide as the intermediate shell, and a thin layer of gold as the outer shell for multimodal imaging and photothermal therapy. They asserted that the uptake of nanoparticles was enhanced about 8-fold under a tumor-targeting magnetic field. Mejias *et al.* [21,22] also reported that by applying an external magnetic field, the targeting of IFN- $\gamma$ -loaded magnetic nanoparticles at the tumor site becomes more efficient. These pioneering studies all demonstrate the successful drug delivery of such materials as well as their application in magnetic-guided chemotherapy.

Coordination polymers are of great importance nowadays because of their wide range of applications such as catalysis, gas storage, biosensing, electrochemistry, and drug delivery [23,24]. Prussian Blue (PB) and its analogues, as a large family of coordination polymers, have drawn significant attention because of their high surface area, uniform pore arrangement and tunability in their particle size and shape [25-29]. PB ( $\text{Fe}_4[\text{Fe}(\text{CN})_6]_3 \cdot x\text{H}_2\text{O}$ ), in which iron ions are bridged by cyano groups ( $\text{Fe}^{\text{III}}-\text{C}\equiv\text{N}-\text{Fe}^{\text{II}}$ ), is considered as a potential precursor for nanoporous iron oxides with high surface areas. The iron components can be oxidized and the organic components ( $-\text{C}\equiv\text{N}-$ ) can be removed by thermal decomposition in air [30,31].

In this work, I report the thermal conversion of PB nanocubes into nanoporous iron oxides with superparamagnetic behavior. Furthermore, the cytotoxicity of PB-derived nanoporous Fe oxides is examined by MTT assays on bladder cancer cells (*i.e.*, T24). Even at high dosage ( $800 \text{ mg mL}^{-1}$ ), the cell viability remains 100%, indicating an excellent biocompatibility. Consequently, PB-derived materials can be utilized as an anticancer drug capsule for magnetic guiding chemotherapy.

## 4-1.2. Experimental Section

### 4-1.2.1. Chemicals

PVP (Polyvinylpyrrolidone) (K30) was purchased from Nacalai Tesque. Potassium hexacyanoferrate (III) ( $K_3[Fe(CN)_6] \cdot 3H_2O$ ) was purchased from Merck KGaA, Germany. Hydrochloric acid was purchased from Wako Pure Chemical Industries, Ltd. 5-Dimethylthiazol-2-yl-2,5-diphenyl tetrazolium bromide (MTT), Triton X-100, 4',6-diamidino-2-phenylindole (DAPI) and o-phenylenediamine (o-PDA) were supplied by Sigma-Aldrich. N,N-Dimethylformamide (DMF) was supplied by MBI, USA. Dimethyl sulfoxide (DMSO) was supplied by J. T. Baker, USA.

### 4-1.2.2. Preparation of PB Nanocubes

For the preparation of PB nanocubes, PVP (polyvinylpyrrolidone) (K30) (6.0 g) and  $K_3[Fe(CN)_6] \cdot 3H_2O$  (264 mg) were dissolved in a 0.01 M HCl aqueous solution (80.0 mL) under magnetic stirring. After 30 min of stirring, a clear yellow solution was obtained. The vial was then placed into an electric oven and heated at 80 °C for 30 h. After aging, the precipitates were collected by centrifugation and washed several times in distilled water and ethanol. After drying at room temperature for 24 h, PB nanocubes of approximately 80 nm in particle size were obtained. For the preparation of nanoporous iron oxide, the obtained PB powder (50.0 mg) was placed into a melting pot which was then heated inside an electronic furnace at a heating rate of 1 °C min<sup>-1</sup> from room temperature to a designated temperature (250 °C and 400 °C) and kept for 1 h to achieve complete thermal decomposition. After that, the powders were left to cool inside the furnace. Finally, the obtained powders were collected separately for characterization. All

calcination processes were performed in air. The obtained PB-derived nanoporous Fe oxides calcined at 250 °C and 400 °C are labeled as 'PB\_250' and 'PB\_400', respectively.

### 4-1.2.3. Cell-Related Experiments

Bladder cancer cells (T24) were maintained under standard cell culture conditions, in high glucose Dulbecco's Modified Eagle's Medium (DMEM) (Gibco, NY, USA) with 10% fetal bovine serum (Gibco, NY, USA) in a 37 °C, 5% CO<sub>2</sub> humidified incubator. Before measuring the cytotoxicity, the cancer cells were transferred from the culture dish into a 96-well plate (2×10<sup>4</sup> cells per well) and cultured for 1 day. Subsequently, the PB\_250 and Cis@PB\_250 samples of various concentrations were added into the cell media in the 96-well plate. After incubating for 24 h, the 96-well plate was washed with phosphate buffered saline (PBS) to remove the dead cells and the PB NPs in the media. Next, MTT (5 mg mL<sup>-1</sup>) was added into each well to achieve a final concentration of 0.5 mg mL<sup>-1</sup>, followed by further incubation for 2 h at 37 °C. After that, the cell medium containing MTT was removed from each well. A DMSO solution (0.1 mL) was then added into each well to dissolve the formazan crystals, and the absorbance at 570 nm was recorded by using an ELISA reader.

In order to observe the effect of magnetic guiding, T24 cells were cultured on a 12-well plate (2×10<sup>5</sup> cells per well) for 1 day. After washing with PBS, 1 mL of Cis@PB\_250-containing solution (100 mg mL<sup>-1</sup>) was added into each well, followed by culturing for 24 h. A magnet was put underneath the cell plate for guiding during the culturing period. After that, the plate was washed with modified PBS (PBS with 4% paraformaldehyde) three times, and 0.5 mL of DAPI (antibody titer 1:2000)-containing PBS solution (2.8×10<sup>-5</sup> M) was then added into the plate for 30 min to stain the nucleus of the living cells. Finally, the plate was washed with PBS and stored in PBS solution. The distribution of DAPI-stained cells was analyzed by confocal fluorescence

microscopy.

#### 4-1.2.4. Characterization

SEM images were obtained with a Hitachi SU8000 scanning microscope at an accelerating voltage of 5 kV. Wide-angle powder X-ray diffraction (XRD) patterns were obtained with a Rigaku RINT 2500X diffractometer using monochromated  $\text{Cu}_{K\alpha}$  radiation (40 kV, 40 mA) at a scanning rate of  $2^\circ \text{ min}^{-1}$ . Nitrogen adsorption-desorption data were obtained by using a Quantachrome Autosorb Automated Gas Sorption System at 77 K. Prior to the measurements, the samples were degassed in vacuum. The surface areas were calculated by the BET method using the adsorption branches of the isotherm. The concentration of MB in the aqueous solution was determined by measuring the absorbance at  $\lambda_{\text{max}} = 664 \text{ nm}$  using a JASCO V-570 UV/Vis/NIR spectrophotometer. The absorbance at 704 nm was measured to follow the adsorption of cisplatin in PBs.

### 4-1.3. Results and Discussion

The surface morphology of the prepared PB nanocubes before and after calcination was examined using a scanning electron microscope (SEM), as shown in **Figure 4-1.1a**. The average size of the PB nanocubes is around 80 nm (**Figure 4-1.1a-1**). The morphology of the obtained PB-derivatives after calcination (PB\_250 and PB\_400) remains nanocubes, but their sizes were slightly reduced and their surface roughness increased (**Figure 4-1.1a-2** and **4-1.1a-3**). The reduction of the particles size is mainly caused by removing the cyano-groups and the interstitial water molecules during calcination. To retain the original shapes of the nanocubes, it is found that the aging time of the PB particles before calcination has a critical effect. Along aging time

effectively solidifies the metal-organic framework. After calcinating the PB particles aged for a short time (15 h instead of 30 h), the original cubic shape is destroyed, as shown in **Figure 4-1.2**. In addition, I have checked the dispersy of the particles in water. Even after 15 h, the particles are still well dispersed (**Figure 4-1.3**). I also performed dynamic light scattering (DLS) analysis for investigating the particle size distribution (**Figure 4-1.4**). The predominant particle size is around 100 nm which is in agreement with the SEM data.

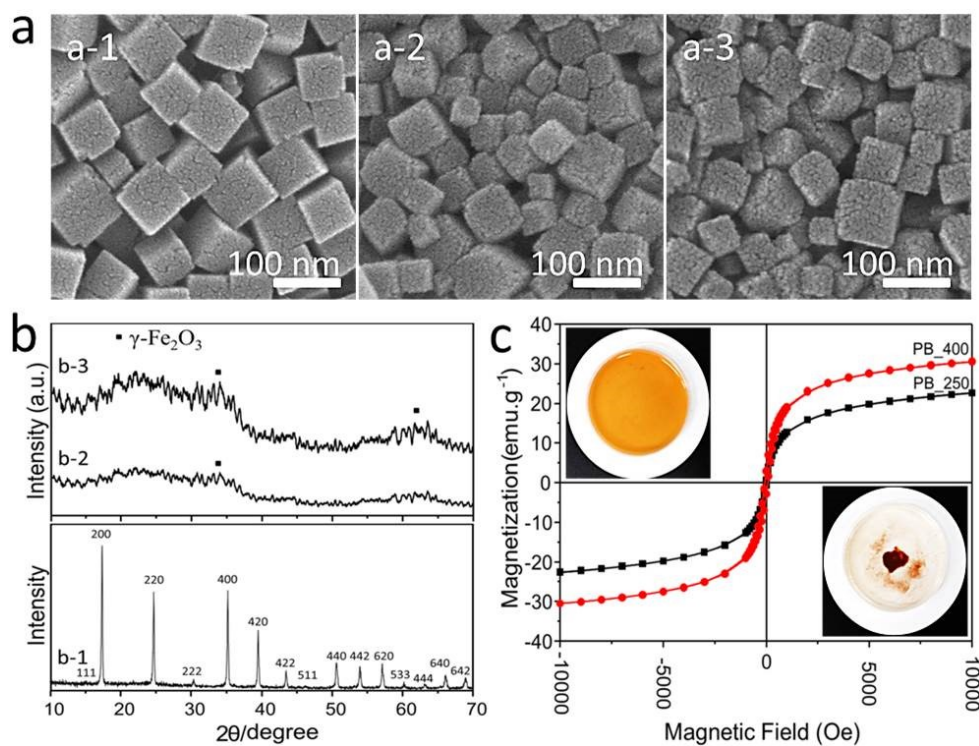


**Figure 4-1.1.** (a) SEM images of PB (a-1), PB<sub>250</sub> (a-2), and PB<sub>400</sub> (a-3). (b) Wide-angle XRD patterns of PB (b-1), PB<sub>250</sub> (b-2), and PB<sub>400</sub> (b-3). (c) Magnetization curves of PB<sub>250</sub> and PB<sub>400</sub> samples measured at 300 K. Insets: Two photographs showing the solution colors containing iron oxide nanoparticles before (top left) and after (bottom right) magnetic collection. When the magnet approaches the center, the iron oxide nanoparticles are easily collected

The crystal phase of the final products and the degree of crystallinity were characterized by using wide-angle XRD measurements (**Figure 4-1.1b**). The as-prepared PB particles show the same face-centered cubic diffraction patterns as the bulk PB crystals (JCPDS card 73-0687) (**Figure**

**4-1.1b-1).** No peaks derived from impurities were detected, which indicates the high purity of the PB particles. In the original PB crystals, iron atoms are separated by cyano-bridges, which provide good conditions for small-sized  $\gamma\text{-Fe}_2\text{O}_3$  particles during the oxidization process. Considering that 250 °C is a relatively low temperature for solid-state reactions, the aggregation or fusion of  $\gamma\text{-Fe}_2\text{O}_3$  during the calcination is greatly hindered. Indeed, PB\_250 shows no obvious XRD peaks, indicating that the phase in the frameworks is mostly amorphous (**Figure 4-1.1b-2**). In the case of PB\_400, very weak and broad peaks observed at  $2\theta = 35^\circ$  and  $63^\circ$  can be assigned to the  $\gamma\text{-Fe}_2\text{O}_3$  crystal structure (**Figure 4-1.1b-3**). In few parts, the frameworks are partially crystallized into the  $\gamma\text{-Fe}_2\text{O}_3$  phase. To investigate the surface areas of the synthesized PB, PB\_250, and PB\_400 in detail,  $\text{N}_2$  gas adsorption-desorption isotherms were measured. In comparison to the original PB sample ( $74 \text{ m}^2 \text{ g}^{-1}$ ) before calcination, both PB\_250 and PB\_400 samples show relatively high surface area ( $175 \text{ m}^2 \text{ g}^{-1}$  and  $228 \text{ m}^2 \text{ g}^{-1}$ , respectively).

It is well known that  $\gamma\text{-Fe}_2\text{O}_3$  shows a magnetic property, unlike  $\alpha\text{-Fe}_2\text{O}_3$ . As mentioned above, my PB-derived nanoporous Fe oxide is composed of an amorphous phase or small sized  $\gamma\text{-Fe}_2\text{O}_3$  crystals depending on the calcination conditions. Generally, such small ferromagnetic grains show a superparamagnetic behavior. However, not each grain shows a ferromagnetic state due to the thermal fluctuation of the magnetic moment at room temperature. From the magnetization curve (**Figure 4-1.1c**), no hysteresis could be observed, and both the coercive forces ( $H_c$ ) and the residual magnetization ( $M_r$ ) were nearly zero, which is a typical behavior for superparamagnetic materials. The saturation magnetization ( $M_s$ ) values measured at 10000 Oe are  $30.6 \text{ emu g}^{-1}$  (for PB\_400) and  $22.3 \text{ emu g}^{-1}$  (for PB\_250), respectively. This increase is attributed to an improved crystallization of  $\gamma\text{-Fe}_2\text{O}_3$  by increasing the calcination temperature. Due to these sufficient  $M_s$  values, the samples can be easily collected by a neodymium magnet (**inset in Figure 4-1.1c**).

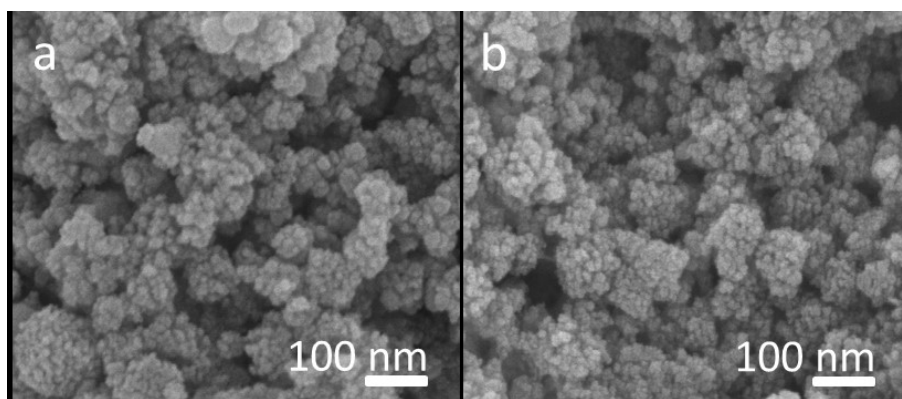


**Figure 4-1.2.** SEM images of PB-derived Fe oxide particles, a) PB\_250 and b) PB\_400, prepared using PB nanocubes aged at 80 °C for 15 hours.

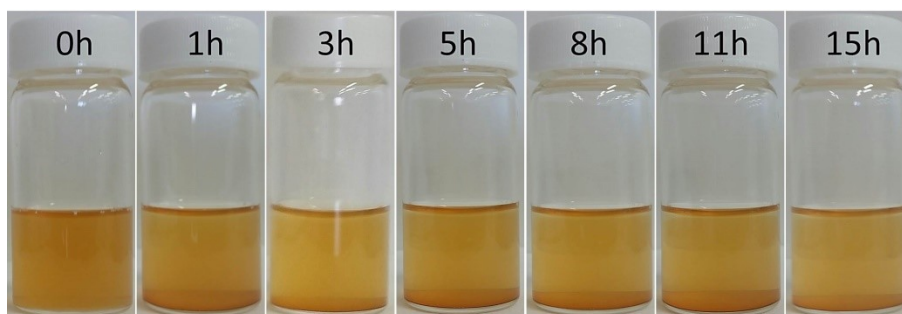


**Figure 4-1.3.** Photos of the synthesized iron oxides suspended in water for different times.

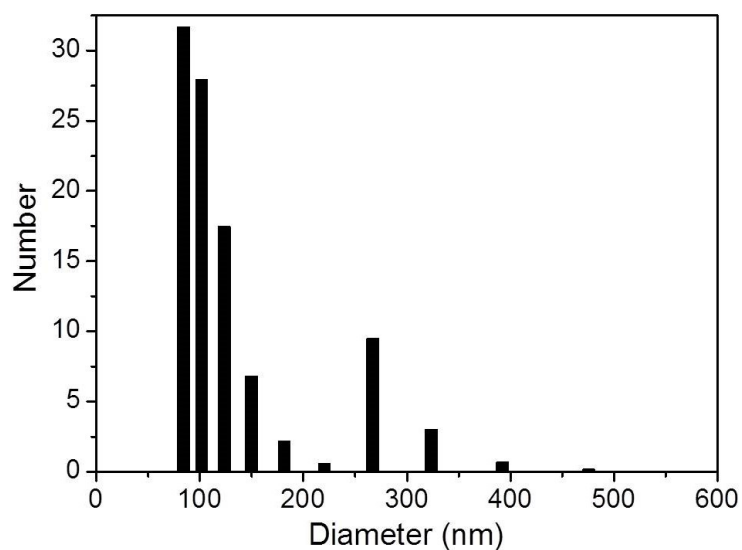


**Figure 4-1.4.** Hydrodynamic diameter of the synthesized iron oxides.

To show the potential of this material as a drug carrier, I investigated the ability of PB\_250 and

PB\_400 to trap guest molecules. **Figure 4-1.5a** represents the dynamic adsorption of methylene blue (MB) dye into the synthesized PB\_250 and PB\_400. Each sample (PB\_250 and PB\_400, 10 mg) was mixed with 50 mL of MB solution (0.02 M). The dye was separated from the adsorbent by centrifugation and the supernatant was taken out for UV/Vis measurements. The MB concentration was determined by measuring the absorbance at  $\lambda_{max} = 664$  nm. After measuring  $A_{max}$ , the concentration of MB was calculated using the Lambert-Beer law ( $A_{max} = \epsilon \times c \times l$ , where  $\epsilon = 74028 \text{ L mol}^{-1} \text{ cm}^{-1}$  and  $l = 1 \text{ cm}$ ). The MB amounts adsorbed into the PB\_250 and PB\_400 samples were calculated by subtracting the final solution concentration from the initial concentration of the dye solutions. The amount of the MB adsorbed into my samples,  $Q_e$  ( $\text{mg g}^{-1}$ ), was calculated from the following equation:

$$Q_e = (C_0 - C_e) \times V \times m^{-1} \quad (4-1.1)$$

Where;  $C_0$  is the initial MB concentration in the aqueous solution ( $\text{mg L}^{-1}$ ),  $C_e$  is the final MB concentration at equilibrium ( $\text{mg L}^{-1}$ ),  $V$  is the volume of MB solution (L), and  $m$  is the mass of adsorbent used (g). The adsorption process of MB into both samples was completed within about 1 h and the amount of adsorbed MB in PB\_400 was measured to be approximately twice higher than that adsorbed in PB\_250, reaching  $22.1 \text{ mg g}^{-1}$ . The difference in adsorption is due to the difference in surface area, as mentioned before.

The effect of the initial MB concentration on the adsorption behavior was also studied. **Figure 4-1.5b** shows the adsorption capacities depending on the initial MB concentrations. For each sample, 50 mL of MB solutions were mixed with 10 mg of particles, sonicated for 15 min, and then stirred for 4 h in the dark at room temperature. The dye was separated from the adsorbent by centrifugation and the supernatant was taken out for UV/Vis measurements at  $\lambda_{max} = 664$  nm for MB. The initial MB concentrations were set to be 0.8, 1.6, 3.2, 4.8, and  $6.4 \text{ mg L}^{-1}$ . From the plot of the adsorption capacity versus the MB concentration (**Figure 4-1.5b**), it is found



that, as the initial MB concentration increases, the adsorption efficiency also linearly increases.

My PB-derived nanoporous Fe oxides are expected to be utilized as an anticancer drug (*i.e.*, cisplatin) capsule for magnetic-guided chemotherapy of Bladder cancer cells (T24). The loading capacities and the release percentages were studied, as presented in **Figure 4-1.6**. For the loading test, the original PB and the synthesized PB\_250 sample (20 mg) were immersed into 4 mL of cisplatin aqueous solution ( $0.5 \text{ mg mL}^{-1}$ ) and the adsorption kinetics were studied (**Figure 4-1.6a**). The cisplatin concentration was determined by mixing the latter with an o-phenylenediamine solution in DMF ( $1.2 \text{ mg mL}^{-1}$ ) in a 1:1 volume ratio. After heating the mixture at  $100 \text{ }^\circ\text{C}$  for 10 min, the maximum absorbance was measured at 704 nm. The adsorption process was finished within 180 min, and the loading efficiencies were determined to be 100% for both PB and PB\_250. Such a rapid adsorption rate and high loading are attributed to the open nanoporous structure with a high surface area. The release test of cisplatin was then performed (**Figure 4-1.6b**). The cisplatin-loaded PB\_250 (Cis@PB\_250, 20 mg) was added to water (2 mL) and the release proceeded under stirring at room temperature. The release profile of cisplatin from Cis@PB\_250 was measured by UV/Vis measurements and was found to yield 17.1% and 32.2% of the initial load after 180 min for PB and PB\_250, respectively. The observed release profiles follow a pseudo-first order.

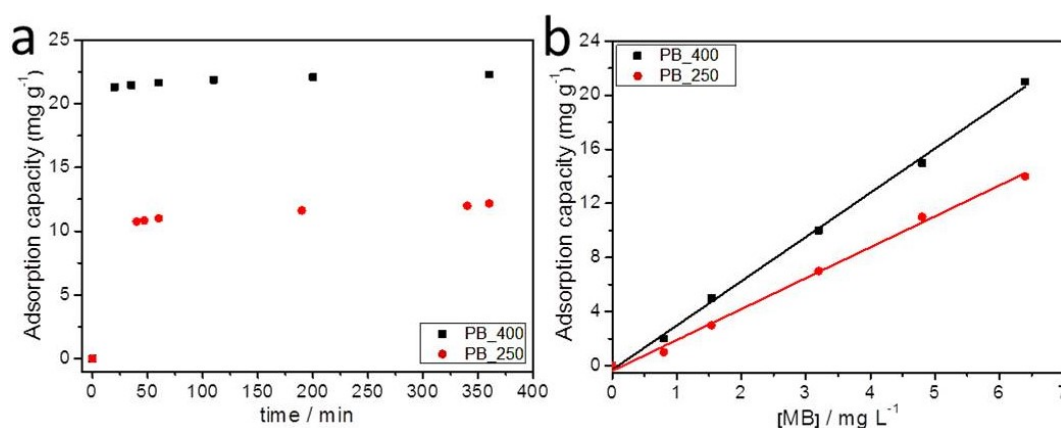


**Figure 4-1.5.** (a) Equilibrium adsorption capacities versus time of adsorption of MB dye and (b) the adsorption capacities versus the concentration of MB dye into the surface of SPB\_250 and

SPB\_400 samples.

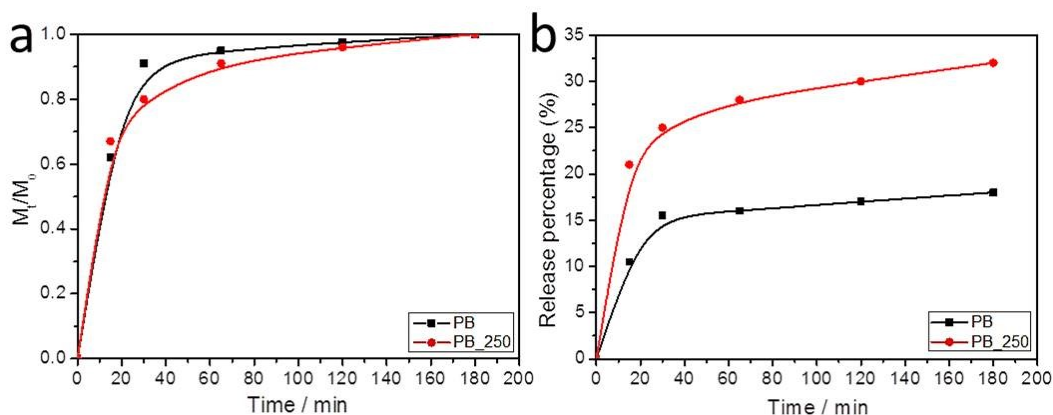


**Figure 4-1.6.** (a) The adsorption kinetics of cisplatin into PB and (b) measurement of the release profile of cisplatin from the cisplatin-loaded PB (Cis@PB).

The study of the biocompatibility of PB\_250 is critical for further medical application. The cytotoxicity of PB\_250 was examined by MTT assays of Bladder cancer cells (T24), as shown in **Figure 4-1.7a**. The cell images after uptake are shown in **Figure 4-1.8**. The results show that the cell viability is around 100%, even when the dosage of PBs was as high as  $800 \text{ mg mL}^{-1}$ , thus indicating an excellent biocompatibility. Such a high biocompatibility is very promising for intracellular applications. Furthermore, the cytotoxicity of Cis@PB\_250 was estimated by using the same cancer cells (**Figure 4-1.7c**). In contrast to PB\_250, the viability of the bladder cancer cells treated with Cis@PB\_250 decreased with increasing dosages, suggesting a dose-dependent effect. Cisplatin crosslinks with DNA through the displacement of its chloride anions with guanine of DNA. This crosslinking ability of cisplatin with DNA depends on the release of cisplatin from PB\_250. Thus, Cis@PB\_250 has good efficacy for the intercellular drug delivery in T24 cells.

In order to demonstrate the magnetic guiding ability of PB\_250, we cultured T-24 cells with and without a magnetic stone underneath the slide glass. After the addition of Cis@PB\_250 to the T-24 cells for 4 h, the cells were washed to remove the dead cells. The cell nuclei were then stained with the blue fluorescent dye DAPI. DAPI can bind strongly to the AT-rich regions in

DNA and can stain cell nuclei [32,33]. When no magnetic guiding is applied, many healthy cells are distributed all over the observation area (**Figure 4-1.7b**), while magnetic guiding leads to a clear boundary between the bright stains and the dark field (**Figure 4-1.7d**), indicating that most of the cells located inside the magnetic field died while the cells located outside were kept alive after the treatment with Cis@PB\_250.

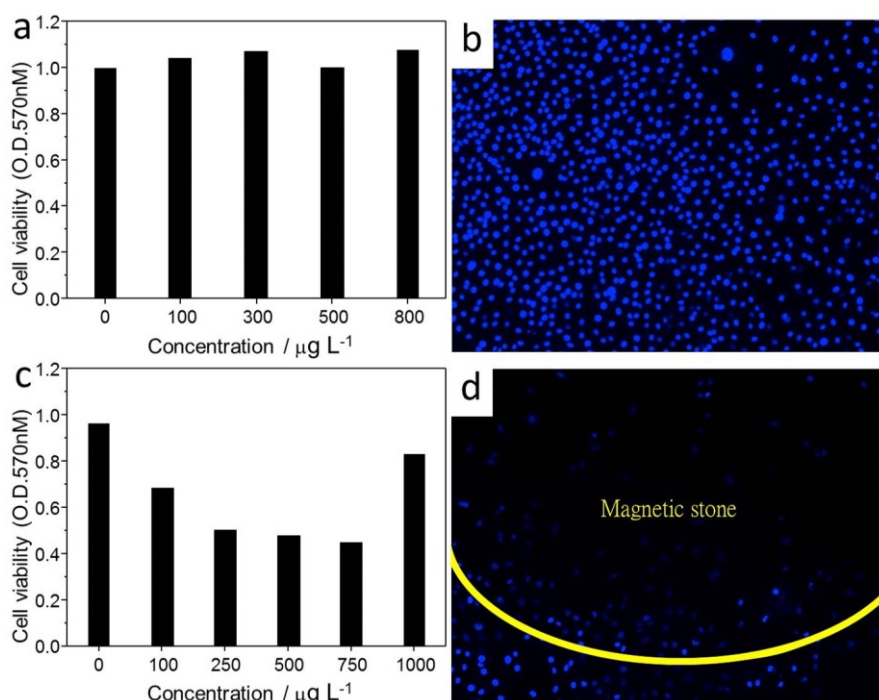


**Figure 4-1.7.** (a and c) MTT assays of (a) PB\_250 and (c) Cis@PB\_250 and (b and d) cell imaging of PB\_250 without (b) and with (d) a magnetic stone, respectively.

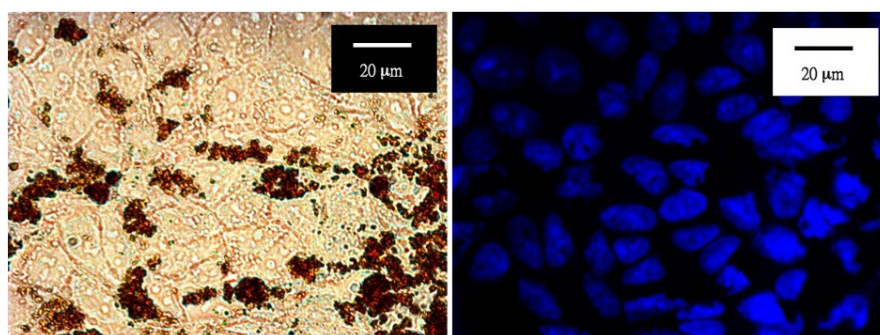


**Figure 4-1.8.** Fluorescent images of cells after uptake of cisplatin-loaded iron oxide nanoparticles for 24 hours. (Left) Transmission mode and (right) DAPI mode. The cell nuclei were stained with the fluorescent dye DAPI so they show blue fluorescence. The dark brown spots indicate the positions of cisplatin-loaded iron oxide nanoparticles.

In addition, the cancer cell-killing ability of Cis@PB\_250 was superior than that of free cisplatin (**Figure 4-1.9**). The drug loaded magnetic nanoparticles can be guided to a specific position by external magnetic guiding. Compared with the passive accumulation by the enhanced permeability and retention (EPR) effect, magnetic guiding provides the advantage of a fast and accurate accumulation of magnetic nanoparticles at a desired location. This property can reduce the leakage of drug during the circulation which would otherwise lead to unnecessary hazardous effects on the health of the cells [34]. Fuchigami *et al.* used doxorubicin-loaded FePt nanoparticles to treat gastric cancer cells with magnetic guiding [35]. They reported that 70% of the cancer cells died during 15 min of guiding, whereas 0% died when no magnetic guiding was used. Bladder cancers affecting most of the patients belong to the category of non-muscle-invasive bladder cancer (NMIBC) [36]. The standard treatment for NMIBC is a transurethral resection followed by an intravesical therapy [37]. In these cases, the magnetic guiding of magnetic and drug-containing nanoparticles can greatly enhance the delivery efficacy [38,39].

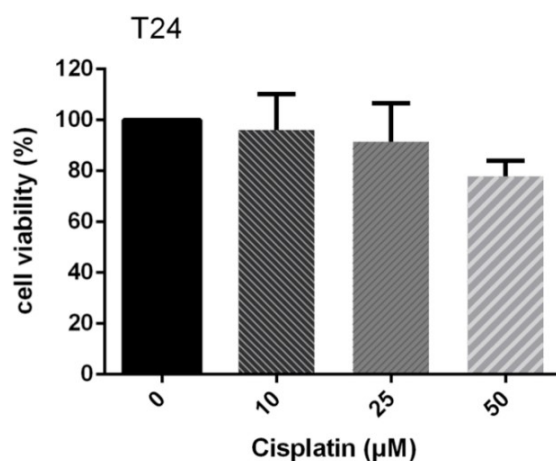


**Figure 4-1.9.** MTT assay of T-24 cancer cells treated with free cisplatin.

## 4-1.4. Conclusion

I established a facile route to prepare nanoporous iron oxides with a high content of amorphous  $\gamma$ -Fe<sub>2</sub>O<sub>3</sub> phase by thermal decomposition of PB nanocubes in air. The obtained oxides showed a high adsorption capacity toward the dye MB attributed to their large surface area and have a super paramagnetic behavior. The PB-derived nanoporous Fe oxides are highly biocompatible and consequently can be utilized as anticancer drug (*i.e.*, cisplatin) capsules for the chemotherapy of Bladder cancer cells (T24). The use of PB as the starting material is a new and unique technology, and further use of various PB analogues with different compositions will produce more functional materials in the future.

## 4-1.5. Acknowledgements

Mohamed B. Zakaria thanks the Culture Affairs & Missions Sector of the Ministry of Higher Education in Egypt for the financial support. K. C.-W. Wu acknowledges the financial support from the Ministry of Science and Technology (MOST), Taiwan (101-2628-E-002-015-MY3), National Taiwan University (102R7842 and 102R7740), Center of Strategic Materials Alliance for Research and Technology (SMART Center), National Taiwan University (102R104100), and National Health Research Institutes of Taiwan (03A1-BNMP14-014).

## 4-1.6. References

- [1] Y.A. Luqmani, *Med. Princ. Pract.* **2005**, *14*, 35-48.
- [2] G. Szakács, J.K. Paterson, J.A. Ludwig, C. Booth-Genthe, M.M. Gottesman, *Nat. Rev. Drug Discovery* **2006**, *5*, 219-234.

- [3] L.S. Jabr-Milane, L.E. van Vlerken, S. Yadav, M.M. Amiji, *Cancer Treat Rev.* **2008**, *34*, 592-602.
- [4] M. Ferrari, *Nat. Rev. Cancer* **2005**, *5*, 161-171.
- [5] C. Mamot, D.C. Drummond, K. Hong, D.B. Kirpotin, J.W. Park, *Drug Resist. Updates* **2003**, *6*, 271-279.
- [6] Y.-H. Lin, H.-F. Liang, C.-K. Chung, M.-C. Chen, H.-W. Sung, *Biomaterials* **2005**, *26*, 2105-2113.
- [7] F. Kratz, *J. Control. Release* **2008**, *132*, 171-183.
- [8] S. Dhar, F.X. Gu, R. Langer, O.C. Farokhzad, S.J. Lippard, *Proc. Natl. Acad. Sci. USA* **2008**, *105*, 17356-17361.
- [9] I.I. Slowing, J.L. Vivero-Escoto, C.-W. Wu, V. S.-Y. Lin, *Adv. Drug Delivery Rev.* **2008**, *60*, 1278-1288.
- [10] C.Y. Lai, B.G. Trewyn, D.M. Jeftinija, K. Jeftinija, S. Xu, S. Jeftinija, V. S.-Y. Lin, *J. Am. Chem. Soc.* **2003**, *125*, 4451-4459.
- [11] A.K. Gupta, M. Gupta, *Biomaterials* **2005**, *26*, 3995-4021.
- [12] X. Huang, I.H. El-Sayed, W. Qian, M.A. El-Sayed, *J. Am. Chem. Soc.* **2006**, *128*, 2115-2120.
- [13] Y. Cheng, A.C. Samia, J.D. Meyers, I. Panagopoulos, B. Fei, C. Burda, *J. Am. Chem. Soc.* **2008**, *130*, 10643-10647.
- [14] Y. Yoshizawa, Y. Kono, K.-i. Ogawara, T. Kimura, K. Higaki, *Int. J. Pharm.* **2011**, *412*, 132-141.
- [15] J. Sudimack, R.J. Lee, *Adv. Drug Delivery Rev.* **2000**, *41*, 147-162.
- [16] Z.M. Qian, H. Li, H. Sun, K. Ho, *Pharmacol. Rev.* **2002**, *54*, 561-587.
- [17] X. Gao, Y. Cui, R.M. Levenson, L.W.K. Chung, S. Nie, *Nat. Biotechnol.* **2004**, *22*, 969-976.

- [18] L. Cheng, K. Yang, Y. Li, X. Zeng, M. Shao, S.-T. Lee, Z. Liu, *Biomaterials* **2012**, *33*, 2215-2222.
- [19] S. Jiang, K.Y. Win, S. Liu, C.P. Teng, Y. Zheng, M.-Y. Han, *Nanoscale* **2013**, *5*, 3127-3148.
- [20] Y. Namiki, T. Namiki, H. Yoshida, Y. Ishii, A. Tsubota, S. Koido, K. Nariai, M. Mitsunaga, S. Yanagisawa, H. Kashiwagi, Y. Mabashi, Y. Yumoto, S. Hoshina, K. Fujise, N. Tada, *Nat. Nanotechnol.* **2009**, *4*, 598-606.
- [21] R. Mejías, S. Pérez-Yaguee, L. Gutiérrez, L.I. Cabrera, R. Spada, P. Acedo, C.J. Serna, F.J. Lázaro, Á. Villanueva, M. del Puerto Morales, D.F. Barber, *Biomaterials* **2011**, *32*, 2938-2952.
- [22] J. Kim, J.E. Lee, S.H. Lee, J.H. Yu, J.H. Lee, T.G. Park, T. Hyeon, *Adv. Mater.* **2008**, *20*, 478-483.
- [23] S. Bureekaew, S. Shimomura, S. Kitagawa, *Sci. Technol. Adv. Mater.* **2008**, *9*, 014108.
- [24] W. Lin, W.J. Rieter, K.M.L. Taylor, *Angew. Chem. Int. Ed.* **2009**, *48*, 650-658.
- [25] H. Ming, N.L.K. Torad, Y.-D. Chiang, K. C.-W. Wu, Y. Yamauchi, *CrystEngComm.* **2012**, *14*, 3387-3396.
- [26] N.L. Torad, M. Hu, M. Imura, M. Naito, Y. Yamauchi, *J. Mater. Chem.* **2012**, *22*, 18261-18267.
- [27] M. Hu, S. Furukawa, R. Ohtani, H. Sukegawa, Y. Nemoto, J. Reboul, S. Kitagawa, Y. Yamauchi, *Angew. Chem. Int. Ed.* **2012**, *51*, 984-988; *Angew. Chem.* **2012**, *124*, 1008-1012.
- [28] X. Roy, J. K.-H. Hui, M. Rabnawaz, G. Liu, M.J. MacLachlan, *J. Am. Chem. Soc.* **2011**, *133*, 8420-8423.
- [29] M. Taguchi, K. Yamada, K. Suzuki, O. Sato, Y. Einaga, *Chem. Mater.* **2005**, *17*, 4554-4559.
- [30] M.B. Zakaria, M. Hu, N. Hayashi, Y. Tsujimoto, S. Ishihara, M. Imura, N. Suzuki, Y.-Y. Huang, Y. Sakka, K. Ariga, K. C.-W. Wu, Y. Yamauchi, *Eur. J. Inorg. Chem.* **2014**,

1137-1141.

- [31] M. Hu, A.A. Belik, M. Imura, K. Mibu, Y. Tsujimoto, Y. Yamauchi, *Chem. Mater.* **2012**, *24*, 2698-2707.
- [32] J. Kapuscinski, *Biotech. Histochem.* **1995**, *70*, 220-233.
- [33] Y. Hirota, Y. Akiyama, Y. Izumi, S. Nishijima, *Physica C* **2009**, *469*, 1853-1856.
- [34] J.D.G. Durán, J.L. Arias, V. Gallardo, A.V. Delgado, *J. Pharm. sci.* **2008**, *97*, 2948-2983.
- [35] T. Fuchigami, R. Kawamura, Y. Kitamoto, M. Nakagawa, Y. Namiki, *Biomaterials* **2012**, *33*, 1682-1687.
- [36] A.V. van Lingen, J.A. Witjes, *Expert Opin. Biol. Ther.* **2013**, *13*, 1371-1385.
- [37] M. Babjuk, M. Burger, R. Zigeuner, S.F. Shariat, B.W.G. van Rhijn, E. Compérat, R.J. Sylvester, E. Kaasinen, A. Böhle, J.P. Redorta, M. Rouprêt, *Eur. Urol.* **2013**, *64*, 639-653.
- [38] Z. Li, S. Yin, L. Cheng, K. Yang, Y. Li, Z. Liu, *Adv. Funct. Mater.* **2014**, *24*, 2312-2321.
- [39] Z. Li, C. Wang, L. Cheng, H. Gong, S. Yin, Q. Gong, Y. Li, Z. Liu, *Biomaterials* **2013**, *34*, 9160-9170.



## Chapter 4-2

### 4-2. Thermal Conversion of Hollow Prussian Blue Nanoparticles into Nanoporous Iron Oxides with Crystallized Hematite Phase

#### 4-2.1. Introduction

Various inorganic nanoporous materials have been drawing intense research interest not only for their unique structural, optical, and surface properties, but also for their broad range of applications such as catalyst, drug delivery, and chemical storage. Among these materials, iron oxides are potentially useful for catalysts [1] and lithium ion batteries [2]. Iron oxides can exhibit several crystal structures, including wüstite (FeO), magnetite (Fe<sub>3</sub>O<sub>4</sub>), maghemite ( $\gamma$ -Fe<sub>2</sub>O<sub>3</sub>), cubic ( $\beta$ -Fe<sub>2</sub>O<sub>3</sub>), hematite ( $\alpha$ -Fe<sub>2</sub>O<sub>3</sub>), and orthorhombic ( $\epsilon$ -Fe<sub>2</sub>O<sub>3</sub>). In particular, the interest in hematite ( $\alpha$ -Fe<sub>2</sub>O<sub>3</sub>) has recently increased, due to the unique optical and magnetic behavior, high catalytic activity, suitable band gap, and low toxicity.

Developing new routes for preparation of nanoporous  $\alpha$ -Fe<sub>2</sub>O<sub>3</sub> and investigating their distinct properties are of considerable interest. In a recent study,  $\alpha$ -Fe<sub>2</sub>O<sub>3</sub> hollow spheres with sheet-like subunits were synthesized by a facile quasiemulsion-templated method, in which

glycerol was dispersed in water to form oil-in-water quasiemulsion microdroplets [3]. Porous  $\alpha$ -Fe<sub>2</sub>O<sub>3</sub> nanorods with diameters of 30-60 nm were also synthesized through thermal decomposition of FeC<sub>2</sub>O<sub>4</sub>·2H<sub>2</sub>O nanorods prepared by a poly (vinyl alcohol)-assisted precipitation process. Compared to commercial submicrometer-sized  $\alpha$ -Fe<sub>2</sub>O<sub>3</sub> powders, the porous  $\alpha$ -Fe<sub>2</sub>O<sub>3</sub> nanorods exhibited significantly enhanced capability as an electrode material for lithium-ion batteries [4]. As another example, 3D flowerlike iron oxide showed an excellent ability to remove heavy-metal ions and other pollutants in water treatment [5]. Thus, nanoporous  $\alpha$ -Fe<sub>2</sub>O<sub>3</sub> materials with high surface areas have exhibited very interesting properties, which are not attainable by bulk  $\alpha$ -Fe<sub>2</sub>O<sub>3</sub> without nanopores. **Table 4-2.1** summarizes the structural parameters of various nanoporous  $\alpha$ -Fe<sub>2</sub>O<sub>3</sub> previously reported [6-21].

Recently, synthesis of hollow Prussian Blue (PB) coordination polymers by chemical etching was demonstrated [22] and their thermal conversion to nanoporous iron oxide particles as well is reported [23]. PB coordination polymer, in which iron ions are bridged by cyano groups (–Fe<sup>(II)</sup>–CN–Fe<sup>(III)</sup>–), is considered a potential precursor for nanoporous iron oxides with high surface areas, because the iron component can be oxidized and the organic components can be removed by calcination in air. This approach is simple and convenient, which is useful for further preparation of several iron oxides with different crystalline degrees and structures. Herein, I extend this concept to synthesize nanoporous iron oxides with  $\alpha$ -Fe<sub>2</sub>O<sub>3</sub> phase. The obtained samples were carefully characterized with scanning electron microscopy (SEM), wide-angle X-ray diffraction (XRD), nitrogen gas adsorption-desorption isotherms, transmission electron microscopy (TEM), and Mössbauer spectroscopy.

## 4-2.2. Experimental Details

### 4-2.2.1. Preparation of Hollow PB Nanoparticles

According to the previous papers [22-23], PVP (K30, 3.0 g) and  $K_3[Fe(CN)_6] \cdot 3H_2O$  (132 mg) were added to 0.01 M HCl solution (40.0 mL) under magnetic stirring. After 30 min of stirring, a clear solution was obtained. The vial was then placed into an electric oven and heated at 80 °C for 20 h. After aging, the precipitates were collected by centrifugation and washed several times in distilled water and ethanol. After drying at room temperature for 12 h, PB nanocubes of approximately 100 nm in particle size were obtained. For creation of a hollow cavity, PB nanocubes (40.0 mg) and PVP (200 mg) were added to 1.0 M HCl solution (40 mL) in a Teflon vessel under magnetic stirring. After 2 h, the vessel was transferred into a stainless autoclave and heated at 140 °C for 4 h in an electric oven. After aging, the precipitates were collected by centrifugation and washed in distilled water and ethanol several times. After drying at room temperature for 12 h, hollow PB nanocubes were obtained.

**Table 4-2.1** Summary of nanostructured  $\alpha$ -Fe<sub>2</sub>O<sub>3</sub> materials previously reported.

Shape	Fe source	Surface area (m <sup>2</sup> ·g <sup>-1</sup> )	Ref.
Hollow spheres	FeSO <sub>4</sub> ·7H <sub>2</sub> O	103	[3]
Porous nanorods	FeC <sub>2</sub> O <sub>4</sub> ·2H <sub>2</sub> O	11.8	[4]
3D flowerlike	FeCl <sub>3</sub> ·6H <sub>2</sub> O	40.0	[5]
Porous nanorods	FeCl <sub>3</sub> ·6H <sub>2</sub> O	---	[6]
Spherical nanoparticles	FeC <sub>2</sub> O <sub>4</sub> ·2H <sub>2</sub> O	---	[7]
Mesoporous films	FeCl <sub>3</sub>	---	[8]
Flute-like porous nanorods	β-FeOOH	125	[9]
3D urchin-like superstructures	FeSO <sub>4</sub> ·7H <sub>2</sub> O	86.8	[10]
Mesoporous nanorods	Fe(NO <sub>3</sub> ) <sub>3</sub> ·9H <sub>2</sub> O	105	[11]
Mesoporous nanorods	α-FeC <sub>2</sub> O <sub>4</sub>	125	[12]
Porous nanoparticles	FeCl <sub>3</sub>	22.3	[13]
Porous nanorods	FeCl <sub>3</sub> ·6H <sub>2</sub> O	82.6	[14]
Spindle-like nanostructures	Fe(NO <sub>3</sub> ) <sub>3</sub> ·9H <sub>2</sub> O	66.8	[14]
Mesoporous thin films	Fe(NO <sub>3</sub> ) <sub>3</sub> ·9H <sub>2</sub> O	190	[15]
Mesoporous nanospheres	FeCl <sub>3</sub>	18.2	[16]

Hollow-structured particles	$\text{FeCl}_3 \cdot 6\text{H}_2\text{O}$	---	[17]
Nanotube	$\text{Fe}(\text{NO}_3)_3 \cdot 9\text{H}_2\text{O}$	---	[18]
Hollow microsphere	$\text{FeCl}_3 \cdot 7\text{H}_2\text{O}$	---	[19]
Hollow sphere	Ferric potassium oxalate	41.1	[20]
Mesoporous particle	$\text{FeCl}_3$	335	[21]

#### 4-2.2.2. Characterization.

SEM images were taken with a Hitachi SU8000 scanning microscope at an accelerating voltage of 5 kV. TEM observation was performed using a JEM-2100F TEM system that was operated at 200 kV and equipped for energy-dispersive spectrometer analysis. Wide-angle powder X-ray diffraction (XRD) patterns were obtained with a Rigaku RINT 2500X diffractometer using monochromated  $\text{Cu-K}\alpha$  radiation (40 kV, 40 mA) at a scanning rate of  $2^\circ \text{ min}^{-1}$ .  $\text{N}_2$  adsorption-desorption isotherms were measured on a high precision adsorption measuring apparatus BELSORP-mini (BEL Japan) and quanta chrome Autosorb1 Automated Gas Sorption System. Prior to the measurements, the samples were degassed in vacuum. The surface areas were calculated by BET method using the adsorption branches of the isotherm.  $^{57}\text{Fe}$  Mössbauer spectra were recorded at room temperature in transmission geometry using a  $^{57}\text{Co/Rh}$   $\gamma$ -ray source. The source velocity was calibrated using  $\alpha$ -Fe as a reference material. TG-DTA-MS was measured with a Rigaku Thermo Mass Photo TG-DTA-PIMS 410/S. The detection range of the MS was from 1 to 250 m/z. The sample and  $\alpha$ - $\text{Al}_2\text{O}_3$  standard were separately loaded inside platinum pans, and heated from room temperature to 1000 °C at  $10^\circ \text{C min}^{-1}$  under  $\text{He/O}_2$  flow to analyze the mass spectrometry of thermally produced compounds.

### 4-2.3. Results and Discussion

For the creation of the hollow cavity, the synthesized PB particles (**Figure 4-2.1a**) were treated

with 1.0 M HCl solution in the presence of PVP. The PVP polymer was on the external surface of the PB particles and thus could serve as a protecting agent during the HCl etching process [22]. Even after the etching, the average diameter of the PB particles was not changed (around 100 nm), and the corresponding particle size distribution was very narrow, as shown in **Figure 4-2.1b**. The diameter of the internal cavity was calculated to be around 80 nm. To prepare nanoporous iron oxides with hematite ( $\alpha$ -Fe<sub>2</sub>O<sub>3</sub>) phase, I further calcined the hollow PB particles at 400 °C for different time durations (4, 5, 6, and 7 h). The samples were heated inside an electric furnace from room temperature to 400 °C at a heating rate of 1 °C min<sup>-1</sup>. After that, the powder was allowed to cool inside the furnace. Finally, the obtained powders were collected for further characterization. The entire calcination process was performed in air.

The morphology of the calcined samples was observed by scanning electron microscopy (SEM), as shown in **Figure 4-2.1c-f**. After calcination at 400 °C for 5 h, the surface structure of hollow particles obviously changed due to the crystallization of the PB shell to iron oxide (**Figure 4-2.1d**). With further increase in the calcination time to 6 and 7 h (**Figure 4-2.1e-f**), the hollow structure completely collapsed. In the starting PB crystals, the Fe atoms were stabilized by cyano bridges. Upon calcination at high temperatures under air flow, the C–N bridges can be removed to form Fe oxides. After the calcination, no carbon content was confirmed in the final product. The result of TG-DTA-MS under He/O<sub>2</sub> flow (Volume ratio: 80/20, Flow rate: 200 ml min<sup>-1</sup>) indicated several exothermic peaks at around 260-310 and 470 °C, accompanied with the production of CO<sub>2</sub> and/or N<sub>2</sub>O ( $m/z = 44$ ) as well as N<sub>2</sub> and/or CO ( $m/z = m/z$ ), which is typical for the combustion reaction of CN-containing material. Emission of adsorbed H<sub>2</sub>O ( $m/z = 18$ ) was also detected. Molecules with masses larger than  $m/z = 50$  were not detected by TG-DTA-MS up to 1000 °C.

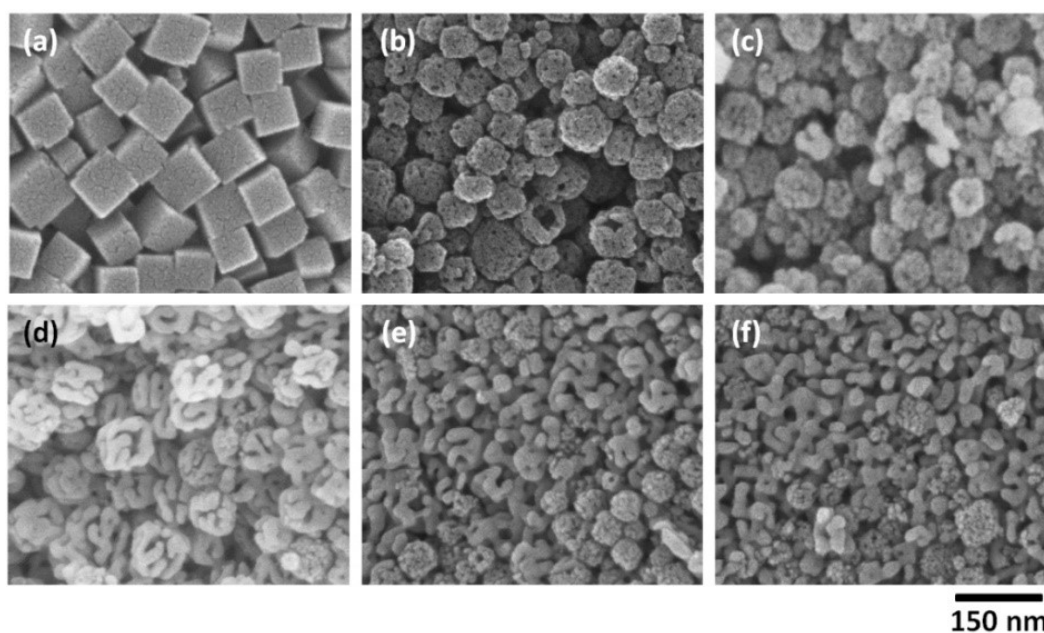


**Figure 4-2.1.** SEM images of (a) PB nanoparticles before chemical etching, (b) PB nanoparticles after chemical etching, and samples calcined for (c) 4, (d) 5, (e) 6, and (f) 7 h.

To investigate the effect of calcination time on the crystalline phases and degrees, I performed wide-angle XRD measurement, as shown in **Figure 4-2.2**. With the increase in calcination time, the intensities of  $\alpha$ - $\text{Fe}_2\text{O}_3$  phase peaks gradually increased, indicating the enhancement of crystal growth. The crystalline sizes were calculated by using the Scherrer equation. The average sizes were varied from around 12.2 nm (for 4 h), 15.4 nm (for 5 h), 17.1 nm (for 6 h), to 17.1 nm (for 7 h). Thus, the increase of calcination time promoted the crystallization of  $\alpha$ - $\text{Fe}_2\text{O}_3$ , thereby leading to collapse of the original hollow structure. As clearly seen in **Figure 4-2.1e-f**, the formation of large-sized nanopores was caused by the gradual crystallization of iron oxides.

To further understand the crystalline structure, we collected  $^{57}\text{Fe}$  Mössbauer spectra from the calcined PB samples for 5 and 7 h, as shown in **Figure 4-2.3**. The spectral data could be well resolved into a sextet peak and a doublet peak with a peak-area ratio of 0.3:0.7, respectively. On the basis of the obtained Mössbauer parameters listed in **Table 4-2.2**, the former is assigned as  $\alpha$ - $\text{Fe}_2\text{O}_3$ . The latter exhibits an isomer shift characteristic of  $\text{Fe}^{\text{III}}$ , which was caused by the

presence of impurities such as amorphous iron oxide and/or  $\gamma\text{-Fe}_2\text{O}_3$  phases. Increasing the calcination time up to 7 h significantly improved the quality and volume fraction of  $\alpha\text{-Fe}_2\text{O}_3$  to 65 % (Table 4-2.2 and Figure 4-2.3b). This is in good agreement with the XRD data below (Figure 4-2.2).

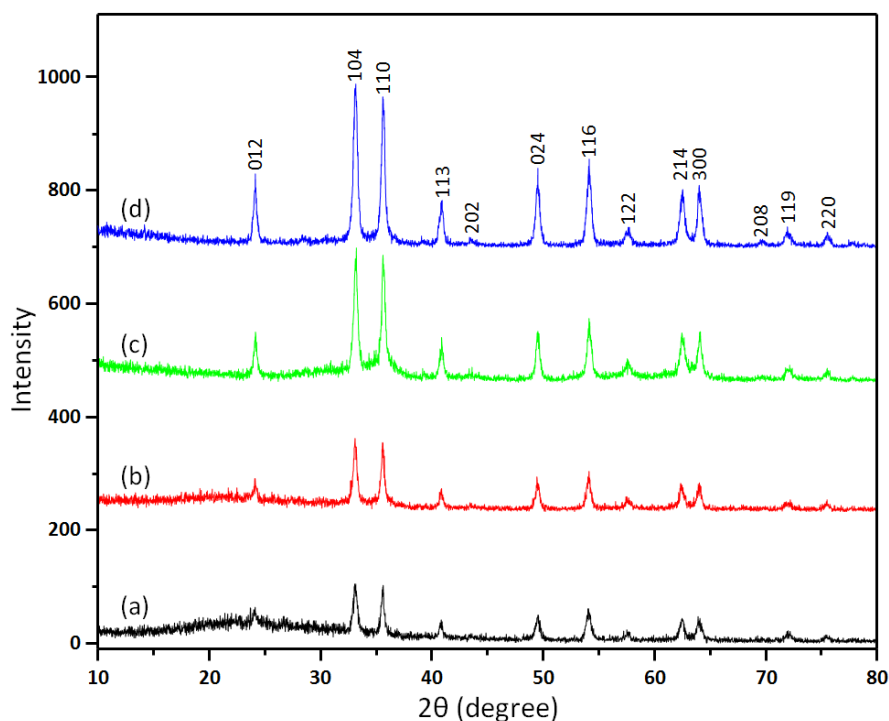


**Figure 4-2.2.** Wide-angle XRD profiles for samples calcined for (a) 4, (b) 5, (c) 6, and (d) 7 h.

The hollow structure of the starting hollow PB particles and the crystalline structure of the calcined iron oxide samples were examined by transmission electron microscopy (TEM), as shown in Figure 4-2.4. Solid PB nanocubes were transformed into hollow cubes after chemical etching (Figure 4-2.4a). The calcined sample for 5 h showed similar morphology to that of the original hollow PB particles with similar particle sizes (Figure 4-2.4b). The hollow structure was well retained even after the crystallization of iron oxides. Selected-area electron diffraction (ED) showed very intense spots assignable to  $\alpha\text{-Fe}_2\text{O}_3$ , indicating the formation of a highly crystallized  $\alpha\text{-Fe}_2\text{O}_3$  phase. Because several  $\alpha\text{-Fe}_2\text{O}_3$  crystals were randomly oriented in different directions,

several patterns were mixed with each other. From a high-resolution TEM image, clear lattice fringes were oriented in the same direction at the edge of the cube, which confirmed the formation of  $\alpha$ -Fe<sub>2</sub>O<sub>3</sub> crystalline phase (**Figure 4-2.5a**). The surface area and pore volume were calculated to be 163 m<sup>2</sup> g<sup>-1</sup> and 0.89 cm<sup>3</sup> g<sup>-1</sup>, respectively, from the corresponding N<sub>2</sub> adsorption-desorption isotherm. These values were much lower than those of the calcined sample for 4 h (480 m<sup>2</sup> g<sup>-1</sup> and 1.5 cm<sup>3</sup> g<sup>-1</sup>, respectively) [23].

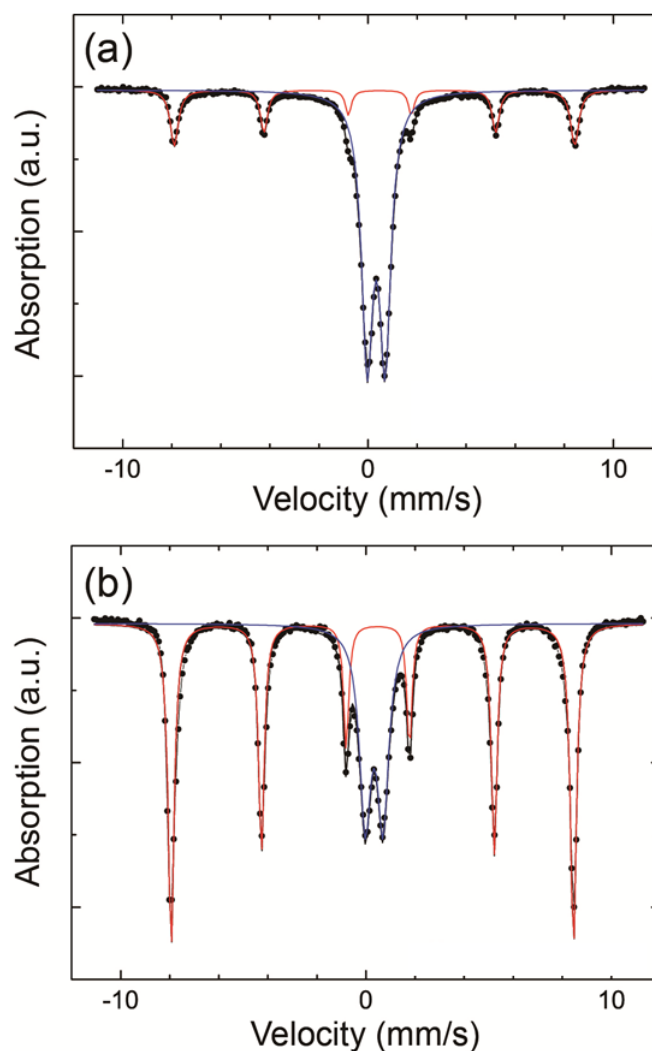


**Figure 4-2.3.** <sup>57</sup>Fe Mössbauer spectra collected at room temperature from calcined samples for (a) 5 and (b) 7 h. Red and blue lines represent the contributions from  $\alpha$ -Fe<sub>2</sub>O<sub>3</sub> and some impurity phases (amorphous and/or  $\gamma$ -Fe<sub>2</sub>O<sub>3</sub>).



**Table 4-2.2** Mössbauer parameters of calcined samples for 5 and 7 h.

Calcination time [h]	Isomer shift [ $\text{mm}\cdot\text{s}^{-1}$ ]	Hyperfine field [kOe]	Quadrupole splitting [ $\text{mm}\cdot\text{s}^{-1}$ ]	FWHM [ $\text{mm}\cdot\text{s}^{-1}$ ]	Peak area [%]	Phase
5	0.374	505.5	-0.21 <sup>[b]</sup>	0.34	23	$\alpha\text{-Fe}_2\text{O}_3$
5	0.335	0	0.73	0.56	76	
7	0.372	505.8	-0.22 <sup>[b]</sup>	0.28	64	$\alpha\text{-Fe}_2\text{O}_3$
7	0.334	0	0.729	0.57	35	

In contrast, long calcination times of 7 h destroyed the original hollow structures (**Figures 4-2.4c**). However, a continuous nanoporous structure derived from the original hollow structure was well developed. The surface areas and pore volumes were calculated to be  $100 \text{ m}^2 \text{ g}^{-1}$  and  $0.50 \text{ cm}^3 \text{ g}^{-1}$  (for 6 h), and  $70.0 \text{ m}^2 \text{ g}^{-1}$  and  $0.41 \text{ cm}^3 \text{ g}^{-1}$  (for 7 h), respectively. Although longer calcination time decreased the surface areas of the samples upon the crystallization of  $\alpha\text{-Fe}_2\text{O}_3$ , these values are relatively high compared to those of other nanostructured  $\alpha\text{-Fe}_2\text{O}_3$  previously reported (**Table 4-2.1**).

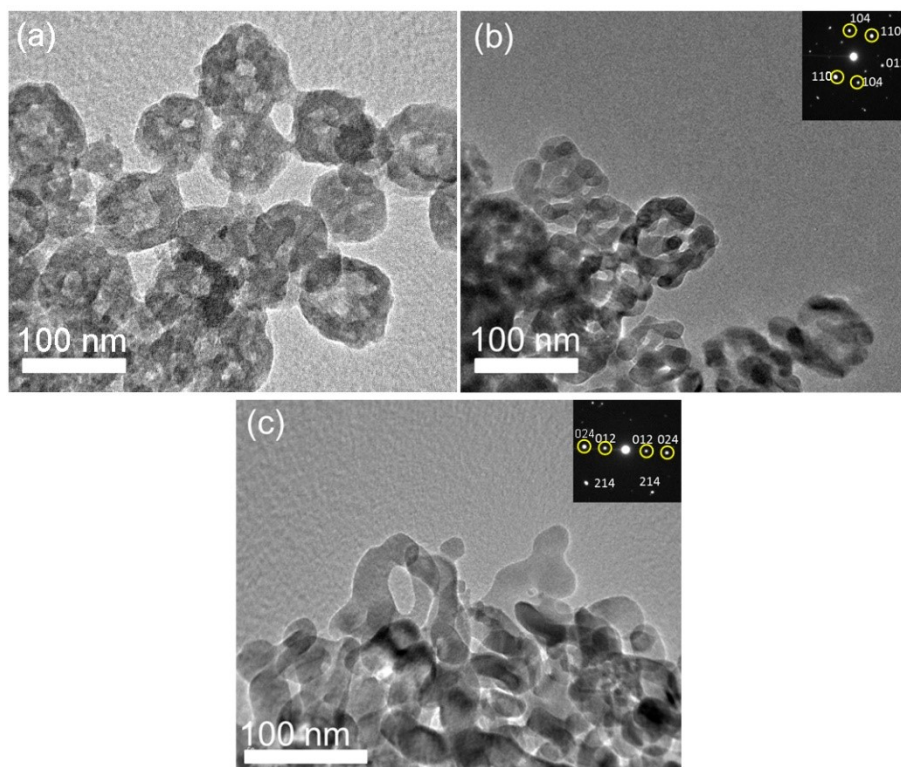


**Figure 4-2.4.** TEM images and the corresponding ED patterns of (a) PB nanoparticles after chemical etching, and (b-c) calcined samples for (b) 5 and (c) 7 h.

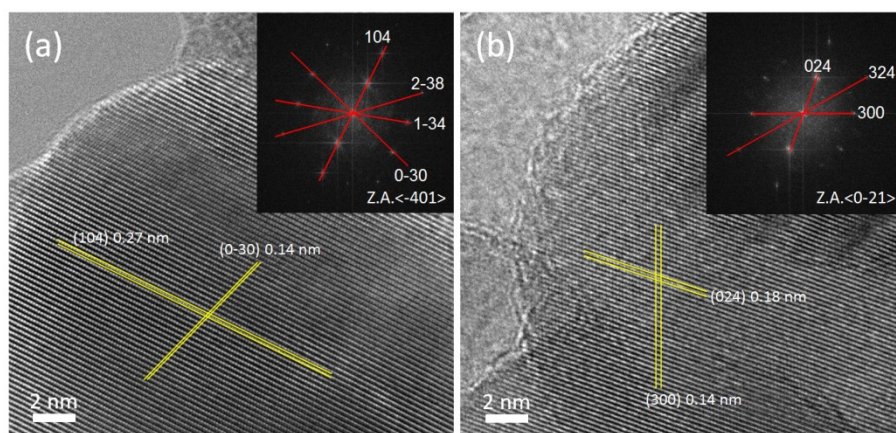


**Figure 4-2.5.** High resolution TEM images and corresponding Fast Fourier Transform (FFT) images of calcined samples for (a) 5 and (b) 7 h.

My porous iron oxides with  $\alpha$ - $\text{Fe}_2\text{O}_3$  phase are useful as a photocatalyst. To investigate the photocatalytic activity, 5.0 mg of the photocatalyst (several iron oxide samples calcined for 5, 6, and 7 h) was mixed with 15 ml of methylene blue (MB, 0.01 mM, 15 mL), and then sonicated in a cool water bath for 5 min. Afterward, the suspension was magnetically stirred in dark for 4 h to reach the complete adsorption-desorption equilibrium, followed by the addition of hydrogen peroxide solution (30 wt. %, 0.2 mL), then the bottle was exposed to UV light irradiation at room temperature.

The time-dependent UV/Vis absorption spectra in the absence and presence of iron oxides are shown in **Figure 4-2.6**. The remaining MB concentration was analyzed by measuring the peak intensity derived from MB at 664 nm. With increasing the irradiation time, the maximum absorption intensity gradually decreased, suggesting the decolorization and decomposition of MB molecules (**Figure 4-2.6**). In a control experimental without the photocatalyst, the decomposition rate under UV light was very slow. In the presence of the photocatalyst, the decomposition rate was significantly increased. With the increase of the hematite ( $\alpha$ - $\text{Fe}_2\text{O}_3$ ) content (*i.e.*, with the increase of the calcination time), the decomposition rate of MB molecules was increased (**Figure 4-2.7**). The sample calcined for 7 h exhibited the highest

decomposition rate compared to the others, due to high content of crystallized hematite phase ( $\alpha\text{-Fe}_2\text{O}_3$ ), which was confirmed by Mössbauer spectra (**Figure 4-2.3**). The suggested mechanism of the dye decomposition occurs on the photocatalyst surface rather than the bulk solution. Some electrons generated on the surface under UV light are directly trapped by  $\text{H}_2\text{O}_2$  to form  $\text{OH}^\cdot$  radicals. As a result, the  $\text{OH}^\cdot$  radicals lead to the photocatalytic reaction [24].

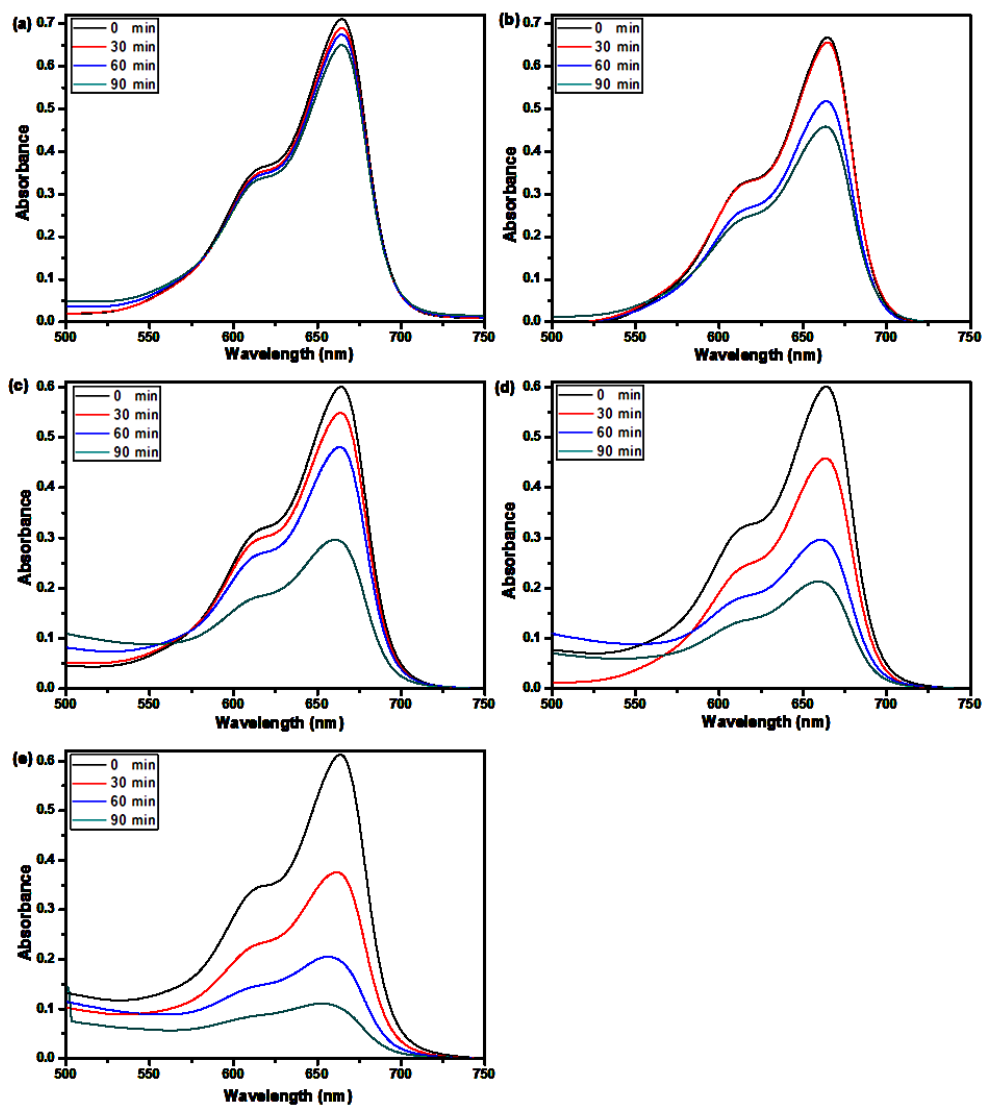


**Figure 4-2.6.** Time-dependent UV-VIS spectra on photocatalytic decomposition of MB under UV light in the presence of  $\text{H}_2\text{O}_2$  ((a) MB (without catalyst), (b) MB and  $\text{H}_2\text{O}_2$  (without catalyst), and (c-e) the samples calcined for (c) 5, (d) 6, and (e) 7 h, respectively).

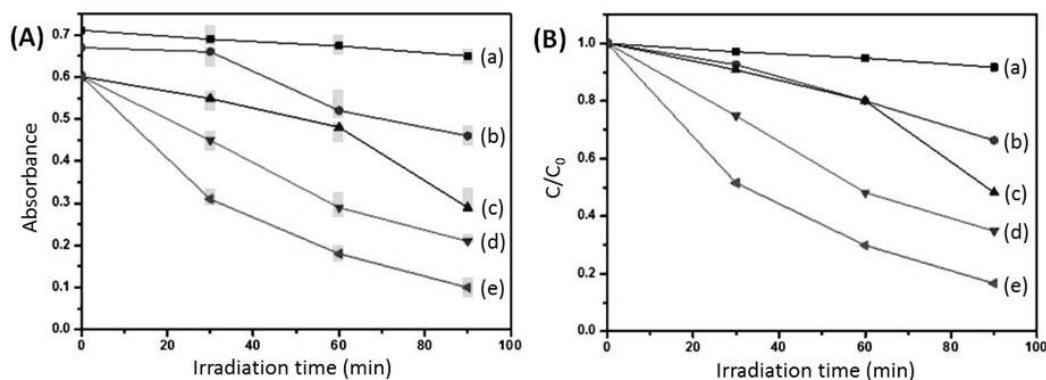


**Figure 4-2.7.** Time-dependent change of (A) absorbance at 664 nm and (B) MB concentration ( $C_0$  means the initial MB concentration before UV irradiation): (a) MB (without catalyst), (b) MB and H<sub>2</sub>O<sub>2</sub> (without catalyst), and samples calcined for (c) 5, (d) 6, and (e) 7 h. The error bars are also shown in Figure A.

## 4-2.4. Conclusion

I established a facile route to prepare nanoporous iron oxides with an  $\alpha$ -Fe<sub>2</sub>O<sub>3</sub> crystalline phase by thermal decomposition of PB coordination polymers. By using hollow PB particles as the starting material, I prepared well-organized nanoporous iron oxides with high surface areas and large pore volumes. Their crystalline phases and degrees were controlled by several calcination conditions. The use of PB as the starting material is a new and unique technology, and further use of various PB analogues with different compositions will produce more functional materials in the future.

## 4-2.5. Acknowledgments

Mr. Natsuhiko Sugimura, Mr. Takahiro Yatsu, and Dr. Takeo Suga (Waseda University, Japan) are acknowledged for kind assistance with the TG-DTA-MS measurements. K. C.-W. Wu would like to thank the following institutions for funding support: National Science Council of Taiwan

(101-2628-E-002-015-MY3), National Taiwan University (102R7842 and 102R7740), Center of Strategic Materials Alliance for Research and Technology (SMART Center), National Taiwan University (102R104100).

## 4-2.6. References

- [1] B.V. Reddy, S.N. Khanna, *Phys. Rev. Lett.* **2004**, *93*, 068301.
- [2] a) P. Poizot, S. Laruelle, S. Grugeon, L. Dupont, J.M. Tarascon, *Nature* **2000**, *407*, 496; b) B. Koo, H. Xiong, M.D. Slater, V.B. Prakapenka, M. Balasubramanian, P. Podsiadlo, C.S. Johnson, T. Rajh, E. V. Shevchenko, *Nano Lett.* **2012**, *12*, 2429.
- [3] B. Wang, J.S. Chen, H.B. Wu, Z. Wang, X.W. (D.) Lou, *J. Am. Chem. Soc.* **2011**, *133*, 17146.
- [4] X. Yao, C. Tang, G. Yuan, P. Cui, X. Xu, Z. Liu, *Electrochem. Commun.* **2011**, *13*, 1439.
- [5] L.S. Zhong, J.S. Hu, H.P. Liang, A.M. Cao, W.G. Song, L.J. Wan, *Adv. Mater.* **2006**, *18*, 2426.
- [6] Y. Song, S. Qin, Y. Zhang, W. Gao, J. Liu, *J. Phys. Chem. C* **2010**, *114*, 21158.
- [7] A.K. Ganguli, T. Ahmad, *J. Nanosci. Nanotechnol.* **2007**, *7*, 2029.
- [8] C.Y. Cummings, F. Marken, L.M. Peter, K.G. Wijayantha, A.A. Tahir, *J. Am. Chem. Soc.* **2012**, *134*, 1228.
- [9] X. Gou, G. Wang, X. Kong, D. Wexler, J. Horvat, J. Yang, J. Park, *Chem. Eur. J.* **2008**, *14*, 5996.
- [10] L.P. Zhu, H.M. Xiao, X.M. Liu, S.Y. Fu, *J. Mater. Chem.* **2006**, *16*, 1794.
- [11] G.Y. Zhang, Y. Feng, Y.Y. Xu, D.Z. Gao, Y.Q. Sun, *Mater. Res. Bull.* **2012**, *47*, 625.
- [12] Z. Jia, Q. Wang, D. Ren, R. Zhu, *Appl. Surf. Sci.* **2013**, *264*, 255.
- [13] H.C. Liang, Z.H. Ye, S.Z. Yu, L.Z. Min, *Sci. China Chem.*, **2010**, *7*, 1502.

- [14] S. Bharathi, D. Nataraj, D. Mangalaraj, Y. Masuda, K. Senthil, K. Yong, *J. Phys. D: Appl. Phys.* **2010**, *43*, 015501.
- [15] K. Brezesinski, J. Haetge, J. Wang, S. Mascotto, C. Reitz, A. Rein, S. H. Tolbert, J. Perlich, B. Dunn, T. Brezesinski, *Small* **2011**, *7*, 407.
- [16] G. Li, M. Liu, H. Kou, *Chem. Eur. J.* **2011**, *17*, 4323.
- [17] D. Chen, D. Chen, X. Jiao, Y. Zhao, *J. Mater. Chem.* **2003**, *13*, 2266
- [18] J. Chen, L. Xu, W. Li, X. Gou, *Adv. Mater.* **2005**, *17*, 582.
- [19] H.J. Song, N. Li, X.Q. Shen, *Appl Phys A: Mater. Sci. Process.* **2011**, *102*, 559.
- [20] Z. Wu, K. Yu, S. Zhang, Y. Xie, *J. Phys. Chem. C* **2008**, *112*, 11307.
- [21] A. Mitra, C. Vázquez-Vázquez, M.A. López-Quintela, B.K. Paul, A. Bhaumik, *Microporous Mesoporous Mater.* **2010**, *131*, 373.
- [22] M. Hu, S. Furukawa, R. Ohtani, H. Sukegawa, Y. Nemoto, J. Reboul, S. Kitagawa, Y. Yamauchi, *Angew. Chem.* **2012**, *124*, 1008; *Angew. Chem. Int. Ed* **2012**, *51*, 984.
- [23] M. Hu, A.A. Belik, M. Imura, K. Mibu, Y. Tsujimoto, Y. Yamauchi, *Chem. Mater.* **2012**, *24*, 2698.
- [24] X. Zhou, H. Yang, C. Wang, X. Mao, Y. Wang, Y. Yang, G. Liu, *J. Phys. Chem. C* **2010**, *114*, 17051.

# Chapter 5

## Chapter 5

# 5. Controlled Crystallization of Cyano-Bridged Cu-Pt Coordination Polymers with Two-Dimensional Morphology

### 5.1. Introduction

In recent years, coordination polymers (CPs), including metal-organic frameworks (MOFs) and porous coordination polymers (PCPs), have received much attention [1]. Their tunable pore structures and controlled compositions and shapes make them attractive materials for many applications such as catalysts, drug delivery, magnetism, gas storage, and ion exchange. Cyano-bridged coordination CPs consist of metal ions and cyanide ligands, in which the metal ions are bridged by cyano groups. Cyano-bridged CPs can serve as precursors for the preparation of various nanoporous metals oxides [2].

So far, CPs with various morphologies have been reported using different synthetic conditions. The morphologies were determined to be one (1D), two (2D), or three dimensional (3D). A 1D morphology (*e.g.*, tube) extends in a straight line (along the x-axis), a 2D morphology (*e.g.*, sheet, flake) extends in a plane (two directions, x- and y-axes); a 3D



morphology (*e.g.*, cube) extends in all three directions (x-, y-, and z-axes). Among them, a 2D morphology is quite interesting because it shows many properties that are not observed in the bulk chemistry. The 2D CPs have a highly accessible surface area that permits guest molecules to effectively access the micropores in the CPs. Moreover, 2D CPs have many active sites for catalytic and electrochemical reactions, and furthermore assembled CPs can be used as membrane filters.

Several efforts have thus been made towards the successful preparation of 2D CPs [3]. Kitagawa and co-workers prepared a MOF-2 nanofilm by using a layer-by-layer growth method [3a]. Xu and co-workers [3b] proposed a delamination process from bulk crystals of a layered MOF, and Cheetham and co-workers [3c] reported an ultrasonication-induced exfoliation approach to prepare MOF nanosheets. Although some important advantages have been identified in previous studies, I believe that these approaches are somewhat inconvenient because of the need for complicated synthetic conditions and special equipment.

My recent study demonstrated that 2D cyano-bridged CPs with a nanoflake shape can be synthesized under a controlled crystallization process using trisodium citrate as a chelating agent [4]. In this study, I have extended this concept to synthesize new 2D cyano-bridged Cu-Pt CPs with nanoflake shapes. Although Falvello reported the synthesis of Cu-Pt CPs [5], synthetic methods demonstrating shape and/or size control have not been reported. By changing the amount of trisodium citrate and the copper sources, I clarified that the presence of trisodium citrate plays an important key role in the formation of the 2D nanoflake shape. My method is based on a bottom-up design and this will be useful for the preparation of other types of CP nanoflakes/nanosheets in the future.

## 5.2. Preparation of 2D Cu-Pt Nanosheets

The typical preparation conditions of 2D Cu-Pt nanosheets/flakes are as follows: copper(II) acetate and trisodium citrate (as a chelating agent) were mixed well with distilled water in a round-bottomed flask until the solution was clear. In another flask, potassium tetracyanoplatinate(II)( $K_2Pt(CN)_4$ ) was dissolved in distilled water until the solution was clear. The two flasks were mixed under static conditions for 24 h. After the reaction was terminated, the solid precipitates were then collected by centrifugation. Then, the precipitates were washed several times with distilled water and ethanol. After drying at room temperature, the solid powders were obtained. The amount and types of precursors are varied in this study, and the data are summarized in **Table 5.1**. To study the effect of the chelating agent on the crystallization, the amount of Cu and Pt sources was fixed and only the amount of trisodium citrate was varied.

**Table 5.1** Compositions of the starting solutions for various Cu-Pt PCs.

Sample No	Cu source	Conc.	$K_2Pt(CN)_4$	Trisodium citrate
A	$Cu(COOCH_3)_2$	0.4 mM	0.4 mM	0.0 mM
B	$Cu(COOCH_3)_2$	0.4 mM	0.4 mM	0.1 mM
C	$Cu(COOCH_3)_2$	0.4 mM	0.4 mM	0.2 mM
D	$Cu(COOCH_3)_2$	0.4 mM	0.4 mM	0.3 mM
E	$Cu(COOCH_3)_2$	0.4 mM	0.4 mM	0.4 mM
F	$Cu(COOCH_3)_2$	0.4 mM	0.4 mM	0.5 mM
G	$CuCl_2$	0.4 mM	0.4 mM	0.5 mM
H	$Cu(NO_3)_2$	0.4 mM	0.4 mM	0.5 mM
I	$CuSO_4$	0.4 mM	0.4 mM	0.5 mM

## 5.3. Apparatus

SEM images were taken with a Hitachi SU8000 scanning microscope at an accelerating voltage of 5 kV. Wide-angle powder X-ray diffraction (XRD) patterns were obtained with a Rigaku RINT 2500X diffractometer using monochromated  $Cu_{K\alpha}$  radiation (40 kV, 40 mA) at a scanning

rate of  $1^\circ \text{ min}^{-1}$ .  $^1\text{H}$  NMR spectra were obtained at  $25^\circ \text{C}$  using an AL300 BX spectrometer (JEOL, Tokyo, Japan).  $\text{D}_2\text{O}$  was obtained from Cambridge Isotope Laboratories, Inc.  $\text{K}_2[\text{Pt}(\text{CN})_4]$  hydrate was dried under vacuum overnight at  $40^\circ \text{C}$ . Trisodium citrate and  $\text{Cu}(\text{OAc})_2$  were used as received.  $\text{Cu}(\text{OAc})_2$  (0.4 mm) and trisodium citrate (0.45 mm) were dissolved in  $\text{D}_2\text{O}$  (20 mL) to form a clear solution A. In the meantime,  $\text{K}_2[\text{Pt}(\text{CN})_4]$  (0.4 mm) was dissolved in  $\text{D}_2\text{O}$  (20 mL) to form clear solution B. Solutions A and B were then mixed. The obtained solution was measured by  $^1\text{H}$  NMR spectroscopy. Before measurements were taken, the solution was filtered (0.25 mm mesh Teflon) to remove the light green precipitate that was responsible for broadening of all  $^1\text{H}$  NMR signals.

## 5.4. Characterization of Various 2D Cu-Pt Nanosheets

The obtained powders were characterized by using SEM (**Figure 5.1**). The nanoflakes gradually increased in size by increasing the amount of trisodium citrate. The obtained Cu-Pt CP nanoflakes were well dispersed in solutions (**Figure 5.2a**). A clear Tyndall light-scattering effect was observed by a side-incident light beam. A TEM image of the Cu-Pt CP nanoflakes is shown in **Figure 5.2b**. A TEM grid was immersed in the colloidal suspension for one minute, and this was rinsed with water and dried under a  $\text{N}_2$  stream. The nanoflakes were routinely observed; the crystal structure of the obtained 2D Cu-Pt CP nanoflakes was also characterized by using wide-angle X-ray diffraction (XRD; **Figure 5.3**). In the absence of the chelating agent (trisodium citrate), the peaks were broad, thereby implying the incomplete crystallinity and/or the presence of an amorphous phase (**Figure 5.3a**). By increasing the amount of the chelating agent to 0.5 mm, the peaks became sharper and their intensities were increased, thus indicating the formation of large crystals (**Figure 5.3f**). In the absence of trisodium citrate, poorly developed nanoparticles were obtained. When a suitable amount of trisodium citrate was used, well-defined nanoflakes

were obtained. It is noteworthy that the obtained CPs have a flake-like morphology, and this corresponds to the inherent crystal structure. To assign the XRD patterns, the automatic indexing program (DICVOL) was employed [6]. The most reliable crystal system was the orthorhombic cell with  $a=13.486(9)$  Å,  $b=10.135(5)$  Å, and  $c=3.461(2)$  Å (**Figure 5.4**). The XRD results were consistent with the electron diffraction (ED) patterns. The lattice constants obtained by XRD were consistent with those calculated by the ED patterns.

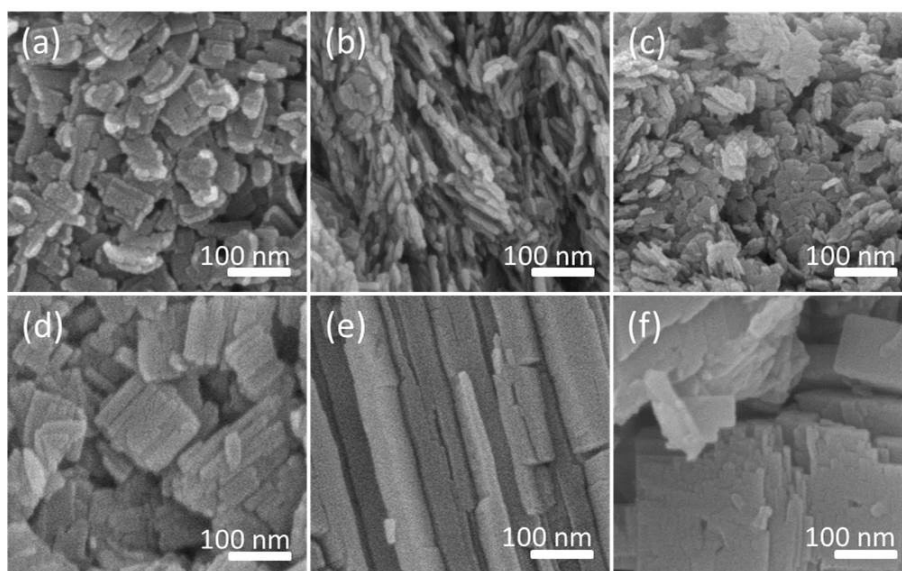


**Figure 5.1.** SEM images of various Cu-Pt CPs prepared from different reaction solutions ((a) Sample A, (b) Sample B, (c) Sample C, (d) Sample D, (e) Sample E, and (f) Sample F).

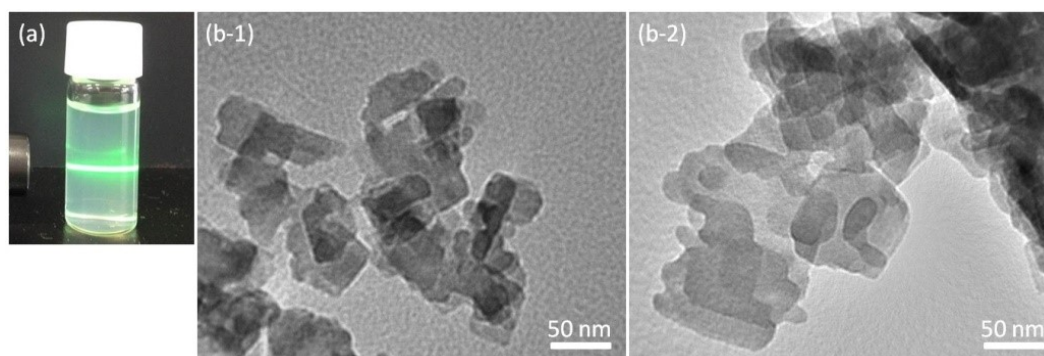


**Figure 5.2.** (a) Photograph of colloidal suspensions containing well-dispersed 2D Cu-Pt CP nanoflakes. The light beam is incident from the side to demonstrate the Tyndall effect. (b) Low-magnified TEM images of (b-1) Sample B and (b-2) Sample C, respectively.

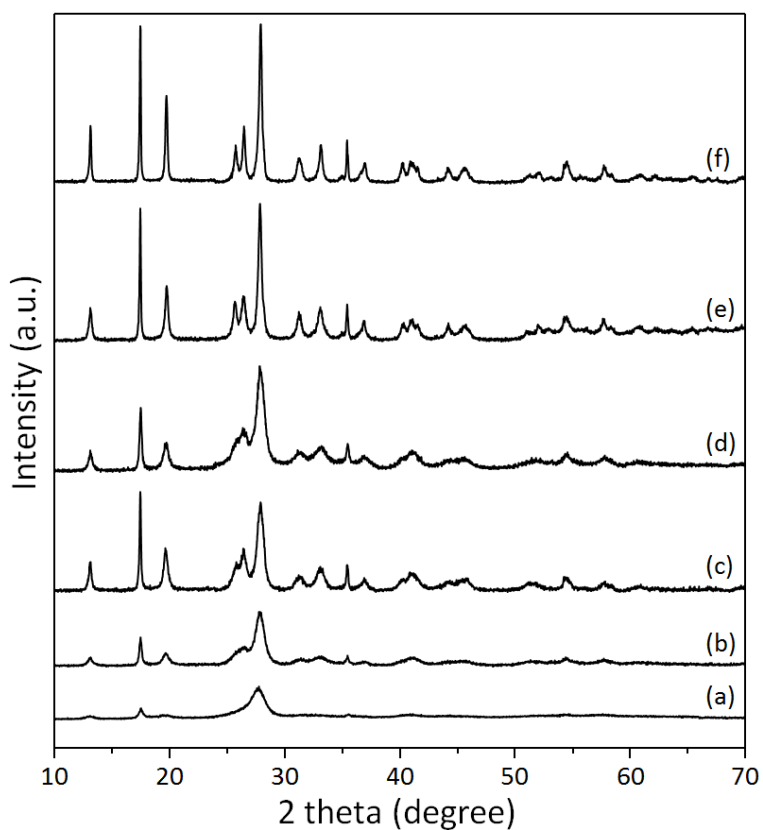


**Figure 5.3.** Wide-angle XRD patterns of various Cu-Pt CPs prepared from different reaction solutions ((a) Sample A, (b) Sample B, (c) Sample C, (d) Sample D, (e) Sample E, and (f) Sample F).

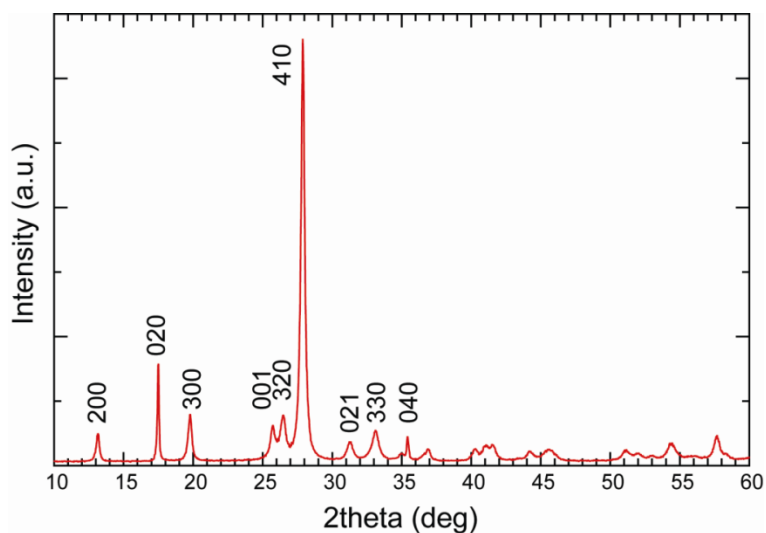


**Figure 5.4.** Assignment of wide-angle XRD patterns by automatic indexing program (DICVOL).

Regarding the porous properties of the obtained samples, I measured the nitrogen gas adsorption-desorption isotherms for five samples (Samples A-E) with different particle sizes. As shown in **Figure 5.5**, a hysteresis loop at high relative pressures was observed. The inter-particles space is generated through the assembly of small-sized particles. The surface areas for Samples A, B, and C were  $52 \text{ m}^2 \text{ g}^{-1}$ ,  $52 \text{ m}^2 \text{ g}^{-1}$ , and  $56 \text{ m}^2 \text{ g}^{-1}$ , respectively. With further increasing the particle sizes, the inter-particles space gradually disappeared and the surface areas gradually decreased from  $40 \text{ m}^2 \text{ g}^{-1}$  (for Sample D) to  $28 \text{ m}^2 \text{ g}^{-1}$  (for Sample E), and  $10 \text{ m}^2 \text{ g}^{-1}$  (for Sample F). Thus, the accessibility of nitrogen gas from the outside into inside of the particle varied, and this depends on the particle size. In the case of large-sized particles, nitrogen molecules could not easily access the whole surface of the particle, and thus lower surface areas were measured.

Trisodium citrate is a well-known chelating agent and can easily coordinate to various transition-metal cations [7,8]. Thus, it is predicted that the citrate ions directly interact with metal ions. A  $^1\text{H-NMR}$  spectroscopic study more clearly revealed the chelating effect of the trisodium citrate with  $\text{Cu}^{2+}$ . As shown in **Figure 5.6a** and **b**, the  $^1\text{H-NMR}$  spectra of the citrate ligand with two doublet peaks at around 2.6 ppm disappeared in the presence of  $\text{Cu}(\text{OAc})_2$ ; this is typical in the formation of a metal-ligand complex involving paramagnetic ions [9]. After the addition of the  $\text{K}_2[\text{Pt}(\text{CN})_4]$  solution in the mixed solution of trisodium citrate and  $\text{Cu}(\text{OAc})_2$ , the  $^1\text{H-NMR}$  peaks (as indicated by arrows) gradually reappeared (**Figure 5.6c-i**) accompanied by a visible precipitate. This result indicates that citrate anions become free from paramagnetic  $\text{Cu}^{2+}$ , while the Cu ions released from the Cu-citrate complex are gradually converted into Cu-Pt CPs in the reaction with  $[\text{Pt}(\text{CN})_4]^{2-}$ . Thus, the  $^1\text{H-NMR}$  spectroscopy study revealed that citrate anions can stabilize  $\text{Cu}^{2+}$  ions in the solution. As a result, the generation speed of Cu-Pt CPs was significantly delayed in the presence of citrate ions, thereby leading to the controlled growth of single crystalline Cu-Pt CPs with fine morphology.

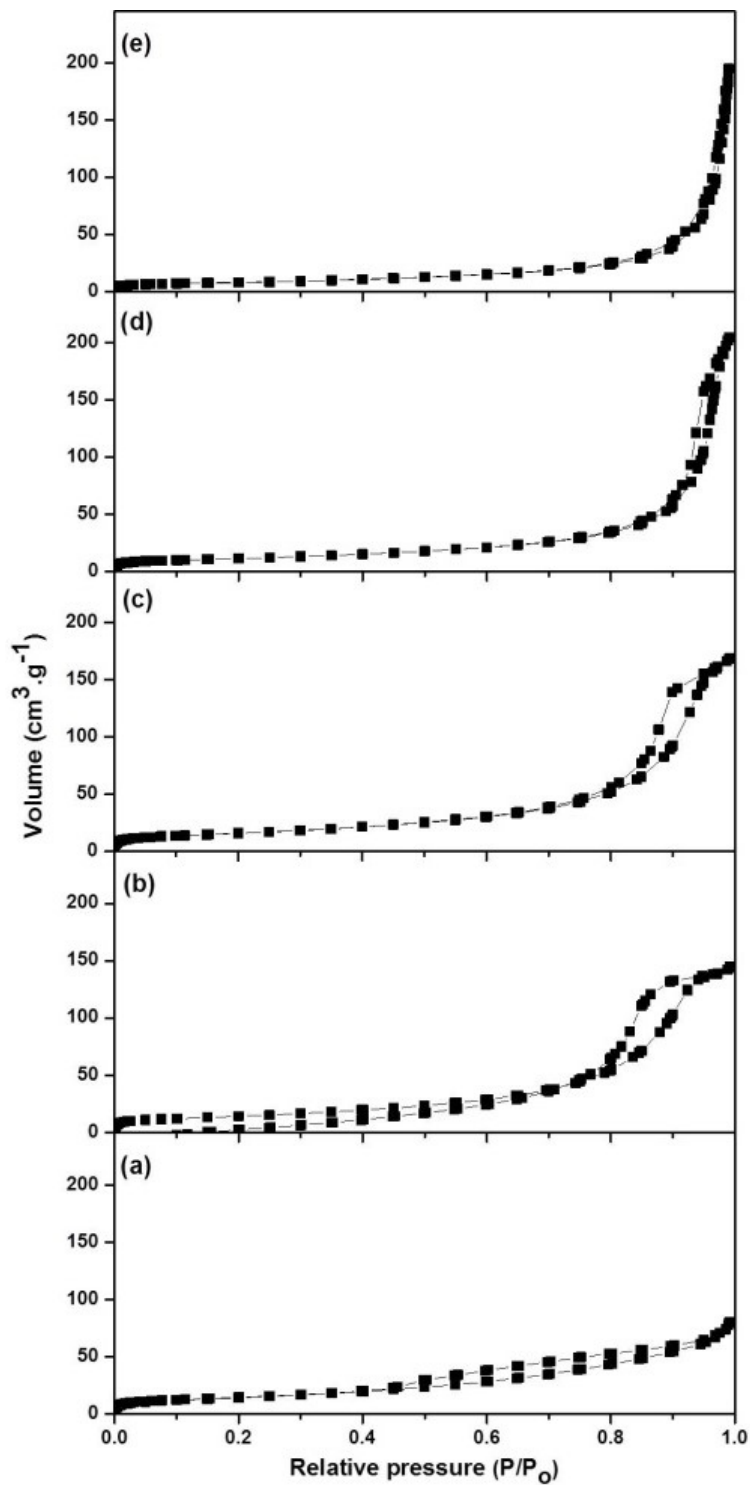


**Figure 5.5.**  $N_2$  gas adsorption-desorption isotherms of various Cu-Pt CPs prepared from different reaction solutions ((a) Sample A, (b) Sample B, (c) Sample C, (d) Sample D, and (e) Sample E).

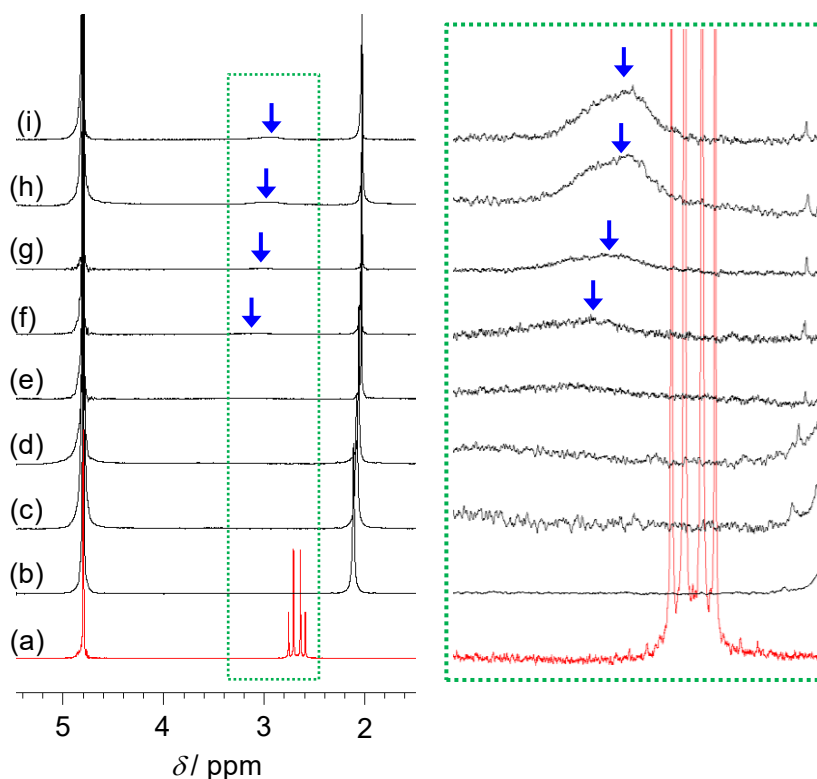
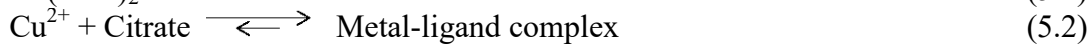


**Figure 5.6.**  $^1\text{H-NMR}$  spectra of sodium citrate in  $\text{D}_2\text{O}$  in the absence (a) and presence (b) of  $\text{Cu}(\text{OAc})_2$ . Time course  $^1\text{H-NMR}$  spectra of sodium citrate and  $\text{Cu}(\text{OAc})_2$  in  $\text{D}_2\text{O}$  measured after addition of  $\text{K}_2[\text{Pt}(\text{CN})_4]$ ; (c) 5 min, (d) 15 min, (e) 25 min, (f) 45 min, (g) 3.5 hr, (h) 10 hr, (i) 30 hr.  $^1\text{H-NMR}$  signals at 2.1 ppm and 4.8 ppm are corresponding to acetate anion and water, respectively. The magnified image was inserted at right side.

In general, a balance between nucleation and crystal growth determines the final size of the particles in the products (**Figure 5.7**). In the present system, free Cu ions are released steadily from the Cu-citrate complex and are treated with  $[\text{Pt}(\text{CN})_4]^{2-}$  at the initial stage of the reaction.

(a)  $\text{Cu}(\text{OAc})_2$



(b)  $\text{CuCl}_2$

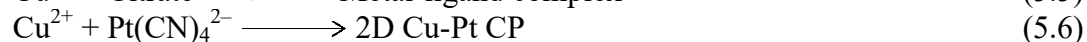


**Figure 5.7.** Reaction system for formation of 2D Cu-Pt PCs ((a)  $\text{Cu}(\text{COOCH}_3)_2$  and (b)  $\text{CuCl}_2$ ).



Then, the nuclei are generated and grow further by interaction of the free Cu ions with  $[\text{Pt}(\text{CN})_4]^{2-}$  to form the final products. Therefore, with an increase in the concentration of trisodium citrate, the number of nuclei formed at the early stage of the reaction is thought to be decreased, and these nuclei further undergo crystal growth by interacting with  $[\text{Pt}(\text{CN})_4]^{2-}$  to afford the final products with larger particle sizes. In contrast, at low concentration of trisodium citrate, more Cu species dissolved in the solution are present as free Cu ions, therefore they can immediately react with  $[\text{Pt}(\text{CN})_4]^{2-}$ . Consequently, there are many nuclei at the early stage of the reaction, and they grow very fast to afford small-sized particles. Wide-angle XRD results (**Figure 5.3**) also nicely confirmed that the variation in crystal sizes depends on the concentration of trisodium citrate used. According to TEM data, I investigated the lateral size distribution for Samples A, B, C, and D (**Figure 5.8**). The amount of trisodium citrate used is very important to determine the lateral sizes of CP nanoflakes.

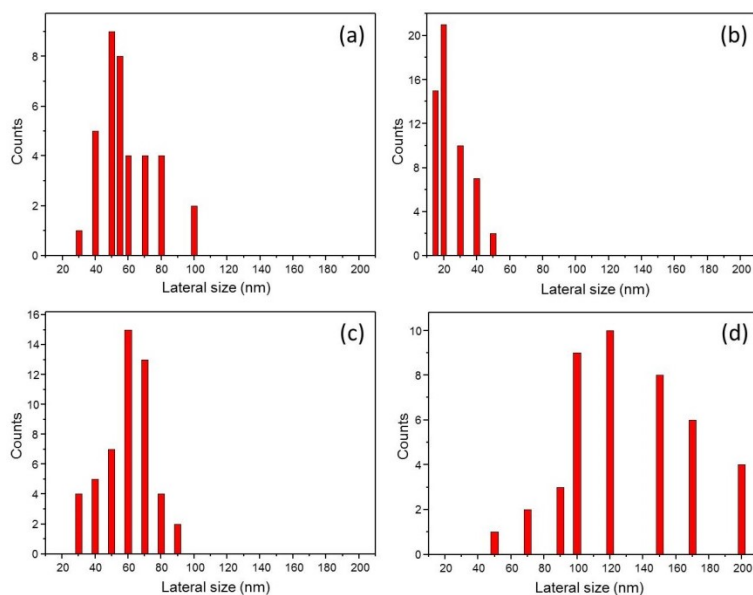


**Figure 5.8.** Lateral size distribution data of various Cu-Pt CPs prepared from different reaction solutions ((a) Sample A, (b) Sample B, (c) Sample C, and (d) Sample D).

I further studied the effect of different Cu sources on the particle size of the final products. Three different Cu sources ( $\text{CuCl}_2$ ,  $\text{Cu}(\text{NO}_3)_2$ , and  $\text{CuSO}_4$ , as shown in **Table 5.1**) were used instead of

copper(II) acetate ( $\text{Cu}(\text{OOCCH}_3)_2$ ). SEM images of the obtained particles are shown in **Figure 5.9**. For the same concentration of trisodium citrate (*i.e.*, 0.5 mM), relative to the product prepared with copper(II) acetate, the sample prepared with the other Cu sources showed smaller particle sizes. The peak intensities in wide-angle XRD profiles significantly decreased by replacing copper(II) acetate with other Cu sources (**Figure 5.10**). In the case of  $\text{CuCl}_2$  (Sample G), when  $\text{CuCl}_2$  is dissolved in an aqueous solution,  $\text{Cu}^{2+}$  and Cl ions are well separated (*i.e.*, the electrolytic dissociation constant is almost 1; **Figure 5.7**). Even when some free Cu ions are protected by citrate anions, the amount of free  $\text{Cu}^{2+}$  ions is higher compared to the copper(II) acetate system. Therefore, more nuclei are formed at the early stage of the reaction, and they grow very fast to afford small-sized particles. A similar situation was observed in  $\text{Cu}(\text{NO}_3)_2$  (for Sample H) and  $\text{CuSO}_4$  (for Sample I). These results significantly indicate that the type of Cu source also affects the particle size of the final products.

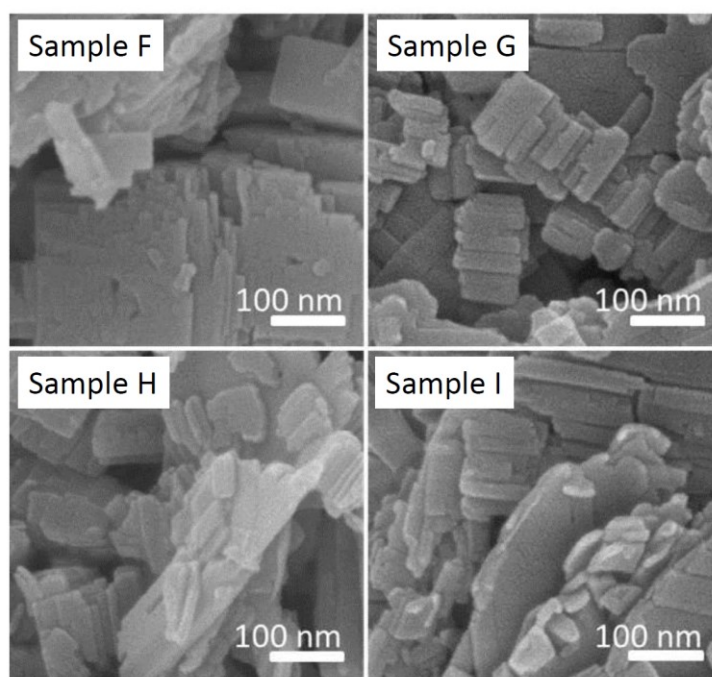


**Figure 5.9.** SEM images of Cu-Pt CPs prepared from several reaction solutions with different Cu sources (Sample F, Sample G, Sample H, and Sample I).

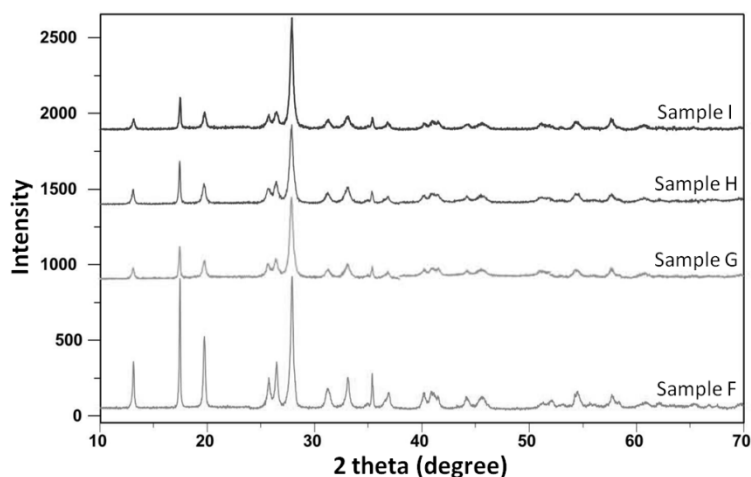


**Figure 5.10.** Wide-angle XRD patterns of Cu-Pt CPs prepared from several reaction solutions with different Cu sources (Sample F, Sample G, Sample H, and Sample I).

## 5.5. Conclusion

In conclusion, I reported a bottom-up synthesis to prepare 2D Cu-Pt CP nanoflakes using trisodium citrate as a chelating agent, which controls the nucleation rate and the crystals growth. I believe that my method will be useful for the preparation of other types of CPs nanoflakes. Such 2D-shaped CPs and their derivatives could potentially have new solid state properties.

## 5.6. References

- [1] a) O.M. Yaghi, M. O'Keeffe, N.W. Ockwig, H.K. Chae, M. Eddaoudi, J. Kim, *Nature* **2003**, *423*, 705; b) S. Kitagawa, R. Kitaura, S.I. Noro, *Angew. Chem. Int. Ed.* **2004**, *43*, 2334; *Angew. Chem.* **2004**, *116*, 2388; c) X. Zhao, B. Xiao, A.J. Fletcher, K.M. Thomas, D. Bradshaw, M.J. Rosseinsky, *Science* **2004**, *306*, 1012; d) S.T. Meek, J.A. Greathouse, M.D. Allendorf, *Adv. Mater.* **2011**, *23*, 249; e) M.C. Das, S. Xiang, Z. Zhang, B. Chen, *Angew. Chem. Int. Ed.* **2011**, *50*, 10510; *Angew. Chem.* **2011**, *123*, 10696; f) J. An, C.M. Shade, D.A. Chengelis-Czegan, S. Petoud, N.L. Rosi, *J. Am. Chem. Soc.* **2011**, *133*, 1220; g) P.

- Dechambenoit, J.R. Long, *Chem. Soc. Rev.* **2011**, *40*, 3249; h) S. Diring, D.O. Wang, C. Kim, M. Kondo, Y. Chen, S. Kitagawa, K.I. Kamei, S. Furukawa, *Nat. Commun.* **2013**, *4*, 2684; i) S. Furukawa, Y. Sakata, S. Kitagawa, *Chem. Lett.* **2013**, *42*, 570.
- [2] a) M. Hu, Y. Yamauchi, *Chem. Asian J.* **2011**, *6*, 2282; b) M. Hu, A.A. Belik, H. Sukegawa, Y. Nemoto, M. Imura, Y. Yamauchi, *Chem. Asian J.* **2011**, *6*, 3195; c) M. Hu, A.A. Belik, M. Imura, K. Mibu, Y. Tsujimoto, Y. Yamauchi, *Chem. Mater.* **2012**, *24*, 2698.
- [3] a) S. Motoyama, R. Makiura, O. Sakata, H. Kitagawa, *J. Am. Chem. Soc.* **2011**, *133*, 5640; b) P.Z. Li, Y. Maeda, Q. Xu, *Chem. Commun.* **2011**, *47*, 8436; c) J.C. Tan, P.J. Saines, E.G. Bithell, A.K. Cheetham, *ACS Nano* **2012**, *6*, 615; d) S. Tricard, C. Costa-Coquelard, F. Volatron, B. Fleury, V. Huc, P.A. Albouy, C. David, F. Miserque, P. Jegou, S. Palacin, T. Mallah, *Dalton Trans.* **2012**, *41*, 1582; e) T. Bauer, Z. Zheng, A. Renn, R. Enning, A. Stemmer, J. Sakamoto, A.D. Schlüter, *Angew. Chem. Int. Ed.* **2011**, *50*, 7879; *Angew. Chem.* **2011**, *123*, 8025; f) P. Amo-Ochoa, L. Welte, R. González-Prieto, P.J.S. Miguel, C.J. Gómez-García, E. Mateo-Martí, S. Delgado, J. Gómez-Herrero, F. Zamora, *Chem. Commun.* **2010**, *46*, 3262.
- [4] M. Hu, S. Ishihara, Y. Yamauchi, *Angew. Chem. Int. Ed.* **2013**, *52*, 1235; *Angew. Chem.* **2013**, *125*, 1273.
- [5] L.R. Falvello, M. Tomás, *Chem. Commun.* **1999**, 273.
- [6] A. Boultif, D. Louër, *J. Appl. Cryst.* **2004**, *37*, 724.
- [7] J. Strouse, S.W. Layten, C.E. Strouse, *J. Am. Chem. Soc.* **1977**, *99*, 562.
- [8] a) Y.D. Chiang, M. Hu, Y. Kamachi, S. Ishihara, K. Takai, Y. Tsujimoto, K. Ariga, K. C.-W. Wu, Y. Yamauchi, *Eur. J. Inorg. Chem.* **2013**, 3141; b) M. Hu, S. Ishihara, K. Ariga, M. Imura, Y. Yamauchi, *Chem. Eur. J.* **2013**, *19*, 1882.
- [9] K.E. Schwarzthans, *Angew. Chem. Int. Ed. Engl.* **1970**, *9*, 946; *Angew. Chem.* **1970**, *82*, 975.

# Chapter 6

## Chapter 6-1

# 6-1. Controlled Synthesis of Nanoporous Nickel Oxides with Two-Dimensional Shapes through Thermal Decomposition of Metal-Cyanide Hybrid Coordination Polymers

### 6-1.1. Introduction

Nanoporous/mesoporous silica-based materials are interesting materials that have been widely applied in many research fields, such as catalysis, sensing, and adsorption [1]. Significant progress has been made in the synthesis of nonsiliceous nanoporous metal oxides [2] ever since the discovery of mesoporous silica prepared through surfactant self-assembly. For example, surfactants (or block copolymers) can self-assemble in non-aqueous solution to form ordered mesophases. Several inorganic methods, using sol-gel reaction, electrochemical reaction or chemical reduction, can be carried out inside the ordered mesophases. After the removal of the templates, various mesoporous crystalline metal oxides (sometimes including metals) [3] with different compositions have been prepared. Shape- and size-controlled synthesis of nanoporous materials is very important for further improving their performance [4]. In particular,

two-dimensional (2D) shapes, such as nanosheets, nanoflakes, and free-standing films are interesting because they show many outstanding properties that are not observable in their bulk counterpart [5]. Two-dimensional nanoporous metal oxides can offer highly accessible surface area that permits guest molecules to effectively access the nanopores and reach their surfaces. Also, they can provide many active sites for catalytic and electrochemical reactions. Therefore, finding an efficient way to achieve the preparation of novel nanoporous metal oxides with 2D architectures is of crucial importance in materials science.

So far, several efforts have been made towards preparing 2D nanoporous materials. Zhao and co-workers have reported the synthesis of  $\gamma$ -Al<sub>2</sub>O<sub>3</sub> with 2D flake-like morphology by a novel hard-templating method [6]. Although there have been several reports on the synthesis of highly crystalline nanoporous transition metal oxides (*e.g.*, Co<sub>3</sub>O<sub>4</sub>, CuO, Fe<sub>2</sub>O<sub>3</sub>, NiO, V<sub>2</sub>O<sub>5</sub>, and WO<sub>3</sub>) by the hard-templating method [7], there have been only a few reports on 2D nanoporous metal oxide materials. Various forms of 2D nanoporous NiO have been prepared by dehydration and recrystallization of  $\beta$ -Ni(OH)<sub>2</sub> nanoplates synthesized by a hydrothermal process [8]. The controlled synthesis of ordered mesoporous carbon nanosheets using low concentration monomicelles has been reported, with the possibility of further converting the obtained material into mesoporous graphene nanosheets by carbonization [9]. Mou *et al.* have reported a freestanding thin sheet form of mesoporous silica material with perpendicular orientation by utilizing a ternary surfactant system [10a,b]. Ordered mesoporous thin carbon plates with short channels perpendicular to the plates have also been synthesized by the replication of mesoporous silica plates [10c]. Such unique structures are much desired for their possible applications in catalysis, masking, and separation. Although several methods for the formation of 2D nanoporous materials have been reported, further development is required in order to extend the list of potential materials to other metal oxide compositions. Thus, it is still a great challenge to

develop facile methods to prepare 2D nanoporous metal oxides in a more predictable way.

CPs, including metal-organic frameworks (MOFs), have recently drawn great attention. Their diverse structural and physical properties, including orderly arranged nanopores, tunable fluorescence, electrochemical behavior, magnetic susceptibility, and biocompatibility, make them attractive materials for many applications [11]. Recent reports have shown that the thermal treatment of MOFs is a promising method for the preparation of nanostructured metal oxides (*e.g.*, Fe oxide [12], ZnO [13], Co<sub>3</sub>O<sub>4</sub> [14], CoFe<sub>2</sub>O<sub>4</sub> [15], Al<sub>2</sub>O<sub>3</sub> [16], and In<sub>2</sub>O<sub>3</sub> [17]). Since MOFs have a large fraction of metal ions as well as organic ligands, the large fraction of metal atoms can be utilized as the metal source, while the organic components, which are removable by simple calcination, can provide abundant nanopores. So far, MOFs with various shapes and sizes have been obtained by purposefully changing the synthetic parameters, including the precursor compositions (*e.g.*, type and concentration of metal salts and ligands, capping and reducing agents, and pH values of the solutions) and the conditions of reaction (*e.g.*, synthetic temperature, aging temperature and time, stirring rates, and sonication). Therefore, we believe that the use of 2D CPs has the potential to overcome the difficulties in the preparation of 2D nanoporous metal oxides by the aforementioned methods.

Metal-cyanide hybrid CPs, which are traditional CPs, can serve as potential precursors for the preparation of various nanoporous metal oxides [18]. Metal-cyanide hybrid CPs featuring different metal contents have been reported, and their shapes and particle sizes are more easily controlled compared to general MOFs [19-21]. Here, I demonstrate that 2D nickel cyanide hybrid CP (abbreviated as “Ni-CP”) can be synthesized by a controlled crystallization process, and I further extend this concept to the preparation of various Ni-CPs with different lateral sizes. By thermal treatment in air, the organic parts ( $-C\equiv N-$ ) can be removed, leaving nanoporous structures. The obtained nanoporous NiO electrodes with high surface area and unique 2D shapes



are found to be promising candidates for high-capacitance energy storage. Electrochemical analysis has demonstrated that my nanoporous NiO materials can serve as efficient electrodes for supercapacitors. My method using metal-cyanide hybrid CPs can also be used to prepare other types of nanoporous oxides with controlled shapes in the future.

## 6-1.2. Experimental Section

### 6-1.2.1. Chemicals

Potassium tetracyanonickelate(II) hydrate ( $K_2[Ni(CN)_4] \cdot xH_2O$ ) was purchased from Sigma-Aldrich. Nickel(II) chloride hexahydrate and trisodium citrate dihydrate were purchased from Nacalai Tesque (Japan). Polyvinylidene difluoride (PVDF 20%), and N-methylpyrrolidone (NMP) solvent were purchased from Wako (Japan). All chemical reagents were used without further purification.

### 6-1.2.2. Synthesis of 2D Ni-CP Nanoflakes

In a typical synthesis (for preparation of sample D),  $NiCl_2 \cdot 6H_2O$  (0.474 g) and trisodium citrate dihydrate (0.441 g) were dissolved in 100 mL water to form a clear solution. In the meantime,  $K_2[Ni(CN)_4] \cdot xH_2O$  (0.482 g) was dissolved in 100 mL water to form another clear solution. Then, both solutions were mixed with each other under magnetic stirring until the mixture became clear. The obtained solution was aged for 30 h until the reaction was complete. Compared to our previous study [20], the amounts of the used chemicals were increased five times to prepare a large amount of NiO samples which are required for study of supercapacitors. After extensive washing in water and ethanol, the precipitates were dried at room temperature. On the basis of

elemental analysis, the chemical composition of the obtained sample was  $\text{Ni}[\text{Ni}(\text{CN})_4]$ , which is abbreviated as “Ni-CP”. For the preparation of different types of Ni-CP nanoflakes with different lateral sizes (samples A, B, C, D and E), the amount of trisodium citrate dihydrate was varied, as shown in **Table 6-1.1**.

**Table 6-1.1** Starting solutions for various 2D Ni-CPs with different lateral sizes and their surface areas calculated from nitrogen gas adsorption isotherms.

Sample name	$\text{NiCl}_2 \cdot 6\text{H}_2\text{O}$ (g)	$\text{K}_2[\text{Ni}(\text{CN})_4]$ (g)	Trisodium citrate dihydrate (g)	Surface area ( $\text{m}^2 \text{g}^{-1}$ )	Average lateral size (nm)
A	0.474	0.482	0.000	97	53
B	0.474	0.482	0.147	79	69
C	0.474	0.482	0.294	64	114
D	0.474	0.482	0.441	80	158
E	0.474	0.482	0.588	7	478

### 6-1.2.3. Thermal Conversion from 2D Ni-CP Nanoflakes to Nanoporous NiO

For thermal conversion to nanoporous NiO, the obtained Ni-CP nanoflakes were used as the precursor. The powder (around 500 mg) was placed in a melting pot. The melting pot was then heated inside an electric furnace from room temperature to the designated temperature with a heating rate of  $5 \text{ }^\circ\text{C min}^{-1}$ . After reaching the designated temperature (300, 400, and 500  $^\circ\text{C}$ ), the sample was annealed for 1 h to completely remove the organic parts (as confirmed by CHN elemental analysis). After that, the powder was naturally cooled to room temperature inside the furnace. Finally, the obtained powder was collected for characterization. The entire calcination process was carried out in air.

### 6-1.2.4. Electrochemical Measurements

The electrochemical measurements were conducted in a three electrode electrochemical cell with

a Pt counter electrode and Ag/AgCl as the reference electrode in 6 M KOH solution. Graphite substrates coated with the various NiO samples were used as the working electrode. Cyclic voltammetry (CV) measurements were conducted using an electrochemical workstation (CHI 660E CH Instruments, USA) in the scan range of 0.0 to 0.5 V. For every experiment, the typical area under consideration was  $1 \times 1 \text{ cm}^2$ . For the preparation of the working electrodes, the graphite substrates were first polished using a fine polisher in flowing water. Then, they were rinsed with deionized water, etched in 0.1 M HCl solution at room temperature for 10 min, and finally rinsed with deionized water in an ultrasonic bath for 30 min. The masses of the electrodes were measured using an ultramicrobalance (Mettler Toledo). Each electrode contained  $1.0 \text{ mg cm}^{-2}$  of electroactive material. The NiO samples were mixed with poly(vinylidene difluoride) (PVDF, 20%) in NMP solvent. The resulting slurry was homogenized by ultrasonication and coated onto the graphite substrates, which was followed by drying at  $80 \text{ }^\circ\text{C}$  for 2 h in a vacuum oven. The specific capacitance ( $C_{\text{sp}}$ ) was calculated by using Equation (6-1.1):

$$C = \frac{1}{ms(V_f - V_i)} \int_{V_i}^{V_f} I(V) dv \quad (6-1.1)$$

Where;  $C$  is the specific capacitance [ $\text{F g}^{-1}$ ],  $m$  is the mass of the active electrode material [g],  $s$  is the potential scan rate [ $\text{mV s}^{-1}$ ],  $V_f$  and  $V_i$  are the integration limits of the voltammetric curve [V], and  $I(V)$  denotes the response current density [ $\text{A cm}^{-2}$ ].

### 6-1.2.5. Characterization

SEM images were collected with a Hitachi SU8000 scanning electron microscope at an accelerating voltage of 5 kV and current of 10 A. TEM observations were performed using a JEM-2100F TEM system that was operated at 200 kV. Wide-angle powder X-ray diffraction (XRD) patterns were obtained with a Rigaku RINT 2500 diffractometer using monochromated  $\text{Cu}_{K\alpha}$  radiation (40 kV, 40 mA) at a scanning rate of  $5^\circ \text{ min}^{-1}$ .  $\text{N}_2$  adsorption-desorption isotherms

were obtained by the use of a Quantachrome Autosorb automated gas sorption system at 77 K. X-ray photoelectronic spectroscopy (XPS) spectra were recorded at room temperature by using a JPS-9010TR (JEOL) instrument with an  $Mg_{K\alpha}$  X-ray source. All binding energies were calibrated by referencing to C 1s (285.0 eV).

## 6-1.3. Results and Discussion

### 6-1.3.1. Formation of 2D-Shaped Ni-CPs

In a typical synthetic strategy, nickel(II) chloride ( $NiCl_2$ ) was dissolved in water in the presence of different amounts of trisodium citrate dihydrate to form various transparent solutions. The resulting solutions were added to  $K_2[Ni(CN)_4]$  solution. After aging, centrifugation, washing, and drying, 2D Ni-CPs were obtained with different lateral sizes (**Table 6-1.1**).  $^1H$  NMR study revealed the chelating effect of the trisodium citrate on  $Ni^{2+}$  ions, as shown in **Figure 6-1.1**. The  $^1H$  NMR spectrum of the citrate ligand features two doublet peaks at around 2.6 ppm that disappear in the presence of  $NiCl_2$ , which is typical during the formation of a metal-ligand complex involving paramagnetic ions. After the addition of  $K_2[Ni(CN)_4]$  solution, the  $^1H$  NMR peak at around 2.6 ppm gradually recovers. This result indicates that the citrate anions are freed from the paramagnetic  $Ni^{2+}$ . The free  $Ni^{2+}$  ions released from the citrate complex can gradually react with  $K_2[Ni(CN)_4]$  to generate Ni-CPs. Moreover, I checked UV/Vis spectroscopy for confirming the formation of Ni-Citrate complex. From the spectra, it is evident that, after the addition of trisodium citrate dihydrate, the strength of the maxima absorption peak of  $NiCl_2$  solution was significantly increased and the position was shifted. This absorbance variation was caused by coordination between citrate anions and  $Ni^{2+}$  ions [20].

The morphology of the obtained Ni-CPs was observed by scanning electron microscope (SEM), as shown in **Figure 6-1.2**. The average lateral sizes were measured from the SEM images

(Figure 6-1.3), and their values are summarized in Table 6-1.1. The concentration of trisodium citrate dihydrate (as a chelating agent) is critical for the determination of the lateral sizes in the final products. As shown in Figure 6-1.2, as the amount of the chelating agent increases, the lateral size gradually increases. It is well known that the balance between nucleation and crystal growth determines the particle size in the final products. In the present system, free  $\text{Ni}^{2+}$  ions are released steadily from the Ni-citrate complex and react with  $[\text{Ni}(\text{CN})_4]^{2-}$  at the initial stage of the reaction. Subsequently, the nuclei are generated and further grow by interaction between the free Ni ions and  $[\text{Ni}(\text{CN})_4]^{2-}$  to form the final Ni-CP products. Therefore, with increasing concentration of trisodium citrate, the number of nuclei formed at the early stage of the reaction is thought to be decreased. These few nuclei undergo crystal growth by interacting with  $[\text{Ni}(\text{CN})_4]^{2-}$ , leading to a final product with larger particle size. In contrast, at lower concentrations of sodium citrate, more Ni species dissolved in the solution are present as free Ni ions and immediately react with  $[\text{Ni}(\text{CN})_4]^{2-}$ . Consequently, there are many nuclei growing relatively fast at the early stage of the reaction, leading to small-sized particles.

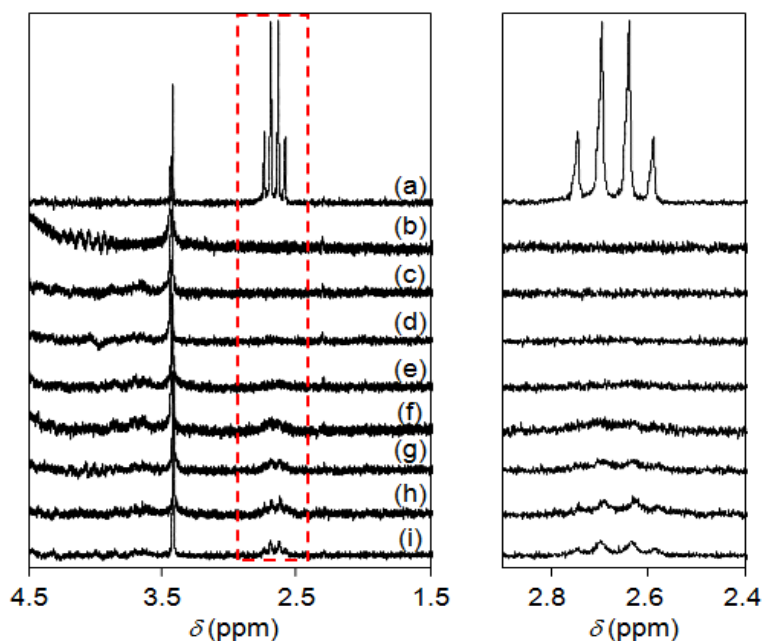


**Figure 6-1.1.**  $^1\text{H}$ -NMR spectra of trisodium citrate in  $\text{D}_2\text{O}$  in the presence (a) and absence (b) of  $\text{NiCl}_2$ . Time course  $^1\text{H}$ -NMR spectra of trisodium citrate and  $\text{NiCl}_2$  in  $\text{D}_2\text{O}$  (containing 0.01

vol. % methanol as a standard) measured after addition of  $K_2[Ni(CN)_4]$ : (c) 10 min, (d) 30 min, (e) 1 h, (f) 3 h, (g) 6 h, (h) 12 h, and (i) 24 h.

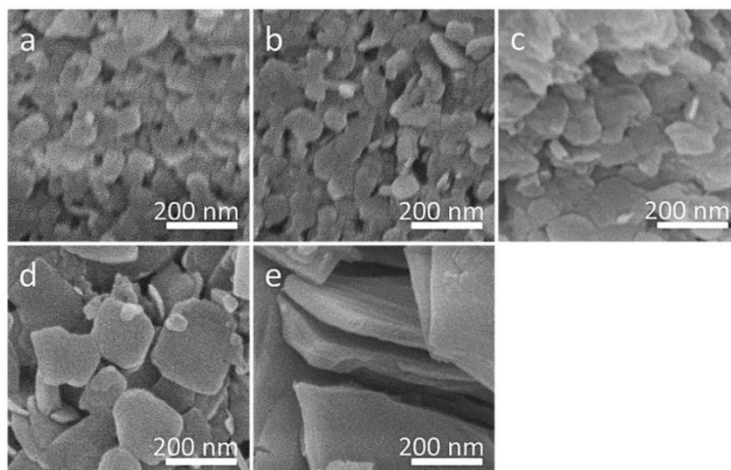


**Figure 6-1.2.** SEM images of various 2D Ni-CPs prepared from different reaction solutions: (a) Sample A, (b) Sample B, (c) Sample C, (d) Sample D, and (e) Sample E.

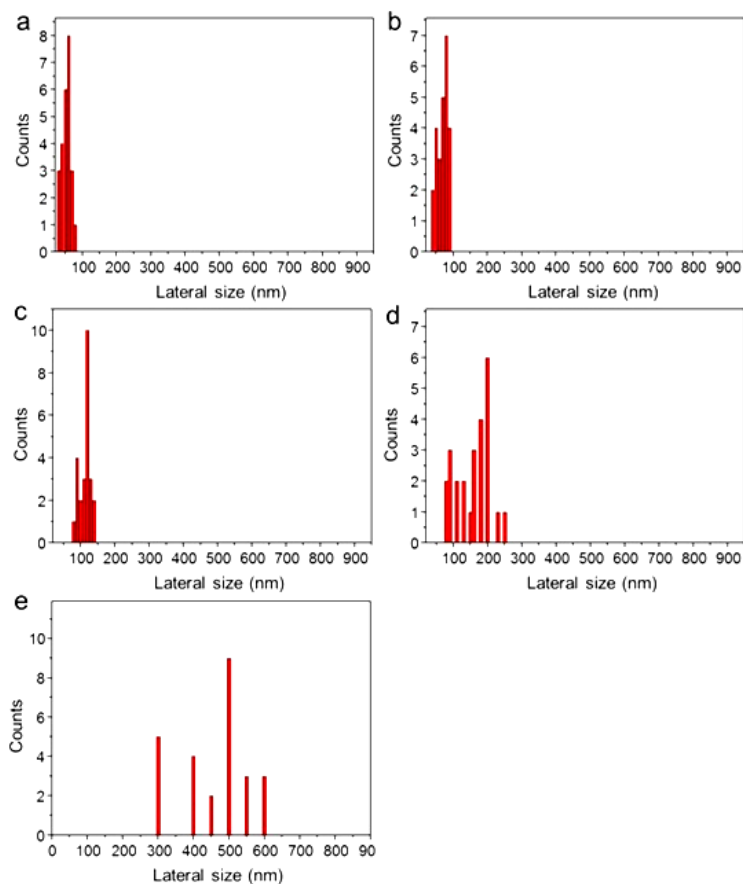


**Figure 6-1.3.** Lateral size distribution data for various 2D Ni-CPs prepared from different reaction solutions: (a) Sample A, (b) Sample B, (c) Sample C, (d) Sample D, and (e) Sample E.

The crystal structure of the obtained Ni-CPs was examined by wide-angle X-ray diffraction (XRD) measurements (**Figure 6-1.4**). The various diffraction peaks can be assigned to an orthorhombic system and clearly match Hofmann-type  $\text{Ni}(\text{H}_2\text{O})_2[\text{Ni}(\text{CN})_4] \cdot x\text{H}_2\text{O}$  with 2D layered structure (**Figure 6-1.4**) [20]. No peaks derived from impurities are detected. In the case of small-sized Ni-CPs (samples A and B; **Figure 6-1.2a** and **b**), the peaks are very broad, implying an incomplete crystallization and/or the presence of an amorphous phase. With increasing the concentration of trisodium citrate, the peaks become sharper and their intensities are drastically increased, indicating the formation of large-sized crystals. Rapid crystallization generally results in fine nanoparticles with irregular shapes, while a slow crystallization can allow the growing crystals to develop a well-defined macroscopic morphology similar to the inherent atomic crystal structure [19-21]. In my case, the Ni-CPs show a flake-like morphology corresponding to a Hofmann-type layered crystal structure.

It is well-known that 2D CPs exhibit porosity in the interlayer spaces. To investigate the porosity of the obtained 2D Ni-CPs, nitrogen gas adsorption-desorption isotherm measurements were performed on samples with different lateral sizes (samples A-E, as listed in **Table 6-1.1**). Their surface areas are summarized in **Table 6-1.1**:  $97 \text{ m}^2 \text{ g}^{-1}$  (sample A),  $79 \text{ m}^2 \text{ g}^{-1}$  (sample B),  $64 \text{ m}^2 \text{ g}^{-1}$  (sample C), and  $80 \text{ m}^2 \text{ g}^{-1}$  (sample D). After further increase of the lateral sizes beyond 150 nm for sample D (**Figure 6-1.3d**), the surface area is drastically decreased to  $7 \text{ m}^2 \text{ g}^{-1}$  (sample E). Thus, the accessibility of nitrogen gas to the particle interior varies according to the particle size (lateral size). In the case of large-sized particles, nitrogen gas cannot easily access the active sites of the particles which, as a result, exhibit a low surface area.

Transmission electron microscope (TEM) images of the Ni CPs prepared from different reaction solutions (samples C and D) are shown in **Figure 6-1.5**. Nanoflakes with different lateral sizes were observed. The sample with a high content of trisodium citrate dihydrate (*i.e.*, sample

D) shows larger lateral-sized nanoflakes than the one with a low content of trisodium citrate dihydrate (*i.e.*, sample C). High-resolution TEM images of edges of nanoflakes show that all lattice fringes are oriented in the same direction without any domain boundaries, although a slight distortion is observed. Selected-area electron diffraction (ED) patterns which are taken from one nanoflake show very intense spots, demonstrating their single-crystalline nature.

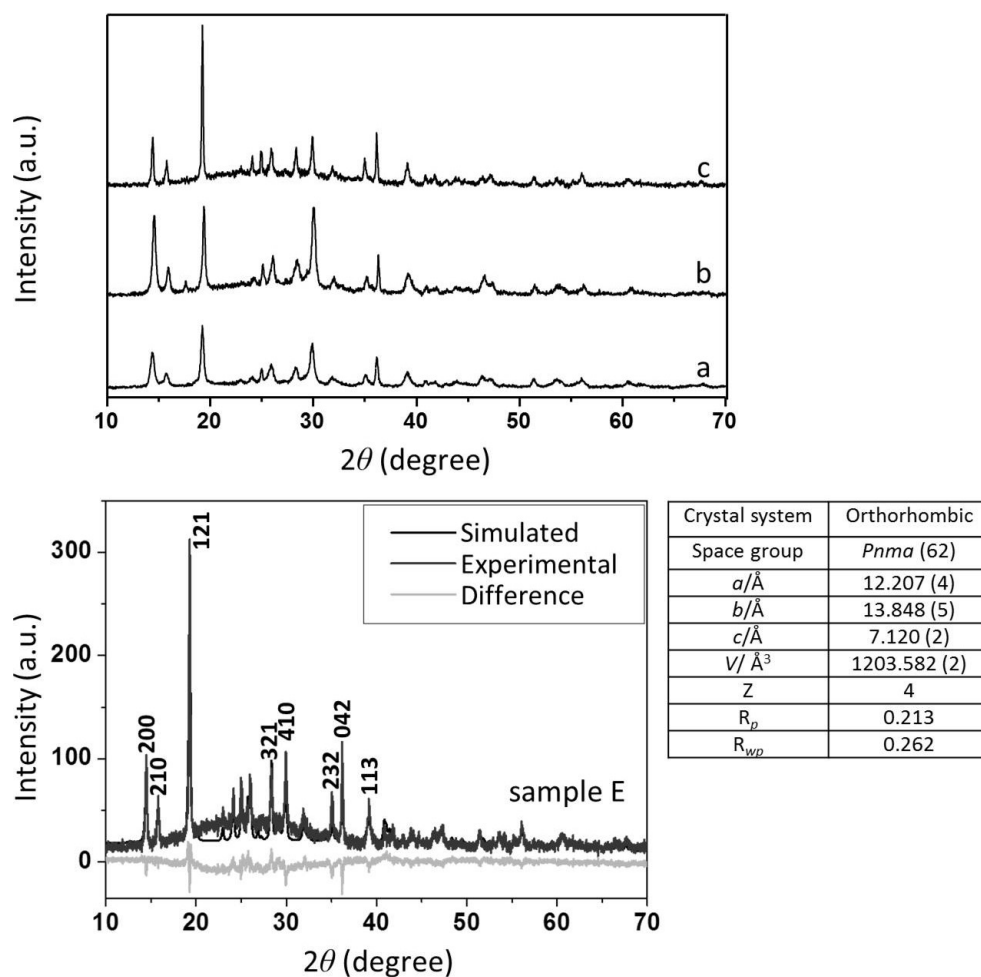


**Figure 6-1.4.** Wide-angle XRD patterns of various 2D Ni-CPs prepared from different reaction solutions: a) sample C, b) sample D, and c) sample E. The peak assignment of sample E is also shown below.



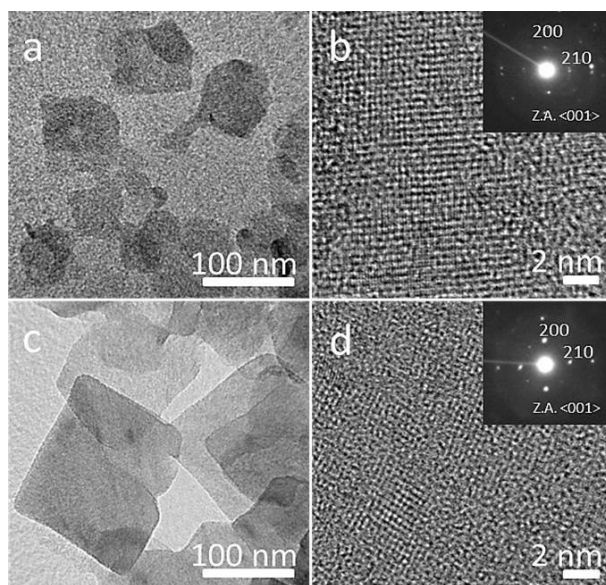


**Figure 6-1.5.** TEM and high resolution TEM images of 2D Ni-CPs nanoflakes prepared from different reaction solutions: (a, b) Sample C and (c, d) Sample D. Insets are corresponding ED patterns taken from one flake.

### 6-1.3.2. Conversion from 2D Ni-CPs to Nanoporous NiO

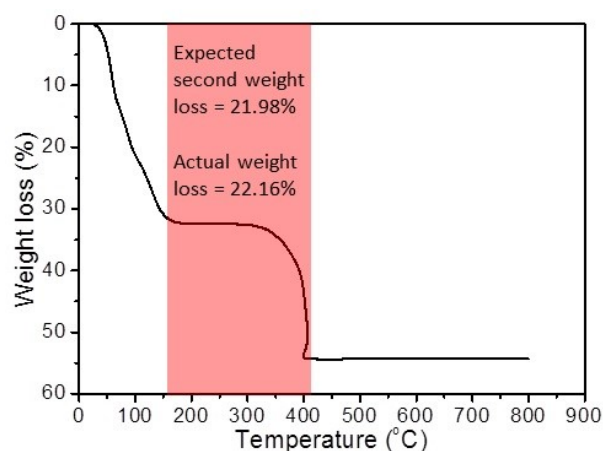
The cyano-groups between metals can be removed by thermal treatment in air. The metals are uniformly separated by cyano-groups in the crystal structure, so it is expected that metal oxides can be obtained. My Ni-CP nanoflakes were heated in air at three different temperatures (300, 400, and 500 °C). Various nanoporous NiO samples were obtained. As shown in **Table 6-1.2**, the obtained heat-treated samples are abbreviated as “X\_Y” where “X” refers to the original sample names (A, B, C, D, and E) and “Y” refers to the applied temperature.

Considering the TGA data (**Figures 6-1.6**), I can calculate the weight loss. It is well-known that a multiple-step transformation often happens during heating of Ni-CPs flakes. In the first stage, water molecules are removed (weight loss of ~32.44%) from room temperature up to ~150 °C. The second weight loss of ~22.16% can be assigned to the CN-groups starting to be released at ~300 °C. During this stage, the nickel is oxidized at the same time. After that, the

recrystallization of NiO is further occurred without any weight loss.

- Calculations:
- After water removal, 67.56% sample is remained
- The composition should be  $\text{Ni}[\text{Ni}(\text{CN})_4]$ .  
The weight is 221.458 g/mol.
- One  $\text{Ni}[\text{Ni}(\text{CN})_4]$  can produce two NiO.  
The weight is 149.384 g/mol.
- My rough calculations of the second weight loss is 67.56% x  
(72.074/221.458) = 21.98%.

Therefore, in the second step, it is revealed that both the organic removal and the oxidation reaction are occurred.



**Figures 6-1.6.** TG curves of Ni-CPs flakes in air at a heating rate of  $5\text{ }^{\circ}\text{C min}^{-1}$  from room temperature up to  $800\text{ }^{\circ}\text{C}$ .

**Table 6-1.2** The surface areas of heat-treated samples.

Sample name	Applied temperature ( $^{\circ}\text{C}$ )		
	300	400	500
A	140	66	24
B	144	64	17
C	107	38	14
D	79	27	9
E	60	13	8

Note: Heat-treated samples are abbreviated as 'X\_Y' where 'X' means the original sample names (A, B, C, D, and E) and 'Y' means the applied temperature, respectively.

The surface morphology of these oxides was examined by SEM, as shown in **Figures 6-1.7**, **6-1.8**, and **6-1.9**. Samples D and E heated at 300 °C (D\_300, E\_300) almost entirely retained the shapes of the original 2D flakes (**Figure 6-1.7 d** and **e**, respectively). During calcination at higher temperatures, however, large structural changes occur due to the fusion of several pores/voids following further crystallization in the framework. The samples heated at 400 and 500 °C are highly crystallized, and the original 2D Ni-CP morphology has been totally destroyed (**Figures 6-1.8** and **6-1.9**), as discussed in detail later.

**Figure 6-1.10** shows wide-angle XRD patterns for typical samples. In the case of sample C, the crystallized NiO phase is predominant, but unoxidized Ni is also formed as a secondary phase (*i.e.*, small peaks corresponding to Ni *fcc* phase are also observed, as marked by the squares). The generation of unoxidized Ni phase may be due to the fast thermal decomposition of Ni-CPs at high temperature. During this stage, the Ni species inside the nanoflakes are not oxidized in air, most likely due to a fast cleavage of the CN bond [20].

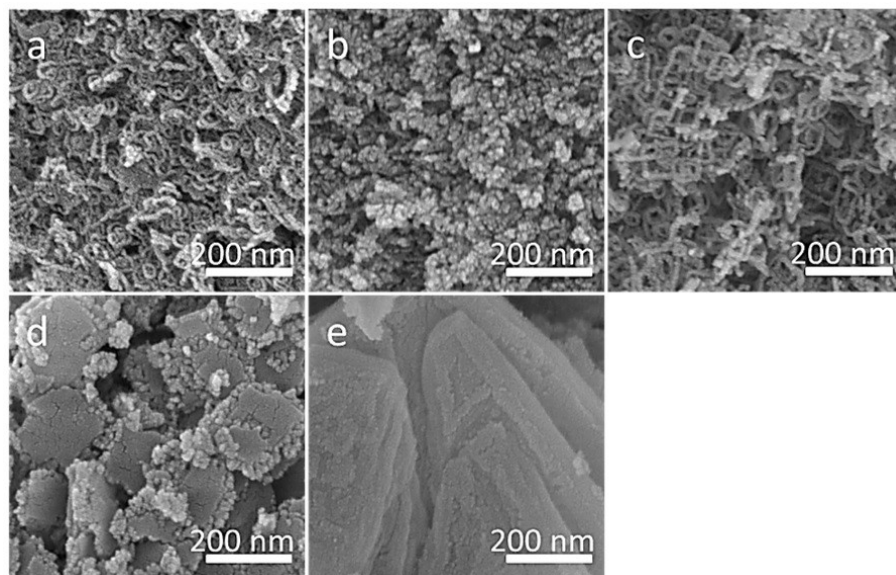


**Figure 6-1.7.** SEM images of NiO samples prepared by heating various 2D Ni-CPs at 300 °C: (a) A\_300, (b) B\_300, (c) C\_300, (d) D\_300, and (e) E\_300.

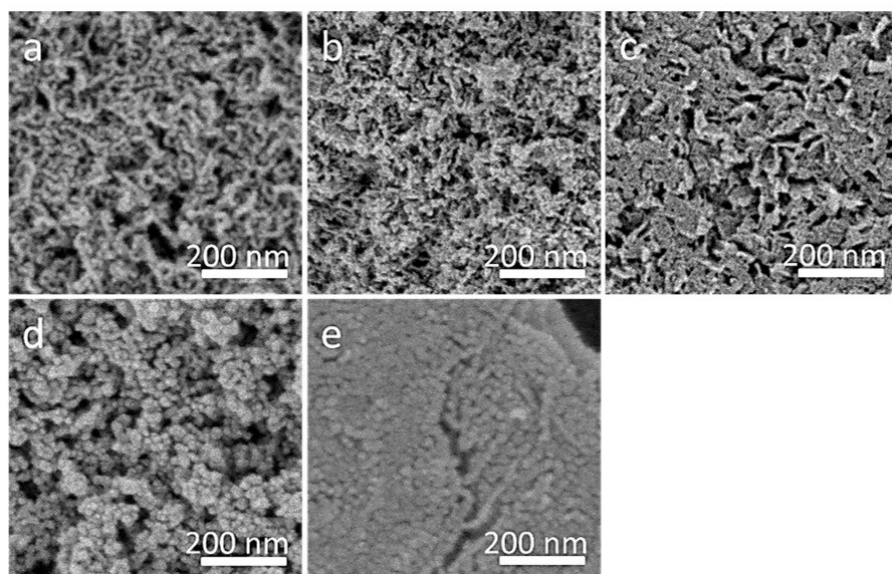


**Figure 6-1.8.** SEM images of NiO samples prepared by heating various 2D Ni-CPs at 400 °C: (a) A\_400, (b) B\_400, (c) C\_400, (d) D\_400, and (e) E\_400.

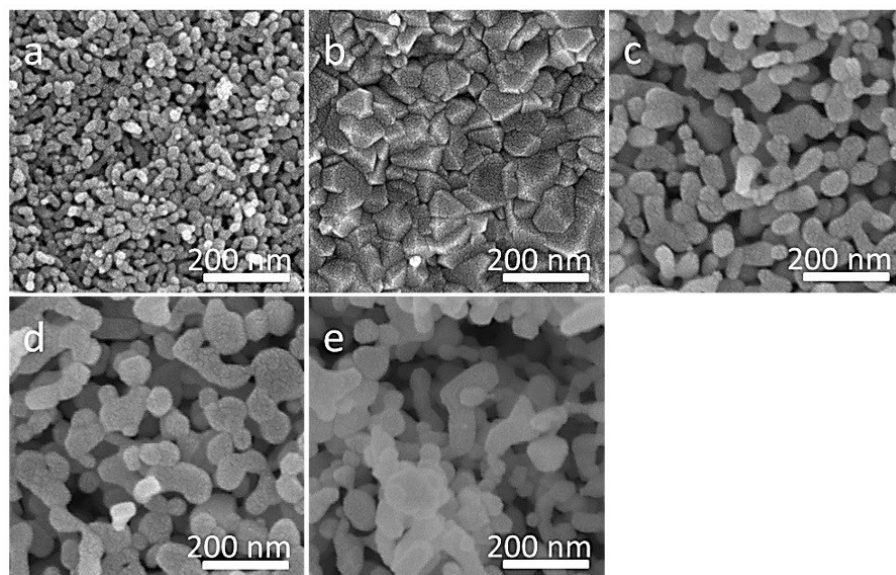


**Figure 6-1.9.** SEM images of NiO samples prepared by heating various 2D Ni-CPs at 500 °C: (a) A\_500, (b) B\_500, (c) C\_500, (d) D\_500, and (e) E\_500.

Another possibility is that the formation of Ni phase is caused by the presence of citrate ions adsorbed onto the surface of the 2D Ni-CP nanoflakes. Even though the as-prepared Ni-CPs were carefully washed with solvents, as described in the Experimental Section, negatively charged

citrate ions are thought to interact with the positively charged  $\text{Ni}^{2+}$  ions that are located on the surfaces of the Ni-CPs. These remaining citrate ions can act as a reducing agent for the NiO phase that is formed during the heat treatment. As shown in **Figure 6-1.10a-c**, by increasing the applied temperature, the amount of unoxidized Ni phase is gradually decreased, because oxygen molecules diffuse more easily through the sample. The degree of crystallinity is also increased, so that the average crystallite size calculated from Scherrer's equation is increased from 5.63 nm (for C\_300) to 12.7 nm (for C\_400) and 16.9 nm (for C\_500). It is interesting to point out that the heat-treated samples with larger lateral sizes (*e.g.*, sample D) show only NiO phase without any formation of unoxidized Ni phase (**Figure 6-1.10d**). By increasing the lateral size, the total amount of adsorbed citrate ions on the external flake surface is decreased to the point where it cannot supply the formation of reduced Ni phase anymore.

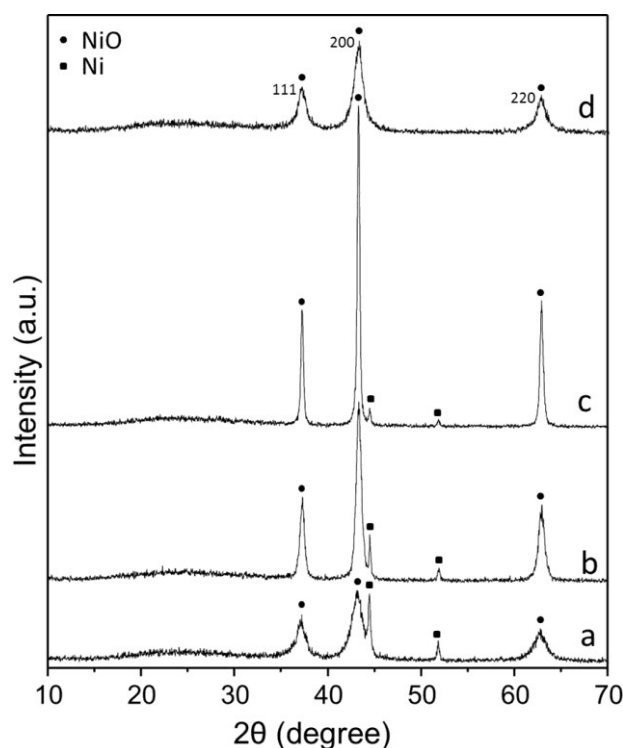


**Figure 6-1.10.** Wide-angle XRD patterns of various NiO samples: (a) NiO prepared by heating Sample C at 300 °C (C\_300), (b) NiO prepared by heating Sample C at 400 °C (C\_400), (c) NiO prepared by heating Sample C at 500 °C (C\_500), and (d) NiO prepared by heating Sample D at 300 °C (D\_300).

After thermal treatment at 300 °C, samples C and D (C\_300, D\_300) were characterized by TEM imaging (**Figure 6-1.11**). Both samples are well crystallized (**Figure 6-1.11b** and **e**) and the observed lattice fringes can be assigned to NiO phase (**Figure 6-1.12**). From the TEM, it is confirmed that sample D almost preserves the flake-like morphology of the precursor (**Figure 6-1.11d**). Only the edges of the flakes seem to have collapsed due to the crystallization, but the original flake-like morphology is well retained at the centers. Meanwhile, in the case of sample C, a large decrease in the lateral size is observed (**Figure 6-1.11a**). High angle annular dark field scanning transmission electron microscope (HAADF-STEM) images and the corresponding elemental mapping data can confirm the nanostructures and determine the distribution of elements (**Figure 6-1.11c** and **f**). The HAADF-STEM images show different contrast over the top surface, and this indicates the conversion of Ni-CP nanoflakes into the corresponding nanoporous oxides after heat treatment (**Figure 6-1.13**). From the elemental mapping, it is confirmed that both nickel and oxygen are uniformly distributed over the whole area.

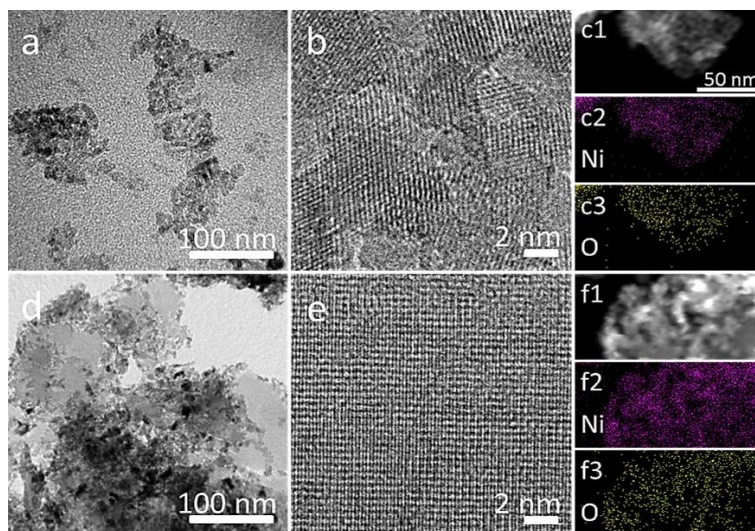


**Figure 6-1.11.** (a, d) TEM images, (b, e) high-resolution TEM images, (c1, f1) HAADF-STEM images, and (c2, c3, f2, f3) the corresponding elemental mapping (nickel and oxygen) of two NiO samples ((a-c) NiO prepared by heating Sample C at 300 °C (C\_300) and (d-f) NiO prepared by heating Sample D at 300 °C (D\_300), respectively).

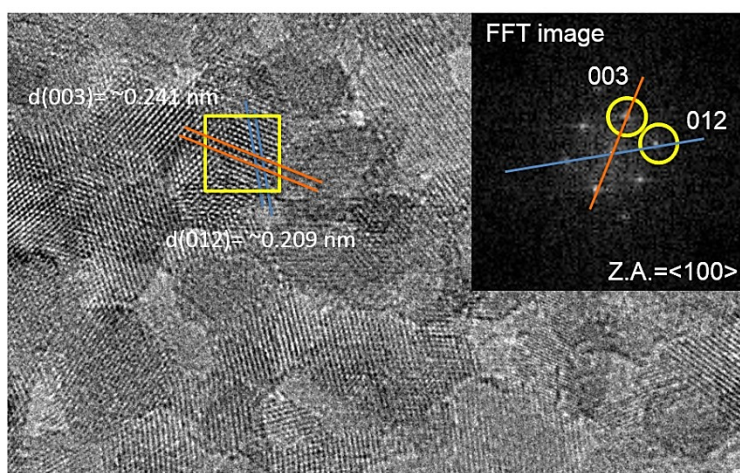


**Figure 6-1.12.** High-resolution TEM image of NiO sample prepared by heating Sample C at 300 °C (C\_300).

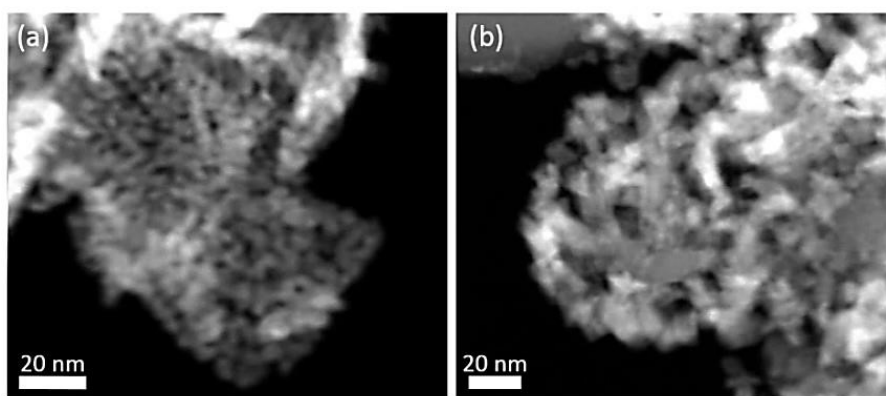


**Figure 6-1.13.** HAADF-STEM images of two NiO samples ((a) NiO prepared by heating Sample C at 300 °C (C\_300) and (b) NiO prepared by heating Sample D at 300 °C (D\_300), respectively).

I calculated the average crystalline sizes by Scherer equation (1) using the peaks of XRD (111, 200, and 220) (**Figure 6-1.14**) in both cases of NiO flakes (D\_300) and particles (A\_300) and values are collected in **Table 6-1.3**.

$$D = \frac{K\lambda}{\beta \cos \theta} \quad (6-1.2)$$

Where,  $D$  is the average crystalline size,  $K$  (0.9) is the shape factor,  $\lambda$  (0.15405 nm) is the wavelength of incident X-ray,  $\beta$  is the full width at half-maximum (FWHM), and  $\theta$  is the peak

position. The estimated crystalline sizes are in a good agreement with the electron diffraction (ED) patterns (**Figure 6-1.14**) which reveal the polycrystalline nature of both the flakes and particles and Scherer equation is believed to be a suitable choice for these calculations. The large NiO particles are formed by the aggregation of small crystallites randomly oriented. Moreover, the crystallites in the NiO flakes are larger than those of the NiO particles, indicating a higher crystallinity.

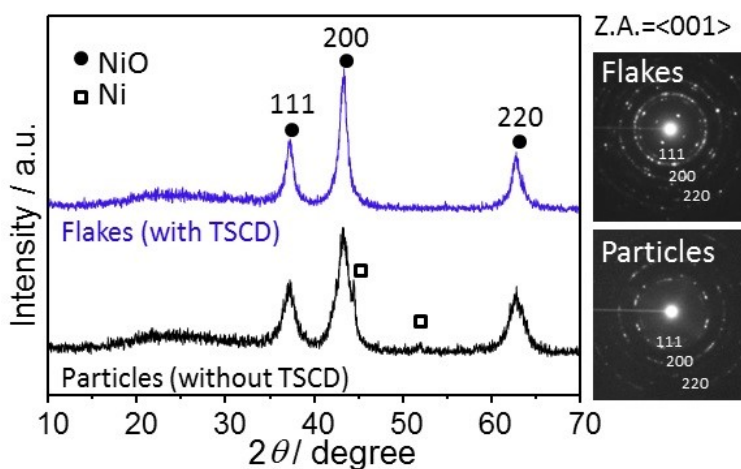


**Figure 6-1.14.** Wide-angle XRD and ED patterns of NiO flakes and particles.

**Table 6-1.3** The average crystalline sizes ( $D$  nm) of NiO flakes (D\_300) and particles (A\_300) calculated using the Scherer equation.

Sample name	$d$	$\beta$ (rad.)	$2\theta^\circ$	$\beta \cdot \cos\theta$	$D$ (nm)
NiO flakes	111	0.0147	37.16	0.0140	9.90
NiO particles	111	0.0254	37.16	0.0240	5.77
NiO flakes	200	0.0172	43.17	0.0159	8.72
NiO particles	200	0.0412	43.17	0.0383	3.62
NiO flakes	220	0.0170	62.73	0.0145	9.56
NiO particles	220	0.0352	62.73	0.0299	4.63

In order to investigate the chemical and electronic states, sample D heat-treated at 300 °C (D\_300) was characterized by X-ray photoelectron spectroscopy (XPS; **Figure 6-1.15**). The Ni  $2p_{3/2}$  peak can be observed at a binding energy of 855.4 eV. I also confirm a satellite peak greater



than the main peak by approximately 5 eV at 860.6 eV. The shoulder peak for Ni  $2p_{1/2}$  is located at 872.8 eV. It has been reported that  $\text{Ni}^{2+}$  gives a characteristic Ni  $2p_{3/2}$  peak with a subpeak for Ni  $2p_{1/2}$  [22]. No peak corresponding to unoxidized  $\text{Ni}^0$  could be observed. This is strong evidence for the presence of the oxidized Ni state. Thus, it is shown that the Ni-CP nanoflakes are completely converted into pure NiO phase after heat treatment at 300 °C, which is in good agreement with the wide-angle XRD data (**Figure 6-1.10**). The O  $1s$  region shows a single strong peak at 529.2 eV and an additional O  $1s$  peak at 531.1 eV associated with the oxygen from the oxide [23]. This evidence also supports the formation of NiO phase after the thermal decomposition of 2D Ni-CP nanoflakes.

The porosity of the heat-treated samples was examined by nitrogen gas adsorption-desorption isotherms. The surface areas are summarized in **Table 6-1.2**. The surface area of the nanoporous NiO samples is higher than the one from the original Ni-CP nanoflakes before heat treatment. The high surface area taking place after heating at 300 °C reduces seriously when the temperature is increased further (up to 500 °C) due to the fusion of the nanopores during the crystallization in the framework [24], as discussed above.

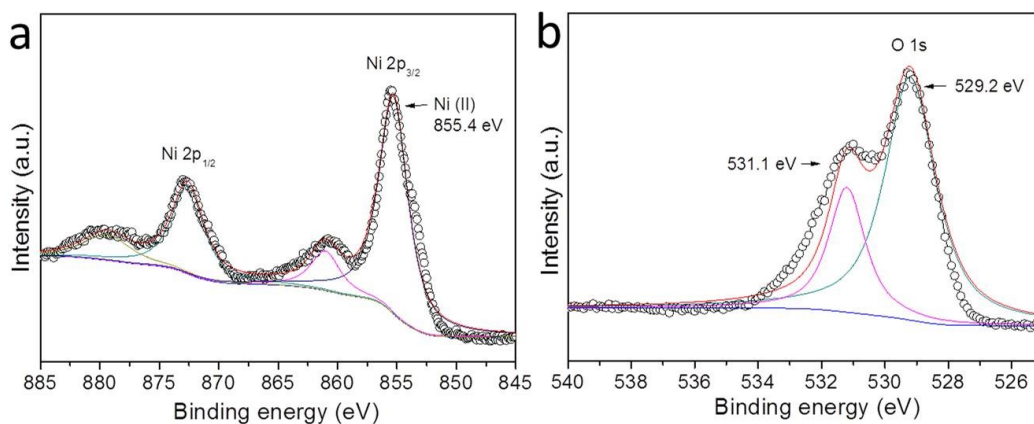


**Figure 6-1.15.** (a) Ni  $2p$  and (b) O  $1s$  XPS spectra of NiO sample prepared by heating Sample D at 300 °C (D\_300).

### 6-1.3.3. Supercapacitor Application Using Nanoporous NiO

The fast growing interest in portable electronic devices and electric vehicles has stimulated extensive research in high performance energy storage devices, such as supercapacitors [25]. Cyclic voltammetry (CV) measurements were performed in the potential range of 0.0-0.5 V for samples A-E which were heat treated at 300 °C (*i.e.*, A\_300, B\_300, C\_300, D\_300, and E\_300).

**Figure 6-1.16a** shows the CV shapes at a scan rate of 5 mV s<sup>-1</sup>.

The oxidation and reduction peak positions vary, however, depending on the lateral sizes. The specific capacitance values calculated from the CV curves are 186 (for A\_300), 225 (for B\_300), 447 (for C\_300), 638 (for D\_300), and 4.53 (for E\_300). The specific capacitances with various scan rates are summarized in **Table 6-1.4**.

**Table 6-1.4** Specific capacitance values for different NiO samples heated at 300 °C. Heat-treated samples are abbreviated as ‘X\_Y’ where ‘X’ means the original sample names (A, B, C, D, and E) and ‘Y’ means the applied temperature, respectively.

Sample name	Specific capacitance (F·g <sup>-1</sup> )				Retention
	5 mV	20 mV	40 mV	60 mV	
A_300	186	132	98	84	45.1 %
B_300	225	136	95	70	31.1 %
C_300	447	289	231	196	43.9 %
D_300	638	459	360	295	46.0 %
E_300	4.53	< 1.00	< 1.00	< 1.00	Undetectable

It is clear that D\_300 shows the highest specific capacitance compared to the other samples. This can be explained as follows. As discussed in the wide-angle XRD data, samples D and E with larger lateral sizes contain a pure NiO phase after heat treatment, whereas the other samples with smaller lateral sizes contain impurities such as Ni metal, which are not useful to redox transition in supercapacitor application. Especially for sample D heat-treated at 300 °C (D\_300), the lateral

size distribution of NiO flakes is found to be uniform. The random aggregation of the flakes (**Figure 6-1.7d**) prevents them from stacking together, thus leading to a relatively high surface area of  $79 \text{ m}^2 \text{ g}^{-1}$ . Such an ideal structure gives the electrolyte easy access to the electrode surface, which ultimately results in a high capacitance value. The CVs at different scan rates for sample D heat-treated at  $300 \text{ }^\circ\text{C}$  (D\_300) are shown in **Figure 6-1.16b**. The specific capacitance decreases when the scan rate is increased (**Figure 6-1.16c**). Higher scan rates result in shorter redox times, leading to incomplete redox transitions at the “inner” active sites. The best specific capacitance value obtained in the present work is significantly higher than the ones previously reported (**Table 6-1.5**) [26]. This result highlights the importance of optimizing both the 2D shape and the crystallinity of the structure in order to improve the energy-storage performance. For more convenience, I also compared the specific capacitance of my NiO flakes with the reported 2D NiO nanosheets/nanoflakes at the same scan rate and electrolyte (**Table 6-1.6**). The best specific capacitance value obtained in the present work is significantly higher than that in previous reports.

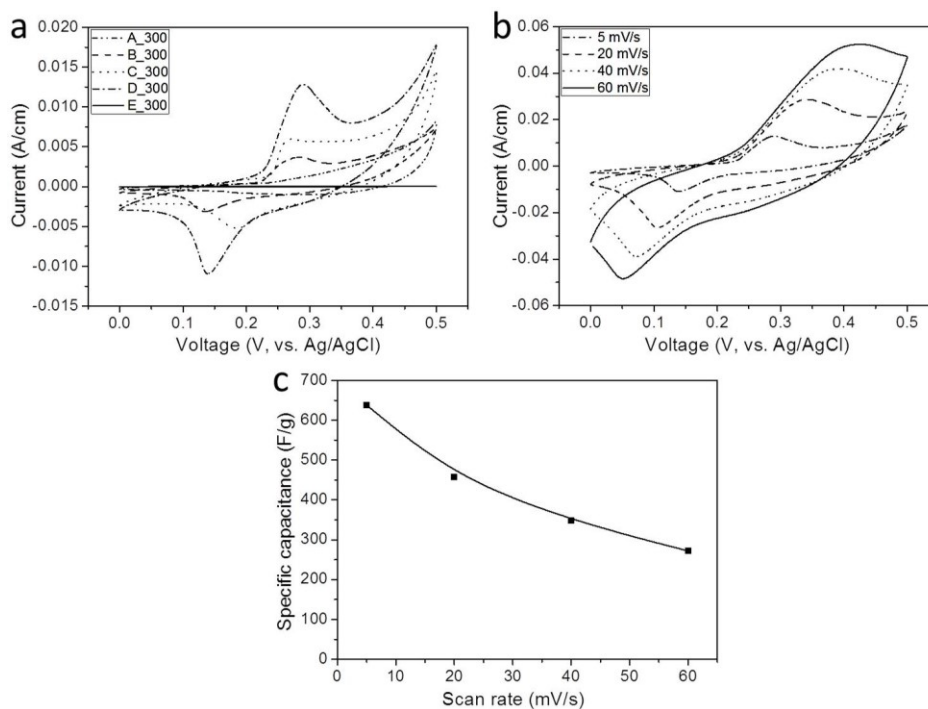


**Figure 6-1.16.** (a) Cyclic voltammograms (CVs) of NiO samples prepared by heating various 2D

Ni-CPs at 300 °C (A\_300, B\_300, C\_300, D\_300, and E\_300, respectively). The scan rate is 5 mV. (b) CVs of NiO sample prepared by heating Sample D at 300 °C (D\_300) at different scan rates. (c) Specific capacitance at different scan rates of D\_300.

**Table 6-1.5** Comparison of capacitance performance of NiO-based supercapacitors.

No.	Morphology	Capacitance (F·g <sup>-1</sup> )	Scan rate (mV·s <sup>-1</sup> )	Potential window (V)	Electrolyte	Ref
1	hollow spheres	346	-	0.0- 0.6	2M KOH	[26a]
2	nanosheets	470	5	0.0- 0.45	6 M KOH	[26b]
3	flower shape	585	-	0.0- 0.45	2 M KOH	[26c]
4	honeycomb	167	20	-0.8- 0.4	2 M KOH	[26d]
5	flower shape	480	-	-0.05- 0.4	2 M KOH	[26e]
6	nanocolumns	390	-	-0.3- 0.7	1 M KOH	[8]
7	nanoflakes	638	5	0.0- 0.5	2M KOH	This study

**Table 6-1.6** Comparison of capacitance performance of 2D NiO-based supercapacitors.

Morphology	Scan rate	Capacitance	Electrolyte	Ref
NiO flakes	5 mV·s <sup>-1</sup>	411 F·g <sup>-1</sup>	2 M KOH	[27]
NiO nanoflakes	5 mV·s <sup>-1</sup>	263 F·g <sup>-1</sup>	2 M KOH	[28]
2D NiO nanosheets	5 mV·s <sup>-1</sup>	527 F·g <sup>-1</sup>	2 M KOH	[29]
NiO nanoflakes	5 mV·s <sup>-1</sup>	402 F·g <sup>-1</sup>	2 M KOH	[30]
NiO nanosheets	5 mV·s <sup>-1</sup>	470 F·g <sup>-1</sup>	2 M KOH	[31]
Mesoporous NiO nanosheets	5 mV·s <sup>-1</sup>	168 F·g <sup>-1</sup>	2 M KOH	[32]
NiO nanosheet hollow sphere	5 mV·s <sup>-1</sup>	556 F·g <sup>-1</sup>	2 M KOH	[33]
NiO Nanoflakes	5 mV·s <sup>-1</sup>	638 F·g <sup>-1</sup>	2M KOH	This study

## 6-1.4. Conclusion

I have demonstrated the bottom-up synthesis of various types of 2D Ni-CP nanoflakes by using trisodium citrate as a chelating agent to control the nucleation rate and the crystal growth. The nanoflake sizes were gradually increased by increasing the concentration of trisodium citrate. These Ni-CP nanoflakes were thermally converted into the corresponding nanoporous NiO with high surface area. It was found that the obtained nanoporous NiO materials could serve as an efficient electrode for supercapacitors. I strongly believe that my method will be useful for the preparation of other types of CP nanoflakes which can serve as potential precursors for the

preparation of various nanoporous metal oxides. Such 2D CPs and their derivatives will open new opportunities in the future.

## 6-1.5. Acknowledgements

This research is partially supported by the Grants-in-Aid for Young Scientists A (Research Project Number: 26708028) of the Japan Society for the Promotion of Science (JSPS), Japanese-Taiwanese Cooperative Program of the Japan Science and Technology Agency (JST), The Canon Foundation, and Auto CRC 2020 (Australia). M.B.Z. thanks the Culture Affairs and Missions Sector of the Ministry of Higher Education in Egypt for financial support.

## 6-1.6. References

- [1] a) J. Wei, Y. Liu, J. Chen, Y. Li, Q. Yue, G. Pan, Y. Yu, Y. Deng, D. Zhao, *Adv. Mater.* **2014**, *26*, 1782; b) D. Xu, Y. Ma, Z. Jing, L. Han, B. Singh, J. Feng, X. Shen, F. Cao, P. Oleynikov, H. Sun, O. Terasaki, S. Che, *Nat. Commun.* **2014**, *5*, 4262; c) J. Gao, X. Zhang, S. Xu, F. Tan, X. Li, Y. Zhang, Z. Qu, X. Quan, J. Liu. *Chem. Eur. J.* **2014**, *20*, 1957.
- [2] a) B. Kong, J. Tang, C. Selomulya, W. Li, J. Wei, Y. Fang, Y. Wang, G. Zheng, D. Zhao, *J. Am. Chem. Soc.* **2014**, *136*, 6822; b) C. Karakaya, Y. Türker, Ö. Dag, *Adv. Funct. Mater.* **2013**, *23*, 4002; c) S. Dutta, A. Bhaumik, *ChemSusChem.* **2013**, *6*, 2039 ; d) H. Atae-Esfahani, M. Imura, Y. Yamauchi, *Angew. Chem. Int. Ed.* **2013**, *52*, 13611; *Angew. Chem.* **2013**, *125*, 13856; e) C. Li, T. Sato, Y. Yamauchi, *Angew. Chem. Int. Ed.* **2013**, *52*, 8050; *Angew. Chem.* **2013**, *125*, 8208; f) X. Li, J. Liu, A.F. Masters, V.K. Pareek, T. Maschmeyer, *APL Mater.* **2013**, *1*, 041101; F. H. Bijarbooneh, Y. Zhao, Z. Sun, Y.U. Heo, V. Malgras, J.H. Kim, S.X. Dou, *APL Mater.* **2013**, *1*, 032106.

- [3] a) G.S. Attard, C.G. Göltner, J.M. Corker, S. Henke, R.H. Templer, *Angew. Chem. Int. Ed. Engl.* **1997**, *36*, 1315; *Angew. Chem.* **1997**, *109*, 1372 ; b) Y. Yamauchi, *J. Ceram. Soc. Jpn.* **2013**, *121*, 831.
- [4] a) K.C.W. Wu, X. Jiang, Y. Yamauchi, *J. Mater. Chem.* **2011**, *21*, 8934; b) K.C.W. Wu, Y. Yamauchi, *J. Mater. Chem.* **2012**, *22*, 1251.
- [5] a) H. Yang, N. Coombs, Ö. Dag, I. Sokolova, G.A. Ozin, *J. Mater. Chem.* **1997**, *7*, 1755; b) Y.H. Lai, S.W. Cheng, S.W. Chen, J.W. Chang, C.J. Su, A.C. Su, H.S. Sheu, C.Y. Mou, U.S. Jeng, *RSC Adv.* **2013**, *3*, 3270.
- [6] Z. Wu, Q. Li, D. Feng, P.A. Webley, D. Zhao, *J. Am. Chem. Soc.* **2010**, *132*, 12042.
- [7] a) A.H. Lu, F. Schüth, *Adv. Mater.* **2006**, *18*, 1793; b) C.Y. Ma, Z. Mu, J.J. Li, Y.G. Jin, J. Cheng, G.Q. Lu, Z.P. Hao, S.Z. Qiao, *J. Am. Chem. Soc.* **2010**, *132*, 2608; c) B. Coasne, A. Mezy, R.J.M. Pellenq, D. Ravot, J.C. Tedenac, *J. Am. Chem. Soc.* **2009**, *131*, 2185.
- [8] X. Zhang, W. Shi, J. Zhu, W. Zhao, J. Ma, S. Mhaisalkar, T.L. Maria, Y. Yang, H. Zhang, H.H. Hng, Q. Yan, *Nano Res.* **2010**, *3*, 643.
- [9] Y. Fang, Y. Lv, R. Che, H. Wu, X. Zhang, D. Gu, G. Zheng, D. Zhao, *J. Am. Chem. Soc.* **2013**, *135*, 1524.
- [10] a) B.C. Chen, H.P. Lin, M.C. Chao, C.Y. Mou, C.Y. Tang, *Adv. Mater.* **2004**, *16*, 1657; b) Y.Q. Yeh, H.P. Lin, C.Y. Tang, C.Y. Mou, *J. Colloid Interface Sci.* **2011**, *362*, 354; c) M.L. Lin, C.C. Huang, M.Y. Lo, C.Y. Mou, *J. Phys. Chem. C* **2008**, *112*, 867.
- [11] a) O.M. Yaghi, M.O. Keffe, N.W. Ockwig, H.K. Chae, M. Eddaoudi, J. Kim, *Nature* **2003**, *423*, 705; b) S. Kitagawa, R. Kitaura, S.I. Noro, *Angew. Chem. Int. Ed.* **2004**, *43*, 2334; *Angew. Chem.* **2004**, *116*, 2388; c) X.B. Zhao, B. Xiao, A.J. Fletcher, K.M. Thomas, D. Bradshaw, M.J. Rosseinsky, *Science* **2004**, *306*, 1012; d) S.T. Meek, J.A. Greathouse, M.D. Allendorf, *Adv. Mater.* **2011**, *23*, 249; e) M.C. Das, S. Xiang, Z. Zhang, B. Chen, *Angew.*

- Chem. Int. Ed.* **2011**, *50*, 10510; *Angew. Chem.* **2011**, *123*, 10696; f) J. An, C.M. Shade, D.A. Chengelis-Czegan, S. Petoud, N.L. Rosi, *J. Am. Chem. Soc.* **2011**, *133*, 1220; g) P. Dechambenoit, J.R. Long, *Chem. Soc. Rev.* **2011**, *40*, 3249; h) S. Furukawa, Y. Sakata, S. Kitagawa, *Chem. Lett.* **2013**, *42*, 570.
- [12] W. Cho, S. Park, M. Oh, *Chem. Commun.* **2011**, *47*, 4138.
- [13] a) S. Jung, W. Cho, H.J. Lee, M. Oh, *Angew. Chem. Int. Ed.* **2009**, *48*, 1459; *Angew. Chem.* **2009**, *121*, 1487; b) H. Thakuria, B.M. Borah, G. Das, *Eur. J. Inorg. Chem.* **2007**, 524.
- [14] W. Wang, Y. Li, R. Zhang, D. He, H. Liu, S. Liao, *Catal. Commun.* **2011**, *12*, 875.
- [15] F.X. Qin, S.Y. Jia, Y. Liu, X. Han, H.T. Ren, W.W. Zhang, J.W. Hou, S.H. Wu, *Mater. Lett.* **2013**, *101*, 93.
- [16] M.S.Y. Parast, A. Morsali, *Inorg. Chem. Commun.* **2011**, *14*, 645.
- [17] W. Cho, Y.H. Lee, H.J. Lee, M. Oh, *Chem. Commun.* **2009**, 4756.
- [18] a) M. Hu, Y. Yamauchi, *Chem. Asian J.* **2011**, *6*, 2282; b) M. Hu, A.A. Belik, H. Sukegawa, Y. Nemoto, M. Imura, Y. Yamauchi, *Chem. Asian J.* **2011**, *6*, 3195; c) M. Hu, A.A. Belik, M. Imura, K. Mibu, Y. Tsujimoto, Y. Yamauchi, *Chem. Mater.* **2012**, *24*, 2698; d) M. Hu, J.S. Jiang, F.X. Bu, X.L. Cheng, C.C. Lin, Y. Zeng, *RSC Adv.* **2012**, *2*, 4782; e) M. Hu, J.S. Jiang, *CrystEngComm* **2010**, *12*, 3391; f) C.J. Du, F.X. Bu, D.M. Jiang, Q.H. Zhang, J.S. Jiang, *CrystEngComm* **2013**, *15*, 10597; g) F.X. Bu, C.J. Du, Q.H. Zhang, J.S. Jiang, *CrystEngComm* **2014**, *16*, 3113.
- [19] M.B. Zakaria, M. Hu, Y. Tsujimoto, Y. Sakka, N. Suzuki, Y. Kamachi, M. Imura, S. Ishihara, K. Ariga, Y. Yamauchi, *Chem Asian J.* **2014**, *9*, 1511.
- [20] M. Hu, S. Ishihara, Y. Yamauchi, *Angew. Chem. Int. Ed.* **2013**, *52*, 1235; *Angew. Chem.* **2013**, *125*, 1273.
- [21] M. Hu, S. Ishihara, K. Ariga, M. Imura, Y. Yamauchi, *Chem. Eur. J.* **2013**, *19*, 1882.

- [22] a) M.H. Koppelman, J.G. Dillard, *Clays Clay Miner.* **1977**, *25*, 457; b) N.S. McIntyre, M.G. Cook, *Anal. Chem.* **1975**, *47*, 2208.
- [23] J.C. Dupin, D. Gonbeau, P. Vinatier, A. Levasseur, *Phys. Chem. Chem. Phys.* **2000**, *2*, 1319.
- [24] a) M.B. Zakaria, M. Hu, N. Hayashi, Y. Tsujimoto, S. Ishihara, M. Imura, N. Suzuki, Y.Y. Huang, Y. Sakka, K. Ariga, K.C.W. Wu, Y. Yamauchi, *Eur. J. Inorg. Chem.* **2014**, 1137; b) B. Lee, D. Lu, J.N. Kondo, K. Domen, *Chem. Commun.* **2001**, 2118.
- [25] a) S. Chen, W. Xing, J. Duan, X. Hu, S.Z. Qiao, *J. Mater. Chem. A* **2013**, *1*, 2941; b) S. Chen, J. Duan, M. Jaroniec, S.Z. Qiao, *J. Mater. Chem. A* **2013**, *1*, 9409; c) Y. Gao, Y.S. Zhou, W. Xiong, L.J. Jiang, M. Mahjouri-samani, P. Thirugnanam, X. Huang, M.M. Wang, L. Jiang, Y.F. Lu, *APL Mater.* **2013**, *1*, 012101; d) T. Funabashi, J. Mizuno, M. Sato, M. Kitajima, M. Matsuura, S. Shoji, *APL Mater.* **2013**, *1*, 032104.
- [26] a) X. Yan, X. Tong, J. Wang, C. Gong, M. Zhang, L. Liang, *Mater. Lett.* **2013**, *95*, 1; b) J.W. Lee, T. Ahn, J.H. Kim, J.M. Ko, J.-D. Kim, *Electrochem. Acta* **2011**, *56*, 4849; c) C.Y. Cao, W. Guo, Z.M. Cui, W.G. Song, W. Cai, *J. Mater. Chem.* **2011**, *21*, 3204; d) U.M. Patil, R.R. Salunkhe, K.V. Gurav, C.D. Lokhande, *Appl. Surf. Sci.* **2008**, *255*, 2603; e) S.I. Kim, J.S. Lee, H.J. Ahn, H.K. Song, J.H. Jang, *ACS Appl. Mater. Interfaces* **2013**, *5*, 1596.
- [27] P. Justin, S. K. Meher, G. R. Rao, *J. Phys. Chem. C*, **2010**, *114*, 5203.
- [28] S. Vijayakumar, S. Nagamuthu, G. Muralidharan, *ACS Appl. Mater. Interfaces* **2013**, *5*, 2188.
- [29] Z. Sun, L. Hui, W. Ran, Y. Lu, D. Jia, *New J. Chem.*, **2016**, *40*, 1100.
- [30] S. Ding, T. Zhu, J.S. Chen, Z. Wang, C. Yuan, X. W. Lou, *J. Mater. Chem.* **2011**, *21*, 6602.
- [31] J.W. Lee, T. Ahn, J.H. Kim, J.M. Ko, J.-D. Kim, *Electrochemi Acta*, **2011**, *56*, 4849.
- [32] C.Z. Yuan, *Mater. Res. Bull.* **2013**, *48*, 840.
- [33] W. Yu, X. Jiang, S. Ding, B. Q. Li, *J. Power Sources*, **2014**, *256*, 440.



## Chapter 6-2

# 6-2. Synthesis of Nanoporous Ni-Co Mixed Oxides by Thermal Decomposition of Metal-Cyanide Coordination Polymers

### 6-2.1. Introduction

Nanoporous/mesoporous metal oxides are interesting materials which have been widely applied in catalysis, sensing, and adsorption. Significant progress has been made in the synthesis of nanoporous metal oxides [1]. For example, various structure-directing agents have been utilized in order to obtain self-assembled nanostructured/mesostructured metal oxides by suitably adjusting the reaction conditions [2]. Current preparation methods are mainly based on wet-chemistry [3a-c], although hard-templating techniques are also available to prepare nanoporous materials [3d-f]. In the case of hard-templating method, large amounts of hazardous chemicals, such as corrosive HF solvent, are required to remove the templates and to successfully prepare nanostructured materials. Shape control in nanoporous metal oxides is also an effective way to further improve their performance. For example, small-sized particles or thin films with nanoporous structures show accelerated adsorption kinetics of guest molecules and controlled

release properties, which cannot be attained by particles with irregular shape [4]. The aforementioned traditional approaches [2,3] are not versatile engineering methods suitable for the control of morphology. Therefore, finding an efficient way to prepare nanoporous metal oxides with good shape control is of fundamental importance.

Thermal treatment of coordination polymers (CPs) including metal-organic frameworks (MOFs) has been proved as a promising strategy for preparing nanoporous metal oxides [5]. CPs have a large fraction of metal ions as well as organic ligands. The considerable amount of metal atoms can be utilized as a metal source, while the organic components can provide voids after being removed by calcination. Under optimized conditions, the original shapes of CPs can be retained in the products. Therefore, this method has the potential to overcome the difficulties met in typical shape-controlled syntheses of nanoporous metal oxides using soft- or hard-templating methods.

Herein, I prepared nanoporous Ni-Co mixed oxides by thermal treatment of monodispersed metal-cyanide CPs. By controlling the composition and the shape, our material could reach an efficient electrocatalytic activity for oxygen evolution reaction (OER). It is generally known that single oxides of solely Co or Ni show lower activity as electrodes, while mixing these oxides results in a more promising performance [6]. Our nanoporous Ni-Co mixed oxide displays good activity for OER, showing the lowest impedance and more negative onset potential on the electrode/electrolyte interface. This high efficiency is probably due to the nanoporous structure and plate-like morphology, which contribute to the diffusion of oxygen, electrolyte, and intermediate species throughout the whole surface of the material.

## 6-2.2. Experimental Section

### 6-2.2.1. Materials Synthesis

**Synthesis of CoCo nanocubes:** In atypical procedure, cobalt chloride (77.9 mg) and trisodium citrate dihydrate (397.1 mg) were dissolved in 20 mL water to form a clear solution (A). Meanwhile,  $K_3[Co(CN)_6]$  (130 mg) was dissolved in 20 mL water to form a second clear solution (B). Then, solution A and solution B were mixed together under magnetic stirring. The obtained solution was aged for 24 h, followed by the formation of a precipitate which was collected by centrifugation. After washing with water and ethanol extensively, the precipitate was dried at room temperature. The crystal structure is shown in **Figure 6-2.1a**.

**Synthesis of NiCo nanocubes:** In atypical procedure, nickel chloride hexahydrate (59.6 mg) and trisodium citrate dihydrate (100 mg) were dissolved in 20 mL water to form a clear solution (A). Meanwhile,  $K_3[Co(CN)_6]$  (130 mg) was dissolved in 20 mL water to form a second clear solution (B). Then, solution A and solution B were mixed together under magnetic stirring. The obtained solution was aged for 24 h, followed by the formation of a precipitate which was collected by centrifugation. After washing with water and ethanol extensively, the precipitate was dried at room temperature. The crystal structure is shown in **Figure 6-2.1b**.

**Synthesis of CoNi nanoflakes:** In atypical procedure, cobalt chloride (59.6 mg) and trisodium citrate dihydrate (100 mg) were dissolved in 20 mL water to form a clear solution (A). Meanwhile,  $K_2[Ni(CN)_4]$  (130 mg) was dissolved in 20 mL water to form a second clear solution (B). Then, solution A and solution B were mixed together under magnetic stirring. The obtained solution was aged for 24 h, followed by the formation of a precipitate which was collected by centrifugation. After washing with water and ethanol extensively, the precipitate was dried at room temperature. The crystal structure is shown in **Figure 6-2.1c**.

**Synthesis of NiNi nanoflakes:** In atypical procedure, nickel chloride hexahydrate (59.6 mg) and trisodium citrate dihydrate (100 mg) were dissolved in 20 mL water to form a clear solution (A). Meanwhile,  $K_2[Ni(CN)_4]$  (130 mg) was dissolved in 20 mL water to form a second clear solution (B). Then, solution A and solution B were mixed together under magnetic stirring. The obtained solution was aged for 24 h, followed by the formation of a precipitate which was collected by centrifugation. After washing with water and ethanol extensively, the precipitate was dried at room temperature. The crystal structure is shown in **Figure 6-2.1d**.

**Conversion to nanoporous metals oxides:** The as-prepared powders were used as precursor for nanoporous oxide materials. The powders (100.0 mg) were placed in a melting pot which was then heated from room temperature to the desired temperature using an electronic furnace at a rate of  $1\text{ }^{\circ}\text{C min}^{-1}$ . After reaching the desired temperature ( $300\text{ }^{\circ}\text{C}$ ), the samples were annealed for 4h to ensure complete thermal decomposition. After that, the powders were cooled inside the furnace at a rate of  $1\text{ }^{\circ}\text{C min}^{-1}$ . Finally, the obtained powder was collected for characterization. All calcination processes were performed in air.

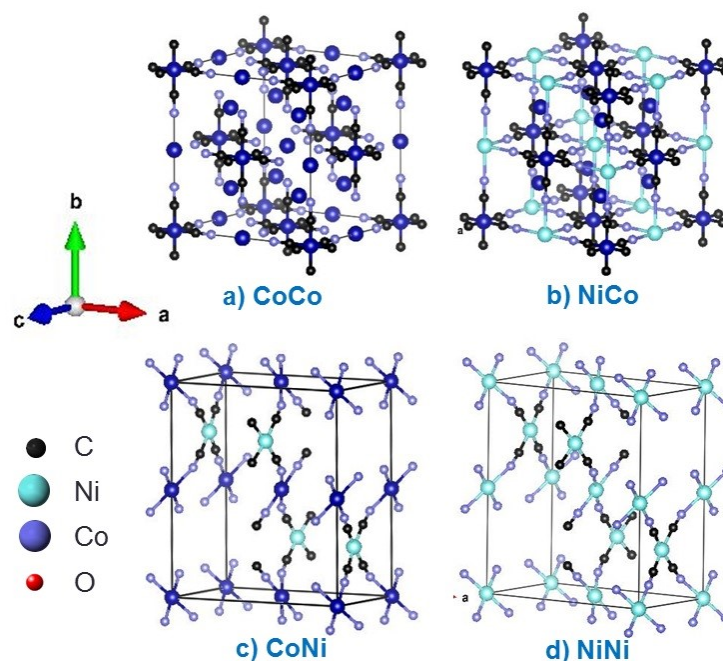


**Figure 6-2.1.** Crystal structures of (a) CoCo, (b) NiCo, (c) CoNi, and (d) NiNi. The water molecules are omitted here.

### 6-2.2.2. Characterization

SEM images were taken with a Hitachi SU8000 scanning microscope at an accelerating voltage of 5 kV. The TEM observation was performed using a JEM-2100F TEM system operated at 200 kV and equipped for energy-dispersive spectrometer analysis. Wide angle powder X-ray diffraction (XRD) patterns were obtained with a Rigaku RINT 2500X diffractometer using monochromated  $\text{Cu}_{K\alpha}$  radiation (40 kV, 40mA) at a scanning rate of  $0.5\text{ }^\circ\text{C min}^{-1}$ . Nitrogen adsorption-desorption data were obtained by using a Quantachrome Autosorb Automated Gas Sorption System at 77 K. Linear sweep voltammetry (LSV), electrochemical impedance spectroscopy (EIS), potentiodynamic polarization curves (Tafel plots) and chronoamperometry for oxygen evolution reaction (OER) were measured on a CHI 660E electrochemical workstation by using a conventional three-electrode cell. Platinum was used as the counter electrode and a saturated Ag/AgCl electrode was used as reference electrode. The glassy carbon electrode coated with the sample was used as the working electrode.

### 6-2.3. Results and Discussion

Firstly, I prepared four types of CPs ( $\text{Co}^{\text{II}}_3[\text{Co}^{\text{III}}(\text{CN})_6]_2 \cdot x\text{H}_2\text{O}$ ,  $\text{Ni}^{\text{II}}_3[\text{Co}^{\text{III}}(\text{CN})_6]_2 \cdot x\text{H}_2\text{O}$ ,  $\text{Co}^{\text{II}}[\text{Ni}^{\text{II}}(\text{CN})_4] \cdot x\text{H}_2\text{O}$ , and  $\text{Ni}^{\text{II}}[\text{Ni}^{\text{II}}(\text{CN})_4] \cdot x\text{H}_2\text{O}$ ) with different shapes and within which cyano-groups are located at the bridges between the metals (see the Experimental Section). These four CPs are abbreviated as CoCo, NiCo, CoNi, and NiNi, respectively. By thermal treatments in air, the organic bridges left nanopores/voids between the metals centers. Finally, the corresponding nanoporous metal oxides were obtained with a faithful reproduction of the parent morphology. The final products are abbreviated as cal-CoCo, cal-NiCo, cal-CoNi, and cal-NiNi.

**Figure 6-2.2a-1** and **b-1** show SEM images of the starting metal-cyanide CPs (CoCo

and NiCo, respectively) with cubic shapes. The size distribution of the particles is relatively uniform. The wide-angle powder XRD patterns indicate that these two samples have a similar crystal structures. All the peaks can be assigned to a face-centered cubic (*fcc*) structure (**Figure 6-2.3**), but the unit cell parameters are slightly different in each case. This is due to the small difference in the metal compositions between the two samples [7]. After calcination, a hollow space is formed at the center of the nanocubes, leading to the transformation into nanocages, as shown in the SEM images (**Figure 6-2.2a-2 and b-2**).

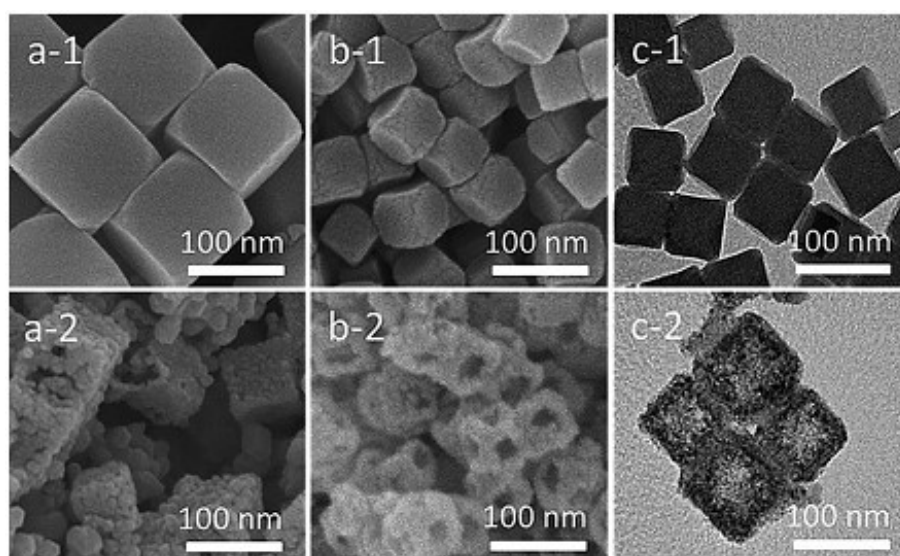


**Figure 6-2.2.** SEM images of (a-1) CoCo,(b-1) NiCo, (a-2) cal-CoCo,and (b-2) calNiCo and TEM images of (c-1) NiCo and (c-2) cal-NiCo.

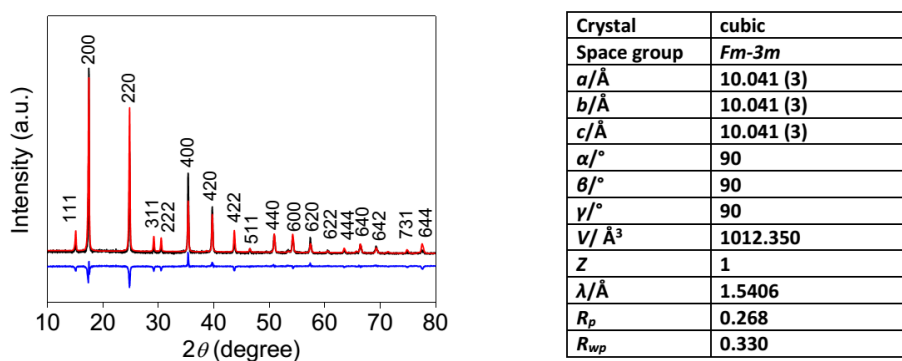


**Figure 6-2.3.a.** (Black) Experimental XRD pattern of NiCo, (Red) computed XRD pattern, and (Blue) difference between the experimental and the computed XRD patterns.

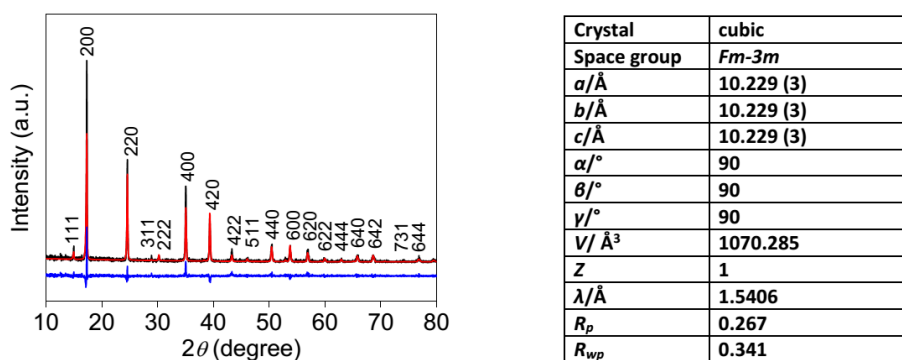


**Figure 6-2.3.b.** (Black) Experimental XRD pattern of CoCo, (Red) computed XRD pattern, and (Blue) difference between the experimental and the computed XRD patterns.

Nanocages from both compositions show a similar size distribution when compared to the original nanocubes. The crystal structure of the calcined materials was confirmed by wide-angle XRD measurement (**Figure 6-2.4**). The sample obtained from CoCo (*i.e.*, cal-CoCo) mostly contains a  $\text{Co}_3\text{O}_4$  phase with a cubic spinel structure (**Figure 6-2.4**), while the sample obtained from NiCo (*i.e.*, cal-NiCo) has a mixture of NiCo oxide and Ni metal with an *fcc* structure (**Figure 6-2.4**). It is well known that Ni is less active than Co in air and thus more difficult to oxidize.

The morphology of NiCo and cal-NiCo with cubic shapes was observed by TEM (**Figure 6-2.2c-1** and **c-2**, respectively). From the TEM image of cal-NiCo (**Figure 6-2.2c-2**) one can observe a clear difference of contrast located between the center and edges. The density at the edges of the nanocubes is much higher than at the center, indicating the formation of nanocages. The surface area was determined by  $\text{N}_2$  gas adsorption-desorption isotherms at 77 K. The surface areas for cal-CoCo and cal-NiCo were calculated to be  $40 \text{ m}^2 \text{ g}^{-1}$  and  $62 \text{ m}^2 \text{ g}^{-1}$ , respectively.

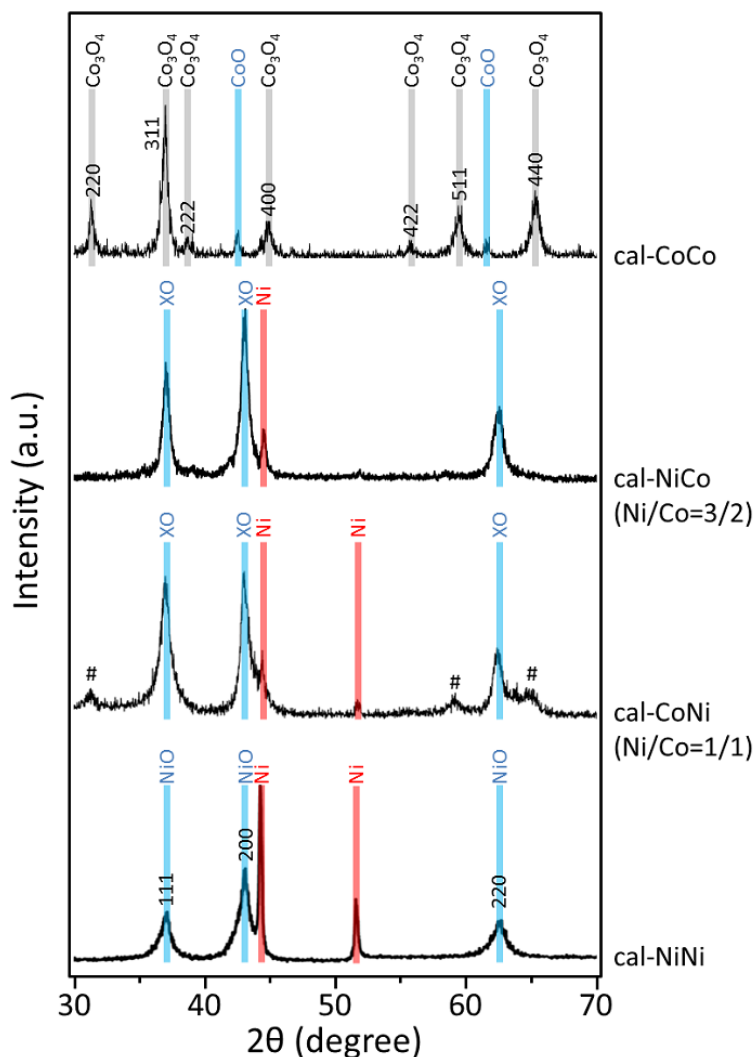


**Figure 6-2.4.** Wide-angle XRD patterns of cal-CoCo, cal-NiCo, cal-CoNi, and cal-NiNi, respectively. The peaks marked by # are assigned to Co<sub>3</sub>O<sub>4</sub> phase.

**Figure 6-2.5a-1** and **b-1** show the SEM images of the starting CoNi and NiNi. Unlike CoCo and NiCo, well-defined flake morphology, originating from a Hoffman-type crystal structure [8], can be observed. The diffraction peaks of these two materials can be assigned to an orthorhombic crystal structure with a Hofmann-type two-dimensional (2D) layered structure. Even after calcination, the initial flake morphology of cal-CoNi and cal-NiNi is well preserved with the additional formation of a nanoporous structure (**Figure 6-2.5a-2** and **b-2**). According to the wide-angle XRD results, both calcined samples contain non-oxidized Ni metal, although



cal-CoNi has less impurity (Ni) than cal-NiNi **Figure 6-2.4**. The surface area of cal-NiNi is around  $120 \text{ m}^2 \text{ g}^{-1}$  which is twice higher than that of cal-CoNi ( $60 \text{ m}^2 \text{ g}^{-1}$ ).

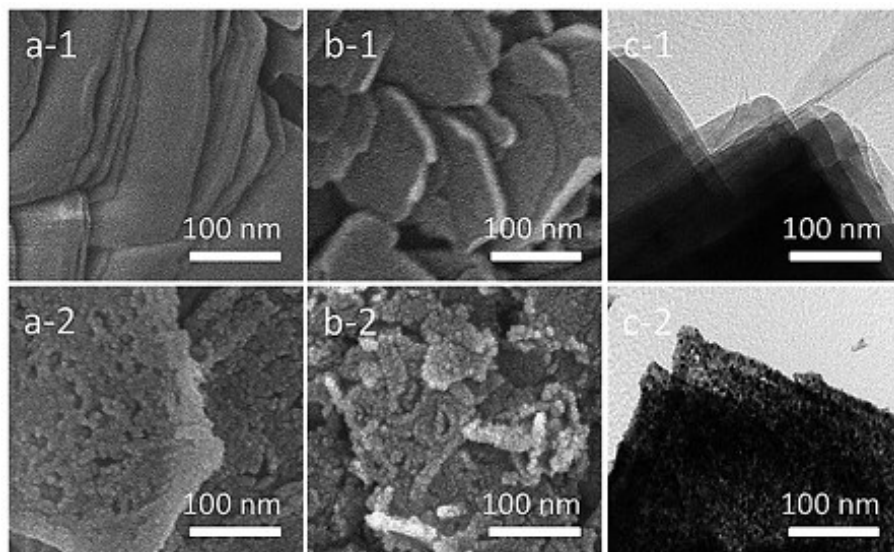


**Figure 6-2.5.** SEM images of (a-1) CoNi, (b-1) NiNi, (a-2) cal-CoNi, (b-2) cal-NiNi and TEM images of (c-1) CoNi and (c-2) cal-CoNi.

On the basis of these results, we conclude that nanocubes can be transformed into nanocages after calcination (**Figure 6-2.2**), while nanoflakes retain their morphology (**Figure 6-2.5**). The thermal transformation of CPs takes place in two steps. Firstly, the thermal decomposition of CP frameworks induces the removal of the organic compounds. Then, the metal ions diffuse and oxidize in order to form the corresponding metal oxides. CoCo and NiCo nanocubes are converted into the corresponding metal oxide nanocages by thermal treatment in air. This phenomenon can be explained by the Kirkendall effect, which is based on a non-equilibrium inter-diffusion process [9]. During the first stage of the thermal oxidation, the oxidized shells are immediately formed, due to the difficulty for oxygen to diffuse towards the inner parts. Therefore, free metal ions tend to move towards the shell region after the decomposition of the organic units in order to react with oxygen, leading to formation of hollow interiors. By contrast, for nanoflakes, their thinness permits oxygen to diffuse quickly and homogeneously throughout the

plates. In this case, a diffusion equilibrium is reached and, consequently, no hollow structure is formed inside the plates.

My NiCo and CoNi samples before and after calcination were further examined by high-angle annular dark-field scanning transmission electron microscopy (HAADF-STEM) and elemental mapping analysis (**Figure 6-2.6**). In the case of the starting NiCo and CoNi materials, I clearly observed the homogeneous distribution of C, Co, Ni, and N atoms over the entire area (**Figure 6-2.6a-1** and **b-1**). Even after the conversion into nanoporous mixed oxides, both Ni and Co were uniformly dispersed without any phase separation (**Figure 6-2.6a-2** and **b-2**). The Ni/Co atomic ratio obtained by inductive coupled plasma (ICP) analysis for NiCo and CoNi was 3:2 and 1:1, respectively [Note: The total compositions of the products (*i.e.*, without any consideration of phase separations) were obtained by ICP analysis. Therefore, the Ni/Co atomic ratios should be considered as the contribution of Ni and Co in all the phases of the final products after calcination]. These values reflect faithfully the stoichiometry of  $\text{Ni}_3[\text{Co}(\text{CN})_6]_2 \cdot x\text{H}_2\text{O}$  and  $\text{Co}[\text{Ni}(\text{CN})_4] \cdot x\text{H}_2\text{O}$ . Thus, after thermal treatment, the samples were converted into their corresponding metals oxides (cal-NiCo and cal-CoNi, respectively) and their Ni/Co atomic ratios remained identical. From the XRD pattern of cal-NiCo (**Figure 6-2.4**), no peaks derived from cobalt oxide ( $\text{Co}_3\text{O}_4$ ) can be observed, and the fcc structure of the Ni oxide based phase is predominately formed, although a low content of Ni metal coexists. Thus, it is found that the Co dopant can be substituted in the inner lattice for Ni atoms without affecting the original *fcc* crystal structure. After increasing the Co content up to 50% (*e.g.*, cal-CoNi), however, cobalt oxide ( $\text{Co}_3\text{O}_4$ ) with a spinel structure is formed as a secondary phase (**Figure 6-2.4**).

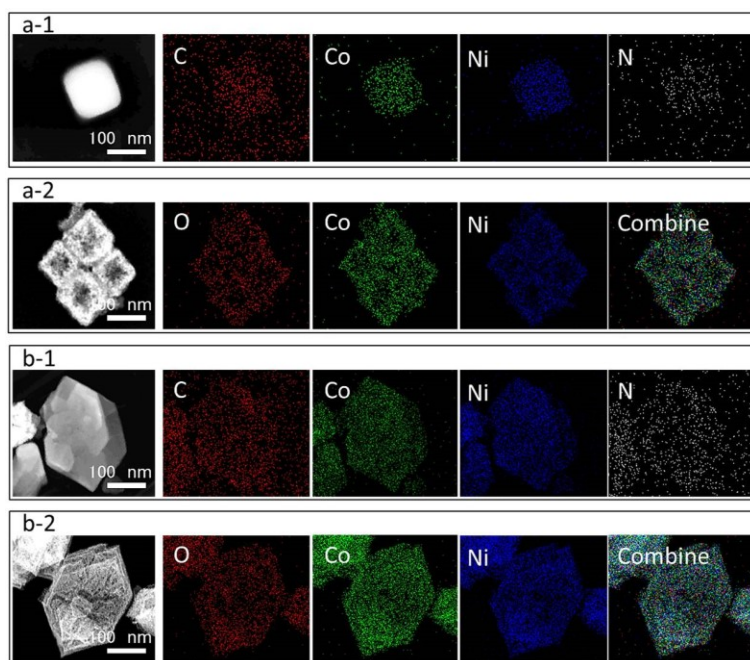


**Figure 6-2.6.** HAADF-STEM and elemental mapping images of (a-1) NiCo, (a-2) cal-NiCo, (b-1) CoNi, (b-2) cal-CoNi samples.

I then investigated the electrochemical performance of the obtain nanoporous metal oxides for oxygen evolution reaction (OER) (**Figure 6-2.7**). The catalytic OER performance for all the samples (cal-CoCo, cal-NiCo, ca-NiNi, and cal-CoNi ) was studied using electrochemical impedance spectra (EIS) in an O<sub>2</sub>-saturated 0.1 M KOH solution at a potential of 0.65 V over the frequency range of 0.01 Hz–100 kHz [10]. The Nyquist complex-plane impedance spectra of the catalysts are shown in **Figure 6-2.8a**. Generally, the arc in the high frequency range indicates the presence of an Ohmic process and of a charge-transfer resistance at the electrode/electrolyte interface. Among all the catalysts, cal-CoNi displays the smallest arc diameter, implying a lower impedance at the electrode/electrolyte interface, reflecting a better diffusion of oxygen, electrolyte, and intermediate species. The potentiodynamic polarization measurements (Tafel plots) were performed in a polarizing potential ranging from -2.0 V to 0.0 V vs. Ag/AgCl, at a scan rate of 10.0 mV s<sup>-1</sup> in 0.1 M KOH solution. The resulting currents are plotted on a logarithmic scale. **Figure 6-2.8b** shows a greater shift of the overpotential to lower values for

cal-CoNi than for the other samples (cal-CoCo, cal-NiCo, and cal-NiNi). Thus, it is revealed that the mixed oxide is fairly efficient in catalyzing oxygen evolution reaction.



**Figure 6-2.7.** Photographs of (a) electrochemical cell, (b) working electrode during measurements at 0.65 V vs. Ag/AgCl (Some bubbles on the working electrode indicate the formation (evolution) of O<sub>2</sub> gas).

The catalytic performance of the oxygen evolution for all the catalysts was examined by linear scan voltammograms (LSVs). **Figure 6-2.8.c** displays typical LSV plots of various catalysts for OER. The oxidation wave can be observed at an onset potential of  $\sim 1.60$  V and is attributed to catalytic water oxidation. Among all the catalysts, cal-CoNi shows the largest oxygen evolving current. The OER of the cal-CoNi sample appears to be shifted towards lower potentials, as highlighted by the horizontal dotted line set at  $10.00 \text{ mA cm}^{-2}$  in **Figure 6-2.8c**. At  $\eta = 0.40$  V, the activity of the cal-CoNi catalyst was also found to be  $3.03 \text{ mA cm}^{-2}$ , thus outperforming the other catalysts ( $2.44$ ,  $1.08$ , and  $0.99 \text{ mA cm}^{-2}$  for cal-NiCo, cal-CoCo, and cal-NiNi catalysts, respectively). Furthermore, cal-CoNi showed negligible performance attenuation ( $< 16\%$ ) in the first 50 s (**Figure 6-2.8d**), in contrast to a noticeable activity loss in cal-NiCo ( $> 36\%$ ) indicative of a superior stability for OER. These results suggest that flake-shaped cal-CoNi can serve as an

efficient catalyst to drive water oxidation with high stability. The oxidation peak observed just before the rising current due to oxygen evolution is ascribed to the transition to higher valence states of nickel and cobalt, which leads to the formation of a specific catalytic phase for OER [11]. The higher peak current observed for the cal-CoNi highlights an easier valence transition of Co and Ni compared to the other samples, which is in good agreement with the lower overpotential observed in the Tafel plots (**Figure 6-2.8b**).

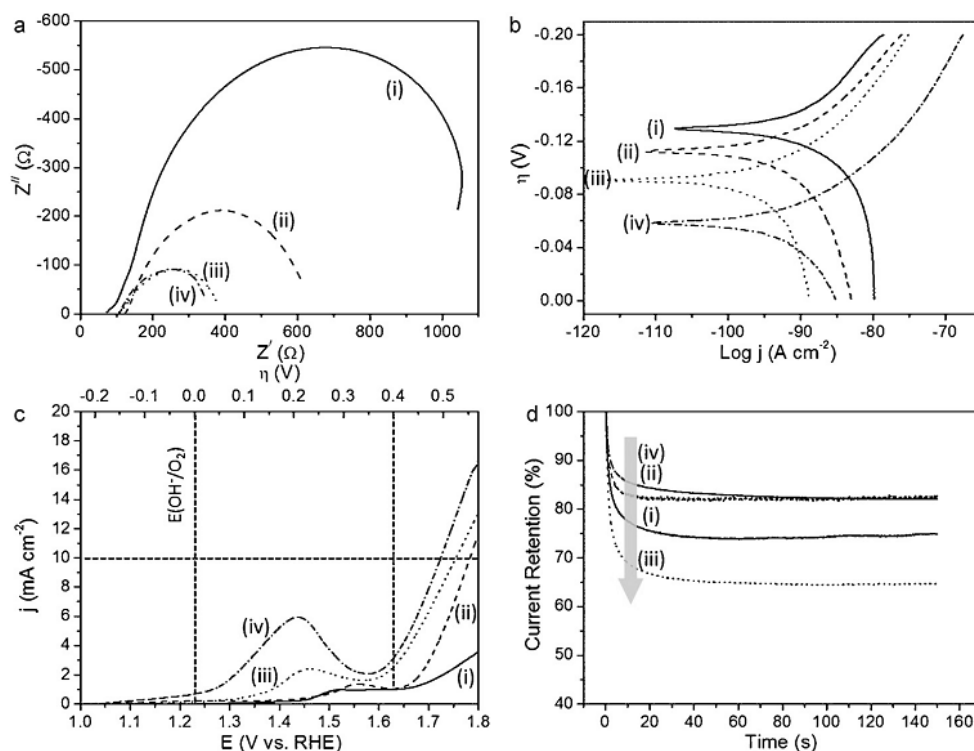


**Figure 6-2.8.** (a) Electrochemical impedance spectra(EIS) curves, (b) Tafel plots, (c) Linear sweep voltammetry (LSV) curves, and (d) chronoamperometric plots recorded at a constant overpotential ( $\eta = 0.38$  V) in 0.1 M KOH for (i) cal-NiNi, (ii) cal-CoCo, (iii) cal-NiCo, and (iv) cal-CoNi, respectively.

I furthermore consider that the shape effect is also critical for the OER catalytic activity. To clarify the shape effect, another control experiment was carried out. Rigorous grinding of the cal-CoNi sample totally destroyed the flake-like shape of the sample. I studied its OER catalytic activity using the LSV technique under the same conditions. **Figure 6-2.9** compares the LSV

curves of the cal-CoNi before and after grinding. There is a sharp decrease in its OER catalytic activity after grinding because of the destruction of the 2D flake shape. The plate-like morphology of cal-CoNi sample is expected to contribute to the diffusion of oxygen, electrolyte, and intermediate species throughout the whole surface of the material.

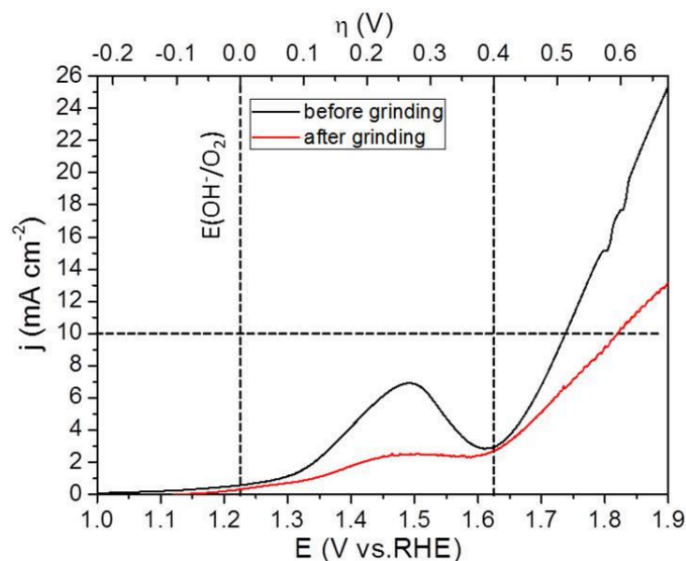


**Figure 6-2.9.** Linear sweep voltammetry (LSV) curves recorded in 0.1 M KOH for cal-CoNi nanoflakes before and after grinding.

## 6-2.4. Conclusion

In this chapter all 2D (CoNi and NiNi) and 3D (CoCo and NiCo) nanostructures are prepared by the same method. Thermal decomposition of the obtained metal-cyanide CPs with well-defined shapes is a powerful method for the preparation of a new family of nanoporous metal oxides. The nanoporous Ni-Co mixed oxides reported herein show excellent electrocatalytic activity for OER. The better catalytic performance of CoNi-oxide flakes than NiCo-oxide cubes for OER is reported to show the shape effect and the advantages of 2D-morphology. This group of materials shows a promising catalytic performance in the field of electrochemistry. Through such an innovative strategy, various nanoporous metal oxides with different compositions and shapes can

be prepared by choosing the appropriate CP precursors, which will broaden their range of applications.

## 6-2.5. Acknowledgements

M.B.Z. thanks the Culture Affairs & Missions Sector of the Ministry of Higher Education in Egypt for the financial support. A.A. extends his appreciation to the financial support by the Deanship of Scientific Research, College of Science Research Center, King Saud University

## 6-2.6. References

- [1] a) F. Schüth, *Chem. Mater.* **2001**, *13*, 3184; b) D. Gu, F. Schüth, *Chem. Soc. Rev.* **2014**, *43*, 313; c) Y. Yamauchi, *J. Ceram. Soc. Jpn.* **2013**, *121*, 831.
- [2] a) P. Yang, D. Zhao, D.I. Margolese, B.F. Chmelka, G.D. Stucky, *Nature* **1998**, *396*, 152; b) N. Dahal, I.A. Ibarra, S.M. Humphrey, *J. Mater. Chem.* **2012**, *22*, 12675; c) H. Oveisi, S. Rahighi, X. Jiang, Y. Nemoto, A. Beitollahi, S. Wakatsuki, Y. Yamauchi, *Chem. Asian J.* **2010**, *5*, 1978.
- [3] a) S. Xiong, C. Yuan, X. Zhang, B. Xi, Y. Qian, *Chem. Eur. J.* **2009**, *15*, 5320; b) W.J. Zhou, J. Zhang, T. Xue, D.D. Zhao, H.L. Li, *J. Mater. Chem.* **2008**, *18*, 905; c) D.D. Zhao, M.W. Xu, W.J. Zhou, J. Zhang, H.L. Li, *Electrochim. Acta* **2008**, *53*, 2699; d) B. Tian, X. Liu, H. Yang, S. Xie, C. Yu, B. Tu, D. Zhao, *Adv. Mater.* **2003**, *15*, 1370; e) H. Tüysüz, M. Comotti, F. Schüth, *Chem. Commun.* **2008**, 4022; f) H. Wang, Y. Teng, L. Radhakrishnan, Y. Nemoto, M. Imura, Y. Shimakawa, Y. Yamauchi, *J. Nanosci. Nanotechnol.* **2011**, *11*, 3843.
- [4] a) K. C.-W. Wu, Y. Yamauchi, *J. Mater. Chem.* **2012**, *22*, 1251; b) H.Y. Lian, Y.H. Liang, Y. Yamauchi, K. C.-W. Wu, *J. Phys. Chem. C* **2011**, *115*, 6581.

- [5] a) W. Cho, S. Park, M. Oh, *Chem. Commun.* **2011**, *47*, 4138; b) S. Jung, W. Cho, H.J. Lee, M. Oh, *Angew. Chem. Int. Ed.* **2009**, *48*, 1459; *Angew. Chem.* **2009**, *121*, 1487; c) W. Wang, Y. Li, R. Zhang, D. He, H. Liu, S. Liao, *Catal. Commun.* **2011**, *12*, 87; d) F.X. Qin, S.Y. Jia, Y. Liu, X. Han, H.T. Ren, W.W. Zhang, J.W. Hou, S.H. Wu, *Mater. Lett.* **2013**, *101*, 93; e) M.S.Y. Parast, A. Morsali, *Inorg. Chem. Commun.* **2011**, *14*, 645; f) W. Cho, Y. H. Lee, H. J. Lee, M. Oh, *Chem. Commun.* **2009**, 4756.
- [6] a) Y.J. Mai, J.P. Tu, X.H. Xia, C.D. Gu, X.L. Wang, *J. Power Sources* **2011**, *196*, 6388; b) P. Ganesan, H. Colon, B. Haran, R. White, B.N. Popov, *J. Power Sources* **2002**, *111*, 109; c) H. Wang, P. Wang, Z. Yin, *Int. J. Electrochem. Sci.* **2013**, *8*, 7734.
- [7] M. Hu, A.A. Belik, M. Imura, Y. Yamauchi, *J. Am. Chem. Soc.* **2013**, *135*, 384.
- [8] a) M.B. Zakaria, M. Hu, Y. Tsujimoto, Y. Sakka, N. Suzuki, Y. Kamachi, M. Imura, S. Ishihara, K. Ariga, Y. Yamauchi, *Chem. Asian J.* **2014**, *9*, 1511; b) M. Hu, S. Ishihara, Y. Yamauchi, *Angew. Chem. Int. Ed.* **2013**, *52*, 1235 ; *Angew. Chem.* **2013**, *125*, 1273.
- [9] L. Hu, N. Yan, Q. Chen, P. Zhang, H. Zhong, X. Zheng, Y. Li, X. Hu, *Chem. Eur. J.* **2012**, *18*, 8971.
- [10] The working electrodes with catalysts were prepared as follows. Firstly, 5 mg of the catalyst was mixed with 950 mL of a mixed solution from distilled water and ethyl alcohol (3:1) and 50 mL of 5 wt% Nafion solution under sonication for 30 min. Secondly, 5 mL of the above suspension was dropped onto a polished glassy carbon electrode with 3 mm diameter and dried under infrared lamp to form a thin film catalyst.
- [11] a) M. Gao, W. Sheng, Z. Zhuang, Q. Fang, S. Gu, J. Jiang, Y. Yan, *J. Am. Chem. Soc.* **2014**, *136*, 7077; b) S. Palmas, F. Ferrara, A. Vacca, M. Mascia, A.M. Polcaro, *Electrochim. Acta* **2007**, *53*, 400; c) C. Bocca, A. Barbucci, M. Delucchi, G. Cerisola, *Int. J. Hydrogen Energy* **1999**, *24*, 21.



# Chapter 7

## Chapter 7-1

### **7-1. Layer-by-Layer Motif Hybridization: Nanoporous Nickel Oxide Flakes Wrapped into Graphene Oxide Sheets toward Enhanced Oxygen Reduction Reaction**

#### **7-1.1. Introduction**

Hybrid materials have many scientific utilities due to the combined effects of two (or more) building blocks. The development of such materials covers a wide range of applications like catalysis, adsorption, electrochemical techniques, sensing, and energy storage. Therefore, finding efficient methods to prepare these materials in high yields is of fundamental importance. Among others, a promising concept is the ‘layer-by-layer’ (LbL) fabrication of nanometer-level layered hybrid structures in a designable manner. LbL approaches are known to be simple, inexpensive, and versatile processes for the fabrication of multilayered hybrid structures with various compositions and have been performed through various interactions, including electrostatic, hydrogen bonding, and charge-transfer, as well as through chemical reactions such as sol-gel, electrochemical coupling, and click reactions [1]. Recently, highly flexible two-dimensional (2D)

graphene oxide (GO) sheets have been attracting a lot of attention for their potential in various applications [2]. In particular, the hybridization of GO sheets with various nanomaterials (*e.g.*, nanoparticles) is a promising strategy because of the unique properties arising from the resulting materials [3].

Fuel cells have attracted significant interest due to their implementation in highly efficient and clean energy storage systems. Therefore, designing suitable electrocatalysts for oxygen reduction reactions (ORRs) is vital in fuel cell research [4]. Tremendous efforts and extensive studies have been devoted to the development of suitable and low-cost catalysts for ORRs with high activity. An important challenge, however, remains unresolved. The main problem associated with GO is its intrinsic low ORR activity, which is usually enhanced by either doping with some heteroatoms or hybridization with transition-metal species. Heteroatoms such as nitrogen (N) are generally used to change the charge density of GO and enhance its catalytic activity [5]. On the other hand, transition-metals, such as Ni, Mn, Co, MoO<sub>3</sub>, Fe<sub>3</sub>O<sub>4</sub>, NiO, MoS<sub>2</sub> and WS<sub>2</sub>, have recently gained noticeable popularity in various nanocomposite systems owing to their low cost and high activity originating from a favorable kinetics phenomenon [6]. Wu *et al.*, have reported that Fe<sub>3</sub>O<sub>4</sub> nanoparticles supported on 3D nitrogen-doped graphene aerogel are promising for improving the ORR performance [7].

Herein, I propose a new LbL approach for the synthesis of multilayered NiO-GO hybrid materials. Rather disordered interfacial structures in LbL films provide abundant nanospaces, which is advantageous for interlayer molecular diffusion. The electrochemical performance of NiO can be enhanced when combined with GO sheets through appropriate chemical interaction. The electrochemical analysis performed in this work demonstrates that our NiO-GO hybrid material can serve as an efficient catalyst for ORR. It also exhibits good stability compared to the PtC-5% catalyst (current loss is about 24.6% for NiO-GO hybrid material compared to 38.3% for

PtC-5%).

## 7-1.2. Experimental Details

### 7-1.2.1. Chemicals

Potassium tetracyanonickelate(II) hydrate was purchased from Sigma-Aldrich, USA. Nickel(II) chloride hexahydrate, trisodium citrate dihydrate, and sulfuric acid were purchased from Nacalai Tesque, Japan. Potassium hydroxide and sodium nitrate was purchased from Wako, Japan. Nanographite platelets (N008-100-N) of 100 nm thickness were used as raw material to prepare graphene oxide (GO), Angestron materials.  $\text{KMNO}_4$  and  $\text{H}_2\text{O}_2$  were purchased from Kanto chemicals Co., INC. Platinum, 5% on carbon was obtained from Alfa Aesar, A Johnson Matthey Company. All chemical reagents were used without further purification.

### 7-1.2.2. Synthesis of NiCNNi Flakes

In a typical procedures,  $\text{NiCl}_2 \cdot 6\text{H}_2\text{O}$  (59.6 mg) and trisodium citrate dihydrate (300 mg) were dissolved in 20 mL water to form a clear solution. Meanwhile,  $\text{K}_2[\text{Ni}(\text{CN})_4]$  (130 mg) was dissolved into 20 mL water to form another clear solution. The two solutions were then mixed together under constant magnetic stirring for 30 min. The obtained solution was aged for 30 h until the reaction was complete and the precipitate is formed. After washing with water and ethanol extensively, the green precipitates were dried at room-temperature. On the basis of elemental analysis, the resulting chemical compound was  $\text{Ni}[\text{Ni}(\text{CN})_4]$ , which is hereafter abbreviated as ‘NiCNNi flakes’.

### 7-1.2.3. Synthesis of GO Sheets

The preparation of GO solutions followed the modified Hummers' method. The procedures are briefly described as follows. Sodium nitrate (0.30 g) was dissolved in sulfuric acid (10 mL). N008-100-N carbon source was added to the solution, which was stirred for 30 min.  $\text{KMNO}_4$  (0.30 g) was further added to the solution and stirred again for 1 h. Then,  $\text{H}_2\text{O}_2$  (10 mL) was added to the solution under stirring. Finally, the solution was centrifuged and then redispersed in water 3 times at different time intervals such as 10, 30, and 45 min. Then, the material was extracted by adding water, mixing with methanol, and keeping for further processing. The GO (10 mg) sheets were dissolved in 25 mL water under stirring for 2 h followed by strong sonication for 30 min.

### 7-1.2.4. Synthesis of NiO-GO Hybrids

The two previously prepared solutions were mixed under vigorous sonication for 30 min. The obtained solution was aged under stirring for 4 h. The precipitate was obtained by centrifugation. After washing with water and ethanol extensively, the NiCNNi-GO hybrid was dried at room temperature. Then, the obtained NiCNNi-GO hybrid (100 mg) was heated inside an electronic furnace to the desired temperature (300 °C) with a heating rate of 5 °C min<sup>-1</sup> and kept for annealing during 1 h. After that, the powder was cooled inside the furnace naturally. Finally, the obtained powder (NiO-GO hybrid) was collected for characterization. The whole calcination process was carried out in the air.

### 7-1.2.5. Electrochemical Measurements

A conventional three-electrode cell was used for oxygen reduction reaction (ORR) measurement, including an Ag/AgCl (saturated KCl) reference electrode, a platinum wire as a counter electrode, and a modified rotating disk electrode (RDE) as a working electrode. The working electrode was prepared as follows. 5 mg of catalyst was dispersed in a mixture of water/ethanol (v/v=3:1, 950  $\mu$ l) and Nafion (5 wt%, 50  $\mu$ l) under sonication for 30 min. Then, 5  $\mu$ L of the above suspension was dropped on the surface of the RDE and dried at room temperature. The cyclic voltammograms were checked at a scan rate of 50 mV s<sup>-1</sup> without any rotation. The linear sweep voltammograms were performed at a potential range between -1.0 V and 0.2 V (vs. Ag/AgCl) with a scan rate of 10 mV s<sup>-1</sup> and rotating speed of 1600 rpm. All the measurements were carried out in 0.1 M KOH with N<sub>2</sub>- or O<sub>2</sub>-saturated.

### 7-1.2.6. Characterization

SEM images were acquired with a Hitachi SU8000 scanning microscope at an accelerating voltage of 5 kV. The TEM observations were performed using a JEM-2100F operating at 200 kV and equipped for energy-dispersive spectrometer analysis. The wide-angle powder X-ray diffraction (XRD) patterns were obtained with a Rigaku RINT 2500X diffractometer using monochromated Cu K $\alpha$  radiation (40 kV, 40 mA). Raman spectra were measured by Horiba-Jovin Yvon T64000 with the excitation Laser 364 nm. Nitrogen adsorption-desorption isotherms data were obtained with a Quantachrome Autosorb Automated Gas Sorption System at 77 K. The electrochemical measurements were conducted in a three-electrode electrochemical cell with a Pt counter electrode and Ag/AgCl as reference electrode in a 6 M KOH solution. A glassy carbon electrode coated with the sample was used as the working electrode. Linear sweep

voltammetry measurements were obtained using an electrochemical workstation (ALS/HCH instruments, electrochemical analyzer/model: 842BZ) in the scan range from 0.2 to -1.0 V.

### 7-1.3. Results and Discussion

The nickel cyano-bridged coordination polymer (NiCNNi) flakes consist of very thin plates with an average lateral size of around 150 nm (**Figure 7-1.1a**). The flakes are highly crystallized, as confirmed by selected area electron diffraction (SAED) patterns. On the other hand, the GO sheets show a typical 2D morphology with lateral sizes as large as 1  $\mu\text{m}$  (**Figure 7-1.1b**). Their surface is smooth and the sheets are detached from each other. The SAED patterns reveal the typical hexagonal arrangement of a crystalline framework characteristic of GO sheets. The lateral size of the NiCNNi flakes is much smaller than that of GO sheets. The NiCNNi flakes and GO sheets are sonicated separately to form colloidal solutions and their measured zeta potentials are 2.97 mV and -30.7 mV, respectively [8].

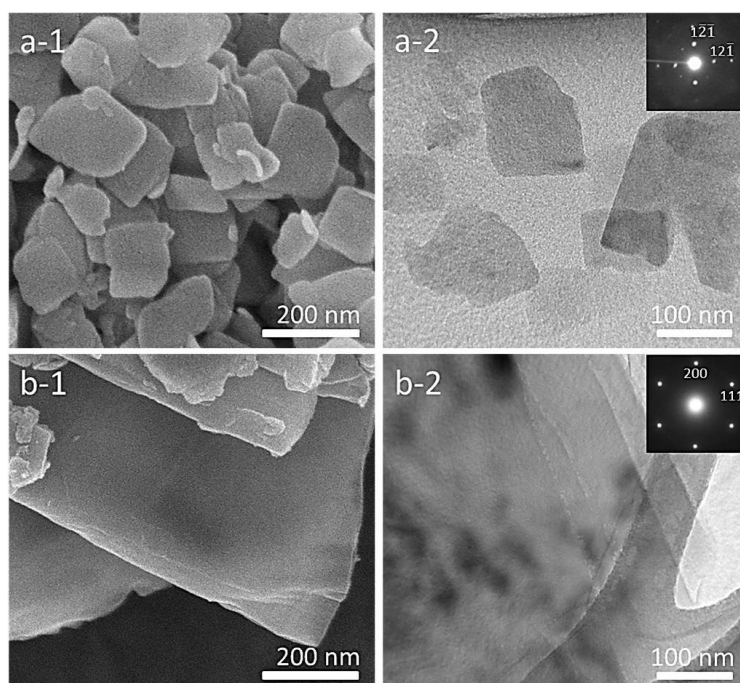
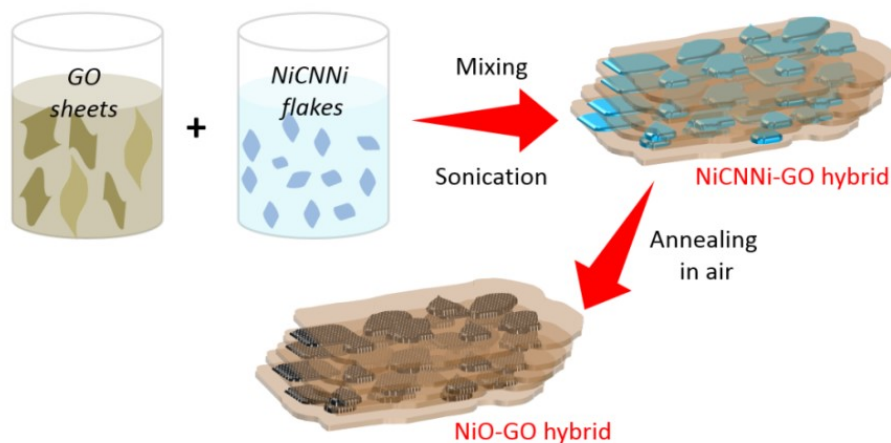


**Figure 7-1.1.** SEM and TEM images of (a) NiCNNi flakes and (b) GO sheets. The corresponding SAED patterns are shown as insets.

The NiO-GO hybrid materials were synthesized by assembling the NiCNNi flakes and GO sheets followed by thermal treatment (**Scheme 7-1.1**). The two colloidal solutions were mixed together under strong sonication. The materials are well dispersed in the suspensions (**Figure 7-1.2**). Through this step, the positively charged NiCNNi flakes become uniformly embedded into the negatively charged GO sheets through electrostatic interactions. By changing the NiCNNi:GO weight ratios, various types of NiO-GO hybrids can be obtained. The zeta potential gradually decreases with increasing GO content.

Scanning electron microscopy (SEM) and transmission electron microscopy (TEM) images of the typical NiCNNi-GO hybrids before thermal treatment (NiCNNi:GO=75:25) are shown in **Figure 7-1.3a**. The introduced NiCNNi flakes can clearly be observed inside the GO sheets. During the thermal treatment at 300 °C, the organic group from NiCNNi can be removed to generate nanoporous NiO flakes [9]. Even after calcination, the NiO flakes are still enclosed by the GO sheets. It is worth noticing that the lateral size of NiO flakes remains mostly unchanged after thermal treatment (**Figure 7-1.3b**).



**Scheme 7-1.1.** Schematic presentation of the synthesis of NiO-GO hybrid materials by assembling the NiCNNi flakes and GO sheets followed by thermal treatment.



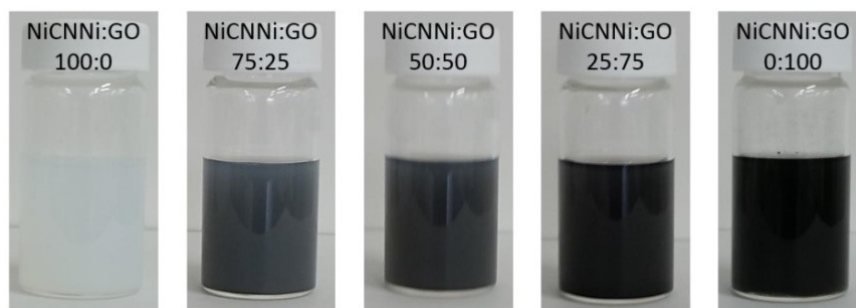


**Figure 7-1.2.** Photographs of the suspensions for the preparation of the NiCNNi-GO hybrids with different NiCNNi:GO ratios.

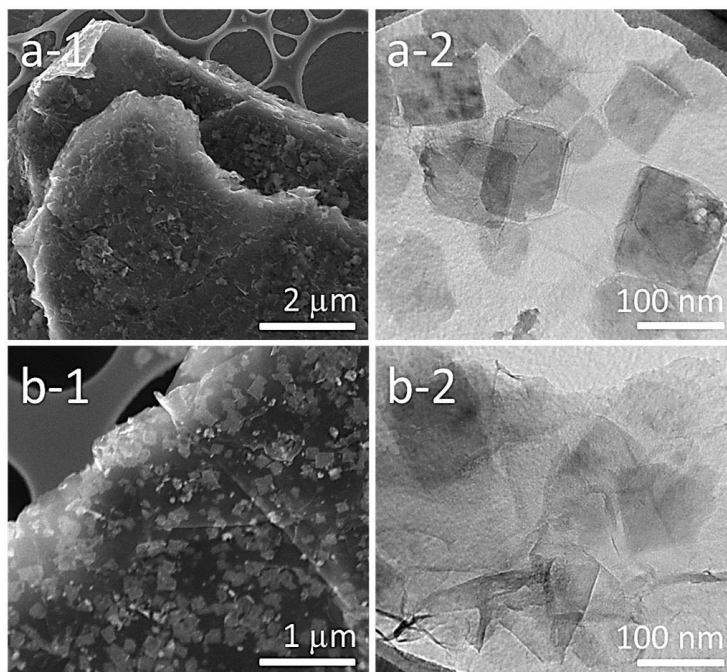


**Figure 7-1.3.** SEM and TEM images of (a) NiCNNi-GO hybrid (NiCNNi:GO=75:25) before thermal treatment and (b) the corresponding NiO-GO hybrid after thermal treatment.

From the elemental mapping, it is found that carbon, oxygen, and nickel atoms are uniformly distributed over the entire area of the hybrid material (**Figure 7-1.4**). However, it is hard to distinguish the NiO flakes from the GO sheets, because several NiO flakes are overlapped. Cross-sectional TEM images and the corresponding HAADF-STEM and the elemental mapping images show a clear layer-by-layer architecture (**Figures 7-1.5** and **7-2.6**). The introduction of the NiO flakes as spacers prevent restacking or aggregation of the GO sheets.

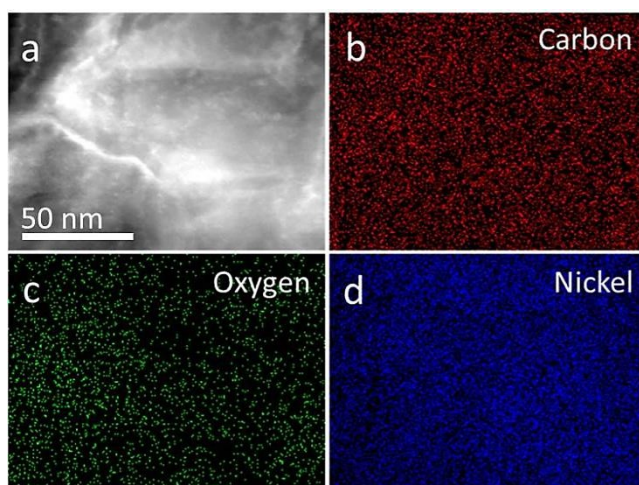


**Figure 7-1.4.** HAADF-STEM image and elemental mapping images (carbon, oxygen, and nickel atoms) of NiO-GO hybrid prepared from prepared from NiCNNi: GO = 75:25.

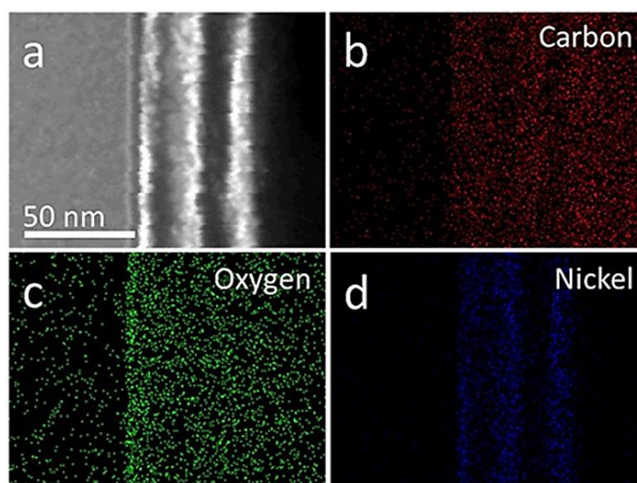


**Figure 7-1.5.** Cross-section HAADF-STEM image and elemental mapping (carbon, oxygen, and nickel) of NiO-GO hybrid prepared from prepared from NiCNNi:GO=75:25.

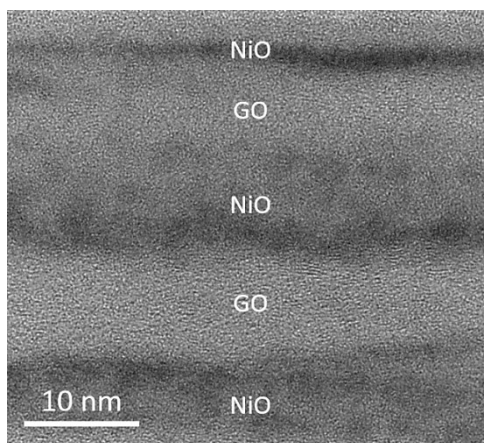


**Figure 7-1.6.** Cross-sectional TEM image of NiO-GO hybrid prepared from NiCNNi: GO=75:25.

The crystal structure of NiO-GO hybrids after thermal treatment was examined by wide-angle X-ray diffraction (XRD) (**Figure 7-1.7a**). For comparison, the spectra of individually calcined NiO flakes and GO sheets are also displayed. The XRD pattern of NiO-GO hybrids matches with the (111), (200), and (220) crystal planes of a standard NiO crystal structure [9]. Another broad diffraction peak could be assigned to the (002) plane of GO sheets [10]. The Raman spectra of the NiO-GO hybrids and thermally-treated GO sheets are shown in **Figure 7-1.7b**. The D and G bands of GO sheets can be clearly observed [11]. The NiO-GO hybrid shows two additional peaks (at 554 and 1077  $\text{cm}^{-1}$ ) corresponding to the NiO phase [12].

The porosity of the obtained materials was investigated by nitrogen adsorption-desorption isotherms (**Figure 7-1.7c**). The corresponding BET surface area is summarized in **Table 7-1.1**. The surface area of the hybrid materials appears to increase gradually upon increasing the content of NiO flakes in the hybrid system. Actually, the GO sheets possess a relatively small surface area as the layers tend to stack and agglomerate. The introduction of the NiO flakes inside the GO sheets as spacers leads to the enhancement of the overall surface area. From the isotherms, uptake at low relative pressure ( $P/P_0 < 0.1$ ) can be observed, indicating the presence of micropores. At higher pressure, the adsorption gradually increases without exhibiting any clear capillary condensation step, which is typical of ordered mesoporous materials [13]. It indicates that pore size distribution inside the interlayer space is not uniform.

**Table 7-1.1** Summary on the surface areas of the obtained samples

Weight ratios	Surface area ( $\text{m}^2 \text{g}^{-1}$ )
NiCNNi:GO = 100:0	78.5
NiCNNi:GO = 75:25	152
NiCNNi:GO = 50:50	99.8
NiCNNi:GO = 25:75	47.8
NiCNNi:GO = 0:100	12.5

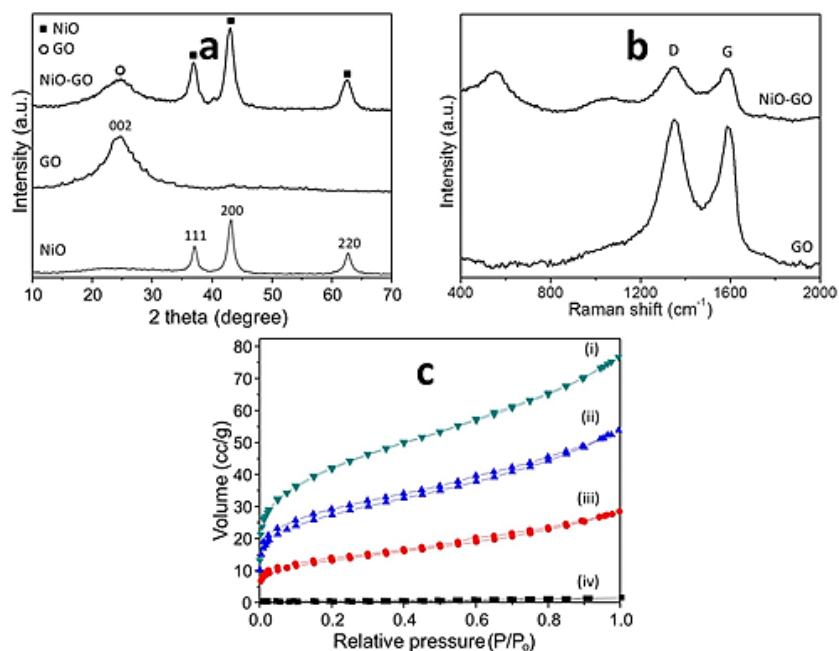


**Figure 7-1.7.** (a) Wide-angle XRD of the calcined NiO flakes, the calcined GO sheets, and the typical NiO-GO hybrid after thermal treatment, (b) Raman spectra of the calcined GO sheets and the typical NiO-GO hybrid after thermal treatment, (c) N<sub>2</sub> adsorption-desorption isotherms of (i-iii) the NiO-GO hybrids prepared from different NiCNNi:GO compositions [(i) NiCNNi:GO=75:25, (ii) NiCNNi:GO=50:50, (iii) NiCNNi:GO=25:75] and (iv) the calcined GO sheets.

The typical NiO-GO hybrid (prepared from NiCNNi:GO=75:25) was examined by X-ray photoelectron spectroscopy (XPS) (**Figure 7-1.8**). The survey spectrum confirms the presence of Ni, O, and C elements in the material. The high resolution spectrum centered at Ni 2p<sub>3/2</sub> reveals that the signal can be divided into at least four contributions, highlighting a multi-coordinated Ni (**Figure 7-1.8b**). While the multiplet located at 855.7, 861.0 and 865.3 eV is a typical signature of NiO [14], the peak at 853.9 eV is believed to originate from the interactions taking place between the NiO flakes and the GO sheets. Indeed, this contribution was not observed for free NiO flakes which are not embedded in GO [9a]. In the case of oxygen, two peaks at 529.4 eV and 531.4 eV are assignable to the O 1s peaks of the NiO phase (**Figure 7-1.8c**) [14]. The C 1s spectrum of GO clearly indicates the presence of a considerable amount of oxidized carbon atoms (**Figure 7-1.8d**).

Four types of carbon atoms in different functional groups are observed: non-oxygenated ring (~284.56 eV), C–O (~286.01 eV), C=O (~288.42 eV), and O–C=O (~290.88 eV) [15]. It is expected that the NiO flakes are more tightly anchored to the surface of GO through functional groups containing oxygen.

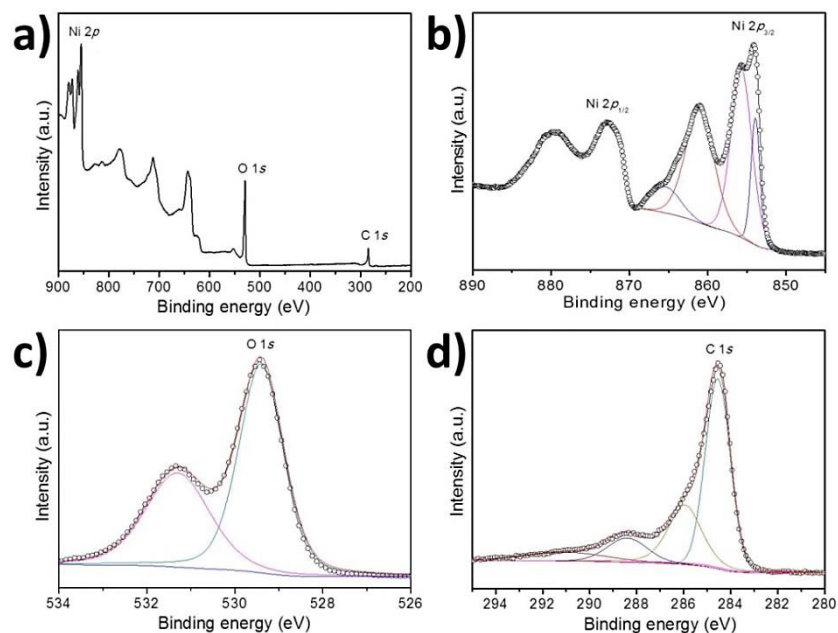


**Figure 7-1.8.** (a) XPS survey and (b, c, and d) high resolution XPS spectra of the NiO-GO hybrid prepared from prepared from NiCNNi:GO=75:25 [(b) Ni 2*p*, (c) O 1*s*, and (d) C 1*s* spectra]. The Ni 2*p*<sub>3/2</sub> peak contains the information necessary for the analysis, thus the Ni 2*p*<sub>1/2</sub> contribution is not fitted.

Inspired by the unique structure of my NiO-GO hybrid materials, ORR was selected to examine their performance in energy conversion systems. Cyclic voltammetric (CV) measurements were performed to compare the ORR activity of the hybrid materials prepared from different NiO:GO compositions. The NiO-GO hybrid prepared from NiCNNi:GO=75:25 shows a significant enhancement in ORR activity, compared to the other samples (**Figure 7-1.9**). From the CV curves obtained in O<sub>2</sub>-saturated 0.1 M KOH, the NiO-GO hybrid prepared from NiCNNi:GO=75:25 showed an onset potential of about 130 mV (**Figure 7-1.10a**), and a

reduction peak at about 370 mV, which are comparable to the previously reported NiO-based catalysts [16]. More importantly, this NiO-GO hybrid shows good tolerance toward small organic fuels (*e.g.*, methanol), compared to a standard 5% Pt supported on carbon (abbreviated as PtC-5%) (**Figure 7-1.10a and b**) [17]. All the results indicated that my NiO-GO hybrid materials are good candidates for ORR and do not suffer from the crossover effects of organic fuels.

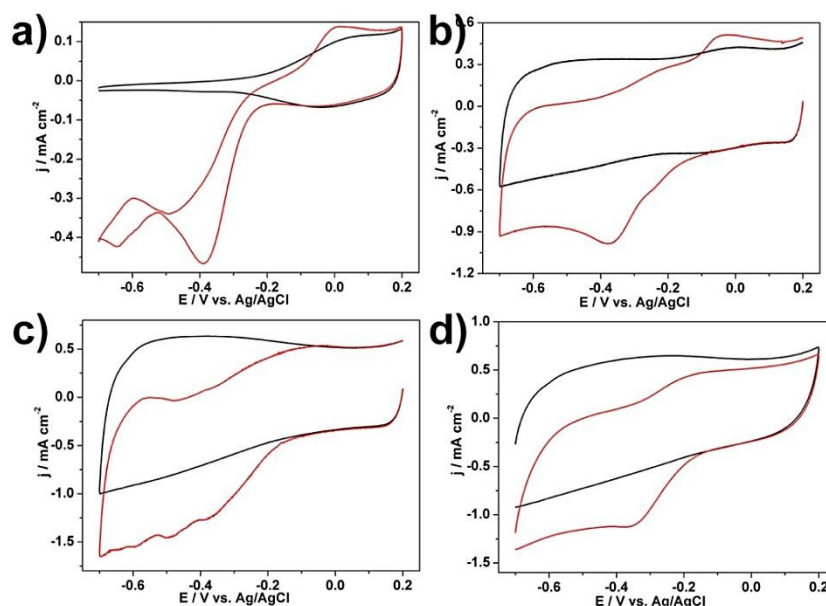


**Figure 7-1.9.** Cyclic voltammetric (CV) curves obtained under (black color)  $N_2$ -, and (red color)  $O_2$ -saturated 0.1 M KOH catalyzed by (a) the calcined NiO flakes, (b, c) the NiO-GO hybrids prepared from different NiCNNi:GO ratios [(b) NiCNNi:GO=50:50, and (c) NiCNNi:GO=25:75], and (d) the calcined GO sheets.

The ORR performance was further tested by using a rotating disk electrode (RDE) in an  $O_2$ -saturated 0.1 M KOH solution at a rotation speed of 1600 rpm. The linear sweep voltammograms (LSVs) of all the samples are shown in **Figure 7-1.10c**. The electrochemical behavior toward the ORR varies depending on the NiO:GO compositions. The NiO-GO hybrid prepared from NiCNNi:GO=75:25 shows the best performance from the standpoints of both onset potential and limiting current. The onset potential of the NiO-GO hybrid prepared from NiCNNi:GO=75:25 (100 mV) for the ORR is more positive compared to the other samples [NiO

(180 mV), the NiO-GO hybrid prepared from NiCNNi:GO=50:50 (100 mV), the NiO-GO hybrid prepared from NiCNNi:GO=25:75 (140 mV), and GO (120 mV)]. A larger surface area can be obtained by increasing the proportion of NiO flakes. The NiO-GO hybrid with a high surface area probably tends to decrease the mass transport resistance and facilitate the access of the electrolyte to the active sites, which is greatly beneficial during the ORR process [18]. A chronoamperometric measurement over a time period of 5000 s was further performed on the NiO-GO hybrid, and benchmarked to the PtC-5% catalyst. The current retention performance is shown in **Figure 7-1.10d**. The NiO-GO hybrid shows a current loss of 24.6%, which is much less than for the PtC-5% catalyst (38.3%).

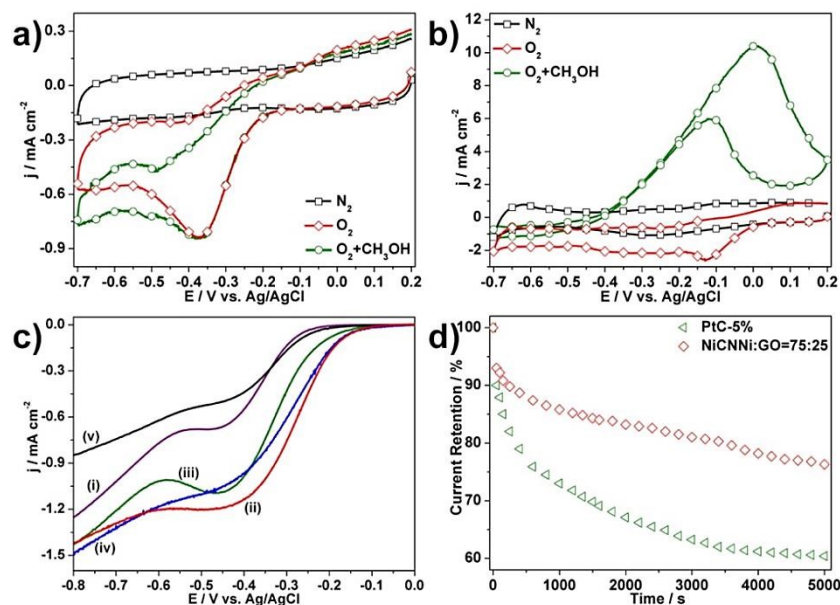


**Figure 7-1.10.** (a,b) CV curves obtained under N<sub>2</sub>- and O<sub>2</sub>-saturated 0.1 M KOH, and O<sub>2</sub>-saturated 0.1 M KOH together with 0.5 M CH<sub>3</sub>OH catalyzed by (a) NiO-GO hybrid prepared from NiCNNi:GO=75:25, and (b) PtC-5%. (c) ORR polarization curves of a RDE modified with (i) the calcined NiO flakes, (ii-iv) the NiO-GO hybrids prepared from different NiCNNi:GO compositions [(ii) NiCNNi:GO=75:25, (iii) NiCNNi:GO=50:50, and (iv) NiCNNi:GO=25:75], and (v) the calcined GO sheets. The plots are obtained in O<sub>2</sub>-saturated 0.1 M KOH at a rotation rate of 1600 rpm with a scan rate of 10 mV s<sup>-1</sup>. (d) Current retention plot during chronoamperometric measurements for NiO-GO hybrid prepared from NiCNNi:GO=75:25 and PtC-5%.

## 7-1.4. Conclusion

In conclusion, I successfully prepared NiO-GO hybrid materials with high surface areas through the thermal conversion of NiCNNi-GO hybrids. The NiO flakes are uniformly distributed and tightly anchored to the surface of the GO sheets, thereby forming a robust hetero-layered structure assembled through the LbL process. The NiO-GO hybrids exhibit an efficient catalytic activity for ORR. Combining the desirable electrochemical properties of both NiO and GO lead to a synergetic improvement in their electrocatalytic activity. My strategy can be applicable in the future for the preparation of various functional metal oxides wrapped in GO sheets for promising electrocatalytic applications.

## 7-1.5. References

- [1] (a) G. Decher, J.D. Hong, J. Schmitt, *Thin Solid Films* **1992**, 210-211, 831; (b) S.S. Shiratori, M.F. Rubner, *Macromolecules* **2000**, 33, 4213; (c) N. Cini, T. Tulun, G. Decher, V. Ball, *J. Am. Chem. Soc.* **2010**, 132, 8264; (d) J. Choi, R. Suntivich, F.A. Plamper, C.V. Synatschke, A.H.E. Müller, V.V. Tsukruk, *J. Am. Chem. Soc.* **2011**, 133, 9592; (e) K. Ariga, Y. Yamauchi, G. Rydzek, Q. Ji, Y. Yonamine, K. C.-W. Wu, J.P. Hill, *Chem. Lett.* **2014**, 43, 36.
- [2] (a) R.R. Salunkhe, S.-H. Hsu, K. C.-W. Wu, Y. Yamauchi, *ChemSusChem* **2014**, 7, 1551; (b) Y. Su, S. Li, D. Wu, F. Zhang, H. Liang, P. Gao, C. Cheng, X. Feng, *ACS Nano* **2012**, 6, 8349; (c) X. Meng, D. Geng, J. Liu, M.N. Banis, Y. Zhang, R. Li, X. Sun, *J. Phys. Chem. C* **2010**, 114, 18330; (d) G. Williams, B. Seger, P.V. Kamat, *ACS Nano* **2008**, 2, 1487.
- [3] (a) X. Zhou, X. Huang, X. Qi, S. Wu, C. Xue, F.Y.C. Boey, Q. Yan, P. Chen, H. Zhang, *J. Phys. Chem. C* **2009**, 113, 10842; (b) Z. Zhang, F. Xu, W. Yang, M. Guo, X. Wang, B.



- Zhang, J. Tang, *Chem. Commun.* **2011**, 47, 6440; (c) S. Yang, G. Cui, S. Pang, Q. Cao, U. Kolb, X. Feng, J. Maier, K. Müllen, *ChemSusChem* **2010**, 3, 236.
- [4] Y. Agawa, H. Tanaka, S. Torisu, S. Endo, A. Tsujimoto, N. Gonohe, V. Malgras, A. Aldalbahi, S.M. Alshehri, Y. Kamachi, C. Li, Y. Yamauchi, *Sci. Technol. Adv. Mater.* **2015**, 16, 024804.
- [5] (a) A. Aijaz, N. Fujiwara and Q. Xu, *J. Am. Chem. Soc.* **2014**, 136, 6790; (b) L. Lin, Q. Zhu A.W. Xu, *J. Am. Chem. Soc.* **2014**, 136, 11027; (c) Y. Meng, D. Voiry, A. Goswami, X. Zou, X. Huang, M. Chhowalla, Z. Liu, T. Asefa, *J. Am. Chem. Soc.* **2014**, 136, 13554.
- [6] (a) T.Y. Ma, S. Dai, M. Jaroniec, S.Z. Qiao, *J. Am. Chem. Soc.* **2014**, 136, 13925; (b) R. Wu, D.P. Wang, X. Rui, B. Liu, K. Zhou, A.W.K. Law, Q. Yan, J. Wei, Z. Chen, *Adv. Mater.* **2015**, 27, 3038; (c) N. Jiang, B. You, M. Sheng, Y. Sun, *Angew. Chem., Int. Ed.* **2015**, 54, 6251; (d) Y. Shi, J. Wang, C. Wang, T.T. Zhai, W.J. Bao, J.J. Xu, X.H. Xia, H.Y. Chen, *J. Am. Chem. Soc.* **2015**, 137, 7365.
- [7] Z.S. Wu, S. Yang, Y. Sun, K. Parvez, X. Feng, K. Müllen, *J. Am. Chem. Soc.* **2012**, 134, 9082.
- [8] (a) W. Zhu, K. Liu, X. Sun, X. Wang, Y. Li, L. Cheng, Z. Liu, *ACS Appl. Mater. Interfaces* **2015**, 7, 11575; (b) S. Yang, X. Feng, S. Ivanovici, K. Müllen, *Angew. Chem., Int. Ed.* **2010**, 49, 8408; (c) L. Zhang, J. Xia, Q. Zhao, L. Liu, Z. Zhang, *Small* **2010**, 6, 537.
- [9] (a) M.B. Zakaria, M. Hu, R.R. Salunkhe, M. Pramanik, K. Takai, V. Malgras, S. Choi, S.X. Dou, J.H. Kim, M. Imura, S. Ishihara, Y. Yamauchi, *Chem. -Eur. J.* **2015**, 21, 3605; (b) M. Hu, S. Ishihara, Y. Yamauchi, *Angew. Chem., Int. Ed.* **2013**, 52, 1235.
- [10] (a) J. Shen, Y. Hu, M. Shi, X. Lu, C. Qin, C. Li, M. Ye, *Chem. Mater.* **2009**, 21, 3514; (b) S. Park, J. An, J.R. Potts, A. Velamakanni, S. Murali, R.S. Ruoff, *Carbon* **2011**, 49, 3019.
- [11] N.L. Torad, R.R. Salunkhe, Y. Li, H. Hamoudi, M. Imura, Y. Sakka, C.C. Hu, Y. Yamauchi,

*Chem. -Eur. J.* **2014**, *20*, 7895.

- [12] (a) B. Zhao, J. Song, P. Liu, W. Xu, T. Fang, Z. Jiao, H. Zhang, Y. Jiang, *J. Mater. Chem.* **2011**, *21*, 18792; (b) N. Mironova-Ulmane, A. Kuzmin, I. Steins, J. Grabis, I. Sildos, M. Pärs, *J. Phys.: Conf. Ser.* **2007**, *93*, 012039; (c) W. Wang, Y. Liu, C. Xu, C. Zheng, G. Wang, *Chem. Phys. Lett.* **2002**, *362*, 119.
- [13] (a) K. Ariga, A. Vinu, Y. Yamauchi, Q. Ji, J.P. Hill, *Bull. Chem. Soc. Jpn.* **2012**, *85*, 1; (b) V. Malgras, Q. Ji, Y. Kamachi, T. Mori, F. Shieh, K.C.W. Wu, K. Ariga, Y. Yamauchi, *Bull. Chem. Soc. Jpn.* **2015**, *88*, 1171.
- [14] (a) X.-Q. Li, W.-X. Zhang, *Langmuir* **2006**, *22*, 4638; (b) M.C. Biesinger, B.P. Payne, A.P. Grosvenor, L.W.M. Lau, A.R. Gerson, R.St.C. Smart, *Appl. Surf. Sci.* **2011**, *257*, 2717; (c) A.P. Grosvenor, M.C. Biesinger, R.St.C. Smart, N.S. McIntyre, *Surf. Sci.* **2006**, *600*, 1771; (d) M.H. Koppelman, J.G. Dillard, *Clays Clay Miner.* **1977**, *25*, 457.
- [15] (a) S. Pei, H.-M. Cheng, *Carbon* **2012**, *50*, 3210; (b) D. Yang, A. Velamakanni, G. Bozoklu, S. Park, M. Stoller, R.D. Piner, S. Stankovich, I. Jung, D.A. Field, C.A. Ventrice Jr, R.S. Ruoff, *Carbon* **2009**, *47*, 145; (c) D.R. Dreyer, S. Park, C.W. Bielawski, R.S. Ruoff, *Chem. Soc. Rev.* **2010**, *39*, 228.
- [16] (a) M. Srivastava, M.E. Uddin, J. Singh, N.H. Kim, J.H. Lee, *J. Alloys Compd.* **2014**, *590*, 266; (b) Q. Wu, L. Jiang, Q. Tang, J. Liu, S. Wang, G. Sun, *Electrochim. Acta* **2013**, *91*, 314.
- [17] (a) Y. Xiao, C. Hu, L. Qu, C. Hu, M. Cao, *Chem. -Eur. J.* **2013**, *19*, 14271; (b) J. Cruickshank, K. Scott, *J. Power Sources* **1998**, *70*, 40; (c) C.Y. Du, T.S. Zhao, W.W. Yang, *Electrochim. Acta* **2007**, *52*, 5266.
- [18] (a) C. Li, T. Sato, Y. Yamauchi, *Angew. Chem., Int. Ed.* **2013**, *52*, 8050; (b) J. Tang, J. Liu, C. Li, Y. Li, M.O. Tade, S. Dai, Y. Yamauchi, *Angew. Chem., Int. Ed.* **2015**, *54*, 588.

## Chapter 7-2

# 7-2. Self-Construction from 2D to 3D: One-Pot Layer-by-Layer Assembly of Graphene Oxide Sheets Held Together by Coordination Polymers

### 7-2.1. Introduction

For the further development of functional materials, a smart approach to the assembly of functional 2D materials into well-defined 3D structures is critical. The best strategy for this purpose is layer-by-layer (LbL) assembly that can provide well-designed alternating layered structures with nanoscale precision from a variety of functional components [1]. For example, methodologies to create artificial layered structures often lead to materials with high level functions that cannot be predicted based on the identity of the original components [2]. However, most of the previous strategies have several disadvantages: 1) in many cases, interlayer materials are nonfunctional polymers and often degrade the functionality of the main components; 2) step-by-step layering processes could be disadvantageous for construction of substantially thicker materials. Although pioneering approaches for non-interlayer-polymer LbL processes have been recently proposed [3], these disadvantages have not yet been properly addressed.

In the novel strategy presented here, I have exploited the layering capabilities of coordination polymers [4] as an interlayer adhesive in a spontaneous self-constructive process implemented in one pot. Typically, Ni-based cyano-bridged coordination polymers (NiCNNi) are deposited on the surface of graphene oxide (GO) sheets. During this reaction (**Figure 7-2.1**), GO sheets spontaneously assemble through binding of NiCNNi flakes in the one-step construction of heterogeneous layered structures whose components all have some potentially useful functionality. In addition, the GO sheets serve not only as building units but also as nucleation sites for the growth of the NiCNNi flakes. Thermal treatment of the layered assembly causes successful conversion of the NiCNNi components to  $\text{Ni}_3\text{C}$  with retention of the original LbL structure, since the inserted GO layers prevent random fusion of the metal source.

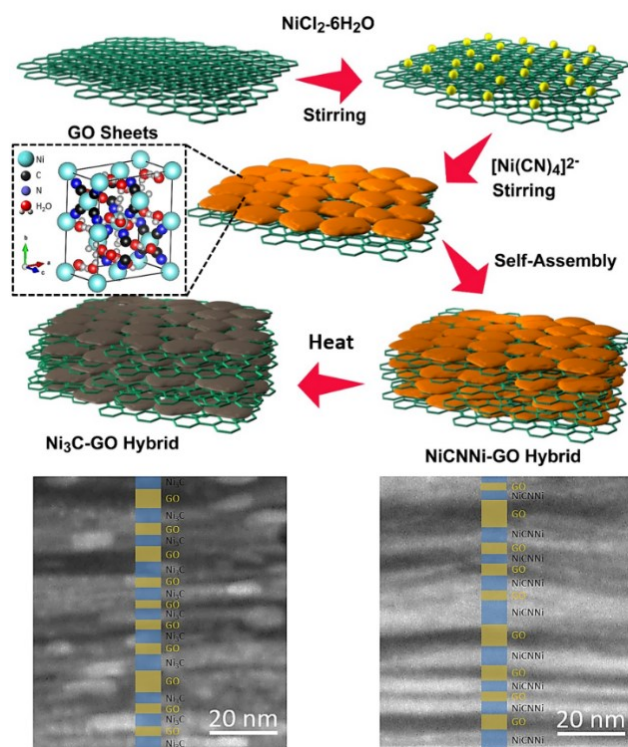


**Figure 7-2.1.** Formation process of NiCNNi-GO hybrids (composites) through coordination-polymer-glued layer-by-layer assembly of graphene oxide sheets, and its thermal conversion to  $\text{Ni}_3\text{C}$ -GO hybrid (composite). Cross-sectional TEM images of NiCNNi-GO hybrid and  $\text{Ni}_3\text{C}$ -GO hybrid and the crystal structure  $\text{Ni}(\text{H}_2\text{O})_2[\text{Ni}(\text{CN})_4]\cdot 4\text{H}_2\text{O}$  (NiCNNi) between the GO sheets are also shown.

## 7-2.2. Experimental Details

### 7-2.2.1. Chemicals

Potassium tetracyanonickelate (II) hydrate was purchased from Sigma-Aldrich, USA. Nickel chloride hexahydrate, trisodium citrate dihydrate (TSCD), and sulfuric acid were purchased from Nacalai Tesque, Japan. Potassium hydroxide and sodium nitrate was purchased from Wako, Japan. Nanographite platelets (N008-100-N) of 100 nm thickness were used as raw material to prepare graphene oxide (GO), Angestron materials.  $\text{KMnO}_4$  and  $\text{H}_2\text{O}_2$  were purchased from Kanto Chemicals Co., Inc. All chemical reagents were used without further purification.

### 7-2.2.2. Synthesis of GO Sheets

Graphite powder (N008-100-N, carbon source) and sodium nitrate were mixed together followed by the addition of 7.67 ml of concentrated sulphuric acid solution under constant stirring for 1 h. Then, 1 g of  $\text{KMnO}_4$  was added gradually to the above solution while keeping the temperature less than 20 °C. The mixture was stirred at 35 °C for 10 h and the resulting solution was diluted by adding 83 ml of pure water under vigorous stirring. To ensure the completion of reaction with  $\text{KMnO}_4$ , the suspension was further treated with 30%  $\text{H}_2\text{O}_2$  solution (1.67 ml). The resulting colloidal solution was kept for the next step.

### 7-2.2.3. In-situ Growth of NiC<sub>2</sub>Ni Flakes onto the Surface of GO Sheets and Thermal Conversion into Ni<sub>3</sub>C-GO Hybrid

$\text{NiCl}_2 \cdot 6\text{H}_2\text{O}$  (94.8 mg) and trisodium citrate dihydrate (88.2 mg) were dissolved in 20 mL water

to form a clear solution. This solution was poured dropwise into 20 mL GO solution (2 mg mL<sup>-1</sup>) and stirred for 30 min. The obtained mixture is gently mixed with another clear solution prepared by dissolving K<sub>2</sub>[Ni(CN)<sub>4</sub>] (96.4 mg) into 20 mL water. Then, the final suspension was aged for two days until the reaction is complete. The precipitate was obtained by centrifugation. After washing with water and ethanol extensively, the as-prepared NiCNNi-GO LbL hybrids were dried at room temperature. Then, the obtained NiCNNi-GO hybrids (100 mg) were heated inside an electronic furnace to the desired temperatures (350 °C, 450 °C, 550 °C, and 650 °C) with a heating rate of 5 °C min<sup>-1</sup> and kept for annealing during 1 h. After that, the powder was cooled inside the furnace naturally. Finally, the obtained powder (Ni<sub>3</sub>C-GO LbL hybrids) was collected for characterization. The whole calcination process was carried out under nitrogen flow (130 mL min<sup>-1</sup>).

#### 7-2.2.4. Characterization

SEM images were acquired with a Hitachi SU8000 scanning microscope at an accelerating voltage of 5 kV. The TEM observations were performed using a JEM-2100F operating at 200 kV and equipped for energy-dispersive spectrometer analysis. The wide-angle powder X-ray diffraction (XRD) patterns were obtained with a Rigaku RINT 2500X diffractometer using monochromated Cu K $\alpha$  radiation (40 kV, 40 mA). Raman spectra were measured by Horiba-Jovin Yvon T64000 with the excitation Laser 364 nm. X-ray photoelectronic spectroscopy (XPS) spectra were recorded at room temperature by using a JPS-9010TR (JEOL) instrument with an Mg K $\alpha$  X-ray source. All binding energies were calibrated by referencing to C 1s (285.0 eV). The UV/Vis spectra were collected using a JASCO V-570 UV/Vis/NIR spectrophotometer.

### 7-2.2.5. Electrochemical Measurements

A conventional three-electrode cell was used for oxygen reduction reaction (ORR) measurement, including an Ag/AgCl (saturated KCl) as reference electrode, a platinum wire as a counter electrode, and a modified rotating ring disk electrode (RRDE) as a working electrode. The working electrode was prepared as follows. 5 mg of catalyst was dispersed in a mixture of water/ethanol ( $v/v = 3:1$ , 950  $\mu\text{L}$ ) and Nafion (5 wt%, 50  $\mu\text{L}$ ) under sonication for 30 min. Then, 5  $\mu\text{L}$  of the above suspension was dropped on the surface of the RDE and dried at room temperature. The cyclic voltammograms were checked at a scan rate of 20  $\text{mV s}^{-1}$  without any rotation. The linear sweep voltammograms were performed at a potential range between 0.0 V and -1.0 V (vs. Ag/AgCl) with a scan rate of 10  $\text{mV s}^{-1}$  and rotating speed of 1600 rpm. All the measurements were carried out in 0.1 M KOH with  $\text{N}_2$ - or  $\text{O}_2$ -saturated. The kinetic parameters can be analyzed on the basis of the following Koutecky-Levich equations:

$$J^{-1} = J_L^{-1} + J_K^{-1} = B^{-1} \omega^{-1/2} + J_K^{-1} \quad (7-2.1)$$

$$B = 0.62nFC_0(D_0)^{2/3} \nu^{-1/6} \quad (7-2.2)$$

, where  $J$  is the measured current density,  $J_K$  and  $J_L$  are the kinetic- and diffusion-limiting current densities,  $\omega$  is the angular velocity of the disk,  $n$  represent the overall number of electrons transferred during the oxygen reduction,  $F = 96485$  ( $\text{C mol}^{-1}$ ) is the Faraday constant,  $C_0$  ( $\text{mol L}^{-1}$ ) is the bulk concentration of  $\text{O}_2$ ,  $\nu$  ( $\text{cm}^2 \text{s}^{-1}$ ) is the kinematic viscosity of the electrolyte,  $D_0$  ( $\text{cm}^2 \text{s}^{-1}$ ) is the diffusion coefficient, and  $k$  is the electron transfer rate constant. The number of electrons transferred ( $n$ ) can be obtained from the slope of the Koutecky-Levich plots.

The electron transfer number per oxygen molecule involved in the ORR was calculated from RRDE voltammograms according to the following equation.

$$n = 4 \times I_d / (I_d + I_r / N) \quad (7-2.3)$$

, where  $I_d$  is the disk current,  $I_r$  is the ring current and  $N = 0.4$  is the collection efficiency of Pt

ring.

### 7-2.3. Results and Discussion

**Figure 7-2.1** shows the formation process of the NiCNNi-GO hybrid structure. The GO sheets have a two-dimensional (2D) morphology with a large average lateral dimension of  $\sim 1 \mu\text{m}$  and are dispersed as a colloidal suspension (**Figure 7-2.2**). The high-resolution TEM image clearly shows lattice fringes which are oriented in two directions. Electron diffraction (ED) patterns reveal a hexagonal arrangement of the diffraction spots, which is a typical crystalline characteristic of GO. Functional groups (*e.g.*, carboxyl, hydroxyl, and epoxy) [5] of GO sheets, which can act as bridging sites simultaneously interacting with  $\text{Ni}^{2+}$  species, confer an overall negative charge on the starting GO suspension. By slow addition of  $[\text{Ni}(\text{CN})_4]^{2-}$  into the reaction system, nucleation of growth occurs, resulting in the growth of fine NiCNNi layers on both sides of the GO sheets. During this reaction, the surface charge of GO sheets changes from  $-30.7 \text{ mV}$  to  $7.75 \text{ mV}$ , according to Zeta potentials measured prior to and following reaction. Subsequently, the NiCNNi-GO components spontaneously assemble forming a highly optimized LbL architecture consisting of alternating layers of NiCNNi and GO.

NiCNNi flakes prepared in the absence of GO sheets exhibit an average lateral size of  $\sim 150 \text{ nm}$  (**Figure 7-2.3a,b**). The ordered lattice fringes of the flakes from high-resolution TEM (**Figure 7-2.3c**) combined with the periodic spots from the electron diffraction (ED) patterns reveal that the flakes are highly crystallized [6]. The surface morphology of the NiCNNi-GO hybrid was examined using scanning electron microscopy (SEM) and transmission electron microscopy (TEM), and the results are shown in **Figure 7-2.4**. From these images it can be clearly observed that the NiCNNi flakes have grown horizontally at the surfaces of the GO sheets with flakes apparently encapsulated between the larger GO sheets. The selected area ED pattern,



indicates that the crystalline structures of both NiCNNi and GO are preserved even after hybridization (**Figure 7-2.4b**). Interestingly, the cross-sectional high-angle annular dark-field scanning transmission electron microscope (HAADF-STEM) images reveal an LbL-type structure of the hybrid consisting of NiCNNi and GO layers (**Figures 7-2.5a and 7-2.6a**). The corresponding elemental mapping image shows heterogeneous distribution of Ni, C, and O atoms, thus also supporting the formation of alternating layered structures with nanometer-level layer thicknesses.

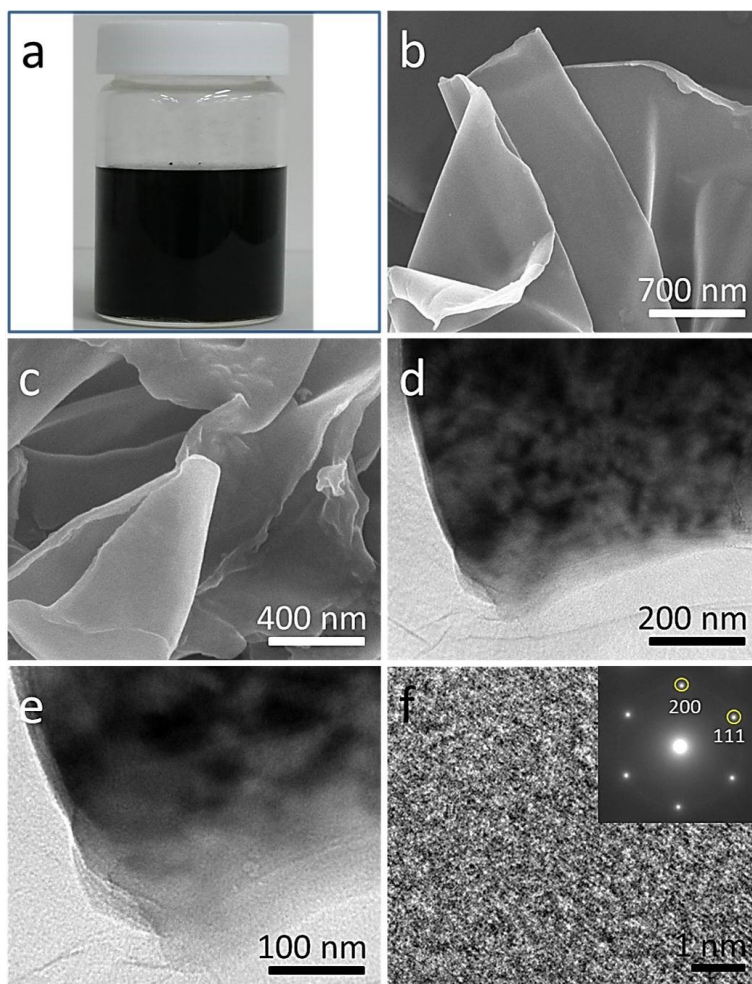


**Figure 7-2.2.** (a) Photograph of GO suspension, (b-c) SEM images of exfoliated GO sheets, (d-e) TEM images of exfoliated GO sheets, and (f) high resolution TEM image of GO sheets. The selected area ED patterns are shown as an inset.

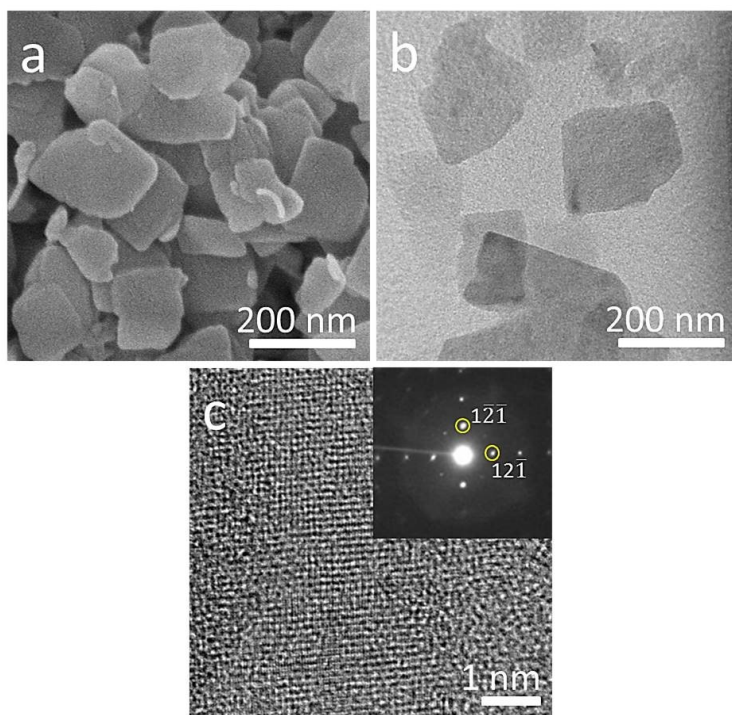


**Figure 7-2.3.** (a) SEM image, (b) TEM image, and (c) high resolution TEM image of NiCNNi flakes. The selected area ED patterns shown as an inset clearly match Hofmann-type crystal structure with  $Pnma$  space group ( $a=12.2$  Å,  $b=13.8$  Å, and  $c=7.12$  Å, respectively).

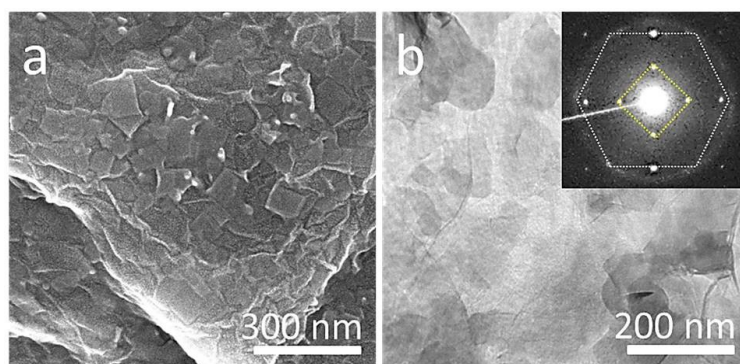


**Figure 7-2.4.** (a) SEM image and (b) TEM image of the NiCNNi-GO hybrid. Selected area ED pattern is shown as an inset. The inside spots are derived from NiCNNi flakes, while the outside ones are derived from GO sheets. The respective assignments are given in **Figure 7-2.2f** and **7-2.3c**.

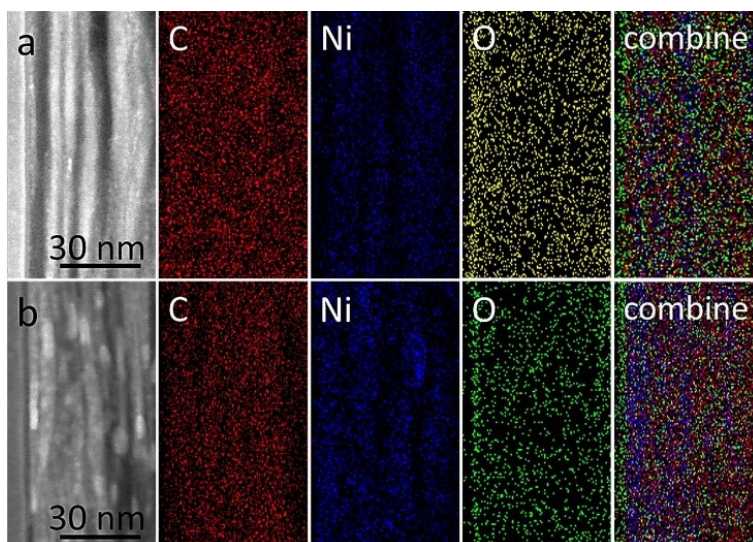


**Figure 7-2.5.** Cross-sectional HAADF-STEM images and elemental mapping images (carbon, oxygen, and nickel atoms) of (a) the as-prepared NiCNNi-GO hybrid and (b) Ni<sub>3</sub>C-GO hybrid after calcination at 450 °C.

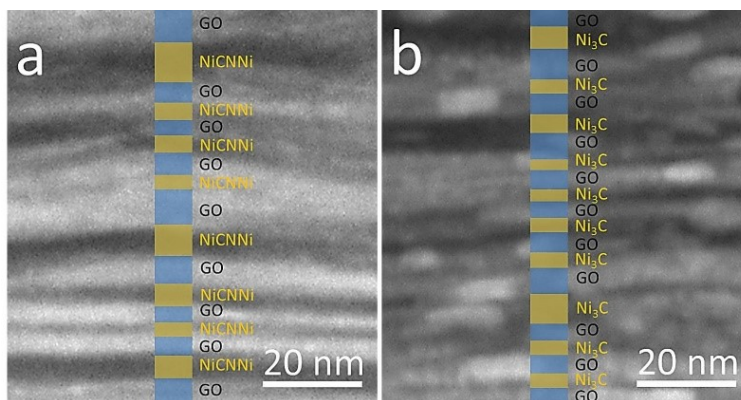


**Figure 7-2.6.** Cross-sectional HAADF-STEM image of (a) NiCNNi-GO hybrid and (b) Ni<sub>3</sub>C-GO hybrid after calcination at 450 °C.

To demonstrate the formation process of NiCNNi flakes on the GO sheets, the assembling of layered NiCNNi-GO hybrids was examined by UV/Vis measurements at different time intervals (**Figure 7-2.7**). UV/Vis absorption spectrum of the as-prepared GO suspension shows an absorption peak at around 230 nm corresponding to  $\pi$ - $\pi^*$  transition of C=C and another shoulder at 290-300 nm corresponding to n- $\pi^*$  transition of the C=O bond [7]. As the reaction time is

increased from 5 to 90 min, the UV/Vis absorption peaks of NiCNNi-GO hybrids gradually are red-shifted from  $\sim 331$  nm to  $\sim 340$  nm, corresponding to the d-d transition of Ni. This is an evidence of gradual growth of the NiCNNi flakes [8].

The crystal structures of GO, NiCNNi, and NiCNNi-GO hybrid were further investigated by wide-angle XRD (**Figure 7-2.8a**). In the case of GO, a diffraction peak at  $2\theta$  (ca.  $9.4^\circ$ ) is observed, corresponding to the 001 reflection (ca. 0.94 nm) [7]. Another diffraction peak is observed at  $2\theta$  (ca.  $25.5^\circ$ ), indicating a highly ordered graphitic structure. The diffraction peaks of the NiCNNi flakes are assignable to an orthorhombic system and clearly match Hofmann-type NiCNNi with 2D layered structure [6]. After the growth of NiCNNi flakes on the GO sheets, the relative peak intensity corresponding to 121 peak is weakened. This can be explained by preferential crystal growth on the GO sheets. As shown in Figure 7-2.4b, the (121) planes are vertically oriented plane to the GO surface.

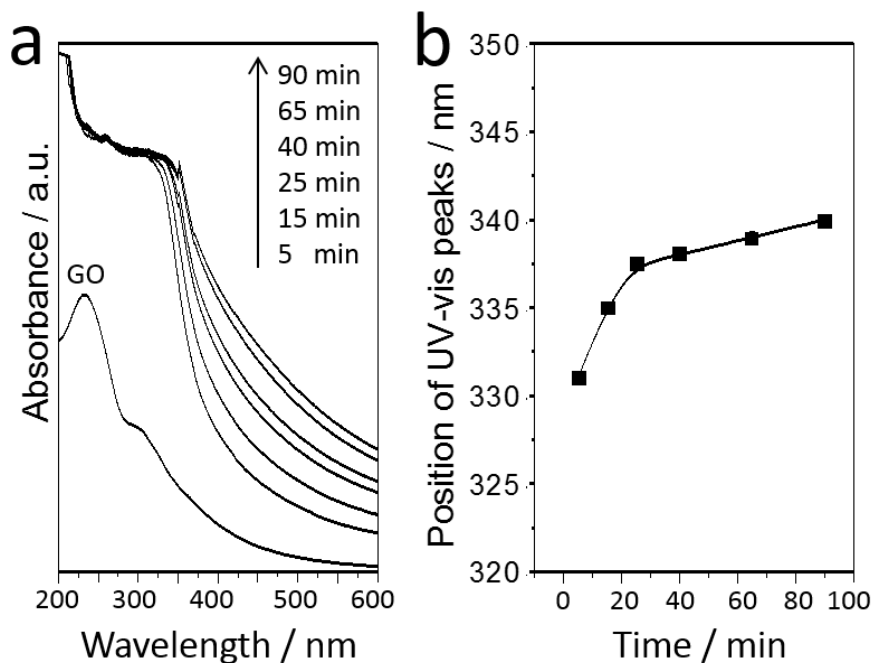


**Figure 7-2.7.** (a) UV-vis spectra of GO suspension and NiCNNi-GO hybrids collected at different time intervals and (b) plots of UV-vis peak positions of NiCNNi-GO hybrids as a function of the reaction times.

The changes of GO structure after the growth of NiCNNi flakes are examined by Raman measurement (**Figure 7-2.8b**). It can be seen that the intensity ratio ( $I_G/I_D$ ) of *D* and *G* bands of GO in the NiCNNi-GO hybrid is increased due to the removal of a large number of oxygen-containing functional groups [7]. It reveals the improvement of the GO sheets with less defects. Therefore, as seen in Figure 7-2.8b, the 001 peak is weakened and shifted to  $2\theta$  (ca.  $10.2^\circ$ ), demonstrating a decrease in the two interlayer distance of GO sheets (from ca. 0.94 nm to ca. 0.87 nm). A sharp peak is observed at  $2185.7\text{ cm}^{-1}$  corresponding to the C-N stretching [9], which remains even after hybridization with GO sheets. Together with XPS analysis (**Figure 7-2.9**), I confirm the presence of NiCNNi layers. As a reference, NiCNNi flakes were measured by high resolution XPS. As shown in **Figure 7-2.9a**, the obtained spectrum reveals a sharp photopeak at  $\sim 855\text{ eV}$  assigned to Ni  $2p_{3/2}$  as well as a Ni  $2p_{1/2}$  at  $872.5\text{ eV}$ , which are in accordance with  $\text{Ni}^{2+}$  species [10]. A photopeak at around  $285\text{ eV}$  is observable with a good symmetry corresponding to C  $1s$  core-level of carbon element in C-N (**Figure 7-2.9b**) [11]. N  $1s$  photopeak at around  $399\text{ eV}$  is characteristic of nitrogen element in C-N (**Figure 7-2.9c**) [12].

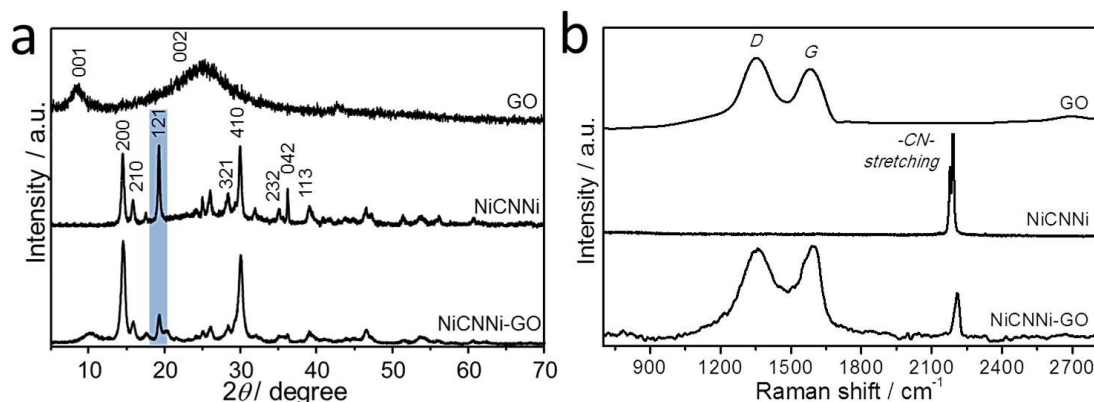


**Figure 7-2.8.** (a) Wide-angle XRD patterns and (b) Raman spectra of the GO, NiCNNi, and NiCNNi-GO hybrid samples.

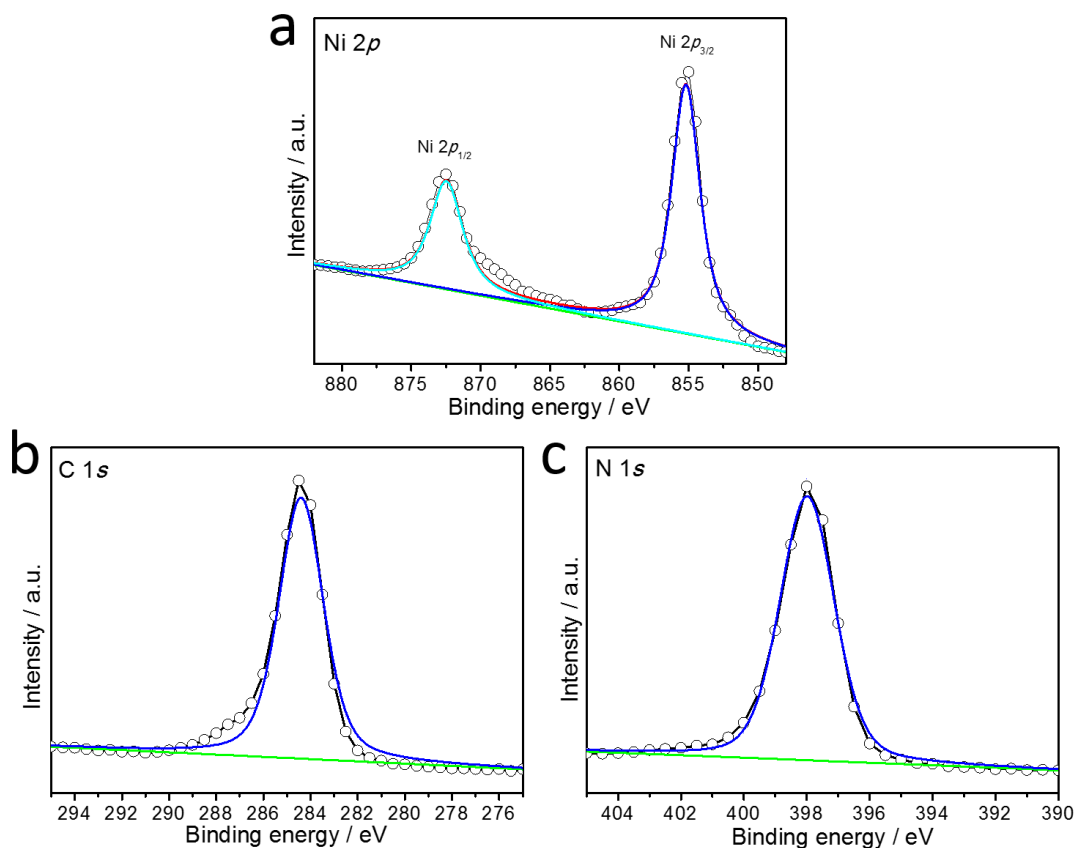


**Figure 7-2.9.** High resolution XPS spectra of (a) Ni 2p, (b) C 1s, and (c) N 1s of NiCNNi flakes as a reference.

It was anticipated that thermal treatment of pristine NiCNNi flakes under nitrogen would result in Ni<sub>3</sub>C with a two-dimensional morphology. To test this, NiCNNi flakes without GO sheets were calcined under nitrogen at different temperatures (*i.e.*, 350 °C, 450 °C, 550 °C, and 650 °C, respectively). The crystal structures and phase purities of the resulting products were examined using wide-angle XRD (**Figure 7-2.10**). The sample calcined at 350 °C underwent incomplete removal of the organic units and the peaks could not be assigned to a specific crystal structure. Interestingly, the sample calcined at 450 °C give a diffraction pattern characteristic of pure crystalline Ni<sub>3</sub>C [13] with XRD patterns assignable to a trigonal (*R-3c*) structure. Further increases in the calcination temperature (500 °C and 650 °C) lead to decomposition of the Ni<sub>3</sub>C structure with some peaks corresponding to metallic *fcc* Ni emerging. Although pure crystalline

$\text{Ni}_3\text{C}$  could be obtained following optimization of the thermal treatment process of NiCNNi flakes (*i.e.* 450 °C under nitrogen), the original 2D form was totally disrupted because of crystallization and fusion of the metal framework, as illustrated by SEM imaging (**Figure 7-2.11**). In contrast, the NiCNNi-GO LbL structure is relatively stable even against thermal treatment at elevated temperatures, yielding the  $\text{Ni}_3\text{C}$ -GO LbL structure. The  $\text{Ni}_3\text{C}$ -GO hybrid has an LbL structure that strongly corresponds with the original NiCNNi-GO hybrid (**Figures 7-2.5b** and **7-2.6b**). As is clearly shown in **Figures 7-2.12** and **7-2.13**, the lateral size and morphology of individual  $\text{Ni}_3\text{C}$  nanosheets remains unchanged.

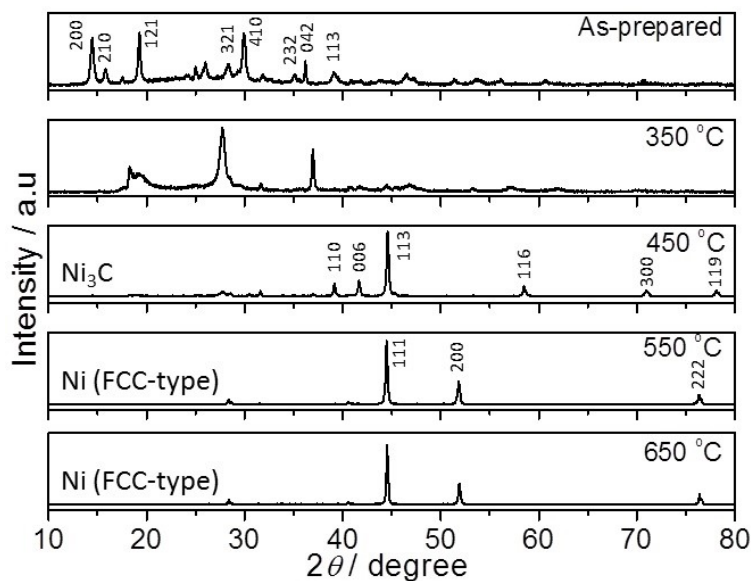


**Figure 7-2.10.** Wide-angle XRD patterns of NiCNNi flakes (without GO sheets) treated at different temperatures.

The  $\text{Ni}_3\text{C}$ -GO hybrid obtained by calcination at 450 °C was examined by high resolution X-ray photoelectron spectroscopy (XPS) (**Figures 7-2.14a-c**). At least seven peaks are found in the C 1s XPS spectrum after deconvolution. The peak at 283.3 eV is assigned to Ni-C bonds [14], with a second peak at 285.5 eV assigned to  $sp^3$  hybridized carbon (C-C,  $sp^3$ ) [14]. Between these two peaks, a third feature at 284.3 eV can be assigned to  $sp^2$  hybridized carbon (C=C,  $sp^2$ ) [14].

Additionally, four types of carbon atoms due to different functional groups can be observed: non-oxygenated ring (284.5 eV), C-O (286.01 eV), C=O (288.42 eV), and O-C=O (292 eV) [15]. In the Ni  $2p_{3/2}$  XPS spectrum, a peak with a binding energy of 855.4 eV with a satellite peak at 861.6 eV were observed. The main peak position is located at a higher binding energy than NiO, Ni(OH)<sub>2</sub>, and metallic Ni phases, and it corresponds to pure Ni<sub>3</sub>C phase. From these XPS data, it can be deduced that the Ni<sub>3</sub>C flakes are more tightly anchored to the surface of GO through functional groups containing oxygen. Raman spectra of GO sheets and Ni<sub>3</sub>C-GO hybrids are shown in **Figure 7-2.14d**. The *D* and *G* bands of GO sheets can be clearly observed in both cases [16], implying the retention of 2D GO structure even after the growth of Ni<sub>3</sub>C during thermal treatment. After heat treatment, the intensity of the graphitic (*G*) band increases relative to that of GO sheets because the functional groups of GO sheets have been thermally decomposed.

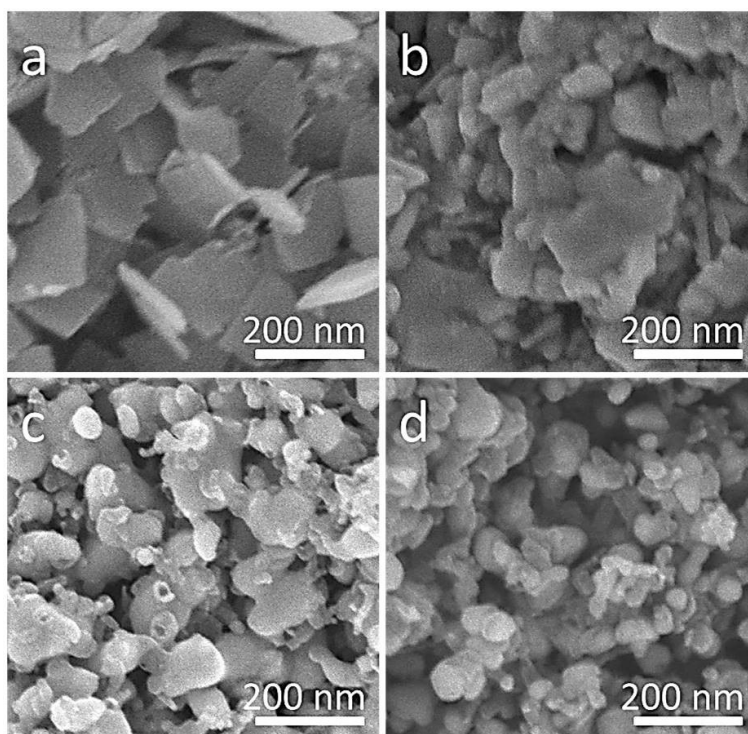


**Figure 7-2.11.** SEM images of NiCNNi flakes (without GO sheets) treated at different temperatures ((a) 350 °C, (b) 450 °C, (c) 550 °C, and (d) 650 °C).



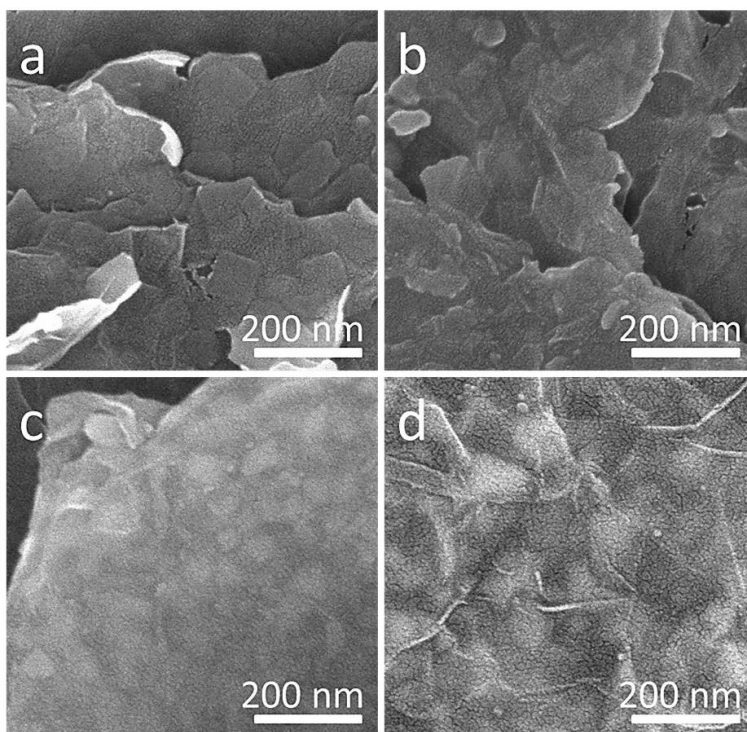


**Figure 7-2.12.** SEM images of the NiCNNi-GO hybrids treated at different temperatures ((a) 350 °C, (b) 450 °C, (c) 550 °C, and (d) 650 °C).

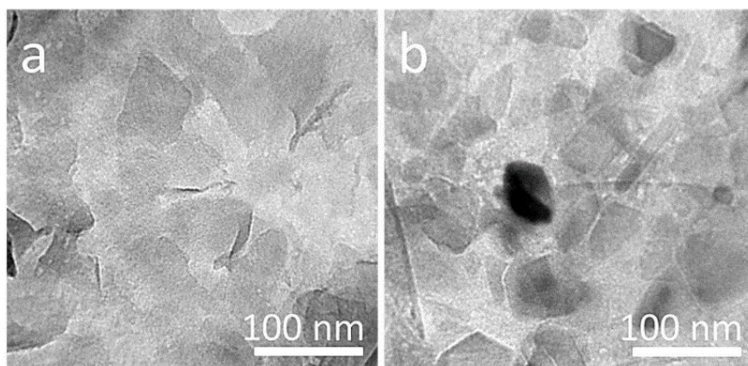


**Figure 7-2.13.** SEM images of the NiCNNi-GO hybrids treated at different temperatures ((a) 450 °C, and (b) 550 °C).

Of the well-known transition metal carbides, nickel carbide ( $\text{Ni}_3\text{C}$ ) has received considerable recent attention owing to its excellent catalytic activity and high chemical stability [17]. It is anticipated that Ni might be a realistic alternative to precious metals like Pt, Au, and Pd, because of its low cost, abundance, and corrosion resistance in alkaline solutions [17]. However,  $\text{Ni}_3\text{C}$  has

been much less investigated because complex synthetic procedures, which require expensive apparatus. A few previous reports have suggested that thermal treatment of nickel-based precursors might open the way for synthesis of high quality  $\text{Ni}_3\text{C}$  [18], although morphological control and particle aggregation at elevated temperatures remain challenging issues. The integration of transition metal carbides and highly conductive carbon materials could also circumvent serious problems associated with the rate capabilities and poor charge transport. The intrinsic properties of graphene (*e.g.*, excellent electrical conductivity, high mechanical strength) would make its hybrids with  $\text{Ni}_3\text{C}$  excellent candidates for various electronic applications. In this work, I demonstrate the significant advantage of an LbL architecture for such materials over simple physically mixed  $\text{Ni}_3\text{C}$ -GO composites.

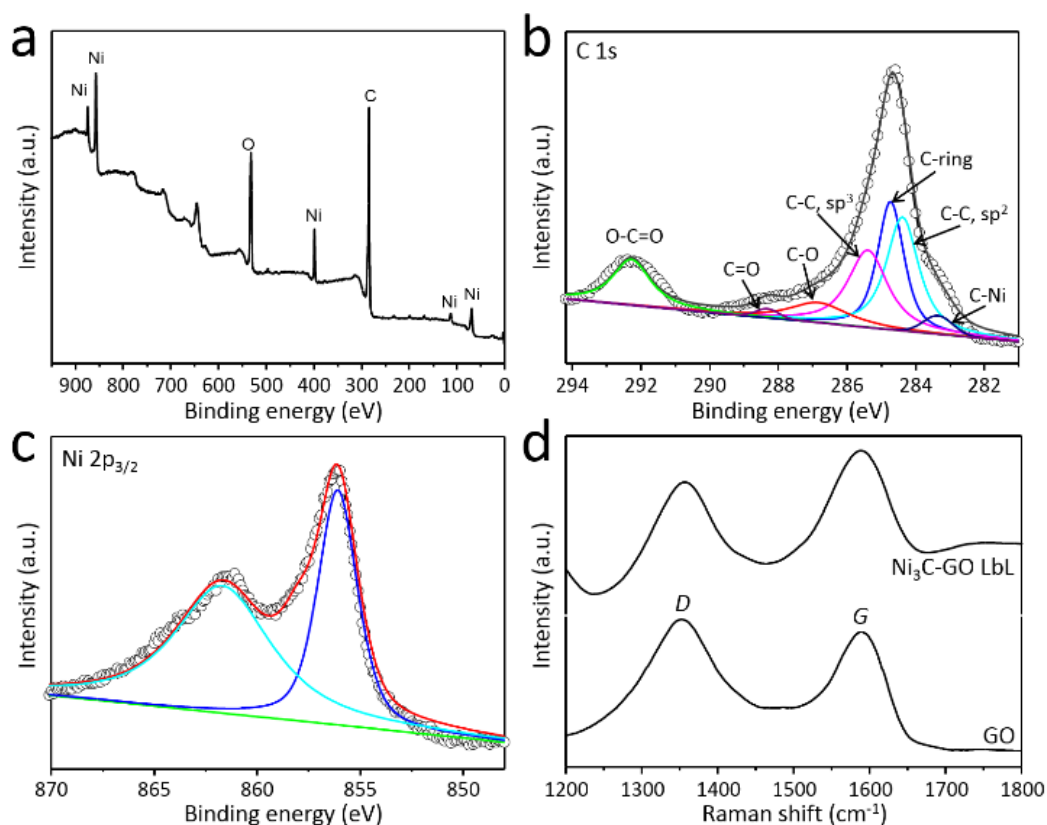


**Figure 7-2.14.** (a) XPS survey spectrum and (b-c) XPS expanded spectra ((b) C 1s, and (c) Ni  $2p_{3/2}$ ) of  $\text{Ni}_3\text{C}$ -GO hybrid after calcination at 450 °C. (d) Raman spectra of GO sheets and  $\text{Ni}_3\text{C}$ -GO hybrid after calcination at 450 °C.

Inspired by the unique form of the LbL-structured Ni<sub>3</sub>C-GO hybrid after calcination at 450 °C (abbreviated as Ni<sub>3</sub>C-GO LbL), the oxygen reduction reaction (ORR) was investigated to explore the potential application of these materials in energy conversion systems. Its electrocatalytic activity was also benchmarked against GO, Ni<sub>3</sub>C and a physically mixed Ni<sub>3</sub>C-GO composite (abbreviated as Ni<sub>3</sub>C-GO mix). The electrocatalytic activities of all the samples were first evaluated by cyclic voltammetry (CV) in 0.1 M KOH solution saturated with N<sub>2</sub> and O<sub>2</sub> at a scan rate of 20 mV s<sup>-1</sup>. The observed oxygen reduction peak of Ni<sub>3</sub>C-GO LbL shifted significantly to more positive potentials (-290 mV vs. Ag/AgCl) than that of GO (-310 mV vs. Ag/AgCl), Ni<sub>3</sub>C (-370 mV vs. Ag/AgCl) or Ni<sub>3</sub>C-GO mix (-360 mV vs. Ag/AgCl), as shown in **Figure 7-2.15**, thus suggesting a significantly enhanced electrocatalytic activity of LbL-structured Ni<sub>3</sub>C-GO hybrid.

The ORR performance of the samples was further examined by using a rotating-ring disk electrode (RRDE) in an O<sub>2</sub>-saturated 0.1 M KOH solution at a rotation speed of 1600 rpm and a scan rate of 10 mV s<sup>-1</sup> (**Figure 7-2.16**). The linear scan voltammograms (LSV) curves in **Figure 7-2.16a** confirm the ORR activity of Ni<sub>3</sub>C-GO LbL catalyst, with an onset potential of around -99 mV vs. Ag/AgCl. Compared to GO (-166 mV vs. Ag/AgCl), Ni<sub>3</sub>C (-240 mV vs. Ag/AgCl) and Ni<sub>3</sub>C-GO mix (-228 mV vs. Ag/AgCl), the Ni<sub>3</sub>C-GO LbL (-99 mV vs. Ag/AgCl) shows a more positive onset potential, thus further confirming the improved electrocatalytic activity of the Ni<sub>3</sub>C-GO LbL catalyst for the ORR. Even when compared to previous reports, my Ni<sub>3</sub>C-GO LbL catalyst shows a more positive onset potential, as summarized in **Table 7-2.1**.

To investigate the effect of the Ni<sub>3</sub>C-GO LbL catalyst on the kinetics of the ORR, the RRDE measurement was performed at different rotation speeds from 200 rpm to 2500 rpm at a constant scan rate of 10 mV s<sup>-1</sup> (**Figure 7-2.16b**). The corresponding Koutecky-Levich plots [19] ( $J^1$  vs.  $\omega^{-1/2}$ ) for my catalyst are parallel with good linearity and constant electron transfer

numbers for ORR at different potentials (-0.35, -0.40, and -0.45 V vs. Ag/AgCl), as shown in **Figure 7-2.16c**. The average transferred electron number ( $n$ ) was estimated to be 2.6 which is slightly higher than that of 2.5 for Ni<sub>3</sub>C-GO mix (**Figure 7-2.17**).

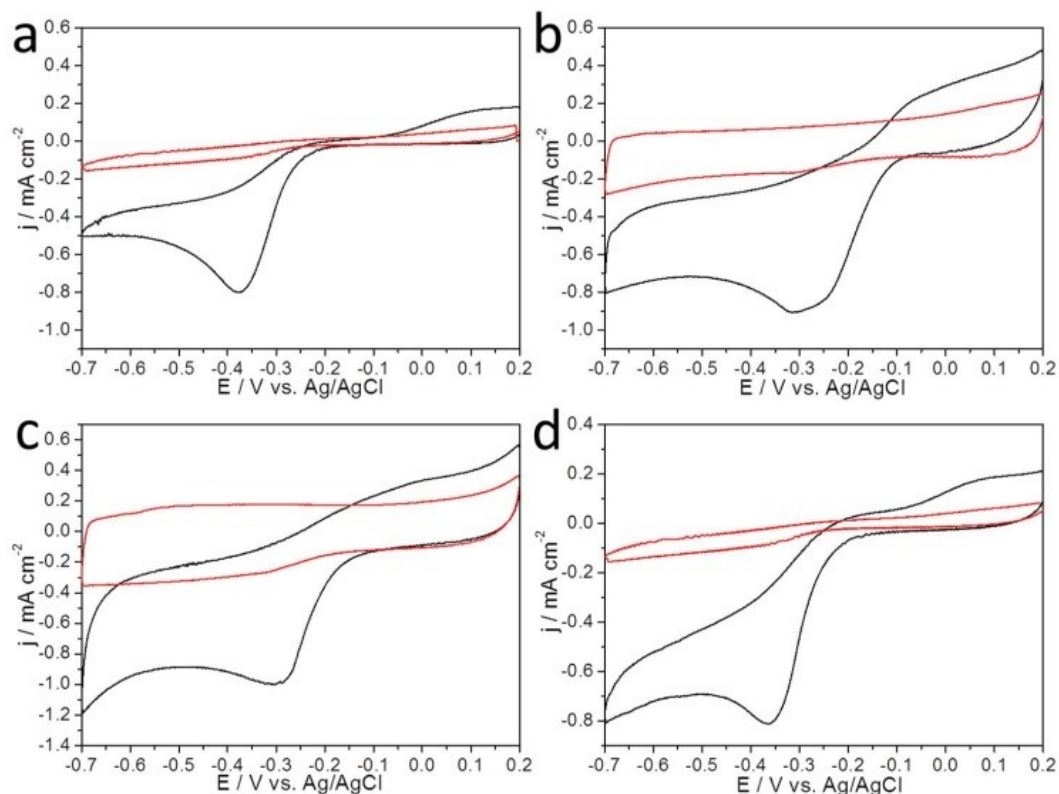


**Figure 7-2.15.** CV curves of the (a) Ni<sub>3</sub>C, (b) GO, (c) Ni<sub>3</sub>C-GO LbL, and (d) Ni<sub>3</sub>C-GO mix, recorded in 0.1 M KOH solution saturated with N<sub>2</sub> (red line) and O<sub>2</sub> (black line) at a scan rate of 20 mV s<sup>-1</sup>.

Moreover, to obtain a more in-depth understanding of the ORR process, electron transfer number ( $n$ ) were estimated from hydrodynamic voltammograms collected from disk and ring electrodes (RRDE). The obtained  $n$  values during the ORR using Ni<sub>3</sub>C-GO LbL catalyst was estimated to be from 2.6 to 3.0 (from -0.4 V to -1.0 V vs. Ag/AgCl) (**Figure 7-2.16d**). Furthermore, the charge transfer resistances of the Ni<sub>3</sub>C-GO LbL and Ni<sub>3</sub>C-GO mix catalysts were investigated by electrochemical impedance spectroscopy (EIS) in 0.1 M KOH over the frequency range from 1 M Hz to 1 Hz. The typical impedance spectra of different catalysts are shown in **Figure 7-2.18**. The

diameters of the semicircle behaviors of the EIS data represent the charge-transfer resistance ( $R_{ct}$ ) at the electrode surface. It is obvious that the layer-by-layer assembled  $\text{Ni}_3\text{C}$ -GO sample shows lower resistance, namely better performance, than the physically mixed sample ( $\text{Ni}_3\text{C}$ -GO mix).

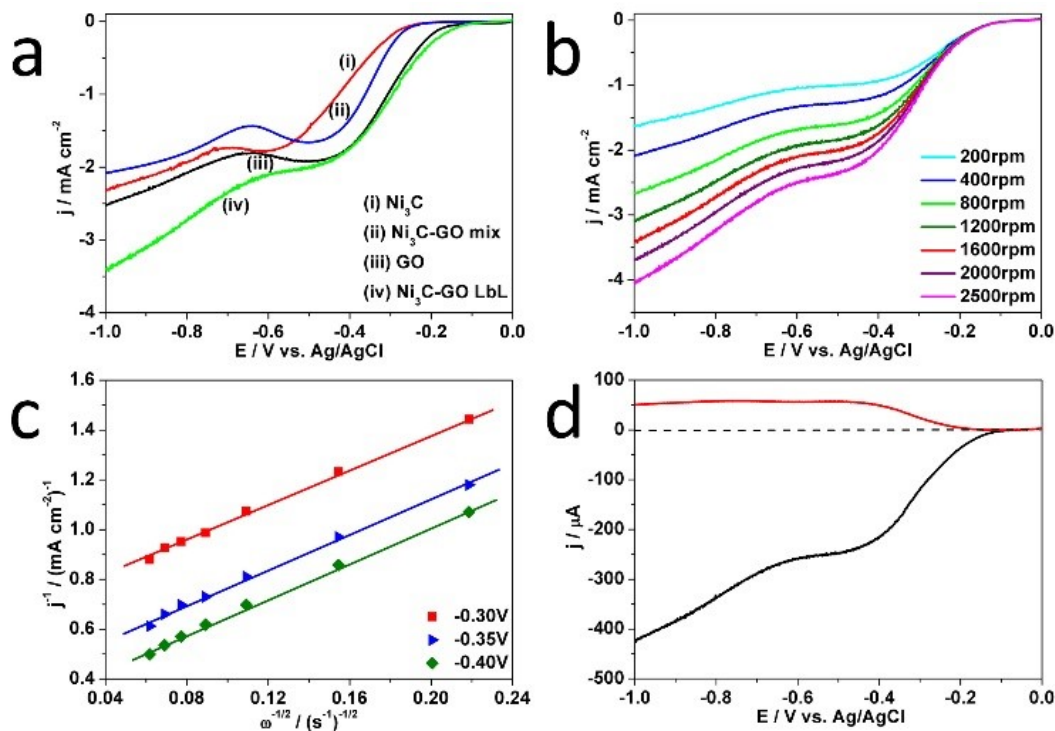


**Figure 7-2.16.** (a) ORR polarization curves of (i)  $\text{Ni}_3\text{C}$ , (ii)  $\text{Ni}_3\text{C}$ -GO mix, (iii) GO, and (iv)  $\text{Ni}_3\text{C}$ -GO LbL, recorded in  $\text{O}_2$ -saturated 0.1 M KOH solution with a sweep rate of  $10 \text{ mV} \cdot \text{s}^{-1}$  at a rotation rate of 1600 rpm, (b) ORR polarization curves of  $\text{Ni}_3\text{C}$ -GO LbL at different rotation rates, and (c) corresponding Koutecky-Levich (K-L) plots of the  $\text{Ni}_3\text{C}$ -GO LbL at different potentials. (d) The current collected on disk and ring electrodes catalyzed by  $\text{Ni}_3\text{C}$ -GO LbL.

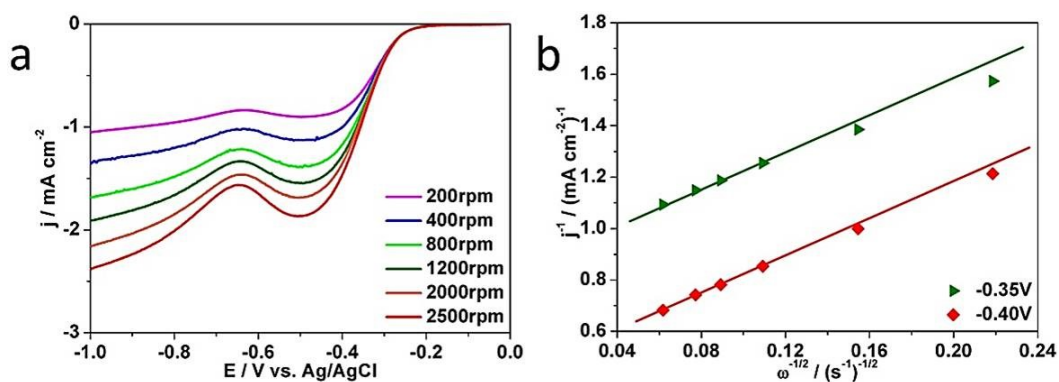


**Figure 7-2.17.** ORR polarization curves of (a)  $\text{Ni}_3\text{C}$ , (c) GO, and (e)  $\text{Ni}_3\text{C}$ -GO mix at different rotation rates recorded in  $\text{O}_2$ -saturated 0.1 M KOH solution with a sweep rate of  $10 \text{ mV} \cdot \text{s}^{-1}$ , and

corresponding Koutecky-Levich (K-L) plots of the (b) Ni<sub>3</sub>C, (d) GO, (f) Ni<sub>3</sub>C-GO mix at different potentials.

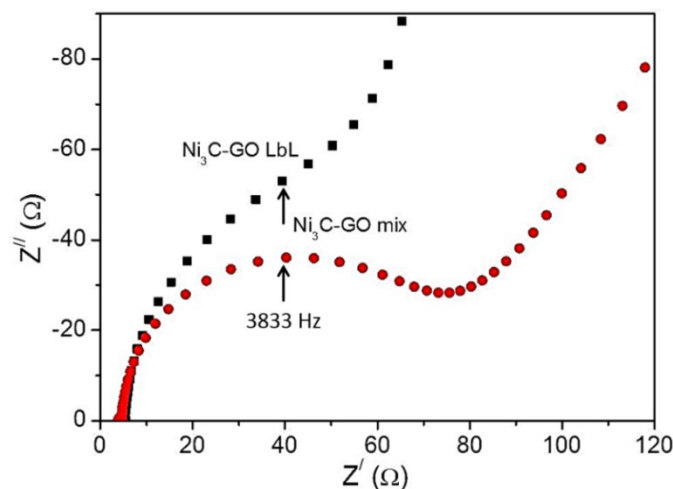


**Figure 7-2.18.** Complex-plane impedance diagrams obtained by the electrochemical impedance spectroscopy (EIS) of different catalysts obtained in 0.1 M KOH.

**Table 7-2.1** Comparison of ORR activity of our ORR catalyst with previously reported materials ( $n$  is the number of electron transferred during the ORR).

Sample information	Electrolyte	Onset potential* (mV vs. RHE)	$n$	References
Ni <sub>3</sub> C-GO LbL	0.1M KOH	861	3.76	<i>Present work</i>
TiO <sub>2</sub>	0.1M KOH	713	2.41	<i>Nat. Commun. 2015, 6:8696</i>
N-doped carbon film	0.1M KOH	---	3.72	<i>Angew. Chem. Int. Ed. 2014, 53, 9503-9507</i>
Mn <sub>3</sub> O <sub>4</sub> Nanoparticles on Nitrogen-Doped Graphene	0.1M KOH	830	3.81	<i>Adv. Funct. Mater. 2014, 24, 2072-2078</i>
covalent organic polymers with Co	0.1M KOH	890	3.56	<i>Angew. Chem. Int. Ed. 2014, 53, 2433-2437</i>
Mesoporous N-doped carbon	0.1M KOH	730	2.6	<i>Adv. Funct. Mater. 2012, 22, 4584</i>
Reduced graphene oxide	0.1M KOH	810	2.7	<i>Chem. Commun. 2013, 49, 6334</i>
N-doped graphene	0.1M KOH	800	2.7	<i>Nat. Mater. 2011, 10, 780</i>
CoMn <sub>2</sub> O <sub>4</sub>	0.1M KOH or KCl	780	2.9	<i>Nat. Chem. 2011, 3, 79</i>
Co <sub>2</sub> MnO <sub>4</sub>	0.1M KOH or KCl	850	3.3	<i>Nat. Chem. 2011, 3, 79</i>
Co <sub>x</sub> Mn <sub>3-x</sub> O <sub>4</sub>	0.1M KOH or KCl	860	3.4	<i>Nat. Chem. 2011, 3, 79</i>
Porous calcium-manganese oxide (Ca <sub>2</sub> Mn <sub>3</sub> O <sub>8</sub> ) microspheres	0.1M KOH	850	3.5	<i>Chem. Sci. 2013, 4, 368</i>
Co <sub>x</sub> Mn <sub>3-x</sub> O <sub>4</sub>	0.1 M KOH or KCl	880	3.7	<i>Nat. Chem. 2011, 3, 79</i>
Co <sub>3</sub> O <sub>4</sub> /graphene composite	1.0M KOH	864	3.7	<i>J. Am. Chem. Soc. 2012, 134, 3517</i>
Manganese oxide containing mesoporous N-doped carbon	0.1M KOH	810	3.8	<i>Adv. Funct. Mater. 2012, 22, 4584</i>

Flower-like manganese oxide on reduced graphene oxide	0.1M KOH	840	3.8	<i>Chem. Commun. 2013, 49, 6334</i>
Spinel MnCo <sub>2</sub> O <sub>4</sub> / graphene composite	1.0M KOH	885	3.9	<i>J. Am. Chem. Soc. 2012, 134, 3517</i>
Co <sub>3</sub> O <sub>4</sub> nanocrystals on graphene	0.1M KOH	880	3.9	<i>Nat. Mater. 2011, 10, 780</i>
Iron-based catalyst (Fe-N/C)	0.1M KOH	700	3.9	<i>Nat. Mater. 2011, 10, 780</i>
Platinum/carbon	0.1M KOH or KCl	50	3.9	<i>Nat. Chem. 2011, 3, 79</i>
Spinel MnCo <sub>2</sub> O <sub>4</sub> nanoparticles + graphene sheet mixture	1.0M KOH	845	4.0	<i>J. Am. Chem. Soc. 2012, 134, 3517</i>
N-doped graphene sheets	1.0M KOH	830	4.0	<i>J. Am. Chem. Soc. 2012, 134, 3517</i>
Manganese oxide (β-MnO <sub>2</sub> )	0.1M KOH	800	4.0	<i>Angew. Chem. Int. Ed. 2013, 52, 2474</i>
Layer-by-layer structured NiO-GO nanocomposite	0.1M KOH	860	---	<i>Chem. Commun. 2015, 51, 16409</i>
Cobalt and nitrogen-functionalized graphene	0.1M KOH	862	---	<i>J. Mater. Chem. A 2013, 1, 3593</i>

\*: All the onset potentials referenced to RHE are calculated through by the following equations.

$$E_{(\text{vs. RHE})} = E_{(\text{vs. Ag/AgCl})} + 0.0592 \times \text{pH} = E_{(\text{vs. SCE})} + 0.0592 \times \text{pH}$$

## 7-2.4. Conclusion

I have synthesized NiCNNi-GO LbL hybrids through coordination-polymer-glued layer-by-layer assembly of graphene oxide sheets, in which the GO sheets serve not only as building units but also as nucleation sites for the growth of NiCNNi flakes. Even after thermal treatment, the layered NiCNNi parts are successfully converted to Ni<sub>3</sub>C with retention of the original LbL structure because the inserted GO layers effectively prevent random fusion of the metal source. My method relies on the layering capabilities of coordination polymers and their interlayer adhesive properties for spontaneous LbL construction. My approach should also be available for the synthesis of many other inorganic-organic hybrids with ordered LbL architectures. Thus, a variety of well-designed alternating layered nanoscale structures with novel properties will be realized by varying the initial functional components in my synthetic scheme.

## 7-2.5. References

- [1] a) K. Ariga, Y. Yamauchi, G. Rydzek, Q. Ji, Y. Yonamine, K. C.-W. Wu, J.P. Hill, *Chem. Lett.* **2014**, *43*, 36-68; b) J. Borges, J.F. Mano, *Chem. Rev.* **2014**, *114*, 8883-8942; c) J.J. Richardson, M. Björnholm, F. Caruso, *Science* **2015**, *348*, 411; d) R.F. Fakhrullin, Y.M. Lvov, *ACS Nano* **2012**, *6*, 4557-4564; e) T.G. Shutava, P.P. Pattekari, K.A. Arapov, V.P. Torchilin, Y.M. Lvov, *Soft Matter* **2012**, *8*, 9418-9427; f) Y. Jia, J. Li, *Chem. Rev.* **2015**, *115*, 1597-1621; g) P. Cai, X. Feng, J. Fei, G. Li, J. Li, J. Huang, J. Li, *Nanoscale* **2015**, *7*, 10908-10911.
- [2] a) M. Osada, T. Sasaki, *Adv. Mater.* **2012**, *24*, 210-228; b) R. Ma, T. Sasaki, *Acc. Chem. Res.* **2015**, *48*, 136-143.
- [3] a) H. Wang, S. Ishihara, K. Ariga, Y. Yamauchi, *J. Am. Chem. Soc.* **2012**, *134*, 10819-10821; b) R. Ma, X. Liu, J. Liang, Y. Bando, T. Sasaki, *Adv. Mater.* **2014**, *26*, 4173-4178.
- [4] a) R. Makiura, S. Motoyama, Y. Umemura, H. Yamanaka, O. Sakata, H. Kitagawa, *Nat. Mater.* **2010**, *9*, 565-571; b) S. Motoyama, R. Makiura, O. Sakata, H. Kitagawa, *J. Am. Chem. Soc.* **2011**, *133*, 5640-5643.
- [5] S. Eigler, A. Hirsch, *Angew. Chem. Int. Ed.* **2014**, *53*, 7720-7738.
- [6] M.B. Zakaria, M. Hu, R.R. Salunkhe, M. Pramanik, K. Takai, V. Malgras, S. Choi, S.X. Dou, J.H. Kim, M. Imura, S. Ishihara, Y. Yamauchi, *Chem. Eur. J.* **2015**, *21*, 3605-3612.
- [7] Z. Luo, Y. Lu, L.A. Somers, A.T.C. Johnson, *J. Am. Chem. Soc.* **2009**, *131*, 898-899
- [8] L. Espinosa-Alonso, K.P. de Jong, B.M. Weckhuysen, *J. Phys. Chem. C* **2008**, *112*, 7201-7209.
- [9] a) M.A. Omary, T.R. Webb, Z. Assefa, G.E. Shankle, H.H. Patterson, *Inorg. Chem.* **1998**, *37*, 1380-1386; b) E. Hesse, J.A. Creighton, *Chem. Phys. Lett.* **1999**, *303*, 101-106.
- [10] F. Wu, J. Tian, Y. Su, J. Wang, C. Zhang, L. Bao, T. He, J. Li, S. Chen, *ACS Appl. Mater.*



*Interfaces* **2015**, *7*, 7702-7708.

- [11] (a) C. Shan, L. Wang, D. Han, F. Li, Q. Zhang, X. Zhang, L. Niu, *Thin Solid Films* **2013**, *534*, 572-576; (b) C. Ronning, H. Feldermann, R. Merk, H. Hofsäss, *Phys. Rev. B* **1998**, *58*, 2207-2215.
- [12] F. Le Normand, J. Hommet, T. Sz er enyi, C. Fuchs, E. Fogarassy, *Phys. Rev. B* **2001**, *64*, 235416.
- [13] W. Zhou, K. Zheng, L. He, R. Wang, L. Guo, C. Chen, X. Han, Z. Zhang, *Nano Lett.* **2008**, *8*, 1147-1152.
- [14] A. Furlan, J. Lu, L. Hultman, U. Jansson, M. Magnuson, *J. Phys.: Condens. Matter* **2014**, *26*, 415501.
- [15] a) D.R. Dreyer, S. Park, C.W. Bielawski, R.S. Ruoff, *Chem. Soc. Rev.* **2010**, *39*, 228-240; b) S. Pei, H.-M. Cheng, *Carbon* **2012**, *50*, 3210-3228.
- [16] a) P. Sun, M. Zhu, K. Wang, M. Zhong, J. Wei, D. Wu, H. Zhu, *ACS Appl. Mater. Interfaces* **2013**, *5*, 9563-9571; b) Z.-S. Wu, W. Ren, L. Gao, J. Zhao, Z. Chen, B. Liu, D. Tang, B. Yu, C. Jiang, H.-M. Cheng, *ACS Nano* **2009**, *3*, 411-417.
- [17] a) M. Jiao, K. Li, W. Guan, Y. Wang, Z. Wu, A. Page, K. Morokuma, *Sci. Rep.* **2015**, *5*, 12091; b) Z. Zhou, J. Wang, W. Liu, C. Yu, B. Kong, Y. Sun, H. Yang, S. Yang, W. Wang, *Nanoscale* **2014**, *6*, 12591-12600.
- [18] a) Y. Goto, K. Taniguchi, T. Omata, S. Otsuka-Yao-Matsuo, N. Ohashi, S. Ueda, H. Yoshikawa, Y. Yamashita, H. Oohashi, K. Kobayashi, *Chem. Mater.* **2008**, *20*, 4156-4160; b) Z.L. Schaefer, K.M. Weeber, R. Misra, P. Schiffer, R.E. Schaak, *Chem. Mater.* **2011**, *23*, 2475-2480.
- [19] J. Tang, J. Liu, C. Li, Y. Li, M.O. Tade, S. Dai, Y. Yamauchi, *Angew. Chem. Int. Ed.* **2015**, *54*, 588-593; *Angew. Chem.* **2015**, *127*, 598-603.

# Chapter 8

# Chapter 8

## 8. General Conclusions and Future Prospects

### 8.1. General Conclusion

Various inorganic nanoporous materials have been drawing intense research interest not only for their unique structural and surface properties, but also for their broad range of applications such as their potential in catalysis, drug delivery, charge transfer, and energy storage and separation. Among these materials, porous coordination polymers (PCPs) have received much attention [1]. Their tunable pore structures, functionality, structural modifications and regularity make them attractive materials for the aforementioned applications. A family of these materials, cyano-bridged coordination (CPs), consisting of transition metal ions and cyanide ligands, in which the metal ions are bridged by cyanide groups ( $-M-C\equiv N-M-$ ) is of great importance. My dissertation demonstrated that various two-dimensional (2D) and three-dimensional (3D) cyano-bridged CPs can be realized. Shapes in a nanoregime can be synthesized under a controlled crystallization process using trisodium citrate dihydrate as a chelating agent [2]. The tailor-made nanostructured cyano-bridged CPs were optimized using a chelating agent, trisodium citrate dihydrate, which determined the size and shape of my products. The concentration of trisodium citrate dihydrate is critical for the determination of the size and the shape of the final products. As

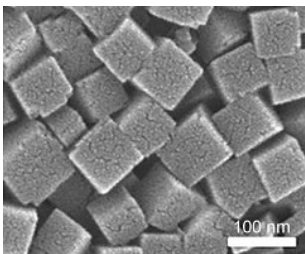
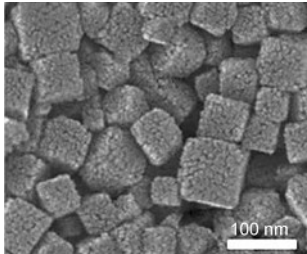
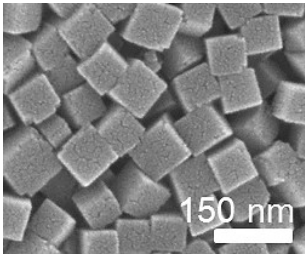
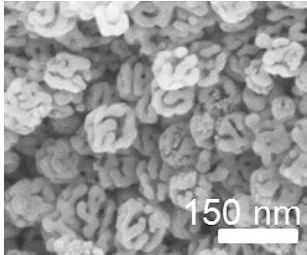
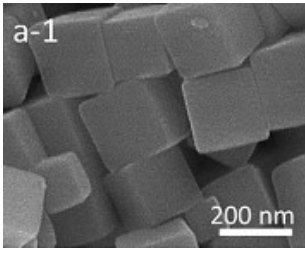
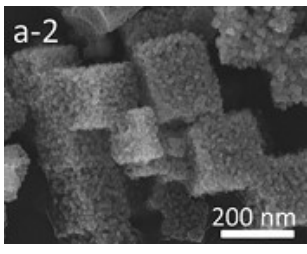
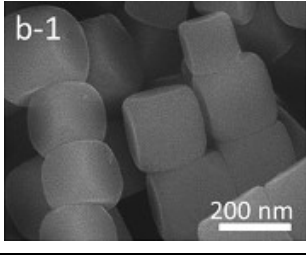
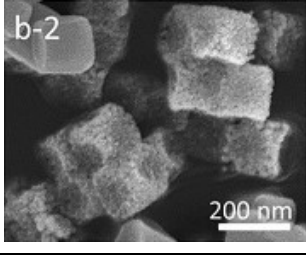
the amount of trisodium citrate dihydrate increases, the final size gradually increases, and the shape improves.

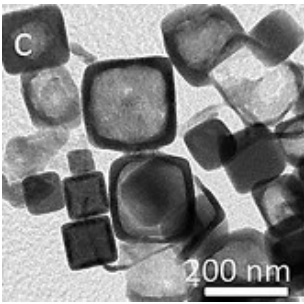
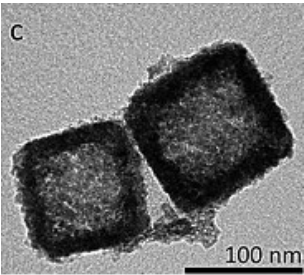
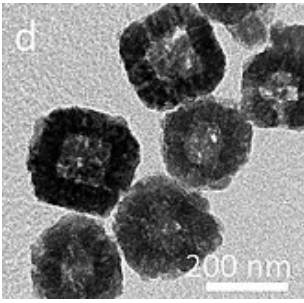
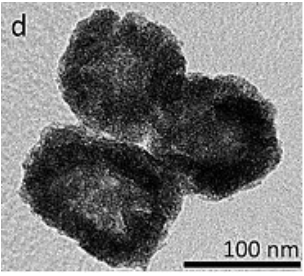
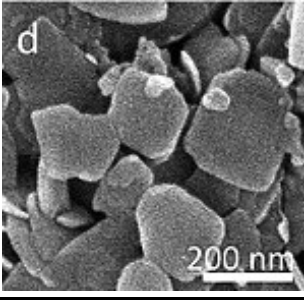
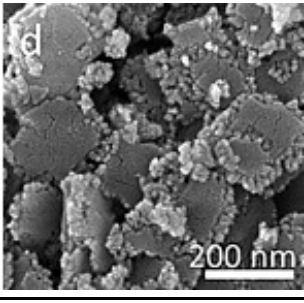
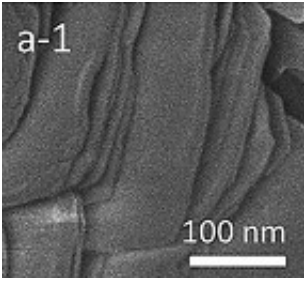
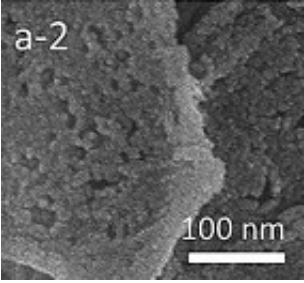
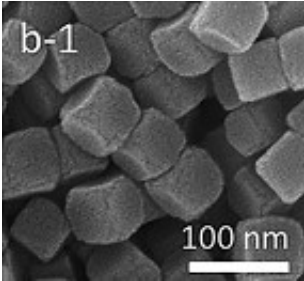
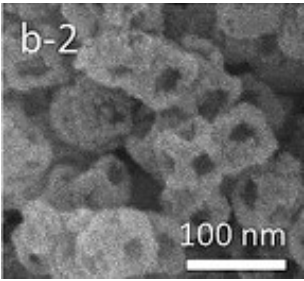
It is well known that the balance between nucleation and crystal growth determines the particle size in the final products. In my study, free metal ions are released steadily and slowly from the metal-citrate complex and react with metal cyanate ligands at the initial stage of the reaction. Subsequently, the nuclei are generated and grow by interaction to form the final CP products with fine crystal structures. Therefore, by increasing the concentration of trisodium citrate dihydrate, the number of nuclei formed at the early stage of the reaction is thought to be decreased. These few nuclei undergo crystal growth, leading to a final product with a larger particle size. In contrast, the absence of the chelating agent resulted in distorted and random particles. According to my strategy, I have realized various fine monocrystalline materials, which can be abbreviated as CoCNC<sub>o</sub>, CoC<sub>N</sub>Ni, NiCNC<sub>o</sub>, NiC<sub>N</sub>Ni, FeCNC<sub>o</sub>, CoCNFe, FeCNFe, NiCNC<sub>r</sub>, MnC<sub>N</sub>Mn, MnCNC<sub>o</sub>, MnC<sub>N</sub>Ru, FeC<sub>N</sub>Ni, and CuCNPt (**Table 8.1**).

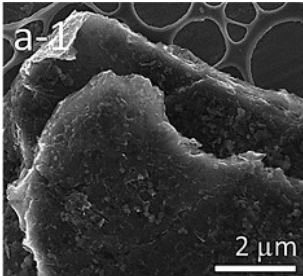
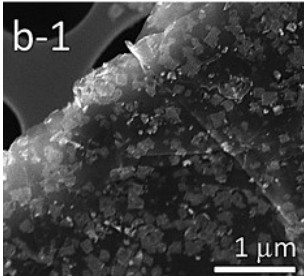
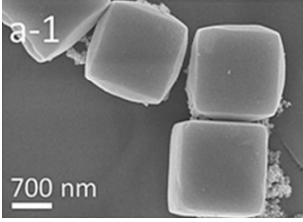
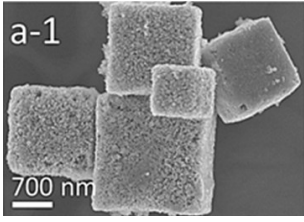
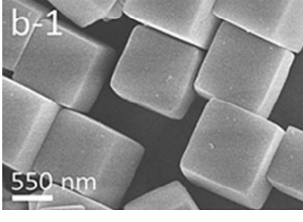
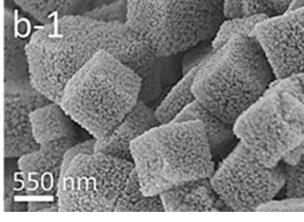
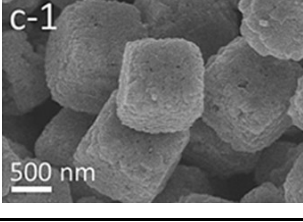
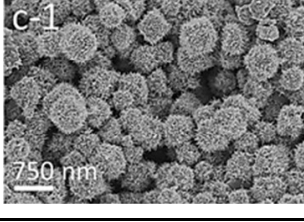
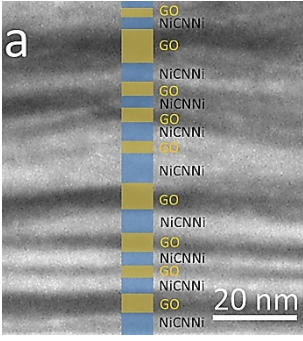
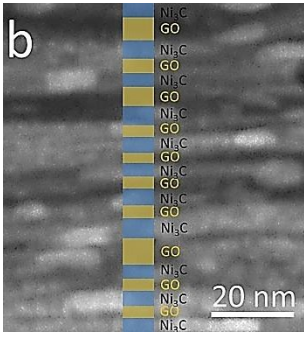
Cyano-bridged CPs could serve as precursors for the preparation of various nanoporous metal oxides and carbides [3]. After regulated thermal treatments in air or under an inert atmosphere, various nanoporous metal oxides and carbides, respectively, were successfully prepared. The original morphology is well retained, even after the thermal treatments. My strategy has proven to be a promising solid-state method for the preparation of nanoporous metal oxides and carbides with fine crystal structures. This method has the potential to overcome the difficulties in preparation through traditional approaches (soft- and hard-templating) thanks to my synthetic procedures. By this strategy, I have already obtained various nanoporous metal oxides, such as spinel Co<sub>3</sub>O<sub>4</sub>, CoNi<sub>2</sub>O<sub>4</sub>, NiCo<sub>2</sub>O<sub>4</sub>, FeCo<sub>2</sub>O<sub>4</sub>, CoFe<sub>2</sub>O<sub>4</sub>, Mn<sub>3</sub>O<sub>4</sub>, Mn<sub>x</sub>Co<sub>3-x</sub>O<sub>4</sub>, and Mn<sub>x</sub>Ru<sub>3-x</sub>O<sub>4</sub>; NiO, α-Fe<sub>2</sub>O<sub>3</sub>, γ-Fe<sub>3</sub>O<sub>4</sub>, Pt/CuO, and CoNiFe-O; carbides, such as Ni<sub>3</sub>C nanoporous flakes; and other nanocomposites, such as layered nickel oxide/graphene oxide (NiO-GO) and

nickel carbide/graphene oxide ( $\text{Ni}_3\text{C-GO}$ ) hybrids (**Table 8.1**). The final products show a significant efficiency and interesting results for supercapacitors, oxygen reduction reaction (ORR) and oxygen evolution reaction (OER),  $\text{H}_2\text{O}_2$  production, drug delivery systems (DDSs), and photocatalytic applications.

**Table 8.1** Electron microscope images of tailored 2D and 3D cyano-bridged CPs nanostructures and their corresponding thermally derived nanoporous metal oxides and carbides.

As-prepared products	Shape	Thermally derived oxides/carbides	Shape	Ref.
FeCNFe nanocubes		Nanoporous $\gamma\text{-Fe}_2\text{O}_3$		[4]
FeCNFe nanocubes		Hollow $\alpha\text{-Fe}_2\text{O}_3$		[5]
CoCNCo nanocubes		Nanoporous spinel $\text{Co}_3\text{O}_4$		[6]
FeCNCo nanocubes		Nanoporous spinel $\text{FeCo}_2\text{O}_4$		[6]

<p>Hollow CoCNFe nanocubes</p>		<p>Hollow CoFe-oxide</p>		<p>[6]</p>
<p>Hollow FeCNFe nanocubes</p>		<p>Hollow Fe-oxide</p>		<p>[6]</p>
<p>NiCNNi nanoflakes</p>		<p>Nanoporous NiO</p>		<p>[7]</p>
<p>CoCNNi nanosheets</p>		<p>Nanoporous CoNi<sub>2</sub>O<sub>4</sub> sheets</p>		<p>[8]</p>
<p>NiCNCo nanocubes</p>		<p>NiCo<sub>2</sub>O<sub>4</sub> nanocages</p>		<p>[8]</p>

Layered NiCNNi-GO hybrids		layered NiO-GO hybrids		[9]
MnCNMn nanocubes		Nanoporous spinel Mn <sub>3</sub> O <sub>4</sub>		[10]
MnCNCo nanocubes		Nanoporous spinel Mn <sub>x</sub> Co <sub>3-x</sub> O <sub>4</sub>		[10]
MnCNRu nanocubes		Nanoporous spinel Mn <sub>x</sub> Ru <sub>3-x</sub> O <sub>4</sub>		[10]
Layered NiCNNi-GO hybrids		layered Ni <sub>3</sub> C-GO hybrids		[11]

The thermal conversion of cyano-bridged CPs into nanostructured metal oxides and carbides can be explained by various pathways as follows:

### 8.1.1. Direct thermal treatments

In general, this reaction is accompanied by the loss of water molecules in the first stage of heating as a normal product. The metal components can be oxidized, and the organic components ( $-\text{C}\equiv\text{N}-$ ) are removed by continuous thermal decomposition in air. Of course, the metal ions are uniformly separated by cyano groups in the crystal system, so it is expected that nanoporous metal oxides with grain sizes can be obtained. As described in **Chapter 4-1**, new nanoporous iron oxide nanoparticles with superparamagnetic behavior were successfully synthesized from Prussian blue (PB) nanocubes through a thermal conversion method (**Figure 8.1**) [4]. PB ( $\text{Fe}_4[\text{Fe}(\text{CN})_6]_3 \cdot x\text{H}_2\text{O}$ ), in which iron ions are bridged by cyano groups ( $\text{Fe}^{\text{III}}-\text{C}\equiv\text{N}-\text{Fe}^{\text{II}}$ ), is considered as a potential precursor for nanoporous iron oxides with high surface areas. The iron components can be oxidized, and the organic components are removed by thermal treatment in air. The morphology of the obtained PB derivatives after calcination (PB\_250 and PB\_400) remains a nanocube, but their sizes were slightly reduced, and their surface roughness increased. The reduction of the particles size is mainly caused by removing the cyano groups and the interstitial water molecules during calcination.

By the same method, I report in **Chapter 3** the controlled crystal growth of various PBA (*i.e.*,  $\text{Mn}_3[\text{Mn}(\text{CN})_6]_2$  (abbreviated as MnCNMn),  $\text{Mn}_3[\text{Co}(\text{CN})_6]_2$  (abbreviated as MnCNCo), and  $\text{Mn}_2[\text{Ru}(\text{CN})_6]$  (abbreviated as MnCNRu)) with tunable particle sizes and cubic shapes. After aerobic calcination, the PBAs are successfully converted into nanoporous Mn-based oxides with different compositions (**Figure 3.10-12; Chapter 3**) [10]. Moreover, by starting with flakes (*e.g.*, NiNi and CoNi), a well-defined 2D morphology, even after calcination, the initial flake



morphology is well preserved with the additional formation of a nanoporous structure of metal oxides (**Figure 8.2**), as demonstrated in **Chapters 6 and 7** [7,8,11].

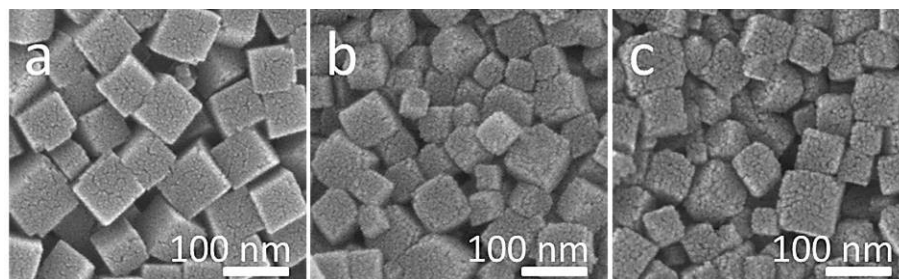


**Figure 8.1.** SEM images of (a) PB nanocubes and thermally derived iron oxides at (b) 250 °C (PB\_250) and (c) 400 °C (PB\_400).

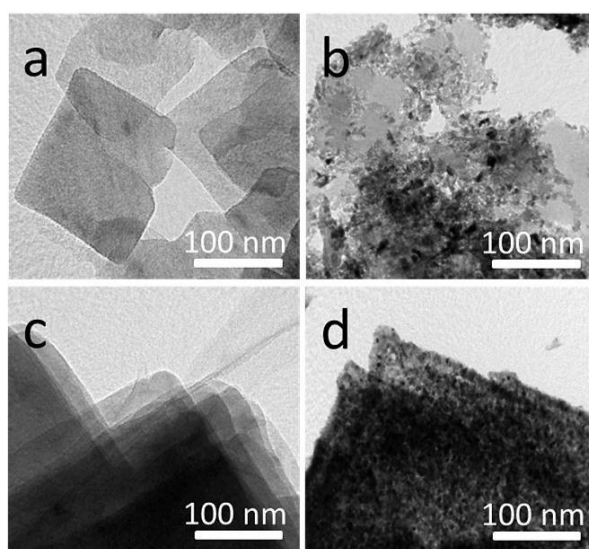


**Figure 8.2.** TEM images of (a) the as-prepared NiNi, (b) nanoporous NiO, (c) the as-prepared CoNi, and (d) nanoporous CoNi-oxide flakes.

### 8.1.2. Kirkendall effect

Originally, the term “Kirkendall effect” referred to the different atomic diffusive rates of the binary elements under thermal treatment. Due to the difference in the diffusion rate of elements during heating, the generation of porosity in the lower-melting component side of the diffusion couple near the interface could create hollow nanostructures. As described in **Chapter 6-2**, starting with CoCo and NiCo nanocubes, after calcination, a hollow space is formed at the center

of the nanocubes, leading to the transformation into nanocages (**Figure 8.3**). Nanocages from both compositions show a similar size distribution when compared to the original nanocubes. The sample obtained from CoCo (*i.e.*, cal-CoCo) mostly contains a  $\text{Co}_3\text{O}_4$  phase with a cubic spinel structure, while the sample obtained from NiCo (*i.e.*, cal-NiCo) has a mixture of NiCo oxide and Ni metal. The formation of the nanocages can be explained by the Kirkendall effect, which is based on a non-equilibrium inter-diffusion process. During the first stage of the thermal oxidation, the oxidized shells are formed immediately, due to the difficulty with which oxygen diffuses toward the inner parts. Therefore, free metal ions tend to move toward the shell region (*i.e.*, outward diffusion) after the decomposition of the organic units in order to react with oxygen, leading to formation of hollow interiors.

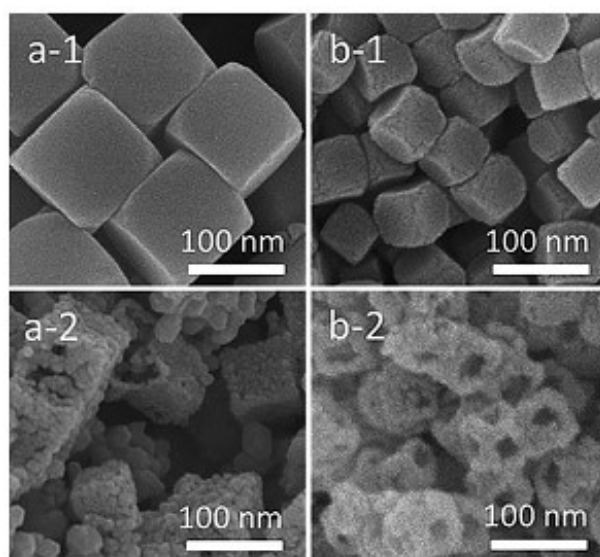


**Figure 8.3.** SEM images of (a-1) CoCo and (b-1) NiCo nanocubes and (a-2) cal-CoCo and (b-2) cal-NiCo nanocages.

### 8.1.3. Etching

For creating an interior hollow cavity, in the general etching process, the etching reaction normally starts from the external surface of the particles. The large PB mesocrystals formed from

the aggregation of small crystallites often have defects/voids. Thus, it was possible for etching agents (*e.g.*, HCl) to diffuse into the inner parts of mesocrystals through the defects, leading to the formation of an interior hollow cavity. The capping agent (*e.g.*, PVP) plays a crucial role in the etching process. It serves as a surface-protecting agent, which can decrease the etching rate on the particle surface. Then, such hollow PB nanocubes offer a great opportunity to make nanoporous iron oxides with hollow interiors, making it possible to realize the advantages of a hollow cavity. After the thermal treatment, nanoporous iron oxide particles with hollow structures and high surface areas were obtained. Surprisingly, the crystalline phases of the obtained iron oxides and their crystalline grain sizes were precisely controlled by the applied calcination temperatures and the volumes of internal hollow cavities of PB particles. As described in **Chapter 4-2**, I demonstrated that Prussian blue (PB) coordination polymers can be successfully etched by acidic solution for the preparation of hollow PB nanoparticles [5]. Using hollow PB nanoparticles as starting materials, I calcined them under various conditions to prepare nanoporous Fe oxides with a crystallized  $\alpha$ -Fe<sub>2</sub>O<sub>3</sub> (hematite) phase (**Figure 8.4**). The obtained  $\alpha$ -Fe<sub>2</sub>O<sub>3</sub> exhibited a high surface area, which will be useful for photocatalytic applications.

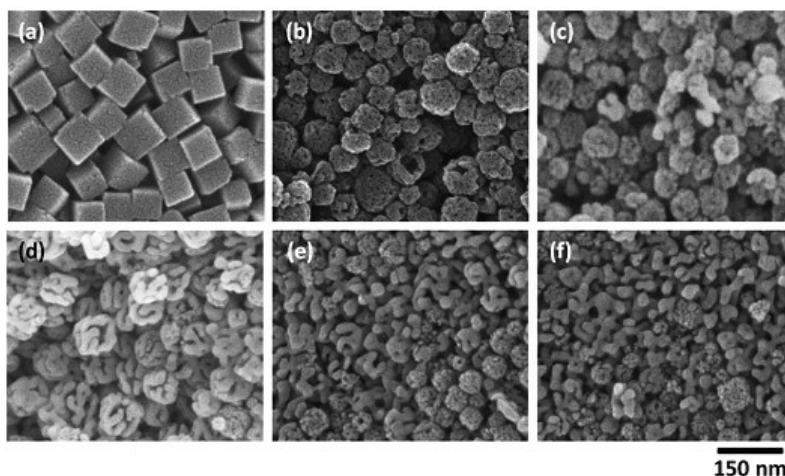


**Figure 8.4.** SEM images of (a) PB nanoparticles before chemical etching, (b) PB nanoparticles after chemical etching, and samples calcined for (c) 4, (d) 5, (e) 6, and (f) 7 h.

### 8.1.4. Hard-templating method

The hard-templating method is very useful for the preparation of highly crystallized frameworks with a nanodimensional porous structure. The porous structure for metal oxide can be printed after removal of the template by treating it with acid and/or by calcination in an aerobic condition, because the porous oxide structure is very susceptible to collapse in both cases. As described in **Chapter 2**, I have used small NiCr nanocubes as a sacrificial template for the synthesis of hollow CoCo, FeCo, CoFe, and FeFe PB analogues [2]. The different dissolution rates enabled the removal of NiCr core by etching using a diluted hydrochloric acid solution (**Figure 8.5**), resulting in hollow spheres of the hard-dissolved PB analogues. After subsequent calcination in air, I succeeded in obtaining nanoporous spinel  $\text{Co}_3\text{O}_4$ ,  $\text{FeCo}_2\text{O}_4$ ,  $\text{CoFe}_2\text{O}_4$ , and  $\text{Fe}_2\text{O}_3$  with hollow interiors.



**Figure 8.5.** Dissolution test of solid NiCr nanocubes, solid CoCo nanocubes, solid FeCo nanocubes, solid CoFe nanocubes, and solid FeFe nanocubes.

## 8.2. Future Perspectives

In my dissertation, several examples of the preparation of functional structures and materials

based on coordination nanoarchitectonics are introduced. Because of the promising advantages offered by coordination chemistry, such as high directionality, wide selection of components, and multivalent nature, the structure of certain materials can be rationally architected from various molecules and metal ions. This is one of the most logical and realistic bottom-up strategies to construct objects at a nanoscale level with a structural precision arising from using molecules (or ions) as building units. The examples shown in this thesis have showcased several attractive features of coordination materials (*i.e.*, cyano-bridged CPs).

Biological systems could be considered as naturally occurring examples of material synthesis through self-assembly. In biological systems, metal coordination is used in some specific functional units, such as heme proteins, but is generally not used in the formation of manmade structures. Self-assembly processes of biological structures are mostly based on van der Waals interactions and hydrophobic effects with the aid of electrostatic interaction and hydrogen bonding. These interactions are individually negligible, but together, they can be a powerful tool to assemble matter in a well-defined manner with sufficient strength. Therefore, biological materials, including living cells, have a flexible, soft structural nature, which makes them highly responsive to external stimuli. In addition, biological systems have multicomponent features with structural hierarchies. If materials produced by coordination nanoarchitectonics included such features, the functions of the coordination materials could be implemented in many advanced applications.

Further efforts are necessary for the development of coordination materials in order to satisfy the above-mentioned requirements. The structural softness of certain coordination materials, such as coordination polymers (CPs) and metal-organic frameworks (MOFs), recently became an attractive research target that can be achieved through several strategies, such as using soft ligand and integrated structures [12]. I believe this research direction can achieve great

success by significantly developing the dynamic functions and applications of coordination materials, including sensing and drug delivery systems. On the other hand, the exploration of methodologies to architect a well-defined multicomponent assembly and highly hierarchical structures needs more effort and consideration. One possible strategy to architect such systems on the basis of coordination bonding would be to construct low-dimensional structures and assemble them into 3D motifs. For example, 2D coordination polymer nanosheets can be assembled into 3D stacked structures through appropriate methods, such as Langmuir-Blodgett and layer-by-layer assembly, as mentioned in the introduction (**Figure 1.6**) and supported by **Chapter 7**. Some strategies enable the construction of multiple components within two dimensions (**Figure 1.8**). These interfacial processes for constructing low-dimensional structures are the keys to synthesizing highly hierarchical structures with coordination materials. A paradigm shift from simple assembly to an interfacial low-dimensional strategy is necessary to further develop functional materials with coordination chemistry.

Another trend, the urgent need for nanoporous metal oxides with definite compositions and highly crystallized frameworks, is motivating scientists to discover novel and facile synthetic methods. A solid-state strategy for the preparation of nanoporous metal oxides with well-defined nanostructures in a predictable way is highly promising and required for large-scale production to meet the requirements of the rapid development of applications. Using cyano-bridged CPs, many nanoporous metal oxides/carbides or even alloys can be prepared by annealing in air or under an inert atmosphere (**Figure 8.6**). Various oxides or carbides can be prepared as much as I have many fine CP structures. I strongly believe that this method has the potential to overcome difficulties in the fabrication of nanoporous metal oxides and carbides by traditional approaches.

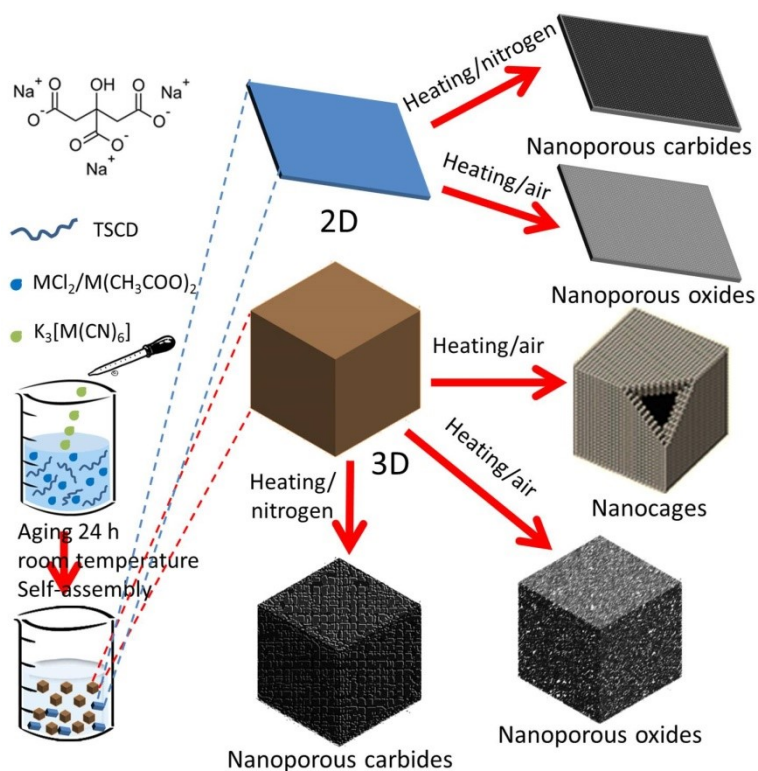


**Figure 8.6.** Schematic illustration of the self-assembled cyano-bridged CPs in 2D and 3D shapes, followed by thermal conversion into well-retained nanoporous inorganic materials.

Moreover, it is well-known that PB is a controlled synthesized material formed from small crystals arranged in large mesocrystals. This feature enables me to use a template to determine the final shape of PB, and therefore I can prepare it in many forms. For instance, Qu *et al.* have reported the preparation of highly regular and ordered in the vertical orientation PB nanowires *via* simple electrochemical deposition with a polycarbonate membrane sacrificial template for the effective modification of glassy carbon electrodes [13]. After dissolution of the template by chloroform, PB nanowires were obtained. I can extend this idea to deposit PB between nanochannels in the top surface of thin metal films as efficient transistors in manufacturing (**Figure 8.7**). This can be extended to prepare ferromagnetic nanocrystal assemblies (*e.g.*, FePt) or other magnetic materials (*e.g.*, CoPt) with chemically and mechanically robust characters that can support high-density magnetization reversal transitions, and porosity can be introduced for

the first time. FePt and CoPt nanoparticles have generated great interest recently because of their chemical stability, efficient catalytic activity toward oxygen reduction reaction, and potential applications in high-density data storage and high-performance permanent magnets.

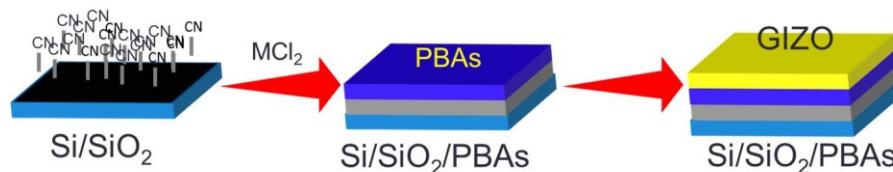


**Figure 8.7.** Controlled crystal growth of PBAs in the top surface of a metal substrate for efficient transistor manufacturing.

Last but not least, capacitors are the critical passive part of electronics. Currently, they can work efficiently at 175°C, but automobile industries require power systems that function up to 250°C, and the aviation industry demands function up to 500 °C [14]. I expected the improvement of semiconductors, especially for high-temperature electronics. In particular, SiC-based active devices, such as transistors and Schottky diodes, are capable of operating at over 500°C. They currently reached an advanced manufacturing stage, and I might be able to control the sizeable space in the module. If I succeed in controlling various layers from PB, PBAs, and their derived nanoporous structures where higher dielectric materials and ferroelectric ones are stacked on semiconductor substrates with high-temperature durability, it will enable innovation in car electronics and expand the variety of materials in the semiconductor industry.

### 8.3. References

- [1] a) O.M. Yaghi, M. O'Keeffe, N.W. Ockwig, H.K. Chae, M. Eddaoudi, J. Kim, *Nature* **2003**, 423, 705; b) S. Kitagawa, R. Kitaura, S.I. Noro, *Angew. Chem. Int. Ed.* **2004**, 43, 2334; *Angew. Chem.* **2004**, 116, 2388; c) X.B. Zhao, B. Xiao, A.J. Fletcher, K.M. Thomas,



- D. Bradshaw, M.J. Rosseinsky, *Science* **2004**, *306*, 1012; d) S.T. Meek, J.A. Greathouse, M.D. Allendorf, *Adv. Mater.* **2011**, *23*, 249; e) M.C. Das, S. Xiang, Z. Zhang, B. Chen, *Angew. Chem. Int. Ed.* **2011**, *50*, 10510; *Angew. Chem.* **2011**, *123*, 10696; f) J. An, C.M. Shade, D.A. Chengelis-Czegán, S. Petoud, N.L. Rosi, *J. Am. Chem. Soc.* **2011**, *133*, 1220; g) P. Dechambenoit, J.R. Long, *Chem. Soc. Rev.* **2011**, *40*, 3249; h) S. Furukawa, Y. Sakata, S. Kitagawa, *Chem. Lett.* **2013**, *42*, 570.
- [2] M. Hu, S. Ishihara, Y. Yamauchi, *Angew. Chem. Int. Ed.* **2013**, *52*, 1235; *Angew. Chem.* **2013**, *125*, 1273.
- [3] a) M. Hu, Y. Yamauchi, *Chem. Asian J.* **2011**, *6*, 2282; b) M. Hu, A.A. Belik, H. Sukegawa, Y. Nemoto, M. Imura, Y. Yamauchi, *Chem. Asian J.* **2011**, *6*, 3195; c) M. Hu, A.A. Belik, M. Imura, K. Mibu, Y. Tsujimoto, Y. Yamauchi, *Chem. Mater.* **2012**, *24*, 2698.
- [4] M.B. Zakaria, A.A. Belik, C.-H. Liu, H.-Y. Hsieh, Y.-T. Liao, V. Malgras, Y. Yamauchi, K. C.-W. Wu, *Chem. Asian J.* **2015**, *10*, 1457-1462.
- [5] M.B. Zakaria, M. Hu, N. Hayashi, Y. Tsujimoto, S. Ishihara, M. Imura, N. Suzuki, Y.-Y. Huang, Y. Sakka, K. Ariga, K. C.-W. Wu, Y. Yamauchi, *Eur. J. Inorg. Chem.* **2014**, 1137-1141.
- [6] M.B. Zakaria, H. Ming, M. Imura, R.R. Salunkhe, N. Umezawa, H. Hamoudi, A.A. Belik, Y. Yamauchi, *Chem. Eur. J.* **2014**, *20*, 17375 -17384.
- [7] M.B. Zakaria, M. Hu, R.R. Salunkhe, M. Pramanik, K. Takai, V. Malgras, S. Choi, S. Xue Dou, J.H. Kim, M. Imura, S. Ishihara, Y. Yamauchi, *Chem. Eur. J.* **2015**, *21*, 3605-3612.
- [8] M.B. Zakaria, M. Hu, M. Pramanik, C. Li, J. Tang, A. Aldalbahi, S.M. Alshehri, V. Malgras, Y. Yamauchi, *Chem. Asian J.* **2015**, *10*, 1541-1545.
- [9] M.B. Zakaria, V. Malgras, T. Takei, C. Li, Y. Yamauchi, *Chem. Commun.* **2015**, *51*, 16409-16412.

- [10] M.B. Zakaria, C. Li, M. Pramanik, Y. Tsujimoto, M. Hu, V. Malgras, S. Tominaka, Y. Yamauchi, *J. Mater. Chem. A* **2016**, *4*, 9266-9274.
- [11] M.B. Zakaria, C. Li, Q. Ji, B. Jiang, S. Tominaka, Y. Ide, J.P. Hill, K. Ariga, Y. Yamauchi, *Angew. Chem. Int. Ed.* **2016**, *55*, 8426-8430.
- [12] (a) S. Horike, S. Shimomura, S. Kitagawa, *Nat. Chem.* **2009**, *1*, 695-704; (b) J. Cui, Y.-L. Wong, M. Zeller, A.D. Hunter, Z. Xu, *Angew. Chem. Int. Ed.* **2014**, *53*, 14438-14442; (c) A. Schneemann, V. Bon, I. Schwedler, I. Senkovska, S. Kaskel, *Chem. Soc. Rev.* **2014**, *43*, 6062-6096; (d) Z. Li, H.C. Zeng, *J. Am. Chem. Soc.* **2014**, *136*, 5631-5639; (e) H. Sato, W. Kosaka, R. Matsuda, A. Hori, Y. Hijikata, R.V. Belosludov, S. Sakaki, M. Takata, S. Kitagawa, *Science* **2014**, *343*, 167-170; (f) B. Saccoccia, A.M. Bohnsack, N.W. Waggoner, K.H. Cho, J.S. Lee, D.-Y. Hong, V.M. Lynch, J.-S. Chang, S.M. Humphrey, *Angew. Chem. Int. Ed.* **2015**, *54*, 5394-5398.
- [13] F. Qu, A. Shi, M. Yang, J. Jiang, G. Shen, R. Yu, *Anal. Chim. Acta* **2007**, *605*, 28-33.
- [14] a) S. Oh, R. Hayakawa, T. Chikyow, Y. Wakayama, *Appl. Phys. Lett.* **2015**, *106*, 243301; b) K. Kurishima, T. Nabatame, A. Ohi, T. Chikyow, A. Ogura, *J. Vac. Sci. Technol. A* **2015**, *33*, 061506.

# List of Achievements

## Papers

1. Preparation of Mesoporous Titania Thin Films with Well-Crystallized Frameworks by Using Thermally-Stable Triblock Copolymer, *Eur. J. Inorg. Chem.* **2013**, 2330-2335. **(March 5, 2013)**  
**Mohamed B. Zakaria**, Norihiro Suzuki, Nagy L. Torad, Mikiya Matsuura, Kazuhiko Maekawa, Hirofumi Tanabe, and Yusuke Yamauchi
2. Thermal Conversion of Hollow Prussian Blue Nanoparticles into Nanoporous Iron Oxides with Crystallized Hematite Phase, *Eur. J. Inorg. Chem.* **2014**, 1137-1141. **(February 6, 2014)**  
**Mohamed B. Zakaria**, Ming Hu, Naoaki Hayashi, Yoshihiro Tsujimoto, Shinsuke Ishihara, Masataka Imura, Norihiro Suzuki, Yu-Yuan Huang, Yoshio Sakka, Katsuhiko Ariga, Kevin C.-W. Wu, and Yusuke Yamauchi
3. Controlled Crystallization of Cyano-Bridged Cu-Pt Coordination Polymers with Two-Dimensional Morphology, *Chem. Asian J.* **2014**, *9*, 1511-1514. **(April 9, 2014)**  
**Mohamed B. Zakaria**, Ming Hu, Yoshihiro Tsujimoto, Yoshio Sakka, Norihiro Suzuki, Yuichiro Kamachi, Masataka Imura, Shinsuke Ishihara, Katsuhiko Ariga, and Yusuke Yamauchi
4. Single-Crystal-like Nanoporous Spinel Oxides: A Strategy for Synthesis of Nanoporous Metal Oxides Utilizing Metal-Cyanide Hybrid Coordination Polymers, *Chem. Eur. J.* **2014**, *20*, 17375 -17384. **(October 30, 2014)**  
**Mohamed B. Zakaria**, Ming Hu, Masataka Imura, Rahul R. Salunkhe, Naoto Umezawa, Hicham Hamoudi, Alexei A. Belik, and Yusuke Yamauchi

5. Controlled Synthesis of Nanoporous Nickel Oxides with Two-Dimensional Shapes through Thermal Decomposition of Metal-Cyanide Hybrid Coordination Polymers, *Chem. Eur. J.* **2015**, *21*, 3605-3612. **(January 9, 2015)**  
**Mohamed B. Zakaria**, Ming Hu, Rahul R. Salunkhe, Malay Pramanik, Kimiko Takai, Victor Malgras, Seyong Choi, Shi Xue Dou, Jung Ho Kim, Masataka Imura, Shinsuke Ishiara, and Yusuke Yamauchi
6. Prussian Blue Derived Nanoporous Iron Oxides as Anti-Cancer Drug Carriers for Magnetic Guiding Chemotherapy, *Chem. Asian J.* **2015**, *10*, 1457-1462. **(June 11, 2015)**  
**Mohamed B. Zakaria**, Alexei A. Belik, Chia-Hung Liu, Han-Yun Hsieh, Yu-Te Liao, Victor Malgras, Yusuke Yamauchi, and Kevin C.-W. Wu
7. Synthesis of Nanoporous Ni-Co Mixed Oxides by Thermal Decomposition of Metal-Cyanide Coordination Polymers, *Chem. Asian J.* **2015**, *10*, 1541-1545. **(May 12, 2015)**  
**Mohamed B. Zakaria**, Ming Hu, Malay Pramanik, Cuiling Li, Jing Tang, Ali Aldalbahi, Saad M. Alshehri, Victor Malgras, and Yusuke Yamauchi
8. Layer-by-Layer Motif Hybridization: Nanoporous Nickel Oxide Flakes Wrapped into Graphene Oxide Sheets toward Enhanced Oxygen Reduction Reaction, *Chem. Commun.* **2015**, *51*, 16409-16412. **(September 8, 2015)**  
**Mohamed B. Zakaria**, Victor Malgras, Toshiaki Takei, Cuiling Li, and Yusuke Yamauchi
9. Nanoporous Mn-Based Electrocatalysts through Thermal Conversion of Cyano-Bridged Coordination Polymers toward Ultra-High Efficient Hydrogen Peroxide Production, *J. Mater. Chem. A* **2016**, *4*, 9266-9274. **(May 6, 2016)**  
**Mohamed B. Zakaria**, Cuiling Li, Malay Pramanik, Yoshihiro Tsujimoto, Ming Hu, Victor Malgras, Satoshi Tominaka, and Yusuke Yamauchi
10. Self-Construction from 2D to 3D: One-Pot Layer-by-Layer Assembly of Graphene Oxide

Sheets Held Together by Coordination Polymers, *Angew. Chem. Int. Ed.* **2016**, *55*, 8426-8430.

**(May 11, 2016)**

**Mohamed B. Zakaria**, Cuiling Li, Qingmin Ji, Bo Jiang, Satoshi Tominaka, Yusuke Ide, Jonathan P. Hill, Katsuhiko Ariga, and Yusuke Yamauchi

11. Synthesis of Highly Strained Mesostructured SrTiO<sub>3</sub>/BaTiO<sub>3</sub> Composite Films with Robust Ferroelectricity, *Chem. Eur. J.* **2013**, *19*, 4446-4450. **(February 28, 2013)**

Norihiro Suzuki, **Mohamed. B. Zakaria**, Nagy L. Torad, Kevin C.-W. Wu, Yoshihiro Nemoto, Masataka Imura, Minoru Osada, and Yusuke Yamauchi

12. Fabrication of Asymmetric Supercapacitors Based on Coordination Polymer Derived Nanoporous Materials, *Electrochimica. Acta* **2015**, *183*, 94-99. **(May 7, 2015)**

Rahul R. Salunkhe, **Mohamed B. Zakaria**, Yuichiro Kamachi, Saad M. Alshehri, Tansir Ahamad, Nagy L. Torad, Shi Xue Dou, Jung Ho Kim, and Yusuke Yamauchi

13. Reduced graphene oxide nanosheets decorated with Au, Pd and Au-Pd bimetallic nanoparticles as highly efficient catalysts for electrochemical hydrogen generation, *J. Mater. Chem. A* **2015**, *3*, 20254-20266. **(August 20, 2015)**

Gitashree Darabdhara, Mohammed A. Amin, Gaber A. M. Mersal, Emad M. Ahmed, Manash R. Das, **Mohamed B. Zakaria**, Victor Malgras, Saad M. Alshehri, Yusuke Yamauchi, Sabine Szunerits, and Rabah Boukherroub

14. Coordination Nanoarchitectonics at Interfaces between Supramolecular and Materials Chemistry, *Coord. Chem. Rev.* **2016**, *320-321*, 139-152. **(March 14, 2016)**

Katsuhiko Ariga, Victor Malgras, Qingmin Ji, **Mohamed B. Zakaria**, and Yusuke Yamauchi

15. Hydrogels Containing Prussian Blue Nanoparticles toward Removal of Radioactive Cesium Ions, *J. Nanosci. Nanotechnol.* **2016**, *16*, 4200-4204. **( July 21, 2016)**

Yuichiro Kamachi<sup>#</sup>, **Mohamed B. Zakaria**<sup>#</sup>, Nagy L. Torad, Teruyuki Nakato, Tansir

Ahamad, Saad M. Alshehri, Victor Malgras, and Yusuke Yamauchi, # equal contribution

## Verbal presentations

1. Synthesis of Photoactive Nanoporous Hematite Iron Oxide with Hollow Interiors Using Prussian Blue Coordination Polymers, The 4<sup>th</sup> NIMS/MANA-Waseda University International Symposium, March 11<sup>th</sup>, **2013**, National Institute for Materials Science (NIMS), Sengen-site, Tsukuba, Japan

**Mohamed B. Zakaria** and Yusuke Yamauchi

2. Sophisticated Crystallization of Coordination Polymers and Their Thermal Conversion into Nanostructured Metals Oxides, The 5<sup>th</sup> NIMS/MANA-Waseda University International Symposium, March 24<sup>th</sup>, **2014**, National Institute for Materials Science (NIMS), Sengen-site, Tsukuba, Japan

**Mohamed B. Zakaria** and Yusuke Yamauchi

3. Controlled Synthesis of Nanoporous Nickel Oxide with Two Dimensional Shapes through Thermal Decomposition of Metal-Cyanide Hybrid Coordination Polymers, The 6<sup>th</sup> Waseda-NIMS International Symposium, July 29<sup>th</sup>, **2015**, Waseda University, 3-4-1 Okubo, Shinjuku, Tokyo, 169-8555, Japan

**Mohamed B. Zakaria** and Yusuke Yamauchi

## Poster presentations

1. Preparation of Cyano-Bridged Coordination Polymers with Well-Defined Shapes and Their Thermal Conversion into Nanoporous Metal Oxides, The 8<sup>th</sup> International Mesostructured Materials Symposium (IMMS-8), May 20-24, **2013**, Awaji Island, Hyogo, Japan.

**Mohamed B. Zakaria**, Ming Hu, and Yusuke Yamauchi

2. Controlled Synthesis of Nanoporous Nickel Oxides with Two-Dimensional Shapes through Thermal Decomposition of Metal-Cyanide Hybrid Coordination Polymers, The International Conference of the Nanospace Materials, June 23-25<sup>th</sup>, 2015, Department of Chemistry, National Taiwan University, Taipei, Taiwan

**Mohamed B. Zakaria** and Yusuke Yamauchi

3. Layer-by-Layer Motif Hybridization: Nanoporous Nickel Oxide Flakes Wrapped into Graphene Oxide Sheets toward Enhanced Oxygen Reduction Reaction, MANA-RSC symposium: Materials for Energy Generation and Storage, October 15-16<sup>th</sup>, 2015, National Institute for Materials Science (NIMS), Namiki-site, Tsukuba, Japan.

**Mohamed B. Zakaria** and Yusuke Yamauchi

4. Two Dimensional Pt/CuO-GO Nanocomposites through Thermal Treatment of Cyano-Bridged Coordination Polymer, The 6<sup>th</sup> Waseda-NIMS International Symposium, July 29<sup>th</sup>, 2015, Waseda University, 3-4-1 Okubo, Shinjuku, Tokyo, 169-8555, Japan  
Azhar S. Alowasheir, **Mohamed B. Zakaria**, Cuiling Li, and Yusuke Yamauchi

## Awards

1. API, APL Materials Poster Award, The International Conference of the Nanospace Materials, June 23-25, 2015, Department of Chemistry, National Taiwan University, Taipei, Taiwan

**Mohamed B. Zakaria**

2. Energy & Environmental Science journal Poster award, MANA-RSC symposium: Materials for Energy Generation and Storage, October 15-16<sup>th</sup>, 2015, National Institute for Materials Science (NIMS), Namiki-site, Tsukuba, Japan

**Mohamed B. Zakaria**

# Acknowledgments

It is my duty, as a start to praise Almighty Allah, lord of the world, whose guidance, blessings and help enabled me to take my first step on the path of improving my knowledge through this humble effort.

Then I want to express the love from my deep heart to my lovely wife “**Dina**” for her unconditional love and support. She did not hesitate to help me and always underestimate the difficulties of life. She is always by my side and encourages me to put more effort and to improve my skills for perfecting my work. I have known what happiness means and really tasted the beauty of life with her. She is for me a wife, a mother, a sister, and the love. I've always continued to work for a long time until late hours of the night and sometimes I was spending my night in the laboratory, she was never complaining, but was pushing me to continue. As for my kids “**Aasr**” and “**Moaiad**”, you are the happiness, hope, life, and beauty. When they laugh, I feel happy and hope. I saw in them the innocence of childhood and knew the meaning of parenthood, the meaning of friendship, the meaning of brotherhood, the meaning of love and the meaning of the beautiful and warm family life. Their smile underestimates many difficulties and innocence gives me hope in life. I dedicate this work to **Dina, Aasr, and Moaiad** and wish they would all beside me at every moment and anywhere. A very special appreciation is due to my **parents, sisters, and brothers** not only for their constant encouragement but also for their patience and understanding throughout. I miss them a lot, I am always far away from them, but they understand. God bless them in all their endeavors.

I would like to express my deepest respect and most sincere gratitude to my supervisor, **Prof. Yusuke Yamauchi**, I am really thankful for him. He initiated and assigned my PhD study. Thanks so much for his valuable advice, help, guidance, encouragement at all stages of my work, stimulating discussion and also reviewing critically the manuscripts. His constructive criticism and comments from the initial conception to the end of this work are highly appreciated. I am greatly indebted to his assistance and understanding in matters of non-academic concern, which have helped me endure some difficult times during my study period. I am fully grateful and wish him the best.

I am happy with the constructive criticism and nice comments from **Prof. Kazuyuki Kuroda, Prof. Turo Asahi, Prof. Yoshiyuki Sugahara, and Prof. Kiyoshi Shimamura**. I would like to say thank you for taking much time for reviewing of my PhD thesis and consideration the presentation. Their invaluable comments and academic advices are appreciated which have made me think more deeply about my research. I have learnt lots from the comments and will think deeply and carefully in the scientific research. Moreover, I wish to thank **Prof. Toyohiro Chikyow, Prof. Yoshio Bando, and Prof. Kevin C.-W. Wu** for their helpful comments,



cooperation, encouragement, and kindness.

I also wish to express my heartfelt thanks and appreciation to **Dr. Cuiling Li, Dr. Ming Hu, Dr. Norihiro Suzuki, Dr. Hamed Atae-Esfahani,** and **Dr. Nagy L. Torad** for their support, tolerance, fruitful and valuable advice, help, guidance, and encouragement at all stages of my work, and also reviewing critically the manuscripts. Also, I would like to thank my lab seniors, mates, and coworkers, **Prof. Dr. Satoshi Tominaka, Prof. Dr. Yusuke Ide, Prof. Dr. Joel Henzie, Dr. Rahul, Dr. Malay, Dr. Victor, Dr. Bishnu Bastakoti, Dr. Yunqi Li, Dr. Monika Ostrowsk, Ms. Jing Tang, Ms. Kimiko Takai, Ms. Sakai, Ms. Azhar, Mr. Jiang Bo, Mr. Muhammed Iqbal, Mr. Asep Sugih, Mr. Mei, Mr. Qian, Ms. Yanna, Mr. Tan, Mr. Yuichiro Kamachi, Ms. Young, Dr. Hongjing Wang, Dr. Xiangfen Jiang** for their cooperation and assistance during the achievement of this work.

I would like to thank the staff of the International Center at Waseda University for their assistance and their time during my PhD study. I thank all administrative and technical staff at Research Division for Materials Nanoarchitectonics (MANA), National Institute for Materials Science (NIMS) for their support. I acknowledge the TST staff at MANA/NIMS, especially **Mr. Iiyama** and **Mr. Nakatsu**, for facilities teaching and use. I greatly appreciate **Mr. Takei** and **Mr. Yamada** for their support on TEM measurements, **Ms. Kaneta Naoko, Ms. Aki Futaesaku, Ms. Hiroko Komura,** and **Ms. Akemi Tateno** for their kindly support.

I acknowledge the financial support from the Ministry of Higher Education in Egypt for four years and thank all members in the Egyptian Culture Office and Embassy of the Arab Republic of Egypt in Tokyo for their kindness and cooperation during my PhD study. I appreciate the support, kindness, and continuous advice of **Prof. Dr. Elrefaey Kenawy**, Head of Chemistry Department, and **Prof. Dr. Ebrahim Salem**, Vice-President for Post-Graduate Studies and Research of Tanta University. In the end, I also wish to express my heartfelt thanks and appreciation to **Prof. Dr. El-Zeiny M. Ebeid**, for his support, tolerance, fruitful and valuable advice, help, kindness, guidance, and encouragement from the start of my scientific journey until now.

*Mohamed B. Zakaria*  
*Waseda University*  
*July 2016*